UNIVERSITY OF SOUTHAMPTON
FACULTY OF ENGINEERING, SCIENCE AND MATHEMATICS
INSTITUTE OF SOUND AND VIBRATION RESEARCH

Least squares estimation of acoustic reflection coefficient

by

Youngjae Cho

Submitted for the Degree of
Doctor of Philosophy

June 2005

UNIVERSITY OF SOUTHAMPTON

ABSTRACT

FACULTY OF ENGINEERING, SCIENCE AND MATHEMATICS
INSTITUTE OF SOUND AND VIBRATION RESEARCH

Doctor of Philosophy

Least squares estimation of acoustic reflection coefficient

by Youngjae Cho

The work presented in this thesis develops further the two-microphone transfer function method used for the measurement of acoustic reflection coefficient of a porous material in an impedance tube. With the use of a least squares solution, the measurement of the transfer functions between multiple microphones can be used to produce an optimal estimation of reflection coefficient. The advantage of using this technique is to extend the frequency range of broadband measurements. The limitations of using the two-microphone transfer function method are analysed in terms of the microphone separations that dictate the upper frequency limit of measurements and it is shown how the measurement of multiple transfer functions can assist in extending the frequency range. Least squares estimation with multiple transfer functions is also applied to free-field measurements based on an image source model of the reflection process. The use of an image source model is found to give good results when used with the least squares solution for measurement of reflection coefficient at normal incidence. Results at oblique incidence seem more difficult to measure accurately in practice because of the precision required in locating microphones. The use of a reflection model, that is associated with plane wave decomposition, is also introduced although this needs a numerical approach in order to enable the application of least squares estimation. The numerical process is demonstrated in a simulation that suggests this technique may ultimately be of practical use.

Acknowledgements

I would like to give my sincere gratitude to Prof. P. A. Nelson. He always has been an great encouragement to me for this work of immense effort, and perhaps I might not be able to appreciate him highly enough. For the technical aspect of this thesis, Dr. K. R. Holland has been a great help and inspiration to me in every respect. I cannot forget the time I spent experiencing measurements in a dreary anechoic chamber. But now suddenly I feel it is my home.

I thank my wife for her devoted support for me during this work. This thesis is dedicated to my Dad and Mum who have done every thing they could do for me.

은혜에 감사드리며 이 논문을 아버지, 어머니에게 헌정합니다.

Contents

Chapter 1 Introduction [1]

1.1 Plane waves [3]

1.2 Spherical waves [6]

1.3 Reflections at a plane boundary and an image source [7]

1.4 The contribution of the thesis [10]

Chapter 2 Literature review [13]

2.1 Measurement of reflection coefficient in a standing wave tube [13]

2.1.1 The standing wave ratio method [14]

2.1.2 The multi-point method [20]

2.1.3 The two-microphone transfer function method [24]

2.2 Measurement of reflection coefficients in a free-field [28]

2.2.1 The surface pressure method [28]

2.2.2 The signal separation method [30]

2.2.3 The two-microphone method [31]

2.2.4 The virtual source method [33]

2.2.5 The spatial Fourier-transform method [35]

2.2.6 The impedance deduction method [37]

2.2.7 The subtraction method [40]

2.3 Conclusions [41]

Chapter 3 Least squares estimation of acoustic reflection coefficients in one-dimensional sound fields [42]

3.1 Image source model with two measurement points [42]
3.2 Applying the least squares solution [45]
3.3 Extension of the theory to deal with multiple-point measurements [48]
3.4 Conclusion [52]

Chapter 4 Application of least squares estimation to impedance tube measurements [53]

4.1 Least squares estimation in an impedance tube [53]
4.2 Optimal choice of microphone separation distances in an impedance tube [62]
4.3 The design of an impedance tube [66]
4.4 Measurement results in an impedance tube [68]
4.5 Conclusion [73]

Chapter 5 Least squares estimation in a free field using an image source model [75]

5.1 A point monopole source and an image source in a free field [75]
5.2 Least squares estimation of acoustic reflection coefficients in a free field using an image source model [77]
5.3 Analysis of error frequencies related to the relative positions of microphones [80]
5.4 Error frequencies in an impedance tube [93]

5.5 Conclusion [95]

Chapter 6 Measurement results in a free field using an image source model [96]

6.1 Normal-incidence measurement [96]
6.2 Oblique-incidence measurement [104]
6.3 Discussion of the size of the test sample [108]
6.4 Errors due to mis-positioning of microphones [112]
6.5 Conclusion [121]

Chapter 7 The application of least squares estimation using a model based on the plane-wave decomposition (PWD) in a free field [124]

7.1 The PWD model of acoustic reflection in a free field [125]
  7.1.1 Plane wave decomposition and acoustic reflection [125]
  7.1.2 The cost function described by acoustic reflection [127]
  7.1.3 Optimally estimated acoustic reflection [131]
7.2 Numerical method for the acquisition of impedance [135]
  7.2.1 Evaluation of the Sommerfeld integral [135]
  7.2.2 Acquisition of impedance by the use of the method of steepest descent [139]
7.3 Conclusion [143]

Chapter 8 Simulation results by the use of a PWD model in a free field [145]

8.1 Simulations using the PWD model [145]

8.2 Conclusion [156]

Chapter 9 Conclusion [157]

References [161]

Appendix I: Algebra details for the derivation of Eqs. (7.36), (7.38), (7.40) and (7.42)

Appendix II: The real part of impedance

Appendix III: Other measurements in a tube and in a free field using an image source model

Appendix IV: Trial measurement in a free field using a PWD model

Chapter 1

INTRODUCTION

In the measurement of acoustic reflection coefficients of porous sound-absorbing materials, the two-microphone transfer function method in an impedance tube or a standing wave tube has been widely used. Since broadband measurements can be made, this method is generally regarded as being more convenient than the one-microphone standing wave ratio method that enables only single-frequency measurements.

The accuracy of the two-microphone transfer function method, however, is less reliable than the classical measurement technique of using pure tones and a single microphone in the standing wave tube. The accuracy of geometry is the most important factor in the two-microphone transfer function method. According to the International Standard specification for this method, an accuracy of $\pm 5mm$ or better in the geometric placing microphones is required for the correct measurement of acoustic reflection coefficients (BS ISO 10534-2:1998). A limited measurement frequency range and far less reliable results at low frequencies caused by microphone separation is another problem.

The frequency range of the two-microphone transfer function method is basically limited by the size of the tube. It also depends on the choice of microphone separation distance. To extend the effective measurement bandwidth to higher or lower frequencies, the microphone separation needs to be shorter or longer respectively, i.e., a decrease in the spacing between the microphones improves high frequency performance but results in a deterioration of low frequency performance and vice versa.

This thesis is the result of a search for a more useful and efficient method of broadband measurement of acoustic reflection coefficients that extends the effective frequency range of measurement to much lower frequencies without sacrificing higher frequency results. For this purpose, a multi-measurement point least squares estimation method for the measurement of the acoustic reflection coefficient has been developed and this is presented in Chapter 3. Based on the two-microphone transfer function method, this least squares estimation method has been developed through the use of an image source model and a least squares solution.

The research presented in this thesis is not only restricted to impedance-tube measurements, but also covers free-field measurement assuming that the sound reflects at a locally-reacting infinite plane boundary. The free-field measurement makes use of a reflection model (Suh, 1998) that decomposes a spherical wave into an infinite sum of plane waves for the description of reflected sound pressure. This enables the measurement of reflection coefficient at oblique incidence where the spherical wave-front is not compatible with the plane-reflecting boundary.

Chapter 1 presents some basic descriptions of sound propagation and reflection, and the contribution of the thesis is summarised at the end of this chapter. Chapter 2 introduces the existing methods for measuring acoustic reflection coefficients in an impedance tube and in a free field.

Chapter 3 presents the development of the multi-measurement point least squares estimation of acoustic reflection coefficient by the use of an image source model in one-dimensional sound field where plane waves propagate and reflect. Chapter 4 describes the direct application of this method to the impedance tube measurement and the results of measurements. Chapter 5 describes the application of this method to the free-field measurement and includes an analysis of "error frequencies" that are related to the relative positions of the source, the image source and microphones. The results of measurements in a free field are presented in Chapter 6 with inclusion of analysis of measurement errors.

In Chapter 7, some modifications to the theory developed in Chapter 3 are made to allow the adoption of a model based on the plane-wave decomposition describing the reflected sound pressure in a free field. The simulation of the application of this theory to the measurements is followed in Chapter 8.

This thesis is concluded in Chapter 9 with a summary of its contribution and suggestion for further research.

1.1 Plane waves

One of the basic forms of sound propagation is the travelling plane wave. The wave progresses in one direction, say the $+x$ direction, with equilibrium acoustic pressure infinitely extended in the y and z directions in a system of rectangular Cartesian coordinates. The simplest form of equation describing such a plane wave is the linearised one-dimensional wave equation assuming that the acoustic pressure fluctuations are adiabatic compressions (Morse, 1936). This is given by

$$\frac{\partial^2 p}{\partial x^2}-\frac{1}{c^2}\frac{\partial^2 p}{\partial t^2}=0 \qquad (1.1)$$

where p is the acoustic pressure and c is the speed of sound in the medium supporting acoustic propagation. The solution of Eq. (1.1) is given by

$$p(x,t)=g\left(t-\frac{x}{c}\right) \quad \text{or} \quad p(x,t)=g\left(t+\frac{x}{c}\right) \qquad (1.2)$$

depending on the positive or negative direction of propagation. The solution g is any function differentiable twice with respect to x or t. A particularly important solution, both conceptually and mathematically that describes a harmonic wave travelling in the positive x direction with a single frequency, f, is given by

$$p(x,t)=\mathrm{Re}\left\{Ae^{j(\omega t-kx)}\right\} \qquad (1.3)$$

where $\mathrm{Re}\{\ \}$ denotes the real part of a complex number, ω and k are angular frequency and wavenumber that are given by

$$\omega=2\pi f \quad \text{and} \quad k=\frac{\omega}{c} \qquad (1.4)$$

and A is a complex number of which the modulus, i.e. $|A|$, represents the amplitude of the acoustic wave pressure. The complex exponential form in Eq. (1.3) is for the convenience of mathematical operations. As A can be expressed in polar coordinate as

$$A = |A|e^{j\phi_A} \tag{1.5}$$

where ϕ_A is an arbitrary phase angle of A, Eq. (1.3) reduces to

$$p(x,t) = |A|\cos(\omega t - kx + \phi_A) \tag{1.6}$$

Often only the spatial component of Eq. (1.4) is used for sound field modelling regardless of time dependence. From Eq. (1.4), an expression for a one-dimensional standing wave can be obtained, which is normally generated in a waveguide where the acoustic pressure wave travels back and forth reflected from the ends. For a standing wave, only the spatial term is considered such that the spatially dependent complex acoustic pressure is written as

$$p(x) = Ae^{-jkx} + Be^{jkx} \tag{1.7}$$

where A and B are arbitrary complex numbers that have the amplitude and phase information associated with the waves propagating in the $+x$ and $-x$ directions respectively. Eq. (1.4) can therefore be rewritten as

$$p(x,t) = \mathrm{Re}\left\{p(x)e^{j\omega t}\right\} \tag{1.8}$$

Eq. (1.7) is generally used as a representation of the acoustic pressure in a standing wave tube where the time dependence is not considered for the purpose of measuring impedance or a reflection coefficient.

1.2 Spherical waves

The sound radiated from an omnidirectional source in three-dimensional space spreads outward with spherical symmetry and can be described by the three-dimensional wave equation in spherical coordinates. For the spherically symmetric case, this is given by

$$\frac{1}{r^2}\frac{\partial}{\partial r}\left(r^2\frac{\partial p}{\partial r}\right)-\frac{1}{c^2}\frac{\partial^2 p}{\partial t^2}=0 \tag{1.9}$$

A solution to Eq. (1.9) is given by

$$p(r,t)=\mathrm{Re}\left\{\frac{Ae^{j(\omega t-kr)}}{r}\right\} \tag{1.10}$$

with the radially dependent complex pressure expressed as

$$p(r)=\frac{Ae^{-jkr}}{r} \tag{1.11}$$

From the boundary condition at the surface of a monopole source with a radius of a, the complex value of A can be determined as the product ka becomes far less than unity. It follows that (see, for example, Nelson and Elliott, 1992)

$$A=\frac{j\omega\rho_0 q}{4\pi} \tag{1.12}$$

where ρ_0 is an ambient density of the acoustic medium and q is the strength of the source. Hence Eq. (1.11) is rewritten as

$$p(r)=\frac{j\omega\rho_0 q e^{-jkr}}{4\pi r} \tag{1.13}$$

The acoustic pressure field generated by a point monopole source is generally expressed by Eq. (1.13). Due to the limited size of an actual sound source, Eq. (1.13) is valid in a limited frequency range.

1.3 Reflections at a plane boundary and an image source

When a plane wave is bounded by a plane uniform boundary, the reflected wave can be described in terms of the specific acoustic impedance or unit area acoustic impedance (Pierce, 1981, p107), Z_s, of the reflecting boundary. This is defined by the complex quantity

$$Z_s=\left(\frac{p}{u_n}\right)_{\text{surface}} \tag{1.14}$$

where p is the local complex acoustic pressure and u_n is the complex particle velocity normal to the surface at the same point on the surface of the boundary. The specific acoustic

impedance is usually normalised by dividing it by the characteristic impedance, Z_c of an acoustic medium which is a real quantity and is given by

$$Z_c = \rho_0 c \tag{1.15}$$

such that the definition of dimensionless specific acoustic impedance, ξ, is given by

$$\xi = \frac{Z_s}{\rho_0 c} \tag{1.16}$$

The specific acoustic impedance is a unique character of a reflecting material. Assuming that the boundary is locally reacting, i.e., pushing the surface at one point does not move it elsewhere, the specific acoustic impedance is independent of the angle of an incident wave because it is the complex ratio of local pressure to the normal particle velocity at a given specific point on the boundary.

The reflected plane wave has smaller amplitude and undergoes a phase change. Both changes are described by the pressure reflection factor R (Kuttruff, 2000). With the introduction of this term, the surface impedance can be expressed as

$$Z = \frac{\rho_0 c}{\cos\theta} \frac{1+R}{1-R} \tag{1.17}$$

where θ is the angle of incidence to the normal line of the surface. From Eqs. (1.16) and (1.17), the complex reflection coefficient is obtained, and this is given by

$$R(\theta) = \frac{\xi \cos\theta - 1}{\xi \cos\theta + 1} \tag{1.18}$$

At normal incidence this equation reduces to

$$R = \frac{\xi - 1}{\xi + 1} \tag{1.19}$$

These expressions are valid assuming that only plane waves are incident upon the reflecting surface. In reality, however, sound waves propagate spherically in space. Hence the plane-wave reflection described above is regarded as a useful approximation when the sound source is not too close to the reflecting surface such that the curvature of the wave fronts can be neglected without too much error. With these limitations, the reflection of spherical waves can be approximately described by plane-wave reflection and by introducing an image source, i.e., a replica of the actual source located at the opposite point of symmetry in a free field (Morfey, 2001). This is illustrated in Fig. 1.1.

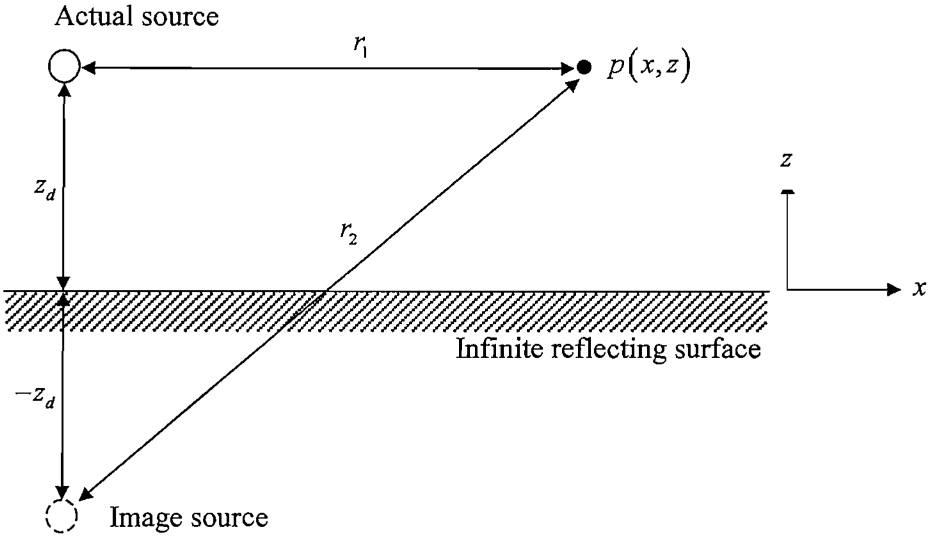

FIG. 1.1: An image source model in the $x-z$ plane

Using Eq. (1.13), the resultant sound pressure at a measurement position can be expressed as an addition of both sound fields generated by an actual source and an image source.

$$p(x,z) = \frac{j\omega\rho_0 q e^{-jkr_1}}{4\pi r_1} + \frac{j\omega\rho_0 q_{\text{image}} e^{-jkr_2}}{4\pi r_2} \tag{1.20}$$

When the strength of the actual source is q, that of the image source can be assigned as a product of the strength of the actual source and a complex reflection coefficient, R, i.e.,

$$q_{\text{image}} = Rq \tag{1.21}$$

Hence Eq. (1.20) can be rewritten as

$$p(x,z) = \frac{j\omega\rho_0 q e^{-jkr_1}}{4\pi r_1} + R\frac{j\omega\rho_0 q e^{-jkr_2}}{4\pi r_2} \tag{1.22}$$

This simple image-source representation can only simulate boundaries whose reflection coefficient is independent of angle of incidence. An exact image-source representation is available only for rigid or pressure-release boundaries (Morfey, 2001). Rigid boundaries have a unit reflection coefficient whereas pressure-release boundaries have a zero pressure over all time. That is

$$\begin{aligned} &R = 1,\ \ |Z| \to \infty \quad \text{for rigid boundaries} \\ &Z = 0,\ \ R = -1 \quad \text{for pressure-release boundaries} \end{aligned} \tag{1.23}$$

1.4 The contribution of the thesis

In Chapter 3, the beginning of the main part of this thesis, a newly developed theory of measuring acoustic reflection coefficient is presented. This theory provides a measurement technique that is an improvement of the existing methods. In essence, this new theory combines two separate theories into one. One of them is the multi-point method (see Section 2.1.2) and the other is the two-microphone transfer function method for the measurement of impedances of porous materials (see Section 2.1.3).

By the use of a least squares solution together with multiple measurement points from which the differences between the analytically modelled and measured transfer functions are minimised, and through this process the acoustic reflection coefficient or impedance is optimally estimated. The most important advantage of this new technique applied to the impedance tube measurement over the existing methods is the convenience of using a single tube over a wide range of frequency for a broadband measurement. The two-microphone transfer function method needs several tubes with different diameters for different frequency range of measurement. Furthermore, experience has shown that the results are very often discontinuous at the boundary where the upper frequency limit of low frequency measurement (with a larger tube) and the lower frequency limit of the high frequency measurement (with a smaller tube). It is then difficult to combine these measurement results into a single representation. The new method presented here, however, results in continuity of the measured values of reflection coefficient over a broad frequency range.

In an impedance tube, the highest frequency that propagates as a plane wave is limited by the diameter of the tube. This limitation, in the application of the two-microphone transfer function method in an impedance tube, restricts the microphone separation to be shorter than a certain criterion. Thus the low frequency information is lost in the measurement. This fact is also related to the error frequencies related to the relative distances between sources and detectors, which is fully explained and analysed in Chapter 5.

The new method overcomes these restrictions and results in a wider measurement bandwidth without any loss of accuracy of measurements. This technique is also applied to the free-field measurement with an image source model and also with a plane-wave decomposition model for a better description of reflection of a spherical wave at a plane boundary. Measurement results at normal incidence with an image source model ascertain that this method can be used in a free field with a certain degree of geometrical accuracy while simulation results with a plane-wave decomposition model suggest some guidelines for a practical usage of this method.

Chapter 2

LITERATURE REVIEW

The measurement of acoustic reflection coefficient or the impedance of reflecting boundaries has been performed in many ways in a standing wave tube and in a free field, and many different representations of an acoustic reflection model have been used for each situation. Due to the well-controlled measurement environment of the standing wave tube, the free-field measurement has always referenced the measurement results of the standing wave tube method. This chapter shows how these methods have developed so far.

2.1 Measurement of reflection coefficient in a standing wave tube

The standing wave tube, also called as an impedance tube, was developed from Kundt's tube, which had been originally designed and invented by Kundt (1866) for measuring the speed of sound in gases. Several methods have been developed to measure the specific acoustic impedance or acoustic reflection coefficient using a standing wave tube. These are reviewed below.

2.1.1 The standing wave ratio method

The conventional standing wave ratio method uses a pure tone sound source and one measurement microphone that is attached to a car, which can slide along a graduated ruler.

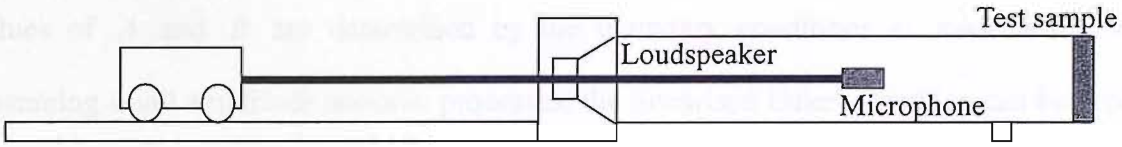

FIG. 2.1: The conventional standing wave tube for SWR method

The pure tone acoustic wave produced by the sound source travels down the tube and reflects from the test sample. The interference between the waves in the tube that are incident upon and reflected from the test sample will result in the formation of a standing wave pattern in the tube. Since the test sample absorbs some of the energy of the incident wave, the amplitude of the reflected wave is smaller than that of the incident wave. Hence the nodes of the standing wave in the tube no longer have zero pressure. The ratio of the maximum pressure at the antinodes to the minimum pressure at the nodes is called the standing wave ratio (SWR) from which the magnitude of reflection coefficients of the sample can be determined.

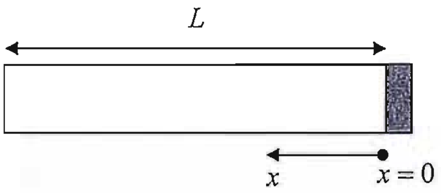

FIG. 2.2: A standing wave tube with a cross-sectional area S and length L.

When the cross-sectional area and the length of the tube are S and L respectively, the acoustic wave pressure in the tube is in the form of (Kinsler *et al*, 1982)

$$p = p_i + p_r = Ae^{j(\omega t - kx)} + Be^{j(\omega t + kx)} \tag{2.1}$$

where the angular frequency is given by ω and k is the wavenumber. The complex values of A and B are determined by the boundary conditions at $x = 0$ and $x = L$. Assuming small amplitude acoustic processes, the linearised Euler's equation can be applied. This is given by

$$\rho_0 \frac{\partial u}{\partial t} = -\nabla p \tag{2.2}$$

where u is the particle velocity and ρ_0 is the density of air in the tube. Substituting Eq. (2.1) into Eq. (2.2) gives

$$u = u_i + u_r = \frac{1}{\rho_0 c}\left[Ae^{j(\omega t - kx)} - Be^{j(\omega t + kx)}\right] \tag{2.3}$$

where u is here assumed to be the complex particle velocity. Then the specific acoustic impedance defined in Eq. (1.14) may, for the standing plane waves in the tube, be expressed as

$$Z_s(x) = \frac{p}{u} = \rho_0 c\left[\frac{Ae^{-jkx} + Be^{jkx}}{Ae^{-jkx} - Be^{jkx}}\right] \tag{2.4}$$

If the complex values of A and B are chosen to be expressed as

$$A = a, \qquad B = be^{j\phi} \tag{2.5}$$

where a and b are real and positive, then the specific acoustic impedance, at $x = 0$, can be rewritten

$$Z_s(x) = \rho_0 c\left[\frac{A+B}{A-B}\right] = \rho_0 c\left[\frac{1+(b/a)e^{j\phi}}{1-(b/a)e^{j\phi}}\right] \tag{2.6}$$

Meanwhile the amplitude of pressure in the tube is obtained by substituting Eq. (2.5) into Eq. (2.1). This gives

$$|p| = \left|ae^{j(\omega t - kx)} + be^{j(\phi + \omega t + kx)}\right| \tag{2.7}$$

For the convenience of further expansion of the above equation, the following terms are defined.

$$\delta \equiv \frac{\omega t - kx}{2}, \quad \gamma \equiv \frac{\phi + \omega t + kx}{2} \quad \text{and} \quad \tau \equiv \gamma - \delta \tag{2.8}$$

Then Eq. (2.7) is rewritten

$$|p| = \left|a(\cos 2\delta + j\sin 2\delta) + b(\cos 2\gamma + j\sin 2\gamma)\right| \tag{2.9}$$

Collecting real part and imaginary parts separately, this becomes

$$|p| = |a\cos 2\delta + b\cos 2\gamma + j(a\sin 2\delta + b\sin 2\gamma)| \tag{2.10}$$

Now the absolute value of the acoustic pressure reduces to

$$\begin{aligned}|p| &= \sqrt{(a\cos 2\delta + b\cos 2\gamma)^2 + (a\sin 2\delta + b\sin 2\gamma)^2} \\ &= \sqrt{a^2 + b^2 + 2ab(\cos 2\delta \cos 2\gamma + \sin 2\delta \sin 2\gamma)} \\ &= \sqrt{a^2 + b^2 + 2ab\cos 2\tau} \\ &= \sqrt{a^2 + b^2 + 2ab(\cos^2\tau - \sin^2\tau)}\end{aligned} \tag{2.11}$$

Using the relationship $\sin^2\theta + \cos^2\theta = 1$ where θ is an arbitrary variable, Eq. (2.11) can be further expanded into

$$\begin{aligned}|p| &= \sqrt{a^2(\cos^2\tau + \sin^2\tau) + b^2(\cos^2\tau + \sin^2\tau) + 2ab(\cos^2\tau - \sin^2\tau)} \\ &= \sqrt{(a^2 + b^2 + 2ab)\cos^2\tau + (a^2 + b^2 - 2ab)\sin^2\tau} \\ &= \sqrt{(a+b)^2\cos^2\tau + (a-b)^2\sin^2\tau}\end{aligned} \tag{2.12}$$

The final result is obtained by substituting Eq. (2.8) into Eq. (2.12) such that

$$|p| = \sqrt{(a+b)^2\cos^2(kx + \phi/2) + (a-b)^2\sin^2(kx + \phi/2)} \tag{2.13}$$

Now the minimum pressure occurs when

$$\cos\left(kx+\phi/2\right)=0 \quad \text{and} \quad \sin\left(kx+\phi/2\right)=1 \tag{2.14}$$

which is also obvious in Eq. (2.11) and this shows that the pressure is at its minimum when

$$\cos 2\left(kx+\phi/2\right)=-1 \tag{2.15}$$

Eq. (2.14) shows that the phase shift of the reflected waves at the first node is

$$\phi=\pi-2kx \tag{2.16}$$

The value of ϕ can therefore be measured by measuring the position (x) of the first node. The positive real values, a and b, cannot be measured directly, but the maximum pressure amplitude of $a+b$ at an antinode and the minimum pressure amplitude of $a-b$ at a node in the resultant standing waves in the tube can be measured.

$$\begin{aligned} &\phi=2n\pi-2kx \quad \text{at antinodes,} \quad n=0,\ 1,\ 2,\ldots \\ &\phi=\left(2n+1\right)\pi-2kx \quad \text{at nodes,} \quad n=0,\ 1,\ 2,\ldots \end{aligned} \tag{2.17}$$

The ratio of maximum pressure to minimum pressure is defined as the standing wave ratio (SWR).

$$\text{SWR}=\frac{a+b}{a-b} \tag{2.18}$$

which can be rearranged to provide the amplitude of the acoustic pressure reflection coefficient

$$|R| = \frac{b}{a} = \frac{\mathrm{SWR}-1}{\mathrm{SWR}+1} \tag{2.19}$$

where the complex acoustic pressure reflection coefficient is defined by

$$R \equiv \frac{B}{A} = \frac{be^{j\phi}}{a} = |R|e^{j\phi} \tag{2.20}$$

and the sound power absorption coefficient, α , which is positive real, is given by

$$\alpha = 1 - |R|^2 \tag{2.21}$$

This method requires the length of the tube to be longer than a half wavelength of the lowest frequency of interest because at least one set of antinode and node should be present within the length of the tube (see Eq. (2.17)). The upper frequency is limited by the diameter of the circular tube or the longer side of the cross section of a rectangular tube since the propagation is restricted to plane waves and the propagation of the first cross mode or above that frequency components must be avoided. Thus

$$f_{\max} < \frac{Kc}{d} \tag{2.22}$$

where $f_{\max}$ is maximum frequency for which a plane wave can propagate in a tube and c is the speed of sound. For circular tubes, d is the diameter of the tube and K is defined as 0.586. For rectangular tubes, d is the longer side of the cross section of the tube and K is defined as 0.500 (ASTM E 1050-98).

2.1.2 The multi-point method

The accuracy of the results obtained from the SWR method depends on the accuracy of measurement of the pressure minimum and maximum. In general the exact measurement of these values is not easy. Fujimori *et al* (1984) suggested using a least squares method to reduce measurement errors for the acquisition of the reflection coefficient at a single frequency, and later on Pope (1986) showed a usage of this method for broadband measurement. Sound pressures are measured at several points along the tube, and then an attempt is made to minimise the errors between the theoretically predicted standing wave pressures and the measured values. Let Ae^{-jkx_n} be the pressure of the incident sound, Be^{jkx_n} be the pressure of the reflected sound and p_n be the measured pressure at a given point. The error function is defined by

$$E = \sum_{n=1}^{N} \left| Ae^{-jkx_n} + Be^{jkx_n} - p_n \right|^2 \tag{2.23}$$

where N is the total number of measurement points. Since A and B are complex values, they can be denoted by

$$A = A_R + jA_I \quad \text{and} \quad B = B_R + jB_I \tag{2.24}$$

and the complex value p_n can be replaced by

$$p_n = |p_n| e^{j\phi_n} \tag{2.25}$$

Following Fujimori *et al* (1984), the complex reflection coefficient R is obtained by substituting Eqs. (2.24) and (2.25) into Eq. (2.23) and applying the minimum condition, i.e.,

$$\frac{\partial E}{\partial A_R} = \frac{\partial E}{\partial A_I} = \frac{\partial E}{\partial B_R} = \frac{\partial E}{\partial B_I} = 0 \tag{2.26}$$

From Eq. (2.26), four independent normal equations are obtained.

$$\begin{aligned}
&\sum_{n=1}^{N} A_R \cos(2kx_n) + \sum_{n=1}^{N} A_I \sin(2kx_n) + \sum_{n=1}^{N} B_R = \sum_{n=1}^{N} |p_n| \cos(kx_n - \phi_n) \\
&-\sum_{n=1}^{N} A_R \sin(2kx_n) + \sum_{n=1}^{N} A_I \cos(2kx_n) + \sum_{n=1}^{N} B_I = \sum_{n=1}^{N} |p_n| \sin(kx_n - \phi_n) \\
&\sum_{n=1}^{N} A_R + \sum_{n=1}^{N} B_R \cos(2kx_n) - \sum_{n=1}^{N} B_I \sin(2kx_n) = \sum_{n=1}^{N} |p_n| \cos(kx_n + \phi_n) \\
&\sum_{n=1}^{N} A_I + \sum_{n=1}^{N} B_R \sin(2kx_n) + \sum_{n=1}^{N} B_I \cos(2kx_n) = \sum_{n=1}^{N} |p_n| \sin(kx_n + \phi_n)
\end{aligned} \tag{2.27}$$

This equation can be rewritten in matrix form.

$$\begin{bmatrix} \sum_{n=1}^{N}\cos(2kx_n) & \sum_{n=1}^{N}\sin(2kx_n) & N & 0 \\ -\sum_{n=1}^{N}\sin(2kx_n) & \sum_{n=1}^{N}\cos(2kx_n) & 0 & N \\ N & 0 & \sum_{n=1}^{N}\cos(2kx_n) & -\sum_{n=1}^{N}\sin(2kx_n) \\ 0 & N & \sum_{n=1}^{N}\sin(2kx_n) & \sum_{n=1}^{N}\cos(2kx_n) \end{bmatrix} \begin{bmatrix} A_R \\ A_I \\ B_R \\ B_I \end{bmatrix} = \begin{bmatrix} \sum_{n=1}^{N}|p_n|\cos(kx_n-\phi_n) \\ \sum_{n=1}^{N}|p_n|\sin(kx_n-\phi_n) \\ \sum_{n=1}^{N}|p_n|\cos(kx_n+\phi_n) \\ \sum_{n=1}^{N}|p_n|\sin(kx_n+\phi_n) \end{bmatrix} \tag{2.28}$$

By using Cramer's rule the value of A_R is obtained by the following equation.

$$A_R = \frac{1}{D}\begin{vmatrix} \sum_{n=1}^{N}|p_n|\cos(kx_n-\phi_n) & \sum_{n=1}^{N}\sin(2kx_n) & N & 0 \\ \sum_{n=1}^{N}|p_n|\sin(kx_n-\phi_n) & \sum_{n=1}^{N}\cos(2kx_n) & 0 & N \\ \sum_{n=1}^{N}|p_n|\cos(kx_n+\phi_n) & 0 & \sum_{n=1}^{N}\cos(2kx_n) & -\sum_{n=1}^{N}\sin(2kx_n) \\ \sum_{n=1}^{N}|p_n|\sin(kx_n+\phi_n) & N & \sum_{n=1}^{N}\sin(2kx_n) & \sum_{n=1}^{N}\cos(2kx_n) \end{vmatrix} \tag{2.29}$$

where D is the determinant of the four by four matrix on the left side of Eq. (2.28). Likewise each value of A_I, B_R and B_I is obtained to give the value of the complex reflection coefficient R. Thus

$$A_I = \frac{1}{D}\begin{vmatrix} \sum_{n=1}^{N}\cos(2kx_n) & \sum_{n=1}^{N}|p_n|\cos(kx_n-\phi_n) & N & 0 \\ -\sum_{n=1}^{N}\sin(2kx_n) & \sum_{n=1}^{N}|p_n|\sin(kx_n-\phi_n) & 0 & N \\ N & \sum_{n=1}^{N}|p_n|\cos(kx_n+\phi_n) & \sum_{n=1}^{N}\cos(2kx_n) & -\sum_{n=1}^{N}\sin(2kx_n) \\ 0 & \sum_{n=1}^{N}|p_n|\sin(kx_n+\phi_n) & \sum_{n=1}^{N}\sin(2kx_n) & \sum_{n=1}^{N}\cos(2kx_n) \end{vmatrix} \tag{2.30}$$

$$B_R = \frac{1}{D} \begin{vmatrix} \sum_{n=1}^{N} \cos(2kx_n) & \sum_{n=1}^{N} \sin(2kx_n) & \sum_{n=1}^{N} |p_n| \cos(kx_n - \phi_n) & 0 \\ -\sum_{n=1}^{N} \sin(2kx_n) & \sum_{n=1}^{N} \cos(2kx_n) & \sum_{n=1}^{N} |p_n| \sin(kx_n - \phi_n) & N \\ N & 0 & \sum_{n=1}^{N} |p_n| \cos(kx_n + \phi_n) & -\sum_{n=1}^{N} \sin(2kx_n) \\ 0 & N & \sum_{n=1}^{N} |p_n| \sin(kx_n + \phi_n) & \sum_{n=1}^{N} \cos(2kx_n) \end{vmatrix} \tag{2.31}$$

$$B_I = \frac{1}{D} \begin{vmatrix} \sum_{n=1}^{N} \cos(2kx_n) & \sum_{n=1}^{N} \sin(2kx_n) & N & \sum_{n=1}^{N} |p_n| \cos(kx_n - \phi_n) \\ -\sum_{n=1}^{N} \sin(2kx_n) & \sum_{n=1}^{N} \cos(2kx_n) & 0 & \sum_{n=1}^{N} |p_n| \sin(kx_n - \phi_n) \\ N & 0 & \sum_{n=1}^{N} \cos(2kx_n) & \sum_{n=1}^{N} |p_n| \cos(kx_n + \phi_n) \\ 0 & N & \sum_{n=1}^{N} \sin(2kx_n) & \sum_{n=1}^{N} |p_n| \sin(kx_n + \phi_n) \end{vmatrix} \tag{2.32}$$

Hence the complex reflection coefficient is obtained from

$$R = \frac{B_R + jB_I}{A_R + jA_I} = \frac{B}{A} \tag{2.33}$$

In this method, a microphone is fixed near the test sample at a hole on the wall of the tube while the main microphone moves in the tube for the measurement of sound pressure at a given point. This is for a compensation of the influence caused by the moving microphone that affects the sound pressure of incident wave on the test sample (Fujimori *et al*, 1984). Jones and Parrott investigated this method in more detail (Jones *et al*, 1989). They measured reflection coefficients of various materials and found that microphone separation of a quarter wavelength, i.e., two measurement points over each one-half wavelength, is generally sufficient for the reconstruction of a standing wave at a given frequency, which had conventionally been referred to as an optimal microphone separation in the SWR method. Increasing the number of measurement points reduces error but it does not have a significant effect for materials for which the magnitude of the reflection coefficient is small. Later on Cheung *et al* (1995) suggested that three measurement points over a half wavelength, i.e.,

$$\Delta x = \lambda/6 \tag{2.34}$$

would yield better accuracy for wave component fitting.

Jones and Stiede (1997) compared all the commonly used methods of measuring reflection coefficients, i.e., the SWR method, the multi-point method and the two-microphone transfer function method described below. They showed that the multi-point method with a single discrete frequency is the most accurate even if it is the most time consuming.

2.1.3 The two-microphone transfer function method

The SWR method is for a single discrete frequency at a time and hence requires much time to complete for a broadband measurement. The transfer function method was developed to eliminate such a time consuming process by using random (white) noise (or other types of signal) as a sound source and by making use of digital technology and the swift FFT processes. This method was first introduced by Seybert and Ross (1977) who used auto- and cross-spectral densities to separate the incident and the reflected waves for the acquisition of acoustic properties at normal incidence.

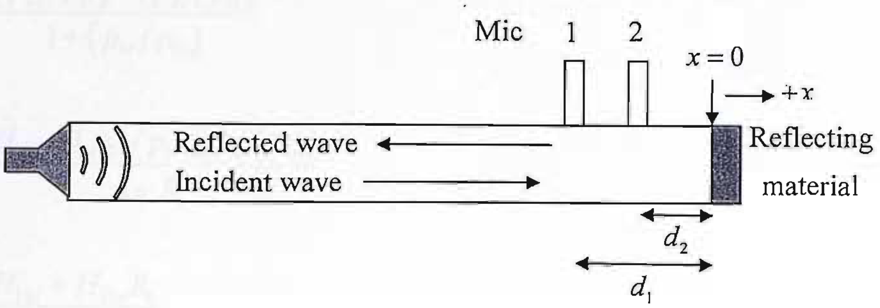

FIG. 2.3: The standing wave tube for transfer function method

In the frequency domain, the measured transfer function between the two microphones is given by (Katz, 2000)

$$H_{12} = \frac{p_2}{p_1} = \frac{p_{2i} + p_{2r}}{p_{1i} + p_{1r}} \tag{2.35}$$

where p_1 and p_2 are sound pressures picked up at microphone 1 and 2 respectively, and subscript i and r correspond to incident sound pressure and reflected sound pressure respectively. At each microphone position, the following transfer functions can be defined.

$$H_{12i} = \frac{p_{2i}}{p_{1i}}, \quad H_{12r} = \frac{p_{2r}}{p_{1r}}, \quad R_1 = \frac{p_{1r}}{p_{1i}}, \quad R_2 = \frac{p_{2r}}{p_{2i}} \tag{2.36}$$

where R_1 and R_2 are complex reflection coefficients at microphone position 1 and 2 respectively. Dividing the numerator and denominator of the right hand side of Eq. (2.35) by p_{1i} and using the relationships given in Eq. (2.36), the transfer function H_{12} can be written as

$$H_{12} = \frac{(p_{2i}/p_{1i}) + (p_{2r}/p_{1i})}{1 + (p_{1r}/p_{1i})}$$

$$= \frac{H_{12i} + (p_{2r}/p_{1r})(p_{1r}/p_{1i})}{1 + R_1} \tag{2.37}$$

$$= \frac{H_{12i} + H_{12r} R_1}{1 + R_1}$$

Rearranging Eq. (2.37) gives the expression for R_1, i.e.,

$$R_1 = \frac{H_{12i} - H_{12}}{H_{12} - H_{12r}} \tag{2.38}$$

Assuming that only plane waves propagate inside the tube, analytical expressions for the transfer functions are

$$H_{12i} = e^{-jk(d_1 - d_2)}, \quad H_{12r} = e^{jk(d_1 - d_2)} \tag{2.39}$$

where d_1 and d_2 are the distances of microphones 1 and 2 respectively from the test sample. Meanwhile from the definition of R_1 in Eq. (2.36), the phase difference between R_1 and R, the reflection coefficient at the reflecting surface where $x = 0$, is e^{j2kd_1}. Hence R is given by

$$R = e^{j2kd_1} R_1 \tag{2.40}$$

Combining Eqs. (2.38), (2.39) and (2.40) leads to

$$
\begin{aligned}
R &= e^{j2kd_1}\left[\frac{H_{12i}-H_{12}}{H_{12}-H_{12r}}\right] \\
&= e^{j2kd_1}\left[\frac{e^{-jk(d_1-d_2)}-H_{12}}{H_{12}-e^{jk(d_1-d_2)}}\right] \\
&= -e^{j2kd_1}\left[\frac{H_{12}-e^{-jk(d_1-d_2)}}{H_{12}-e^{jk(d_1-d_2)}}\right]
\end{aligned}
\tag{2.41}
$$

In this method, the effective frequency range is related to the microphone separation $d_1 - d_2$. The microphone separation should be shorter than one half of the wavelength at the upper frequency limit. A detailed analysis of this relationship is presented in the next chapter. Microphone 1 and 2 should be carefully calibrated for consistency, which is not easy in practice. Chung and Blaser (1980) introduced a microphone-switching technique to minimise errors due to the use of an ill-calibrated pair of microphones, and later the use of single microphone at two different measurement points was suggested by Chu (1986) to eliminate any possible errors, e.g., phase mismatching, from a pair of microphones. Nonetheless Chu also showed that this method is less reliable than the SWR method. Although the choice of microphone separation had been emphasised before, it is Bodén and Åbom (1986) who investigated the possible errors systematically. Bias errors occur from insufficient frequency resolution and ensemble averaging of random signals, and inaccurate geometry yields another significant error. According to ASTM (E1050-98) 0.1*mm* of accuracy is required in positioning microphones. With all these factors considered, Jones and Stiede (1997) compared four possible methods to show the pros and cons of the standing wave method, the two-microphone method without microphone switching, the two-microphone method with microphone switching and the multi-point method. They suggested that the multi-point single microphone method with least squares fit could be a reference for others because it is the most time consuming but the most accurate.

Meanwhile Katz (2000) revisited this method and collected a set of criteria that are required for improved accuracy. This method is particularly interesting because it is the least time consuming. There are some general guidelines to be followed in this method (ASTM E 1050-98). Once the measurement frequency range is decided, then

$$d \leq 0.586c/f_{\max} \quad \text{and} \quad s = c/4f_{\text{centre}} \tag{2.42}$$

where d is the diameter of a circular tube, c is speed of sound in the tube, s is a microphone separation, $f_{\max}$ is a maximum frequency to be measured and f_{centre} is the centre frequency of the whole range of measurement.

2.2 Measurement of reflection coefficients in a free field

Unlike sound propagation in a tube, plane wave propagation is approximated in a free field only when the source is reasonably far away from the detector, and hence the reflection of the wave front can be described with a plane wave model. A spherical-wave reflection model, however, gives a better description of acoustic reflection in a free field. In this section, the methods for the measurement of reflection coefficient in a free field with both plane-wave and spherical-wave reflection models are reviewed.

2.2.1 The surface pressure method

In this method, the pressure amplitude and phase of an incident plane wave in steady state are measured at a point on the surface of the absorptive material, and they are compared with those measured at the same point in a space on the surface of a perfectly reflecting material, or at the same point in free space without any reflecting material.

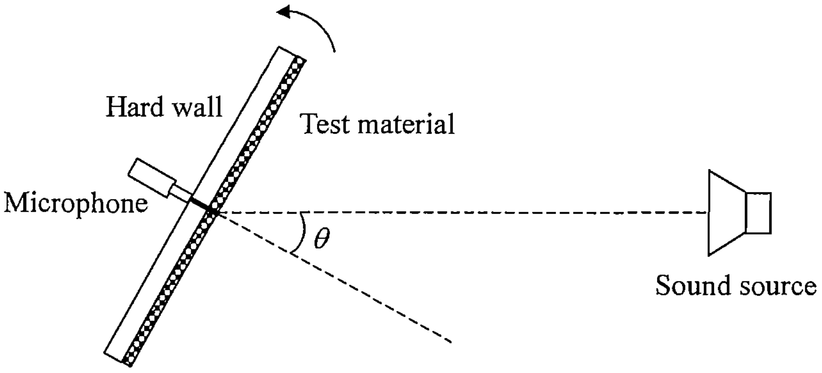

FIG. 2.4: The surface pressure method with a rotating test material

For locally reacting materials, measurement of the normal impedance is enough to derive other relevant properties, i.e., reflection coefficient and absorption coefficient. In practice, however, no absorptive material is perfectly locally reacting and some materials show strong dependence on angle of incidence for their absorption coefficient. Ingård and Bolt measured the incidence-angle dependent absorption coefficient by rotating the test material about a fixed axis which is normal to the direction of incident acoustic waves. This is illustrated in Fig. 2.4. At a hard wall the measured sound pressure is double that of the incident sound pressure, and a certain amount of this incident pressure is reflected at the test material. Let the magnitude and phase measured at a hard wall be $|p_1|$ and ϕ_1, those measured at the surface of test material be $|p_2|$ and ϕ_2, and $\varphi = \phi_1 - \phi_2$, then the absorption coefficient is given by (Ingård and Bolt, 1951)

$$\alpha = \cos^2\phi - 4\left(\frac{|p_1|}{|p_2|} - \frac{1}{2}\cos\phi\right)^2 \tag{2.43}$$

Once the reflection coefficient is obtained at an angle of incidence of θ, the normalised impedance can be calculated. Yuzawa (1975) presented a similar method called the 'cancellation method' where the incident and the reflected sound pressures are measured and calculated from the measurement in free space and the measurement in front of the absorptive material.

2.2.2 The signal separation method

In this method, random noise is used as a sound source rather than a single tone. By the process of correlation and Fourier transform, the frequency response between the source and microphone can be obtained. The frequency response F_s, where s denotes sample of the test material, obtained with the microphone placed between the sound source and the absorptive material should contain information regarding the reflection coefficient of the sample. F_r is the frequency response obtained from the measurement when the sample is replaced by a perfect reflector. In practice, a perfect reflector is not available, so F_r is measured in free space without any reflector. First the direct sound from the source is measured at the original microphone position where it has been for the measurement of F_s, and then the microphone is place further back from the source by twice the distance between the microphone and the test sample. Then in a free field the direct sound is measured and added to the first measurement to yield F_r. In this case the absorption coefficient is given by (Hollin and Jones, 1977)

$$\alpha = 1 - \left| \frac{F_s}{F_r} \right|^2 \tag{2.44}$$

The microphone distance from the sound source and the test sample should be carefully chosen as far as standing waves are concerned. The possibility of broadband measurement is the greatest advantage of this method. Davies and Mulholland (1979) used the same method, but by obtaining impulse responses rather than the frequency response directly, they could window out unwanted reflections before the Fourier transform was performed.

2.2.3 The two-microphone method

Allard and Sieben (1985) used a two-microphone technique for the measurement of impedance. The sound pressure p and the sound particle velocity u at the midpoint, M, of the two microphones, M_1 and M_2 that are spaced very close to each other can be approximated in complex representation by

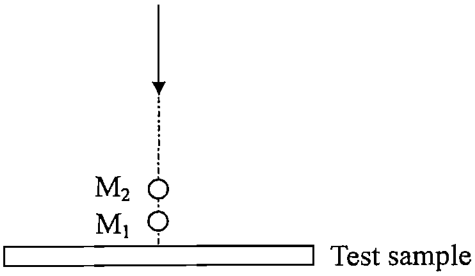

FIG. 2.5: Set-up of two microphones at the axis of normal incident upon the sample

$$u = -\frac{p_2 - p_1}{j\omega\rho d_{12}}$$

$$p = \frac{p_1 + p_2}{2} \tag{2.45}$$

where c is the speed of sound, ω is the angular frequency, ρ is density of air, p_1 and p_2 are sound pressures measured at M_1 and M_2 respectively, and d_{12} is the distance between two microphones. Then the normal acoustic impedance at the point M is expressed as

$$Z_M = -j\omega\rho d_{12}\left(\frac{p_1 + p_2}{2p_2 - 2p_1}\right) \tag{2.46}$$

From the measurement of the transfer function, $H_{12}(\omega)$, between pressures p_1 and p_2, This equation can be rewritten as

$$Z_M = -j\omega\rho d_{12}\left[\frac{H_{12}(\omega)+1}{2-2H_{12}(\omega)}\right] \tag{2.47}$$

Assuming that the plane standing wave is incident upon the sample, the normal impedance at the surface of the sample is found to be

$$Z = \left(Z_M + j\rho c\tan\frac{\omega d}{c}\right)\Big/\left(\rho c + jZ_M\tan\frac{\omega d}{c}\right) \tag{2.48}$$

Allard *et al* (1985) expanded this method to get the impedance at oblique incidence. This is given by

$$Z(\theta)=\frac{\rho c}{\cos\theta}\left(Z_M+\frac{j\rho c}{\cos\theta}\tan\frac{\omega x\cos\theta}{c}\right)\bigg/\left(\frac{\rho c}{\cos\theta}+jZ_M\tan\frac{\omega x\cos\theta}{c}\right) \tag{2.49}$$

where θ is an angle of incidence, x is the distance from the Midpoint M to the surface of the sample. This method has an advantage of using relatively small size of test sample because microphones are placed close to it. Due to the standing wave pattern in front of the sample, however, the importance of the choice of the microphone separation and their distances from the surface was once more emphasised by Minten *et al* (1988). The finite distance approximation, i.e., approximating the particle velocity by a pressure gradient and the pressure by a pressure average (see Eq. (2.45)) causes an inherent error in this method. This error is most important at higher frequencies, large microphone spacings and for small angles of incidence. The appearance of standing waves makes it difficult to measure the exact phase difference between the two microphones especially when small phase difference occurs. This systematic error was analysed as a function of distance from the reflecting surface (Minten *et al*, 1988).

2.2.4 The virtual source model

A spherical-wave representation is used for the description of the incident and the reflected waves. At an oblique incidence angle, by assigning a virtual source the sound pressure measured at a microphone placed in front of the test sample can be expressed as

$$p=\frac{A}{r_1}e^{-jkr_1}+\frac{B}{r_2}e^{-jkr_2} \tag{2.50}$$

where A and B are pressure amplitude of two divergent spherical waves, and r_1 and r_2 are distances to the microphone from the source and virtual source respectively.

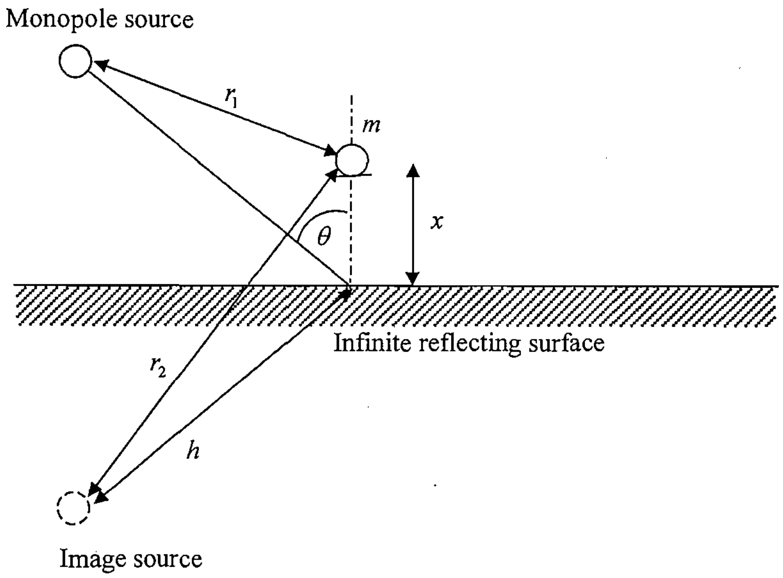

FIG. 2.6: Geometrical representation of incident and reflecting spherical waves

Sides and Mulholland (1971) used this model to get an angle dependant normal impedance with a test sample of which the property is already known, especially the distance, d_1, to the first minimum of pressure measured in the SWR method. From the geometrical information given in Fig. 2.6 where h is defined as the distance from the origin to the image source, the normal layer impedance, which is the ratio of the pressure to normal particle velocity at the surface, is given by

$$Z_n(\theta)=\left.\frac{p(x)}{u_n(x)}\right|_{x=0}=\frac{\rho c\tanh(\alpha+j\beta)}{\cos\theta\left(1+\dfrac{j}{kh}\right)} \tag{2.51}$$

where α and β are given by

$$\beta = \pi + kd_1 \cos\theta$$

$$\alpha = \frac{1}{2}\ln\left[\frac{e^{-(d_1\cos\theta)/h} + re^{-(d_2\cos\theta)/h}}{e^{(d_1\cos\theta)/h} - re^{(d_2\cos\theta)/h}}\right] \tag{2.52}$$

and where d_2 and r are given by

$$d_2 = d_1 + \frac{\lambda}{4}\cos\theta$$

$$r = \frac{|p_{\min}|}{|p_{\max}|} \tag{2.53}$$

Li and Hodgson (1997) combined the virtual source model with two microphone method such that the pre-acquisition of information from the SWR method is unnecessary. They used a single microphone for two measurement points in order to eliminate microphone calibration, and derived expressions for the acoustic impedance with both plane wave and spherical wave models.

2.2.5 The spatial Fourier-transform method

For the measurement of the plane-wave reflection coefficient of the ocean bottom, Frisk *et al* (1980) applied the spatial Fourier-transform method which had been derived from the near-field acoustic holography technique. Tamura (1990) applied this method for the measurement of complex pressure distributions on two parallel planes lying close to the surface of a test material and decomposing each of the complex pressure distributions into plane-wave components by using a two-dimensional spatial Fourier transform.

The complex pressure distribution, $p(x,y,z)$, on a plane at $z=0$ can be decomposed into plane-wave components, $p(k_x,k_y,0)$, by using the spatial Fourier transform given by

$$p(k_x,k_y,0)=\int_{-\infty}^{\infty}\int_{-\infty}^{\infty}p(x,y,0)e^{-j(k_x x+k_y y)}dxdy \tag{2.54}$$

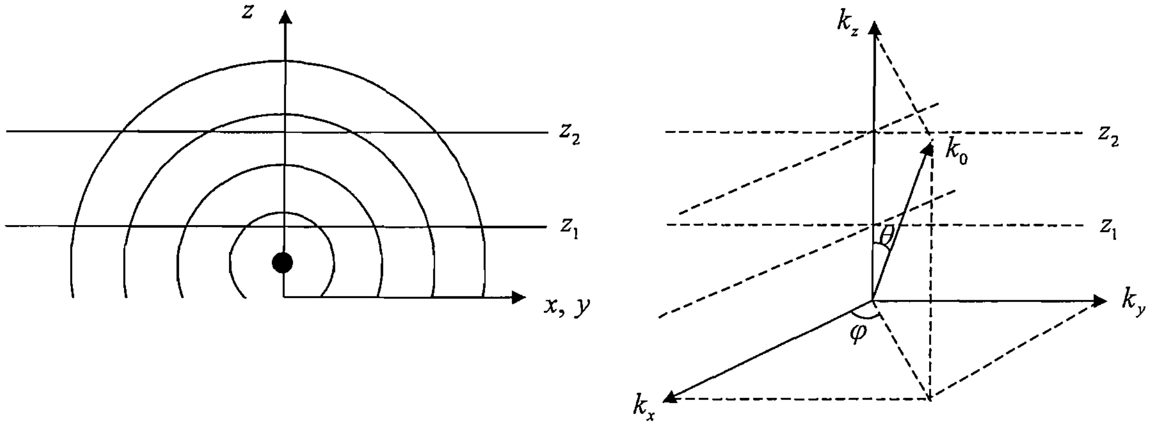

FIG. 2.7: Coordinates for a decomposition of spherical waves into plane-wave components

where each plane-wave component is regarded as a sum of the incident and reflected waves.

$$p(k_x,k_y,0)=p_i(k_x,k_y,0)+p_r(k_x,k_y,0) \tag{2.55}$$

And the reflection coefficient can be expressed as

$$R(k_x,k_y)=\frac{p_r(k_x,k_y,0)}{p_i(k_x,k_y,0)} \tag{2.56}$$

With the plane-wave propagation assumption, the measured plane-wave components at $z = z_1$ and $z = z_2$ can be expressed as

$$
\begin{aligned}
p\left(k_x, k_y, z_1\right) &= p_i\left(k_x, k_y, 0\right)e^{-jk_z z_1} + p_r\left(k_x, k_y, 0\right)e^{jk_z z_1} \\
p\left(k_x, k_y, z_2\right) &= p_i\left(k_x, k_y, 0\right)e^{-jk_z z_2} + p_r\left(k_x, k_y, 0\right)e^{jk_z z_2}
\end{aligned}
\qquad (2.57)
$$

From Eq. (2.57), each component of the incident and reflected waves can be determined and substituted into Eq. (2.56) to get the reflection coefficient. Brouard *et al* (1996) used this method for the measurement and prediction of the reflection coefficient of inhomogeneous waves. The spatial Fourier-transform has the advantage that reflection coefficients at all angles of incidence can be obtained from a set of measurements and the results do not require correction for the effect of sphericity of the sound source since this method makes use of a plane-wave decomposition. In a practical measurement of the complex pressure distribution, however, it requires many measurement points on the measurement plane to obtain the pressure distribution upon it. In most cases, therefore, an automated measurement system is required, which makes the measurement process complex. In addition, the test sample must be sufficiently large to ensure a proper result, especially at lower frequencies, or a highly directional sound source is required in order to minimise the effects of finite size of test material.

2.2.6 The impedance deduction method

The solution for a reflected spherical wave, from a monopole source can be approximated under the assumption that the reflecting boundary is hard, i.e., the impedance of the boundary is high, and is locally reacting (Ingård, 1951; Lawhead and Rudnick, 1951; Wenzel, 1974; Chien and Soroka, 1975 and 1980).

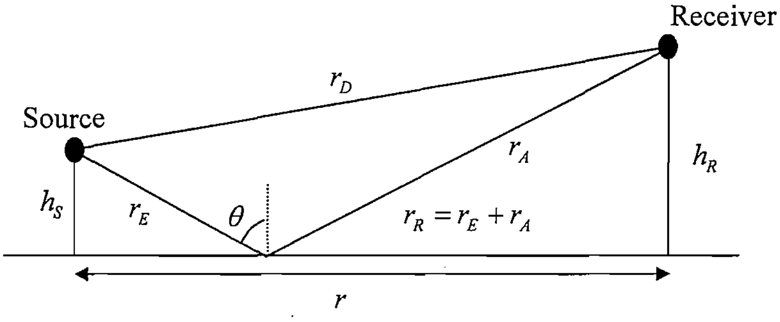

FIG. 2.8: Geometry as used for the impedance deduction method

Nocke *et al* (1997) used this approximation for the deduction of the impedance from the measured transfer function between the direct and reflected sound waves. From the measurement at grazing incidence, the transfer function (H) that is defined by the sound pressure spectrum normalised to the free field value is obtained. The analytical form of this is given by

$$H = 1 + Q\frac{r_R}{r_D}e^{jk(r_R - r_D)} \tag{2.58}$$

where r_d and r_r are direct and reflected path lengths, between the source and the receiver, respectively, and Q is the spherical wave reflection coefficient given by

$$Q = R + (1 - R)F(w) \tag{2.59}$$

In the above equation, R is the plane-wave reflection coefficient and $F(w)$ is the boundary loss factor given by

$$F(w) = 1 + j\sqrt{\pi}we^{-w^2}erfc(-jw) \tag{2.60}$$

where $erfc(-jw)$ is the complementary error function of the numerical distance, w, given by

$$w = \sqrt{\frac{jkr_R}{2}}\left(\frac{1}{\xi} + \cos\theta\right) \tag{2.61}$$

The normalised specific acoustic impedance, ξ, is deduced by comparing the value of Q from the measurement of H with the theoretical value of Q and by minimising the differences with an iterative procedure. This process is time consuming, and the reflecting material should be plane and locally reacting. The poor low frequency performance was improved by applying this method at larger angles of incidence.

The effect due to the finite sample size was also considered by applying the theory of "Fresnel zones". Fresnel's original theory was about the diffraction of light as having a property of waves (Resnick *et al*, 1993). According to Hothersall and Harriott (1994), it was suggested by Slutsky and Bertoni (1987) that the form of the wave reflected by a surface is primarily determined by the region of the surface within elliptical Fresnel zones on the surface. This suggestion was applied and further developed for the evaluation of the proportions of impedance of each type contributing significantly to the excess attenuation at the receiver (Hothersall and Harriott, 1994 and 1995; Boulanger *et al*, 1997).

The Fresnel zones constitute regions, on the impedance boundary, that are centred on a point such that the reflected path length between the source and receiver is shortest when the wave is reflecting at this point. All the other points where the wave reflects, the path lengths are longer than this shortest path length. Hothersall and Harriott (1995) have shown that, in evaluating approximate sound propagation above multi-impedance plane boundaries, there is a transition in the excess attenuation between the two reflecting points where the path length difference is greater than $\lambda/3$. Consequently, Nocke (2000) used this concept for the determination of the required sample size for in-situ acoustic impedance measurement. He also showed a common estimate for the size of the Fresnel zones with the assumption that $\rho_n^2 \ll r_E^2$ and $\rho_n^2 \ll r_A^2$ (see Fig. 2.8) where ρ_n is the radius of n-th Fresnel zone (Cremer and Müller, 1978; Spandöck, 1934, Nocke 2000). However, Nocke also stated that the simplification of the formula for estimating the size of the sample was not valid for low frequencies. More discussions on the size of the test sample will be made in the measurement results in Chapter 6.

2.2.7 The subtraction method

This method is associated with the direct subtraction of the free-field signal produced by the source, in the time domain, from the measured impulse response on a reflecting surface. The theory involved in this method is simple and straightforward, but special attention should be paid to signal processing. The reference signal is measured with the source and the receiver placed far away from the reflecting surface. With the distance between the source and the receiver kept the same, the impulse response on a reflection surface is measured. Then the reference signal is subtracted from it such that only the reflected wave can be obtained.

Mommertz (1995) used this technique for the measurement of reflection coefficient. High frequency performance is affected by the incomplete subtraction of the reference signal due to the geometric error in keeping the distance the same between the source and the receiver. Also the time delay error caused mainly by the different speed of sound due to the change of the temperature should be compensated in this method. As this method requires usage of time-domain windowing in order to eliminate parasitic reflections, low frequency performance is influenced by the windowing effect. In order to reduce the effects due to the parasitic reflections, Karjalainen and Tikander (2001) suggested using a hard surface measurement as a reference, and then this reference is compared with the test sample measurement for the identification of parasitic reflections before applying a window.

2.3 Conclusions

The development of methods for the measurement of acoustic reflection coefficient has been reviewed in this Chapter, for both the measurements in a tube and in a free field. In general, the standing wave ratio method, the two-microphone transfer function method in a tube and the reverberation method in a free field are standardised and the most commonly used. However, these methods still have limitations and weaknesses in some respects. Thus further research and the development of new methods or updated methods is worthwhile.

Chapter 3

LEAST SQUARES ESTIMATION OF ACOUSTIC REFLECTION COEFFICIENTS IN ONE-DIMENSIONAL SOUND FIELDS

The theory of least squares estimation of acoustic reflection coefficients is presented in this chapter. For a general description of this theory, an image source model is adopted and it is assumed that only plane waves propagate and reflect at a plane boundary in one-dimensional sound fields. First of all, a two-microphone or two-measurement point image source model of acoustic reflection in one-dimensional sound field will be presented. Then the theory will be expanded into a method that makes use of multiple measurement points. The estimation of reflection coefficients is based on a least squares solution.

3.1 Image source model with two measurement points

The sound source is assumed to be idealised to generate plane waves in one-dimensional sound field. Two microphones are placed in this sound field, and an image source is presumed to be placed on the other part of the reflecting boundary.

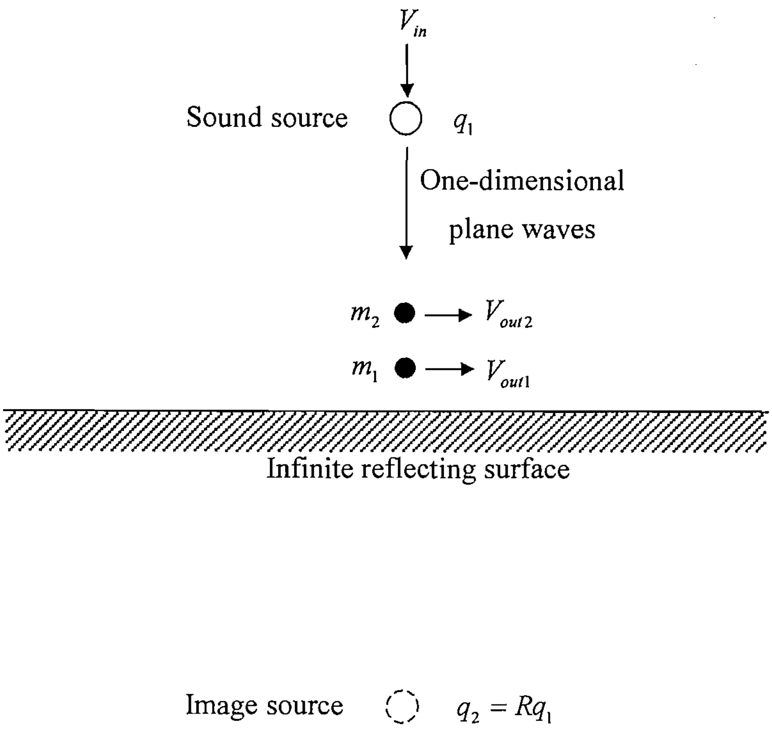

FIG. 3.1: Plane wave propagation and reflection of an image source model in one-dimensional sound field. V_{in} and V_{out} are input and output voltages respectively. R is complex reflection coefficient, and q_1 and q_2 are the strengths of the sound source and image source respectively. The reflecting boundary is perpendicular to the incident waves.

The acoustic pressures picked up at microphones 1 and 2, defined by p_1 and p_2 respectively, can be expressed as

$$\begin{aligned} p_1 &= g_{11}q_1 + g_{12}q_2 \\ p_2 &= g_{21}q_1 + g_{22}q_2 \end{aligned} \qquad (3.1)$$

where g_{11}, g_{12}, g_{21} and g_{22} are Green functions that relate the outputs of the microphones to the inputs of the sound source. The Green function g_{11} relates the "output pressure" of the microphone 1 to the "input strength" of the original sound source, g_{12} is that which relates microphone 1 and the image source, g_{21} is that relating microphone 2 and the original sound source and g_{22} is that relating microphone 2 and the image source. At the moment, the form of these Green functions are not specified here but will later on be specified under the circumstances appropriate to a specific situation.

As shown in Section 1.3, when R is complex reflection coefficient, the strength of image source, q_2, can be expressed in terms of the strength of original source, q_1, by

$$q_2 = Rq_1 \tag{3.2}$$

Then Eq. (3.1) can be written as

$$\begin{aligned} p_1 &= (g_{11} + g_{12}R)q_1 \\ p_2 &= (g_{21} + g_{22}R)q_1 \end{aligned} \tag{3.3}$$

This acoustical model suggests that the transfer function, H_{12}, is defined by

$$H_{12} = \frac{p_2}{p_1} = \frac{g_{21} + g_{22}R}{g_{11} + g_{12}R} \tag{3.4}$$

From Eq. (3.4), the complex reflection coefficient is given by

$$R = \frac{g_{21} - g_{11}H_{12}}{g_{12}H_{12} - g_{22}} \tag{3.5}$$

However we will also define a measured transfer given by

$$\hat{H}_{12} = \hat{h}_2 / \hat{h}_1 \tag{3.6}$$

where the measured values of $\hat{h}_1$ and $\hat{h}_2$ are defined by

$$\begin{aligned} \hat{h}_1 &= V_{out1} / V_{in} \\ \hat{h}_2 &= V_{out2} / V_{in} \end{aligned} \tag{3.7}$$

with the measured input and output voltages of V_{in}, V_{out1} and V_{out2} as illustrated in Figure 3.1.

3.2 Applying the least squares solution

In the practical measurement, the analytically modelled transfer function, H_{12}, is assumed to be replaced by the measured transfer function, $\hat{H}_{12}$. Using a 'least squares' solution, it can be shown that the optimally estimated complex reflection coefficients are obtained by such a replacement.

A cost function, J is defined by

$$J = \left| \frac{\hat{p}_2 - p_2}{q_1} \right|^2 \tag{3.8}$$

where $\hat{p}_2$ is the measured pressure at microphone 2 and p_2 is the pressure at microphone 2 defined by an analytical (or computational) model of the reflection process. The inclusion of q_1 in this equation is useful because the resulting cost function becomes more compact (as shown in the following algebra, especially in proceeding from Eq. (3.12) to Eq. (3.13)).

This expression can be rearranged as

$$J = \left|\frac{\hat{p}_1}{q_1}\right|^2 \left|\frac{\hat{p}_2}{\hat{p}_1} - \frac{p_2}{\hat{p}_1}\right|^2 \tag{3.9}$$

Now the reference pressure in the model, p_1, can be chosen to be fixed such that it is made equal to the measured pressure, $\hat{p}_1$. That is

$$p_1 = \hat{p}_1 \tag{3.10}$$

Then Eq. (3.9) can be written as

$$J = \left|\frac{\hat{p}_1}{q_1}\right|^2 \left|\hat{H}_{12} - H_{12}\right|^2 \tag{3.11}$$

The optimum complex reflection coefficient, R_{opt}, is obtained from the process of minimising the cost function, J. From Eq. (3.4),

$$
\begin{aligned}
J &= \left|\frac{\hat{p}_1}{q_1}\right|^2 \left|\hat{H}_{12} - \frac{g_{21}+g_{22}R}{g_{11}+g_{12}R}\right|^2 \\
&= \left|\frac{\hat{p}_1}{q_1}\right|^2 \left|\frac{\hat{H}_{12}\left(g_{11}+g_{12}R\right)-\left(g_{21}+g_{22}R\right)}{g_{11}+g_{12}R}\right|^2 \\
&= \frac{1}{\left|g_{11}+g_{12}R\right|^2}\left|\frac{\hat{p}_1}{q_1}\right|^2 \left|\left(g_{11}\hat{H}_{12}-g_{21}\right)+\left(g_{12}\hat{H}_{12}-g_{22}\right)R\right|^2
\end{aligned}
\tag{3.12}
$$

From Eqs. (3.1) and (3.10), this expression reduces to

$$
J = \left|\left(g_{11}\hat{H}_{12}-g_{21}\right)+\left(g_{12}\hat{H}_{12}-g_{22}\right)R\right|^2 \tag{3.13}
$$

For simplicity of further expansion of Eq. (3.13), the following terms are defined.

$$
A \equiv g_{11}\hat{H}_{12}-g_{21}, \quad B \equiv g_{12}\hat{H}_{12}-g_{22} \tag{3.14}
$$

Then the cost function can be written as

$$
J = \left|A+BR\right|^2 \tag{3.15}
$$

which when expanded reduces to

$$
J = \left|A\right|^2 + AB^*R^* + BA^*R + \left|B\right|^2\left|R\right|^2 \tag{3.16}
$$

where A^*, B^*, and R^* are complex conjugates of A, B, and R. This defines a quadratic function of the complex variable R. It is well known (Nelson and Elliott, 1992) that the error is at its minimum when the optimally estimated reflection coefficient, R_{opt}, is given by

$$R_{opt} = -\frac{AB^*}{|B|^2} = -\frac{A}{B} = -\frac{g_{11}\hat{H}_{12} - g_{21}}{g_{12}\hat{H}_{12} - g_{22}} \tag{3.17}$$

Rearranging Eq. (3.17) gives

$$R_{opt} = \frac{g_{21} - g_{11}\hat{H}_{12}}{g_{12}\hat{H}_{12} - g_{22}} \tag{3.18}$$

Note that Eq. (3.18) is identical to Eq. (3.5) when $\hat{H}_{12}$ is substituted by H_{12}. This confirms that applying a least squares solution produces the same result as that suggested by the simple acoustical model introduced in the previous section.

3.3 Extension of the theory to deal with multiple-point measurements

With additional microphone positions placed normal to the plane of acoustic reflection (see Fig. 3.2), one may attempt to find R_{opt} that minimises the error between the measured and modelled transfer functions.

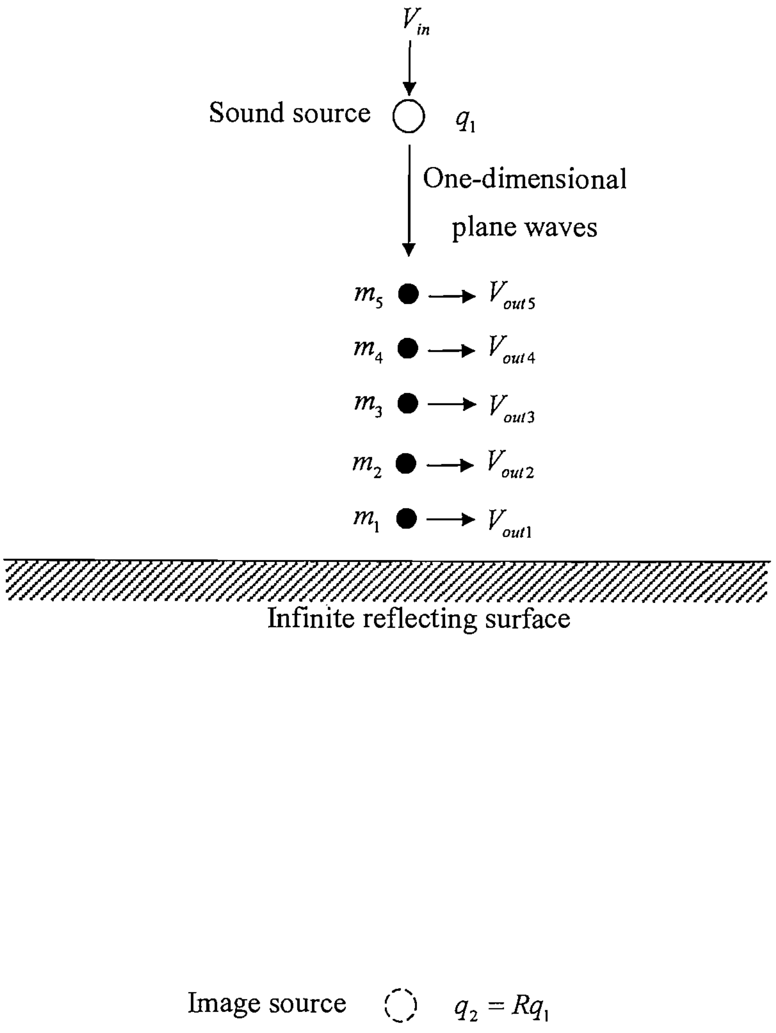

FIG. 3.2: Multiple-microphone array. More than two microphones can be placed in one-dimensional sound field. V_{in} and V_{out} are input and output voltages respectively. R is complex reflection coefficient, and q_1 and q_2 are the strengths of the sound source and image source respectively. The reflecting boundary is perpendicular to the incident waves.

This time the cost function is defined by

$$J = \sum_{m=2}^{M} \left| \frac{\hat{p}_m - p_m}{q_1} \right|^2 \qquad (3.19)$$

where M is the total number of microphones. With the same analysis shown in the previous section referring to Eq. (3.10), the cost function can be written as

$$J = \left|\frac{\hat{p}_1}{q_1}\right|^2 \sum_{m=2}^{M} \left|\hat{H}_{1m} - H_{1m}\right|^2 \tag{3.20}$$

where H_{1m} is analytically expressed transfer function from a model of the sound propagation process and $\hat{H}_{1m}$ is a measured transfer function between microphone 1 and microphone *m*.

In general, H_{1m} is expressed as

$$H_{1m} = \frac{p_m}{p_1} = \frac{g_{m1} + g_{m2}R}{g_{11} + g_{12}R} \tag{3.21}$$

Substituting Eq. (3.21) into Eq. (3.20) gives

$$J = \left|\frac{\hat{p}_1}{q_1}\right|^2 \sum_{m=2}^{M} \left|\hat{H}_{1m} - \frac{g_{m1} + g_{m2}R}{g_{11} + g_{12}R}\right|^2 \tag{3.22}$$

which can be expanded to give

$$\begin{aligned} J &= \left|\frac{\hat{p}_1}{q_1}\right|^2 \sum_{m=2}^{M} \left|\frac{\hat{H}_{1m}\left(g_{11} + g_{12}R\right) - \left(g_{m1} + g_{m2}R\right)}{g_{11} + g_{12}R}\right|^2 \\ &= \frac{1}{\left|g_{11} + g_{12}R\right|^2} \left|\frac{\hat{p}_1}{q_1}\right|^2 \sum_{m=2}^{M} \left|\left(g_{11}\hat{H}_{1m} - g_{m1}\right) + \left(g_{12}\hat{H}_{1m} - g_{m2}\right)R\right|^2 \end{aligned} \tag{3.23}$$

Then once again, from Eqs. (3.1) and (3.10), this expression reduces to

$$J = \sum_{m=2}^{M} \left| \left(g_{11}\hat{H}_{1m} - g_{m1} \right) + \left(g_{12}\hat{H}_{1m} - g_{m2} \right) R \right|^2 \tag{3.24}$$

Now defining

$$A_m \equiv g_{11}\hat{H}_{1m} - g_{m1}, \quad B_m \equiv g_{12}\hat{H}_{1m} - g_{m2} \tag{3.25}$$

shows that J can be expressed in the form

$$J = \sum_{m=2}^{M} \left| A_m + B_m R \right|^2 \tag{3.26}$$

which then can be reduced to

$$J = \sum_{m=2}^{M} |A_m|^2 + \left(\sum_{m=2}^{M} A_m B_m^* \right) R^* + \left(\sum_{m=2}^{M} B_m A_m^* \right) R + \left(\sum_{m=2}^{M} |B_m|^2 \right) |R|^2 \tag{3.27}$$

Again, this is a quadratic function of the complex variable R. The cost function is minimised by

$$R_{opt} = -\frac{\sum_{m=2}^{M} A_m B_m^*}{\sum_{m=2}^{M} |B_m|^2} = -\frac{\sum_{m=2}^{M} \left(g_{11}\hat{H}_{1m} - g_{m1} \right) \left(g_{12}\hat{H}_{1m} - g_{m2} \right)^*}{\sum_{m=2}^{M} \left| g_{12}\hat{H}_{1m} - g_{m2} \right|^2} \tag{3.28}$$

Note that this result was obtained by minimising the sum of errors between each measured and analytically expressed pressures except the reference pressure, which is assumed to be the same as the modelled pressure. As the optimally estimated reflection coefficient is obtained by dividing the sum of numerators by the sum of denominators, this equation is useful for the compensation of the ill conditioning associated with any one of the transfer functions by adding the further terms to both numerator and denominator. This is discussed in detail in Section 4.2. Eq. (3.28) is a general result for any number of microphones in an array. When the total number of microphones, M, is two, the equation exactly reduces to Eq. (3.18) that was obtained by applying the least squares solution with two measurement points.

3.4 Conclusion

In this chapter, we have derived a theory of measurement of acoustic reflection coefficients, in one-dimensional sound fields, by the use of a least squares solution. A transfer function between two measurement points was adopted for an introductory case, and then it was extended to the case of multiple measurement points for which all the transfer functions between the reference measurement point and other measurement points were considered to get the resultant expression of the optimally estimated acoustic reflection coefficient.

Chapter 4

APPLICATION OF LEAST SQUARES ESTIMATION TO IMPEDANCE TUBE MEASUREMENTS

In this chapter, the theory presented in the previous chapter is applied to the measurement of acoustic reflection coefficient in an impedance tube. As plane standing waves form in the tube, it is demonstrated that the application of the theory developed in a one-dimensional sound field is of great assistance in improving the frequency range of reflection coefficient measurement. Note that, in this chapter and onward, the dimensionless specific acoustic impedance, ξ, defined in Eq. (1.16) shall simply be denoted by "impedance".

4.1 Least squares estimation in an impedance tube

In order to determine the Green functions g_{11}, g_{12}, g_{21} and g_{22} defined in Eq. (3.1) for the plane standing waves in an impedance tube with an finite length of L, Fig. 4.1 depicts a rigid wall duct closed at both ends that is excited by a plane monopole source at $x = y$

(see Nelson and Elliott, 1992, p152). In the region upstream of the source, the complex pressure and particle velocity field are given by

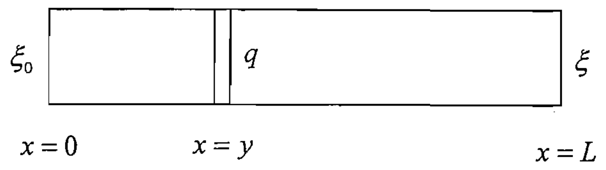

FIG. 4.1: A plane monopole source in a rigid walled tube with a termination of impedance ξ_0, at $x=0$ and ξ at $x=L$.

$$\left\{\begin{aligned} p(x) &= Ae^{-jkx}+Be^{jkx} \\ u(x) &= \frac{Ae^{-jkx}}{\rho_0 c_0}-\frac{Be^{jkx}}{\rho_0 c_0} \end{aligned}\right\}, \qquad 0\le x\le y \tag{4.1}$$

where the complex particle velocity has been deduced from the complex pressure by using the one-dimensional equation of conservation of momentum, and A and B are arbitrary complex constants. Meanwhile, downstream of the monopole source, the complex pressure and the complex particle velocity, with arbitrary complex constants of C and D, are given by

$$\left\{\begin{aligned} p(x) &= Ce^{-jkx}+De^{jkx} \\ u(x) &= \frac{Ce^{-jkx}}{\rho_0 c_0}-\frac{De^{jkx}}{\rho_0 c_0} \end{aligned}\right\}, \qquad y\le x\le L \tag{4.2}$$

In order to determine the arbitrary complex constants A, B, C and D, boundary conditions are applied. With the use of Eqs. (1.14) and (1.16), the impedance at each of the both ends of the duct given by ξ_0 at $x=0$ and ξ at $x=L$ can be written

$$\begin{aligned} \xi_0 &= \rho_0 c_0 \frac{p(0)}{u(0)} = \frac{A+B}{A-B}, \quad \text{at } x=0 \\ \xi &= \rho_0 c_0 \frac{p(L)}{u(L)} = \frac{Ce^{-2jkL}+D}{Ce^{-2jkL}-D}, \quad \text{at } x=L \end{aligned} \tag{4.3}$$

From this equation, the following relationships are obtained.

$$\begin{aligned} B &= \left(\frac{\xi_0-1}{\xi_0+1}\right)A = R_0 A \\ D &= \left(\frac{\xi-1}{\xi+1}\right)Ce^{-2jkL} = RCe^{-2jkL} \end{aligned} \tag{4.4}$$

where the relationship between the complex reflection coefficient, R, and the impedance, ξ, given in Eq. (1.19) is applied.

There can be no discontinuity of pressure across the source, and therefore it can be shown that, with the use of the relationship in Eq. (4.4),

$$p(y) = A\left(e^{-jky} + R_0 e^{jky}\right) = Ce^{-jkL}\left(e^{-jk(y-L)} + Re^{jk(y-L)}\right) \tag{4.5}$$

Similarly, any difference in the particle velocity between the positions of the two hypothetical massless pistons representing the plane monopole source must be exactly equal to the source strength divided by the duct's cross-sectional area, S. This velocity difference can therefore be written as

$$\frac{q(y)}{S}=\frac{C}{\rho_0 c_0}e^{-jkL}\left(e^{-jk(y-L)}-Re^{jk(y-L)}\right)-\frac{A}{\rho_0 c_0}\left(e^{-jky}-R_0 e^{jky}\right) \tag{4.6}$$

From Eqs. (4.5) and (4.6), C is obtained and as a consequence D is obtained as well using Eq. (4.4). Thus

$$\begin{aligned} C&=\frac{\rho_0 c_0 q(y)}{2S}\left(\frac{R_0 e^{jky}+e^{-jky}}{R_0 e^{jkL}-Re^{-jkL}}\right)e^{jkL} \\ D&=\frac{\rho_0 c_0 q(y)}{2S}\left(\frac{R_0 e^{jky}+e^{-jky}}{R_0 e^{jkL}-Re^{-jkL}}\right)Re^{-jkL} \end{aligned} \tag{4.7}$$

Assuming the monopole source is placed at $x=0$, i.e., putting $y=0$ in the above equation and denoting $q(0)$ as simply q_1 shows that

$$\begin{aligned} C&=\frac{\rho_0 c_0 q_1}{2S}\left(\frac{R_0+1}{R_0 e^{jkL}-Re^{-jkL}}\right)e^{jkL} \\ D&=\frac{\rho_0 c_0 q_1}{2S}\left(\frac{R_0+1}{R_0 e^{jkL}-Re^{-jkL}}\right)Re^{-jkL} \end{aligned} \tag{4.8}$$

From Eqs. (4.2) and (4.8), the complex pressure in the region $0\le x\le L$ can be written as

$$p(x)=\frac{\rho_0 c_0 q_1}{2S}\left(\frac{R_0+1}{R_0 e^{jkL}-Re^{-jkL}}\right)e^{jk(L-x)}+\frac{\rho_0 c_0 q_1}{2S}\left(\frac{R_0+1}{R_0 e^{jkL}-Re^{-jkL}}\right)Re^{-jk(L-x)} \tag{4.9}$$

Comparing this equation with Eq. (3.3), the Green functions g_{11}, g_{12}, g_{21} and g_{22} can be deduced.

$$\begin{aligned} g_{11}&=\frac{\rho_0 c_0}{2S}\left(\frac{R_0+1}{R_0 e^{jkL}-Re^{-jkL}}\right)e^{jk(L-x_1)}, & g_{12}&=\frac{\rho_0 c_0}{2S}\left(\frac{R_0+1}{R_0 e^{jkL}-Re^{-jkL}}\right)e^{-jk(L-x_1)} \\ g_{21}&=\frac{\rho_0 c_0}{2S}\left(\frac{R_0+1}{R_0 e^{jkL}-Re^{-jkL}}\right)e^{jk(L-x_2)}, & g_{22}&=\frac{\rho_0 c_0}{2S}\left(\frac{R_0+1}{R_0 e^{jkL}-Re^{-jkL}}\right)e^{-jk(L-x_2)} \end{aligned} \tag{4.10}$$

where x_1 and x_2 are two different positions in the region $0 \le x \le L$. Defining d_1 and d_2 as $L-x_1$ and $L-x_2$, now the Green functions are finalised (see Figs. 4.1 and 4.2).

$$\begin{aligned} g_{11}&=\frac{\rho_0 c_0}{2S}\left(\frac{R_0+1}{R_0 e^{jkL}-Re^{-jkL}}\right)e^{jkd_1}, & g_{12}&=\frac{\rho_0 c_0}{2S}\left(\frac{R_0+1}{R_0 e^{jkL}-Re^{-jkL}}\right)e^{-jkd_1} \\ g_{21}&=\frac{\rho_0 c_0}{2S}\left(\frac{R_0+1}{R_0 e^{jkL}-Re^{-jkL}}\right)e^{jkd_2}, & g_{22}&=\frac{\rho_0 c_0}{2S}\left(\frac{R_0+1}{R_0 e^{jkL}-Re^{-jkL}}\right)e^{-jkd_2} \end{aligned} \tag{4.11}$$

In this thesis, however, the image source model introduced in Section 3.1 will be applied in description of the complex pressure in the impedance tube (Fig. 4.2). Therefore these Green functions can have simpler forms assuming that the length of the tube is infinite (see Nelson and Elliott, 1992, p121).

$$g_{11} = \frac{\rho_0 c_0}{2S} e^{-jk(L-d_1)}, \quad g_{12} = \frac{\rho_0 c_0}{2S} e^{-jk(L+d_1)}$$
$$g_{21} = \frac{\rho_0 c_0}{2S} e^{-jk(L-d_2)}, \quad g_{22} = \frac{\rho_0 c_0}{2S} e^{-jk(L+d_2)} \tag{4.12}$$

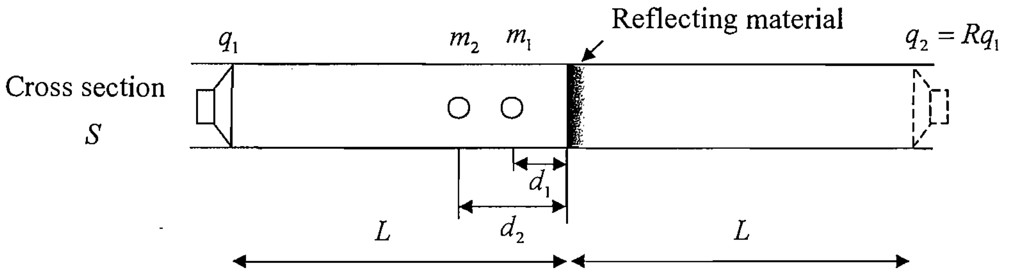

FIG. 4.2: Acoustic propagation and reflection model in an impedance tube. L is the length of the tube, d_1 and d_2 are distances from the test sample to the microphones 1 and 2 such that microphone separation is $d_2 - d_1$

Note that these results are deduced from Eq. (4.11) when $R_0 = 0$ and $R = 1$ as would be expected from the definition in Eq. (3.3). Note also that substituting either Eq. (4.11) or Eq. (4.12) into Eq. (3.5) will result in the same expression for the reflection coefficient. Thus Eq. (3.5) is written as

$$R = \frac{e^{jkd_2} - e^{jkd_1} H_{12}}{e^{-jkd_1} H_{12} - e^{-jkd_2}}$$
$$= \frac{e^{jk(d_2+d_1)} - e^{j2kd_1} H_{12}}{H_{12} - e^{-jk(d_2-d_1)}} \tag{4.13}$$

Hence the analytical expression for the complex reflection coefficient is obtained from

$$R = -e^{j2kd_1}\left[\frac{H_{12} - e^{jk(d_2-d_1)}}{H_{12} - e^{-jk(d_2-d_1)}}\right] \tag{4.14}$$

Eq. (4.14) is the normal expression of complex reflection coefficient analytically modelled in a tube using the two-microphone transfer function (Katz, 2000). However, note that Eq. (4.14) is not exactly the same as the result from the conventional two-microphone transfer function method that is shown in Eq. (2.34) in Section 2.1.3. This is because the numbering of the microphones is deliberately changed in Fig. 4.2 compared with Fig. 2.3 for the purpose of conveniently expanding the two-microphone method into a multi-microphone method. To ensure that the same expression can be obtained by using Eqs. (3.5) and (4.12), one can define a transfer function H_{21}. From Eq. (3.4),

$$H_{21} = \frac{p_1}{p_2} = \frac{g_{11} + g_{12}R}{g_{21} + g_{22}R} \tag{4.15}$$

Then the reflection coefficient R can be expressed in terms of H_{21} as

$$R = \frac{g_{11} - g_{21}H_{21}}{g_{22}H_{21} - g_{12}} \tag{4.16}$$

By substituting Eq. (4.12) into Eq. (4.16),

$$\begin{aligned} R &= \frac{e^{jkd_1} - e^{jkd_2}H_{21}}{e^{-jkd_2}H_{21} - e^{-jkd_1}} \\ &= \frac{e^{jk(d_2+d_1)} - e^{j2kd_2}H_{21}}{H_{21} - e^{jk(d_2-d_1)}} \end{aligned} \tag{4.17}$$

Then R is written as

$$R = -e^{j2kd_2}\left[\frac{H_{21} - e^{-jk(d_2-d_1)}}{H_{21} - e^{jk(d_2-d_1)}}\right] \tag{4.18}$$

This is exactly the same expression as the result of two-microphone transfer function, Eq. (2.34), when the microphone numbering is changed, i.e., H_{21} is replaced by H_{12} , and d_1 and d_2 are interchanged.

In the two-microphone transfer function method, the microphone separation should be shorter than the half wavelength of the maximum frequency which is dictated by the diameter of the circular tube. When the microphone separation is longer than half a wavelength at the maximum frequency, a peak occurs at the frequency at which the half wavelength equals the length of separation and this peak occurs harmonically. In this thesis, these harmonic frequencies are called “error frequencies”, and a detailed analysis is presented in the next chapter.

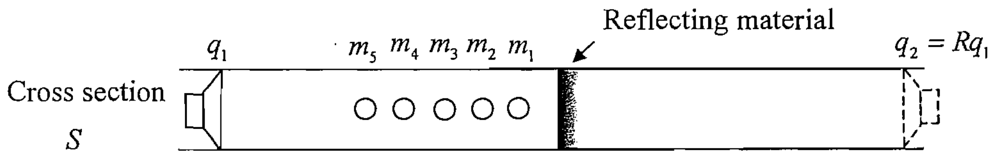

FIG. 4.3: Multi-microphone array in an impedance tube

With a multi-microphone array (see Fig. 4.3), some microphone separations referenced to the microphone position 1 can be chosen to be longer such that the result obtained by using Eq. (3.28) is free from half-wavelength peaks. Hence better measurement accuracy can be obtained at lower frequencies. The simulation results in Section 4.2 and measurement results presented in Section 4.3 confirm this assertion.

When the number of measurement points is chosen to be more than two, i.e., for a multi-microphone measurement, Eq. (3.28) can be used with the substitution of each Green function between each pair of microphones. Thus

$$R_{opt} = -\frac{\sum_{m=2}^{M}\left(g_{11}\hat{H}_{1m} - g_{m1}\right)\left(g_{12}\hat{H}_{1m} - g_{m2}\right)^{*}}{\sum_{m=2}^{M}\left|g_{12}\hat{H}_{1m} - g_{m2}\right|^{2}} \tag{4.19}$$

Eq. (4.19) is repetition of Eq. (3.28). The multi-microphone transfer function method that uses Eq. (4.19) for the measurement of acoustic reflection coefficients in an impedance tube gives very useful advantages over the existing two-microphone transfer function method. Section 4.2 illustrates the advantages in detail.

The multi-point method in an impedance tube using a least squares solution has already been used by Fujimori *et al* (1984, Section 2.1.2) for a single frequency measurement, and the possibility of broadband measurement was proposed by Pope (1986). Both of their researches used a conventional standing wave tube with a running microphone probe.

The method presented in this section, based on the two-microphone transfer function method, makes use of an image source model and a least squares solution such that the equation underlying this method can easily be derived and hence be extended to a multi-transfer function method. By taking into account multi-transfer functions for a single measurement result, this method enables us to extend the measurement frequency range *both lower and higher* than the conventional two-microphone transfer function method. The next section is devoted to explaining this capability.

4.2 Optimal choice of microphone separation distances in an impedance tube

In the measurement of reflection coefficients in the impedance tube, the microphone separation should be shorter than the half wavelength of the maximum frequency of interest. Otherwise the measured results will have error frequencies that are harmonic, i.e., a series of error frequencies occur that are multiples of the lowest frequency. This is fully analysed and explained in the next chapter, and it will be assumed here that harmonic error frequencies occur when the half wavelength of the fundamental frequency is the same as the microphone separation.

For the two-microphone transfer function method used in a $25mm$ diameter tube, the effective bandwidth is $1 \sim 6\,\text{kHz}$ (Katz, 2000), and the microphone separation is chosen to be, in general, a quarter-wavelength at the centre frequency of $3.5\,\text{kHz}$. Assuming that the speed of sound is $340\,m/s$, the microphone separation is $2.43cm$. Hence in the measurement, the error frequencies do not appear in the results since the fundamental error frequency is expected to be at 7 kHz. With this microphone separation, however, the lower frequency performance is unreliable so that it is limited to 1 kHz. The half-wavelength error-frequency problem, which will be shown in the error frequency analysis in Section 5.4, is inherent in the transfer function measurement with the presence of any kind of contaminating noise that interferes with the measurement of the transfer function.

Fig. 4.4 shows the results of a simulation for both a noise-free transfer function measurement and a measurement made in the presence of noise. The simulation performed assumed that the pressures were measured in a semi-infinite tube with a reflecting surface at one end. $\hat{H}_{12}$ was thus computed from the analytically predicted value with 2% measurement noise added. With a microphone separation of $17cm$, which is one half-wavelength at 1kHz, the simulation results show clear peaks at harmonics of this fundamental error frequency.

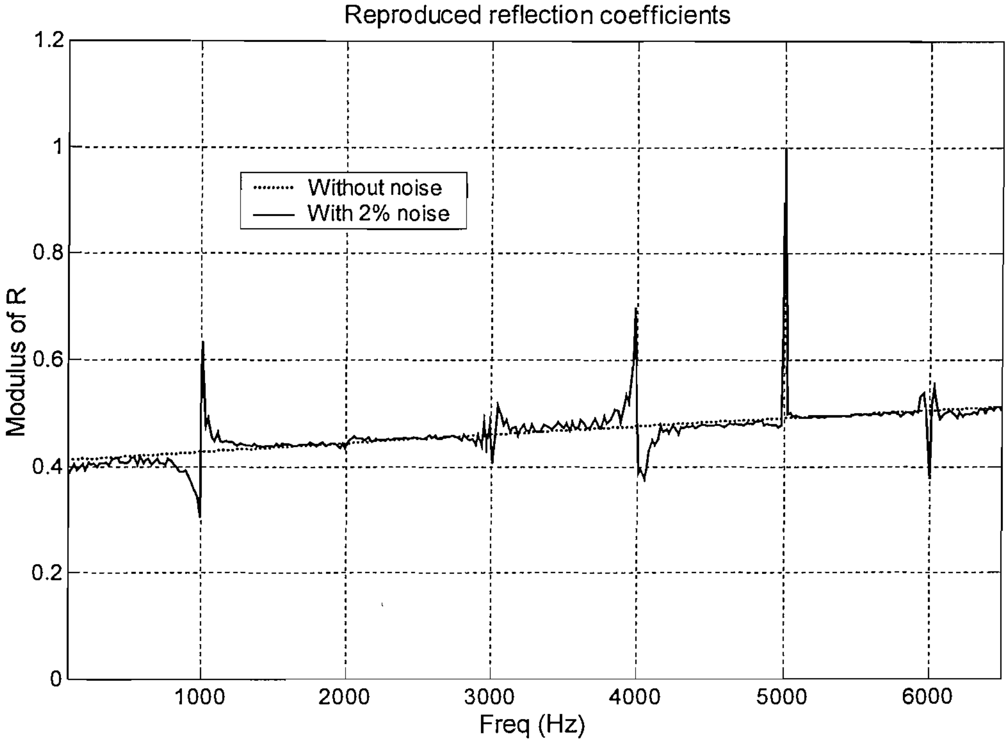

FIG. 4.4: With 2% noise added, a transfer function from the microphone separation of $17cm$ results in error frequencies at 1 kHz and its harmonics assuming that the speed of sound is $340m/s$.

For the multi-microphone least squares estimation method, each of the microphone separations should not have any common multiples with other separations within the frequency range of interest. In order to see how this method performs, the results of a further simulation are presented in Fig. 4.5.

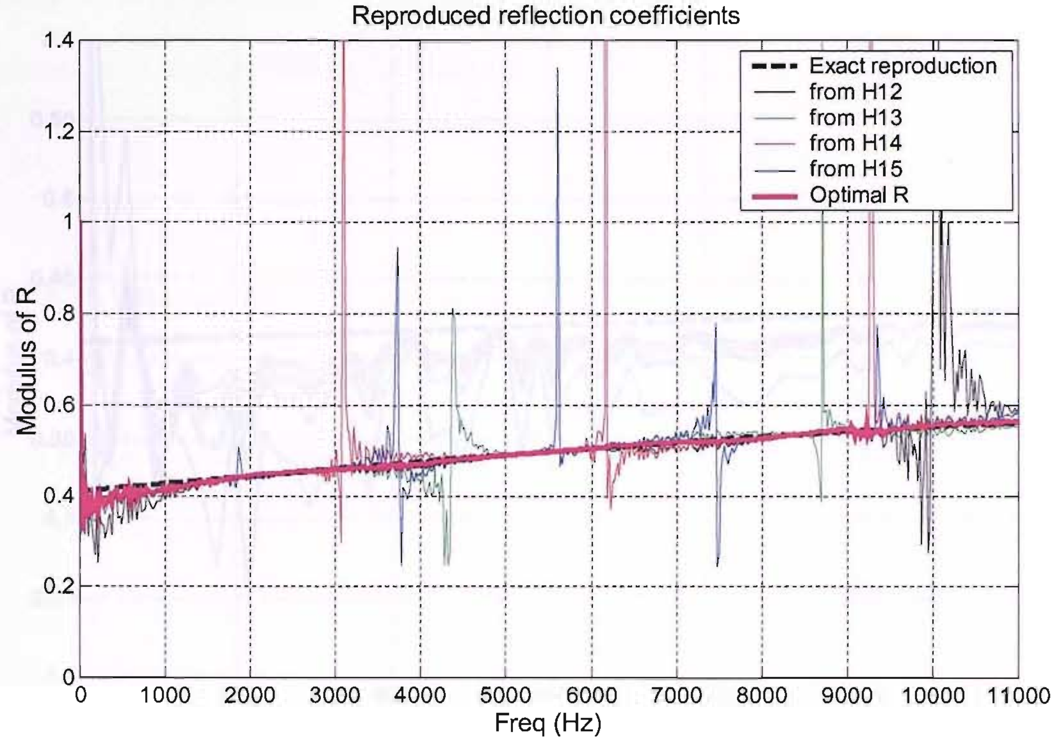

FIG. 4.5: Each transfer function results in error frequencies at 10 kHz, 4.36 kHz, 3.09 kHz, 1.87 kHz and their harmonics, but the optimally estimated reflection coefficients are free from such errors.

Five microphone positions away from the test sample are selected to be $5.3cm$, $7.0cm$, $9.2cm$, $10.8cm$ and $14.4cm$ from which four different microphone separations with reference to microphone position 1 are obtained. The transfer functions corresponding to each of them are labelled $\hat{H}_{12}$, $\hat{H}_{13}$, $\hat{H}_{14}$ and $\hat{H}_{15}$, and each of them is used for the two-microphone case to get a four different results and all of these are used for the multi-microphone least squares estimation method. Each transfer function measurement was again computed from the analytical value with 2% noise added. The expected fundamental error frequencies from the use of each of the transfer functions are 10 kHz, 4.36 kHz, 3.09 kHz and 1.87 kHz. These error frequencies and their harmonics are clearly shown, but the optimally estimated reflection coefficient ("Optimal R" in Fig. 4.5) obtained by using Eq. (4.19) does not have such peaks at those frequencies.

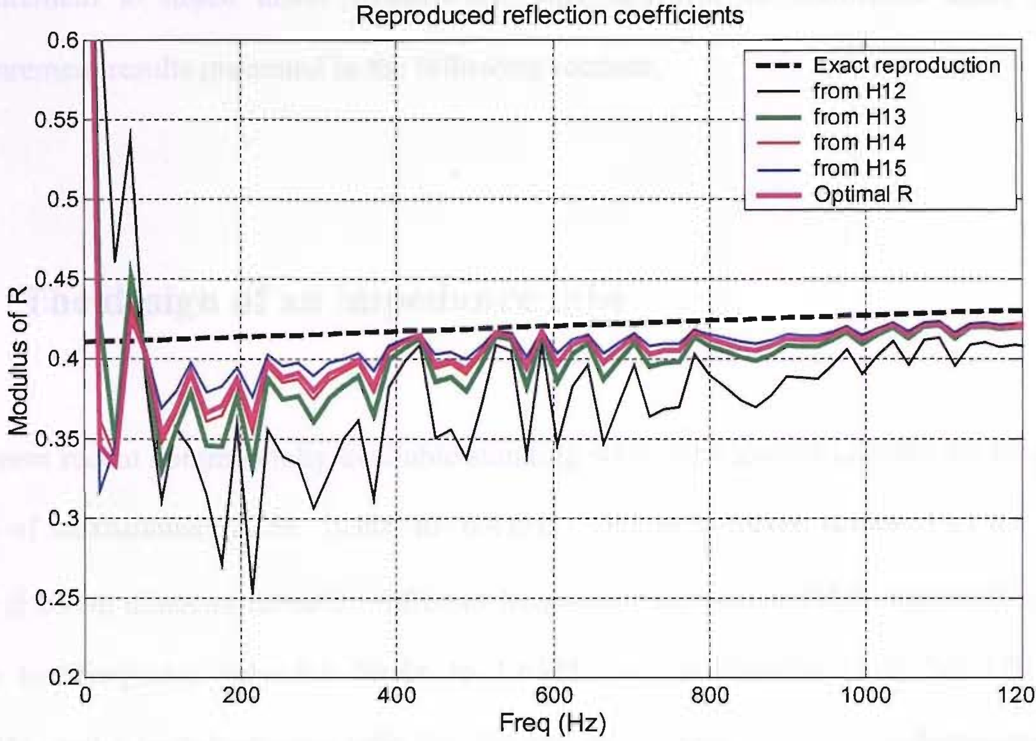

FIG. 4.6: At lower frequencies the optimally estimated reflection coefficients follow the results from the larger microphone separations (from $\hat{H}_{14}$ and $\hat{H}_{15}$).

As a result, especially at lower frequencies, as illustrated in Fig. 4.6, the optimally estimated reflection coefficients perform better than the conventional two-microphone transfer function method (from $\hat{H}_{12}$) by following the results from the larger microphone separations (from $\hat{H}_{14}$ and $\hat{H}_{15}$). The systematic deviation of the results from the exact value at the lower frequencies is due to the lack of phase information in the sound pressure in the measurements at these frequencies as the microphone separation is not large enough. It is natural that the results with the longest microphone separation, i.e. with $\hat{H}_{15}$, show the least deviation except at the fundamental error frequency.

This simulation shows that the least squares estimation of acoustic reflection coefficient by the use of multiple measurement points in a tube has a great advantage over the existing two microphone transfer function method. It does expand the frequency range of measurement to much lower frequencies. This fact will be confirmed again in the measurement results presented in the following sections.

4.3 The design of an impedance tube

The most recent commercially available standing wave tube system enables the frequency range of measurement to be $50\,\text{Hz}$ to $6.4\,\text{kHz}$. This is, however, achieved by the use of three different diameter tubes for different frequency ranges. The B&K Type 4206 system has a low-frequency tube for $50\,\text{Hz}$ to $1.6\,\text{kHz}$, a mid-frequency tube for $100\,\text{Hz}$ to $3.2\,\text{kHz}$ and a high-frequency tube for $500\,\text{Hz}$ to $6.4\,\text{kHz}$. In order to demonstrate the theory of 'least squares estimation of acoustic reflection coefficient' presented in this thesis, it was required to build a new impedance tube. The main difference is that the new tube should have more than two holes for the measurement of transfer functions.

The impedance tube was built according to the International Standard (BS ISO 10534-2:1998) with five holes of $1.5mm$ diameter for a placement of an electret microphone along the measurement line on the tube (see Fig. 4.7). The circular tube is made of $2mm$-thick steel with 1-inch inner diameter and is $109cm$ long. The distances of the holes from the test sample were carefully chosen for the best result. As shown in the previous section, the shortest microphone separation distance covers the upper frequency limit such that error frequencies related to the microphone separations of half-wavelengths will be eliminated by this method. For microphone positioning at $5.3cm$, $7.0cm$, $9.2cm$, $10.8cm$ and $14.4cm$ away from the test sample, $1.5mm$ diameter holes were made along the tube for use of electret microphones. Only one microphone was used to avoid microphone calibration, and the empty microphone holes were blocked with plugs while measurements were undertaken at one of the holes (Fig. 4.8). Each measurement point is labelled as 1, 2, 3, 4 and 5 with the ascending order from nearest one to the test sample. The sample used for most of the investigation related here was rockwool of which the density is $45 kg/m^3$ and the thickness is $75mm$. The sound-generating source was a CELESTION DCR100 which is a 1-inch diameter compression driver.

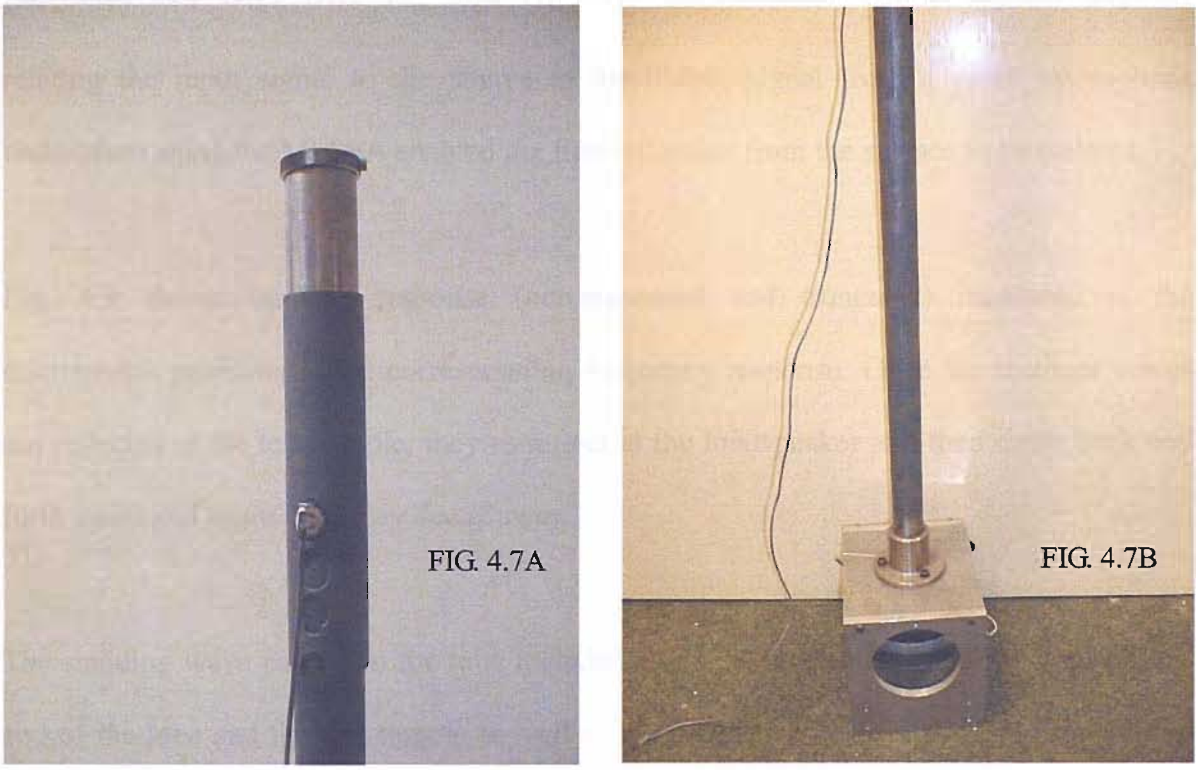

FIG. 4.7: Impedance tube with multi-measurement points. An electret microphone is placed at the reference position, i.e., microphone 1 position (FIG. 4.7A). A 1-inch diameter compression driver is used as a sound source (FIG. 4.7B).

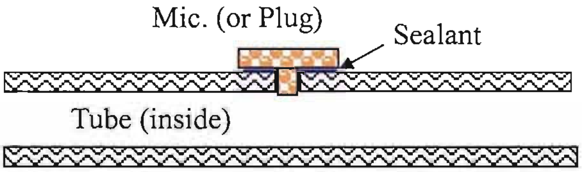

FIG. 4.8: Mounting of a microphone or plugs on empty holes

4.4 Measurement results in an impedance tube

With a single-channel MLSSA (Maximum-length sequence system analyser) measurement (Rife *et al*, 1989 and Rife, 1992), a single microphone is used to measure frequency responses at each of the microphone positions, and then those at microphone positions 2, 3, 4 and 5 are divided by that at microphone position 1 to give four different transfer functions, i.e., $\hat{H}_{12}$, $\hat{H}_{13}$, $\hat{H}_{14}$ and $\hat{H}_{15}$. The measurement of the impulse response relating the input signal to the source to the output signal from a given microphone undertaken using the MLSSA enabled the first reflection from the surface to be isolated.

Fig. 4.9 shows impulse response (non-truncated and truncated) measured at the microphone positions 1 and corresponding frequency response. Once the incident waves are reflected at the test sample, they re-reflect at the loudspeaker and then come back and forth again and again until they decay away.

The standing wave pattern in the tube includes all of the reflections from the loudspeaker end of the tube and the test sample as well as the incident wave and the first reflection at the test sample. The re-reflected waves from the loudspeaker, however, are not well defined in this method and the changes in phase and amplitude of the waves at this end are not the same as those at the test sample.

There is also the possibility that the reflections from the loudspeaker are distorted (non-linearly). The effect of these re-reflections appear to be to add noise to the measurement of the transfer functions. In Fig. 4.10, transfer functions H_{12}, H_{13}, H_{14} and H_{15} for both non-truncated and truncated signals are shown for comparison to show the differences.

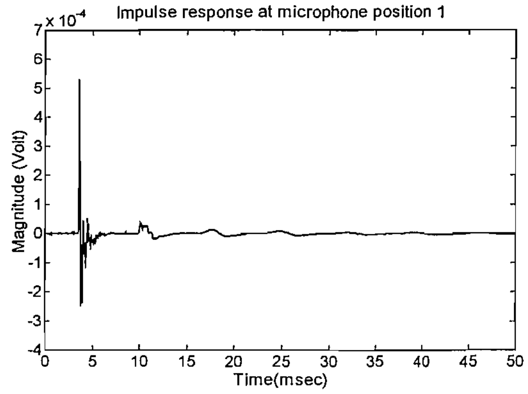

FIG. 4.9A: Non-truncated impulse response at a reference microphone position (Mic. 1).

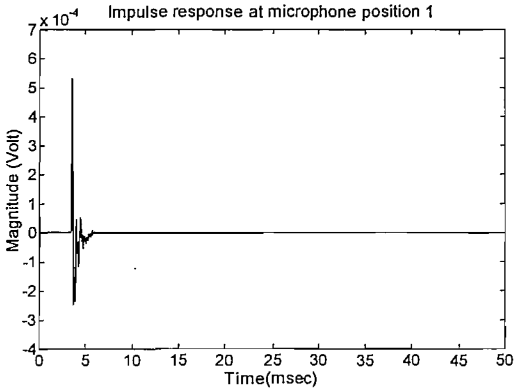

FIG. 4.9B: Truncated impulse response at a reference microphone position (Mic. 1).

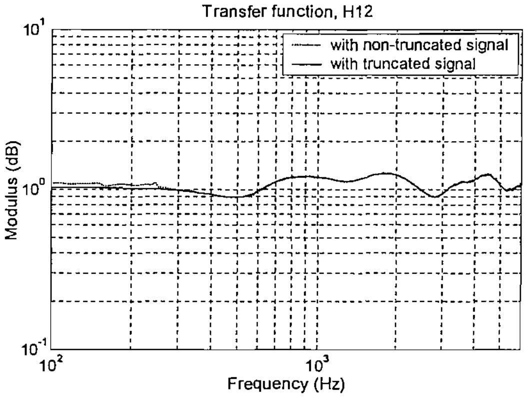

FIG. 4.10A: Transfer function, $\hat{H}_{12}$ with impulse responses at microphones 1 and 2

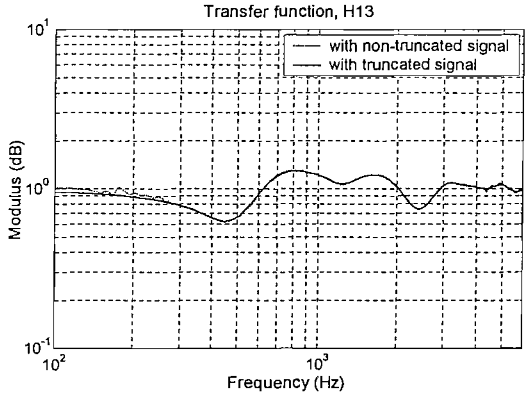

FIG. 4.10B: Transfer function, $\hat{H}_{13}$ with impulse responses at microphones 1 and 3

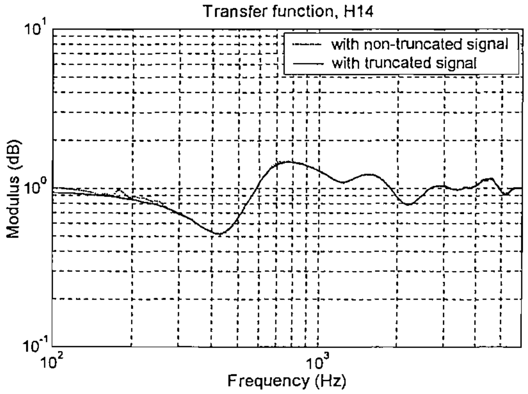

FIG. 4.10C: Transfer function, $\hat{H}_{14}$ with impulse responses at microphones 1 and 4

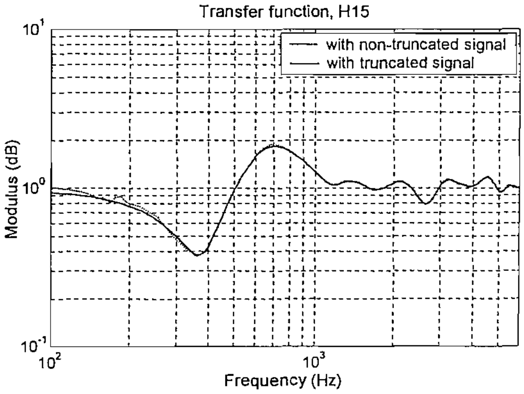

FIG. 4.10D: Transfer function, $\hat{H}_{15}$ with impulse responses at microphones 1 and 5

The transfer functions with non-truncated signals and truncated signals show no distinctive differences (Fig. 4.10) because the non-truncated signals have re-reflections repeated at equal time intervals decided by the length of the tube and the transfer functions count for only the relative differences between two microphones that are under the same condition of sound propagation and reflection. The results shown in Fig. 4.11 are optimally estimated reflection coefficients of rockwool, of which the density is $45 kg/m^3$ and the thickness is $75mm$, obtained by the use of Eq. (4.10). The results are in good agreement with those obtained by using the conventional standing wave ratio (SWR) method. Both a $100mm$ and a $27mm$ diameter tube were used for the frequency range of 100 Hz to 6 kHz in order to obtain reflection coefficients at the centre frequencies of one-third octave bands.

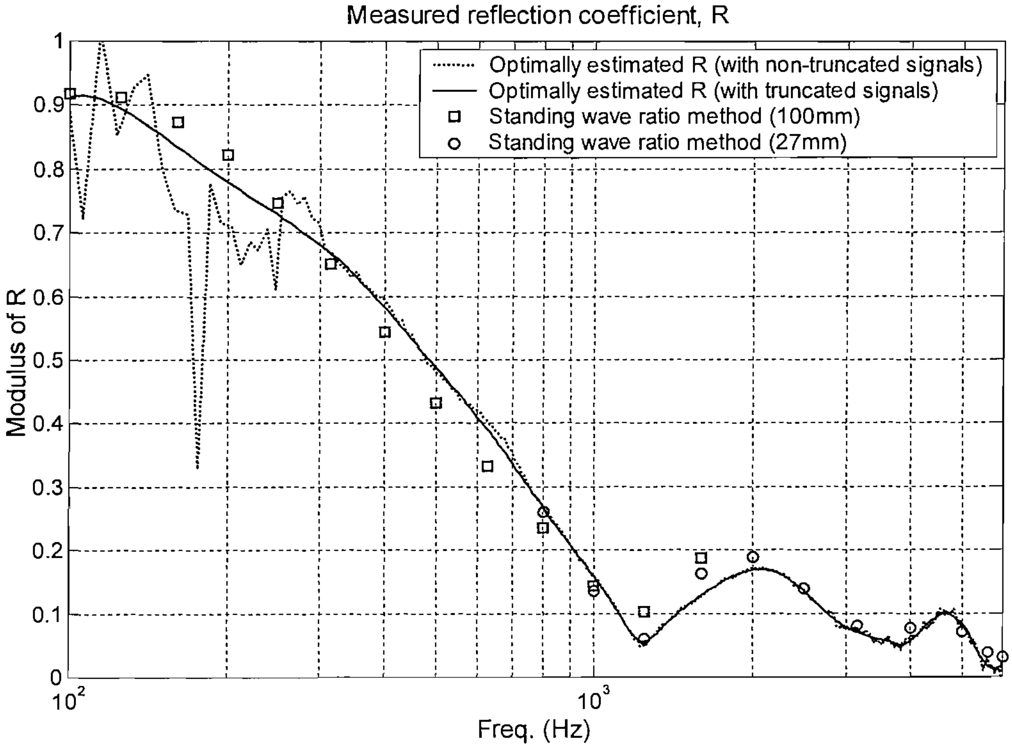

FIG. 4.11A: Modulus of measured reflection coefficients of rockwool for the frequency range of 100 Hz to 6 kHz. The optimally estimated reflection coefficients are obtained with the use of the truncated impulse responses. The reference results from the SWR method used for comparison made use of $100mm$ and $27mm$ diameter tubes at discrete frequencies.

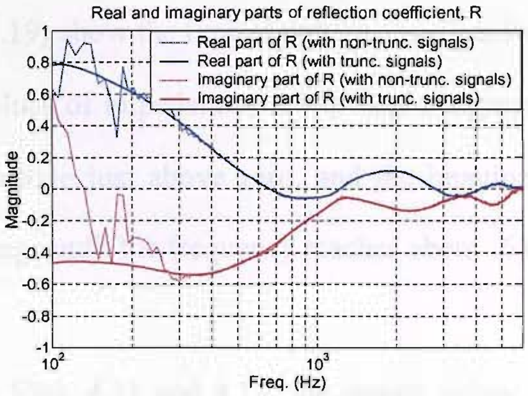

FIG. 4.11B: Real and imaginary parts of measured reflection coefficients

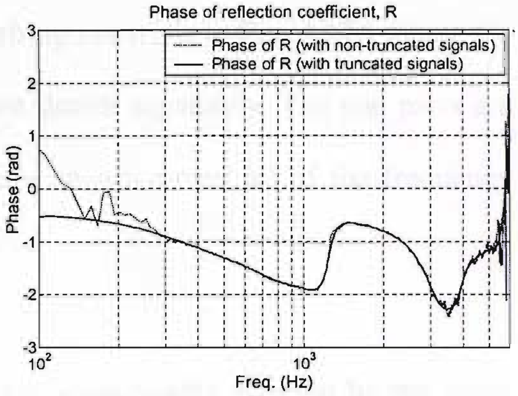

FIG. 4.11C: Phase of measured reflection coefficients

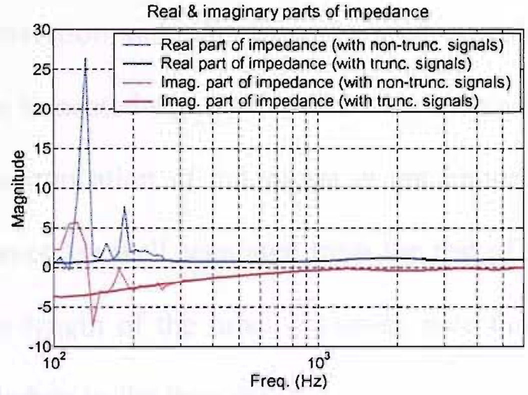

FIG. 4.12A: Real and imaginary parts of normal impedances converted from the optimally estimated reflection coefficients.

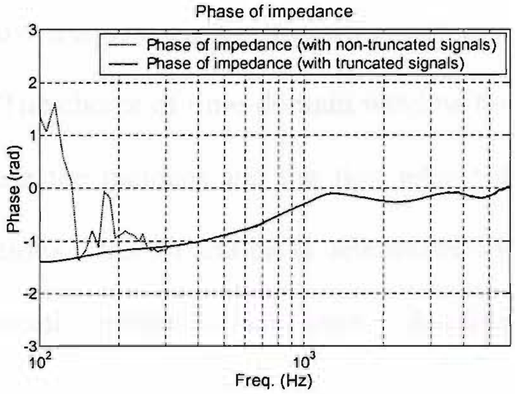

FIG. 4.12B: Phase of normal impedance converted from the optimally estimated reflection coefficient.

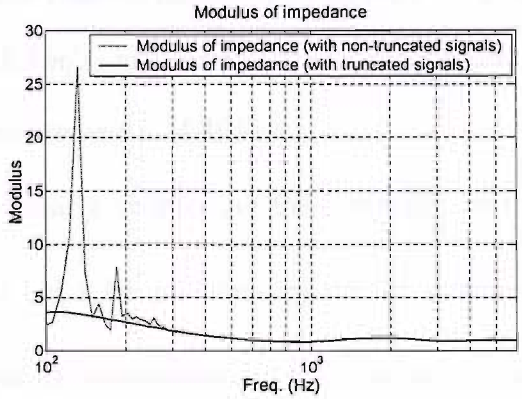

FIG. 4.12C: Modulus of normal impedance converted from the optimally estimated reflection coefficient.

Normal impedances converted from the obtained results of reflection coefficients using Eq. (1.19) show the typical pattern associated with absorbing materials in Fig. 4.12A where the values of impedances in real and imaginary parts are drawn separately. The real parts are positive just above zero, and the imaginary parts are negative over all of the frequency range until the frequency reaches about $6\,\text{kHz}$.

In Figs. 4.11 and 4.12, the results below $300\,\text{Hz}$ are considerably affected by the noise due to the re-reflections. This effect is clearly shown at low frequencies because the phase changes at the loudspeaker end are not consistent and the interference between the generation and reflection of sound is profound at low frequencies. So it is suggested that the truncated signals should be used in this method. The choice of time-domain window for the truncation of the signal is not important because the incident and the first reflected waves are well separated from the rest of the reflections. This separation is determined by the length of the tube. However, note that all the results presented here used a Hanning window in the time domain.

Fig. 4.13 shows how the optimally estimated reflection coefficients are obtained from each of the transfer functions. With the laboratory temperature of $19.5^{\circ}C$, the speed of sound is $342.7\,m/s$, and the expected error frequencies, $10.08\,\text{kHz}$ (beyond the frequency range of measurement), $4.39\,\text{kHz}$, $3.12\,\text{kHz}$ and $1.88\,\text{kHz}$, due to the microphone separations are clearly visible, but the optimally estimated result is not affected at these frequencies. The black line obtained by the use of transfer function $\hat{H}_{12}$ is what one normally obtains from the conventional two-microphone transfer function method. The optimally estimated result is quite similar to that produced by the conventional two-microphone transfer function method within the frequency range except the lower frequencies below $2\,\text{kHz}$. At these low frequencies the optimum result follows the result from the longest microphone separation such that it performs better than the result from the use of $\hat{H}_{12}$. Hence the measurement frequency range is extended to $100\,\mathrm{Hz}$. This extension is limited by the longest microphone separation that is about ten percent of the wavelength of the effective lowest frequency (ASTM E1050-98).

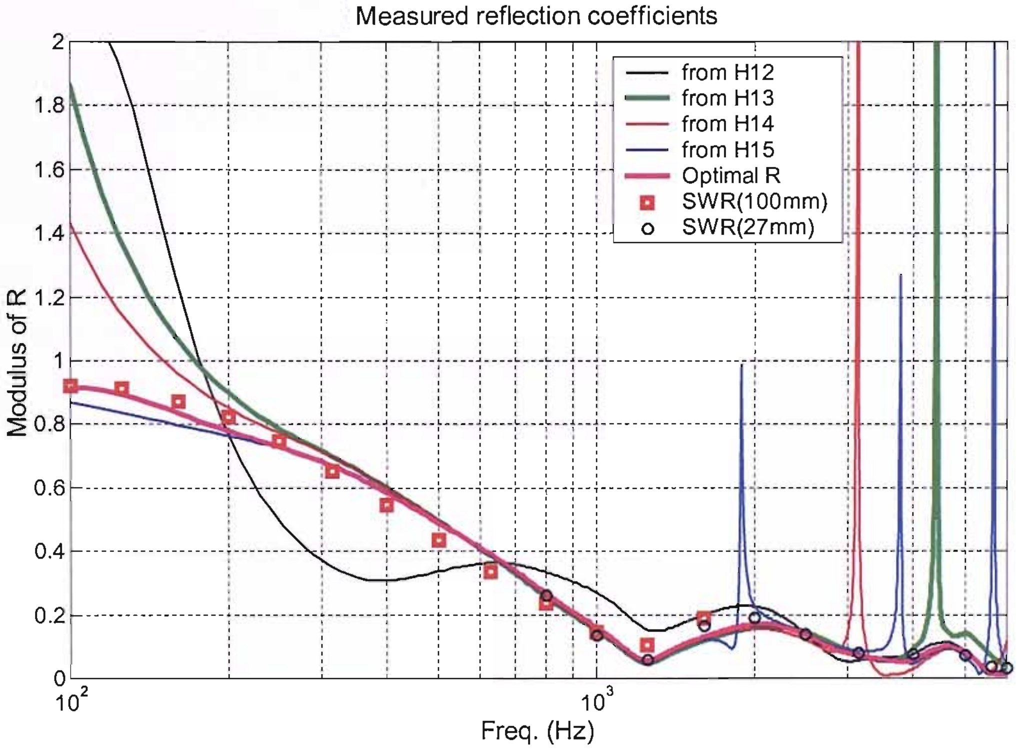

FIG. 4.13: Measured reflection coefficients of rockwool for the frequency range of 100 Hz to 6 kHz. The optimally estimated result is not affected by error frequencies and performs better at low frequencies than the result from the conventional two-microphone method using $\hat{H}_{12}$.

4.5 Conclusion

The theory of the least squares estimation of acoustic reflection coefficients applied to the measurements in an impedance tube does indeed produce promising results. The results of reflection coefficients do match very well to the referenced values obtained from the SWR method. Since this theory is based on the transfer function method, it allows broadband measurement which gives swifter results than the SWR method. Moreover, the measurable lower frequency limit by using $27\,mm$ diameter tube is extended down to $100\,\mathrm{Hz}$. This is a great improvement considering that conventionally bigger diameter tube has been used for low frequency measurements.

Chapter 5

LEAST SQUARES ESTIMATION IN A FREE FIELD USING AN IMAGE SOURCE MODEL

In Chapter 3, the theory of least squares estimation of acoustic reflection coefficients was developed in a one-dimensional sound field, and application of this theory to the impedance tube measurement was successfully demonstrated in Chapter 4. In this Chapter, the least squares estimation of acoustic reflection coefficients using an image source model is directly applied to a three-dimensional acoustic field.

5.1 A point monopole source and an image source in a free field

A point monopole sound source generates spherical waves in a free field. The plane boundary of reflection, however, is not compatible with the spherical waves. Hence an image source model of acoustic reflection is a considerable simplification of an actual acoustic reflection. A more accurate representation of acoustic reflection on an infinite plane boundary is provided by a decomposition of a spherical wave as a superposition of plane-wave components (Brekhovskikh, 1980). In this thesis, this model is called a PWD (plane-wave decomposition) model. The PWD model uses incident angle dependent and frequency dependent complex reflection coefficients, and includes the phase and amplitude changes due to finite distances between image sources and the detector. Adoption of this model is fully discussed and presented in Chapter 7.

However, with a considerable distance between a sound source and a reflecting boundary, an image source model of acoustic reflection is a good approximation. An image source model is preferable in many respects because it gives a much simpler representation of acoustic reflection. Moreover for sound at normal incidence on an absorbent material, it has been shown (Suh and Nelson, 1998) that the reflected sound pressure of an image source model has a marginal error compared with a PWD model. For the purpose that an image source model could yield practically useful approximations, the absorbent material has to be assumed to be locally reacting. A material with high flow resistivity satisfies this criterion reasonably (Fahy, 2001).

The size of the test sample is presumed to be infinite in this method. In practice, however, a reasonably good size is required in order to avoid diffractions from edges. A rough guide for acceptable size of the test sample is given by the theory of Fresnel zone defined by all points at the reflecting surface that can be reached by any reflected path that has a certain maximum difference in length to the specularly reflected path between source and receiver (Nocke, 2000). This concept was stated in Section 2.2.7 and will discussed in the measurement results in Chapter 6.

5.2 Least squares estimation of acoustic reflection coefficients in a free field using an image source model

A point monopole source generates a spherically spreading sound field in a free field, and the pressure, p, can be expressed as given by Eq. (1.13). As mentioned before, this model provides an approximation for the reflections at the plane boundary. It is assumed that the reflecting surface is locally reacting and the sound source is far away from the reflecting surface.

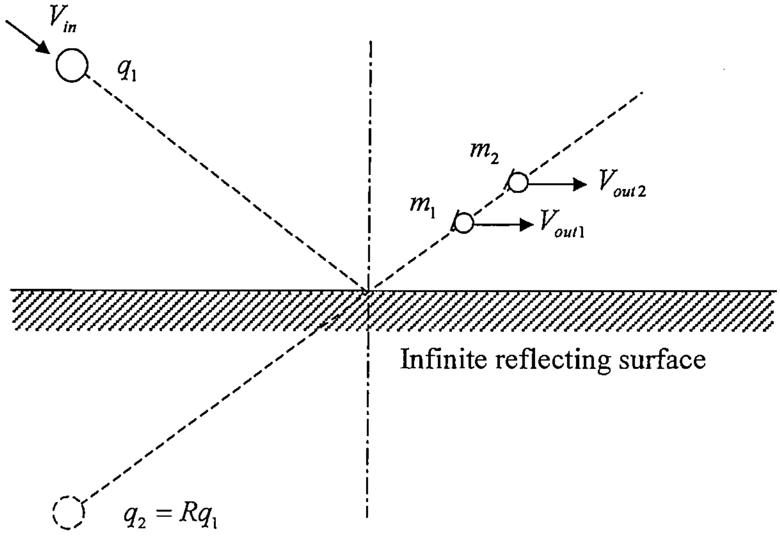

FIG. 5.1: Acoustic propagation and reflection model in a free field. The symbols V_{in} and V_{out} denote input and output voltages respectively. p_1 and p_2 are sound pressures detected by each microphone. R is complex reflection coefficient. q_1 and q_2 are strengths of original source and image source respectively. Microphones m_1 and m_2 are placed in the same plane of acoustic reflection.

The Green functions, g_{11} and g_{21}, which relate the outputs to the original source can be defined by

$$g_{11} = \frac{j\omega\rho_0 e^{-jkr_{11}}}{4\pi r_{11}}, \quad g_{21} = \frac{j\omega\rho_0 e^{-jkr_{21}}}{4\pi r_{21}} \tag{5.1}$$

where r_{11} and r_{21} are distances from the microphone 1 and microphone 2 to the original source respectively. Likewise the Green functions, g_{11} and g_{21}, which relate the outputs to the original source can be defined by

$$g_{21} = \frac{j\omega\rho_0 e^{-jkr_{21}}}{4\pi r_{21}}, \quad g_{22} = \frac{j\omega\rho_0 e^{-jkr_{22}}}{4\pi r_{22}} \tag{5.2}$$

where r_{21} and r_{22} are distances from the microphone 2 to the sound source and its image source respectively. Hence from Eq. (3.1) the sound pressures picked up at each microphone 1 and 2 can be expressed as

$$\begin{aligned} p_1 &= \frac{j\omega\rho_0 q_1 e^{-jkr_{11}}}{4\pi r_{11}} + \frac{j\omega\rho_0 q_2 e^{-jkr_{12}}}{4\pi r_{12}} \\ p_2 &= \frac{j\omega\rho_0 q_1 e^{-jkr_{21}}}{4\pi r_{21}} + \frac{j\omega\rho_0 q_2 e^{-jkr_{22}}}{4\pi r_{22}} \end{aligned} \tag{5.3}$$

By using Eq. (3.2), these equations can also be expressed as

$$\begin{aligned} p_1 &= \frac{j\omega\rho_0 q_1 e^{-jkr_{11}}}{4\pi r_{11}} + R\frac{j\omega\rho_0 q_1 e^{-jkr_{12}}}{4\pi r_{12}} \\ p_2 &= \frac{j\omega\rho_0 q_1 e^{-jkr_{21}}}{4\pi r_{21}} + R\frac{j\omega\rho_0 q_1 e^{-jkr_{22}}}{4\pi r_{22}} \end{aligned} \tag{5.4}$$

With the same analysis as that presented in Chapter 3, the complex reflection coefficient, R, can be obtained as described in Eq. (3.5). In this case therefore

$$R=\frac{\dfrac{e^{-jkr_{21}}}{r_{21}}-\dfrac{e^{-jkr_{11}}}{r_{11}}H_{12}}{\dfrac{e^{-jkr_{12}}}{r_{12}}H_{12}-\dfrac{e^{-jkr_{22}}}{r_{22}}} \tag{5.5}$$

where H_{12} is the transfer function defined in Eq. (3.4).

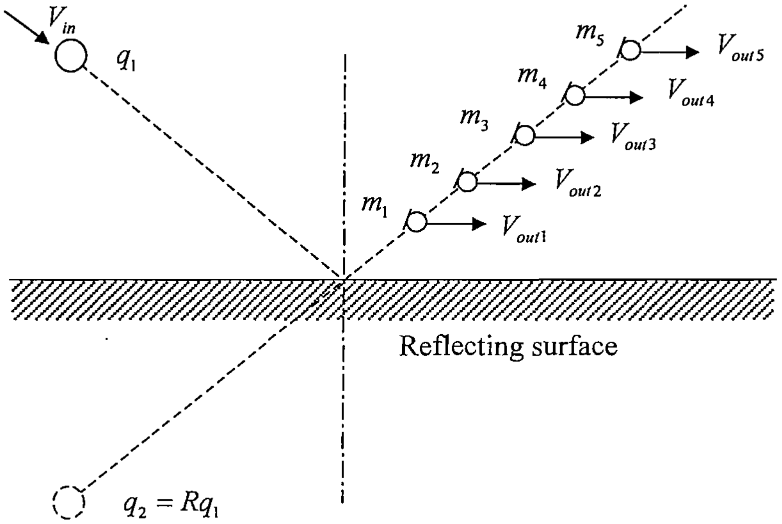

FIG. 5.2: Multiple-microphone array. At least three microphones are placed along the plane of acoustic reflection

The application of the theory presented in Chapter 3 to the free-field image source model is straightforward, and the expressions for the optimally estimated acoustic reflection coefficient, Eq. (3.18) for two-measurement points and Eq. (3.28) for multi-measurement points are directly applicable with condition that the Green functions are defined by Eqs. (5.1) and (5.2). The following two equations are repetition of Eqs. (3.18) and (3.28) and thus recall the resultant expressions for the optimally estimated acoustic reflection coefficient. For two microphone measurement,

$$R_{opt} = \frac{g_{21} - g_{11}\hat{H}_{12}}{g_{12}\hat{H}_{12} - g_{22}} \tag{5.6}$$

and for multiple microphone measurement,

$$R_{opt} = -\frac{\sum_{m=2}^{M} A_m B_m^*}{\sum_{m=2}^{M} \left|B_m\right|^2} = -\frac{\sum_{m=2}^{M} \left(g_{11}\hat{H}_{1m} - g_{m1}\right)\left(g_{12}\hat{H}_{1m} - g_{m2}\right)^*}{\sum_{m=2}^{M} \left|g_{12}\hat{H}_{1m} - g_{m2}\right|^2} \tag{5.7}$$

where $\hat{H}_{12}$ and $\hat{H}_{1m}$ are measured transfer functions, m is microphone index and M is the total number of microphones. It should thus be noted that these results are derived from a direct application of the theory in one dimensional plane wave case to the free-field spherical wave case.

5.3 Analysis of error frequencies related to the relative positions of microphones

In this section, an analysis is presented that identifies the "error frequencies" where the measured results of reflection coefficients tend to "blow up" in the presence of interfering noise signals that produce small uncertainties in the measurements. These frequencies are found to be directly related to the relative position of the microphones. Error frequencies in an impedance tube, as a special case, will be analysed in Section 5.4.

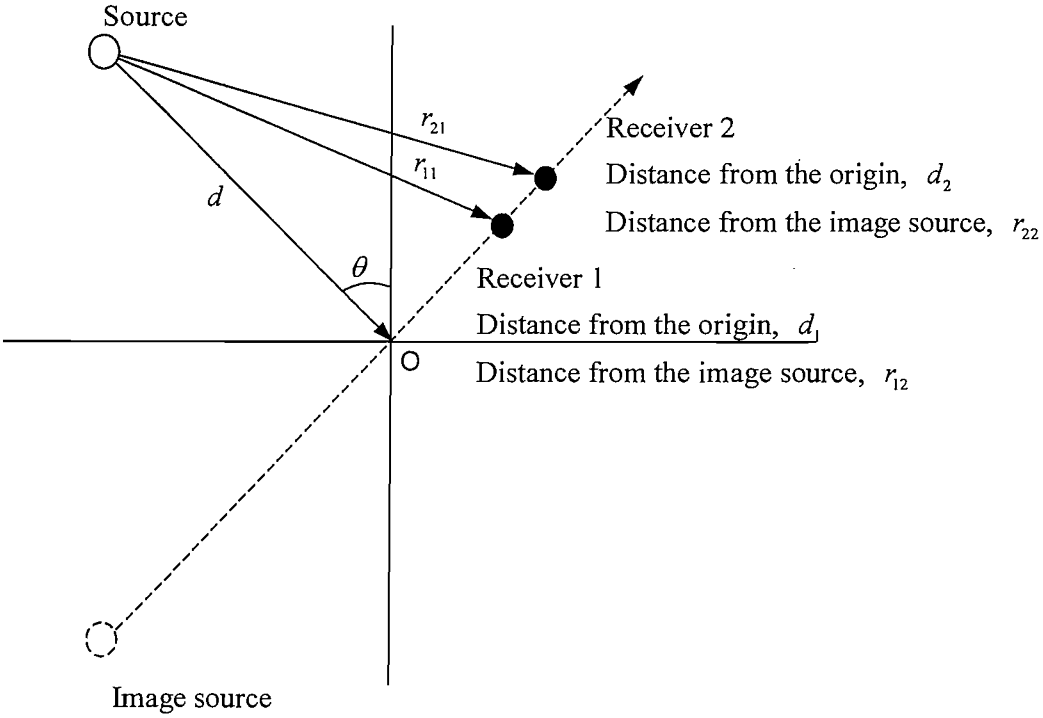

FIG. 5.3: Free field modelling of the measurement of reflection coefficients. The distance from the origin to the source, receivers 1 and 2 are d, d_1 and d_2 respectively and are kept constant. The distances from the image source to receivers 1 and 2 are r_{12} and r_{22}. The source is placed far away from the boundary such that plane wave incidence is approximated and d is always longer than d_1 and d_2.

Eqs. (3.1) and (3.3) can be expressed, in matrix form, as

$$\begin{bmatrix} p_1 \\ p_2 \end{bmatrix} = \begin{bmatrix} g_{11} & g_{12} \\ g_{21} & g_{22} \end{bmatrix} \begin{bmatrix} q_1 \\ q_2 \end{bmatrix} = \begin{bmatrix} g_{11} & g_{12} \\ g_{21} & g_{22} \end{bmatrix} \begin{bmatrix} 1 \\ R \end{bmatrix} q_1 \tag{5.8}$$

where we can define the matrix **G** as

$$\mathbf{G}=\begin{bmatrix} g_{11} & g_{12} \\ g_{21} & g_{22} \end{bmatrix} \tag{5.9}$$

The complex reflection coefficient, *R*, is obtained only when the inverse of matrix **G** is available such that

$$\begin{bmatrix} 1 \\ R \end{bmatrix}=\frac{1}{q_1}\begin{bmatrix} g_{11} & g_{12} \\ g_{21} & g_{22} \end{bmatrix}^{-1}\begin{bmatrix} p_1 \\ p_2 \end{bmatrix} \tag{5.10}$$

and it follows that

$$\begin{bmatrix} 1 \\ R \end{bmatrix}=\frac{1}{q_1\det(\mathrm{G})}\begin{bmatrix} g_{22} & -g_{12} \\ -g_{21} & g_{11} \end{bmatrix}\begin{bmatrix} p_1 \\ p_2 \end{bmatrix} \tag{5.11}$$

where the determinant of matrix **G** must not be zero for the existence of its inverse matrix.

$$\det(\mathbf{G})=g_{22}g_{11}-g_{12}g_{21}\neq 0 \tag{5.12}$$

Therefore the expression for R is given by

$$R=\frac{1}{q_1}\left(\frac{g_{11}p_2-g_{21}p_1}{g_{11}g_{22}-g_{21}g_{12}}\right)=\frac{1}{q_1}\frac{N}{D} \tag{5.13}$$

where the symbols N and D denote numerator and denominator respectively. Since g_{11}, g_{12}, g_{21} and g_{22} are functions of wavenumber, k, for a fixed geometry, the following term is defined in order to investigate its behaviour.

$$D(k) \equiv g_{22}g_{11} - g_{12}g_{21} \tag{5.14}$$

Taking modulus of $D(k)$ gives

$$\begin{aligned} D_m(k) &\equiv \left|D(k)\right| \\ &= \sqrt{\left(g_{22}g_{11} - g_{12}g_{21}\right)\left(g_{22}g_{11} - g_{12}g_{21}\right)^*} \\ &= \sqrt{g_{22}g_{11}g_{22}^*g_{11}^* - g_{22}g_{11}g_{12}^*g_{21}^* - g_{12}g_{21}g_{22}^*g_{11}^* + g_{12}g_{21}g_{12}^*g_{21}^*} \end{aligned} \tag{5.15}$$

Substituting Eqs. (5.1) and (5.2) into Eq. (5.15) results in

$$\begin{aligned} D_m(k) &= \sqrt{\frac{1}{\left(r_{22}r_{11}\right)^2} + \frac{1}{\left(r_{12}r_{21}\right)^2} - \frac{e^{-jk\left(r_{22}+r_{11}-r_{12}-r_{21}\right)} + e^{-jk\left(r_{12}+r_{21}-r_{22}-r_{11}\right)}}{r_{22}r_{11}r_{12}r_{21}}} \\ &= \sqrt{\frac{\left(r_{12}r_{21}\right)^2 + \left(r_{22}r_{11}\right)^2}{\left(r_{22}r_{11}r_{12}r_{21}\right)^2} - \frac{e^{-jk\left(r_{22}+r_{11}-r_{12}-r_{21}\right)} + e^{-jk\left(r_{12}+r_{21}-r_{22}-r_{11}\right)}}{r_{22}r_{11}r_{12}r_{21}}} \\ &= \sqrt{\frac{\left(r_{22}r_{11}\right)^2 + \left(r_{12}r_{21}\right)^2 - r_{22}r_{11}r_{12}r_{21}\left(e^{jk\left(r_{22}+r_{11}-r_{12}-r_{21}\right)} + e^{-jk\left(r_{22}+r_{11}-r_{12}-r_{21}\right)}\right)}{\left(r_{22}r_{11}r_{12}r_{21}\right)^2}} \end{aligned} \tag{5.16}$$

Using Euler's formula, Eq. (5.16) leads to

$$D_m(k)=\frac{\sqrt{(r_{22}r_{11})^2+(r_{12}r_{21})^2-2r_{22}r_{11}r_{12}r_{21}\cos k(r_{22}+r_{11}-r_{12}-r_{21})}}{r_{22}r_{11}r_{12}r_{21}} \tag{5.17}$$

Since $D_m(k)$ is a function of only k, and r_{22}, r_{11}, r_{12} and r_{21} are constants, $D_m(k)$ has a minimum value when

$$\cos k(r_{22}+r_{11}-r_{12}-r_{21})=1 \tag{5.18}$$

i.e., $D_m(k)$ is at its minimum when k is given by k_0.

$$k_0=\frac{2n\pi}{r_{22}+r_{11}-r_{12}-r_{21}} \tag{5.19}$$

where n is an integer. So the minimum value of $D_m(k)$ is given by

$$D_m(k_0)=\frac{\sqrt{(r_{22}r_{11})^2+(r_{12}r_{21})^2-2r_{22}r_{11}r_{12}r_{21}}}{r_{22}r_{11}r_{12}r_{21}}=\frac{r_{22}r_{11}-r_{12}r_{21}}{r_{22}r_{11}r_{12}r_{21}} \tag{5.20}$$

The numerator of Eq. (5.20) can be expressed in terms of d, d_1, d_2 and θ (Fig. 5.3).

$$\begin{aligned} r_{22}&=d+d_2, \quad r_{11}=\sqrt{d^2+d_1^2-2dd_1\cos 2\theta} \\ r_{12}&=d+d_1, \quad r_{21}=\sqrt{d^2+d_2^2-2dd_2\cos 2\theta} \end{aligned} \tag{5.21}$$

So

$$\begin{aligned} r_{22}r_{11} &= \left(d+d_2\right)\sqrt{d^2+d_1^2-2dd_1\cos 2\theta} \\ &= \sqrt{\left(d^2+2dd_2+d_2^2\right)\left(d^2+d_1^2-2dd_1\cos 2\theta\right)} \end{aligned} \tag{5.22}$$

and

$$\begin{aligned} r_{12}r_{21} &= \left(d+d_1\right)\sqrt{d^2+d_2^2-2dd_2\cos 2\theta} \\ &= \sqrt{\left(d^2+2dd_1+d_1^2\right)\left(d^2+d_2^2-2dd_2\cos 2\theta\right)} \end{aligned} \tag{5.23}$$

Subtracting the square of $r_{12}r_{21}$ from that of $r_{22}r_{11}$ shows that

$$\left(r_{22}r_{11}\right)^2-\left(r_{12}r_{21}\right)^2 = 2d\left(1+\cos 2\theta\right)\left\{d_2\left(d+d_1\right)^2-d_1\left(d+d_2\right)^2\right\} \tag{5.24}$$

Now define the following terms

$$\begin{aligned} X &\equiv 2d\left(1+\cos 2\theta\right) \\ Y &\equiv d_2\left(d+d_1\right)^2-d_1\left(d+d_2\right)^2 \end{aligned} \tag{5.25}$$

X cannot be a negative number at any angle of θ since d is a positive real number and

$$0 \le \left(1+\cos 2\theta\right) \le 2 \tag{5.26}$$

Thus X is a positive number except

$$\cos 2\theta = -1, \quad \text{for } \theta = \left(\frac{2n+1}{2}\right)\pi \text{ where } n \text{ is an integer} \tag{5.27}$$

In practice, the angle of incidence is meaningful only when $0 \le \theta < 90^\circ$. Therefore X is positive in this analysis.

Y can further expand to

$$\begin{aligned} Y &= d_2\left(d^2 + 2dd_1 + d_1^2\right) - d_1\left(d^2 + 2dd_2 + d_2^2\right) \\ &= d_2d^2 + d_2d_1^2 - d_1d^2 - d_1d_2^2 \\ &= d^2\left(d_2 - d_1\right) - d_1d_2\left(d_2 - d_1\right) \\ &= \left(d^2 - d_1d_2\right)\left(d_2 - d_1\right) \end{aligned} \tag{5.28}$$

Y is positive as long as the following condition applies in Fig. 5.3.

$$d > d_2 > d_1 \tag{5.29}$$

Hence it can be said that

$$\left(r_{22}r_{11}\right)^2 - \left(r_{12}r_{21}\right)^2 > 0 \tag{5.30}$$

i.e.,

$$r_{22}r_{11} - r_{12}r_{21} > 0 \tag{5.31}$$

considering that r_{11}, r_{12}, r_{21} and r_{22} are all positive real numbers.

Now it is concluded for $D_m(k)$ from Eq. (5.17) that

$$D_m(k) > 0, \quad \text{for } 0 \le \theta < \frac{\pi}{2} \tag{5.32}$$

with the minimum value given when the wavenumber is given by k_0 in Eq. (5.19).

This analysis proves that the determinant of matrix G cannot be zero, and therefore provides a validity of the matrix equation for the reflection coefficient in Eq. (5.11)

Fig. 5.4 shows the reproduced reflection coefficient (R) with the numerator (N) and denominator (D) defined in Eq. (5.13) drawn separately in the same figure, and the same definitions of numerator and denominator of the reflection coefficient are used in Fig. 5.5 and Fig. 5.7 (and $q_1 = 1$ in Eq. (5.13)).

In the above analysis, it has been shown that the denominator is at its minimum when the wavenumber is given by k_0. The numerator, in Fig. 5.4, also has its minimum at k_0. This can be easily understood because the reflection coefficient is a function of only a wavenumber for a fixed geometry and is a fraction of the incident sound pressure. Thus in Fig. 5.4B it is clearly shown that the exact value of reflection coefficient is reproduced even at the point where both numerator and denominator are at their minimum.

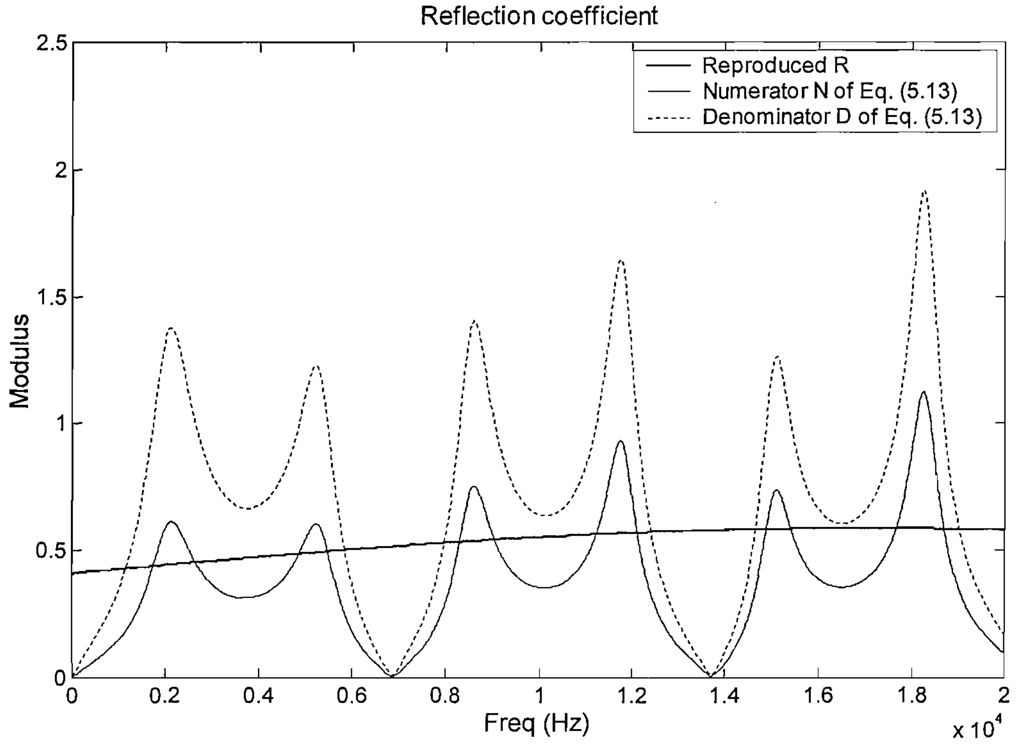

FIG. 5.4A: Simulated reflection coefficients reproduce exact values and do not have any peaks at the frequencies that are related to the microphone separation of $2.5\,\text{cm}$.

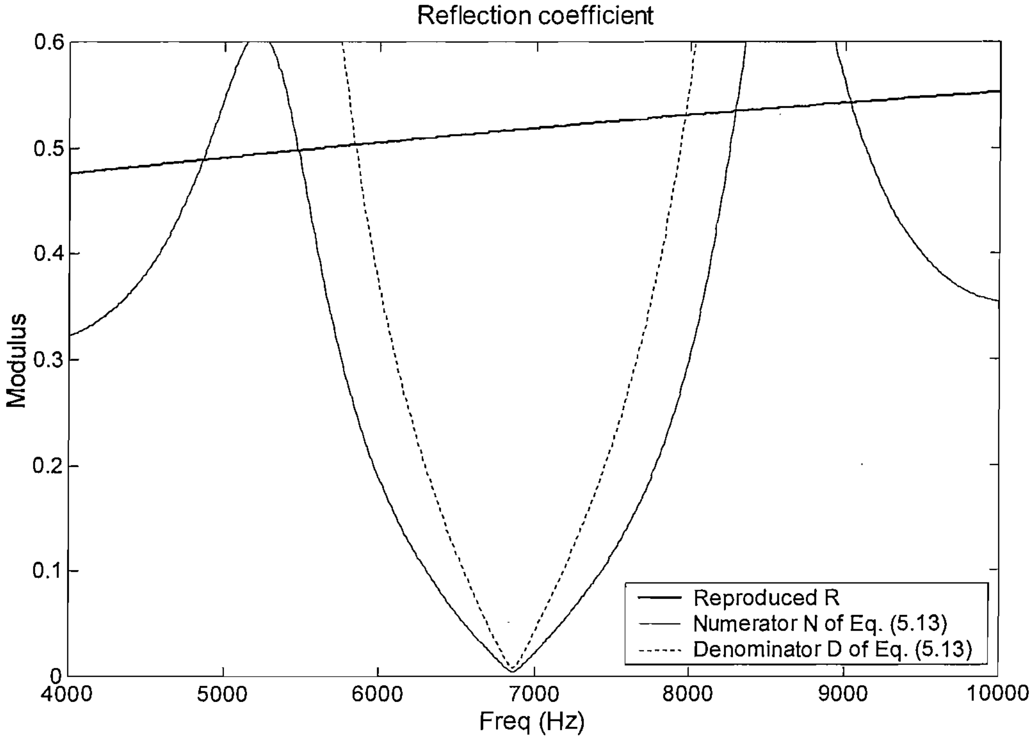

FIG. 5.4B: Numerator and denominator of the simulated reflection coefficients have local minima at the same frequencies.

In the practical measurement, however, there are contaminating noises that could be acoustical, mechanical or electrical and so on, in the transfer function, H_{12}. Thus we define

$$\begin{aligned} \hat{H}_{12} &\equiv H_{12} \text{ with noise} \\ \hat{R} &\equiv R \text{ with noise} \end{aligned} \qquad (5.33)$$

In this case the minimum modulus of both numerator and denominator of $\hat{R}$ happen at slightly different frequencies from k_0. As a result, the modulus of $\hat{R}$ has peaks at the given frequencies of k_0. This is shown in Fig. 5.5.

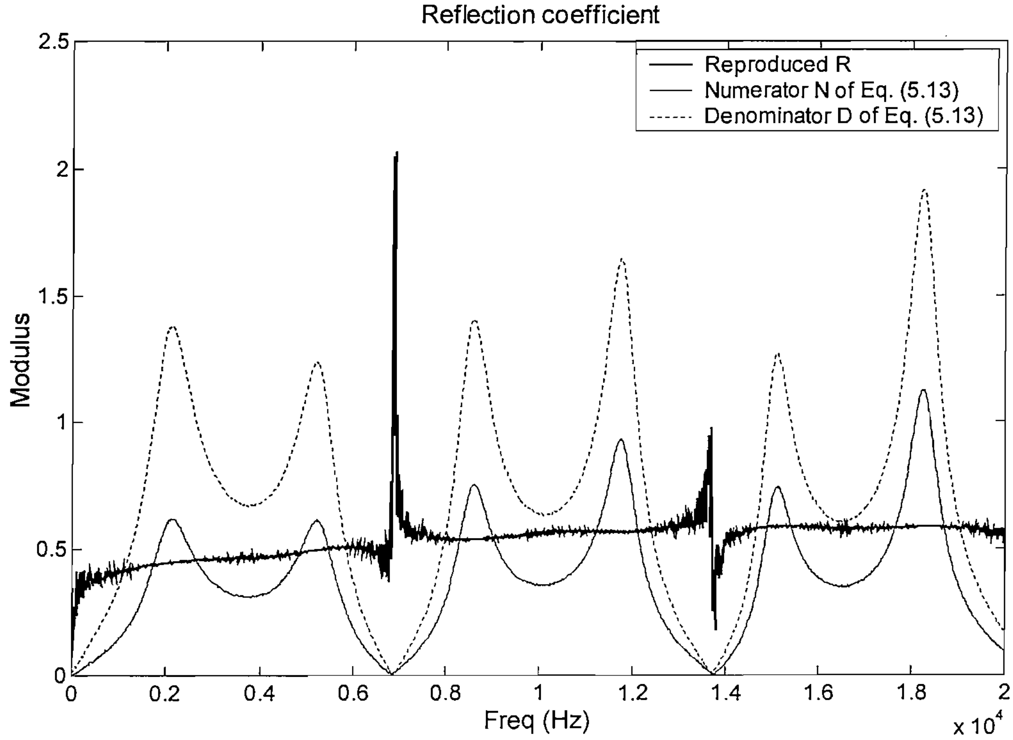

FIG. 5.5A: When the transfer function contains random noise, the simulated reflection coefficients have harmonic peaks at the frequencies that are related to the microphone separation.

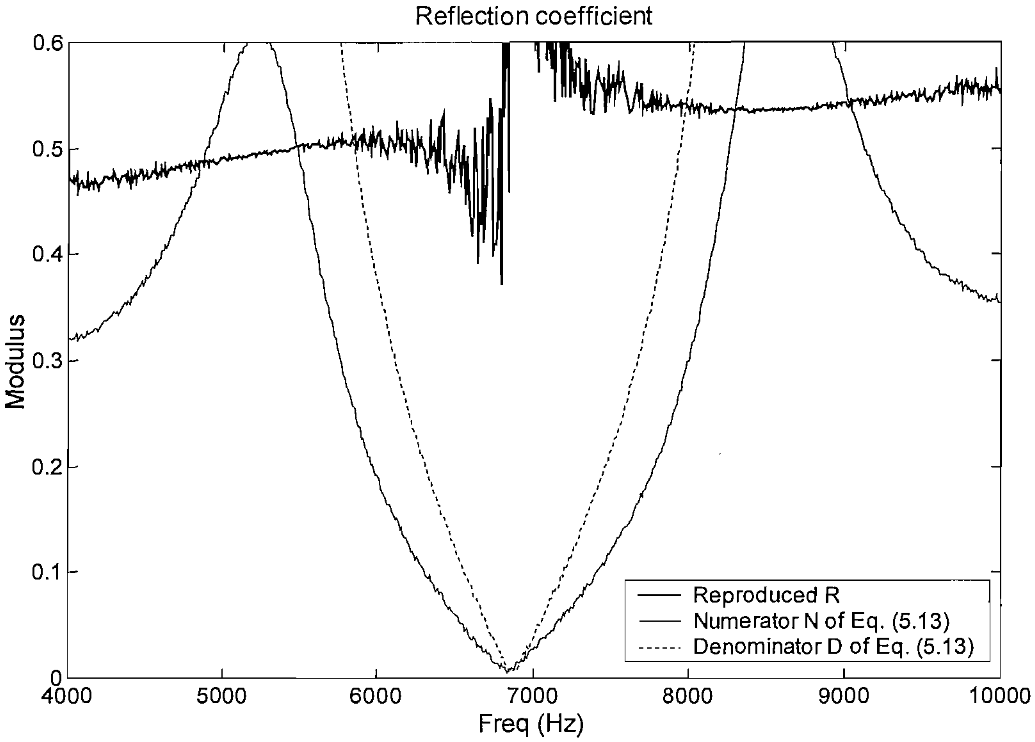

FIG. 5.5B: With contaminating noise, numerator and denominator have local minima at slightly different frequencies, which results in harmonic peaks in the reflection coefficients.

As the angle of incidence θ changes, the distances r_{11} and r_{12} change while d, d_1 and d_2 are kept constant. This results in changes in the wavenumber k_0 where $\hat{R}$ has peaks. To confirm this result, the fundamental frequencies of each first harmonic peak are investigated as the angle of incidence changes. Since the definition of wavenumber is given by

$$k = \frac{2\pi f}{c} \tag{5.34}$$

where c is the speed of sound, from Eq. (5.19) the fundamental peak frequencies are predicted as

$$f_0 = \frac{c}{r_{22} + r_{11} - r_{12} - r_{21}} \tag{5.35}$$

This prediction is confirmed by the simulation results where the angle of incidence changes from 0° to 80° with the step of 10°. See Fig. 5.6 and Fig. 5.7.

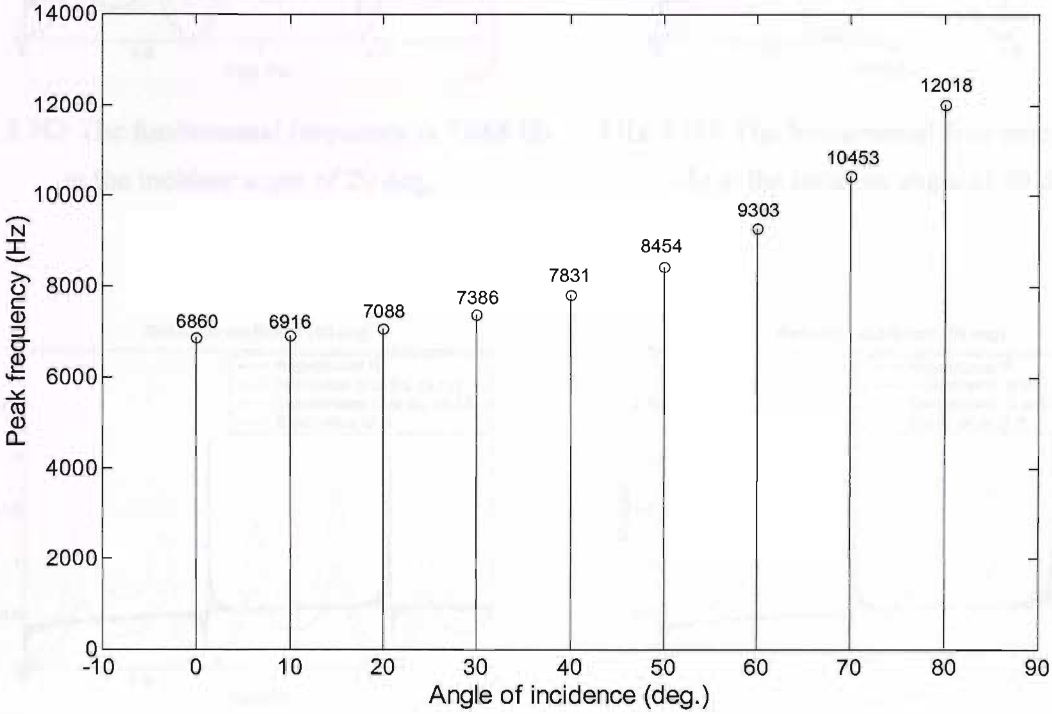

FIG. 5.6: Change of fundamental peak frequency depending on the angle of incidence when $d = 2m$, $d_1 = 5.31cm$, $d_2 = 7.81cm$ and $c = 343m/s$

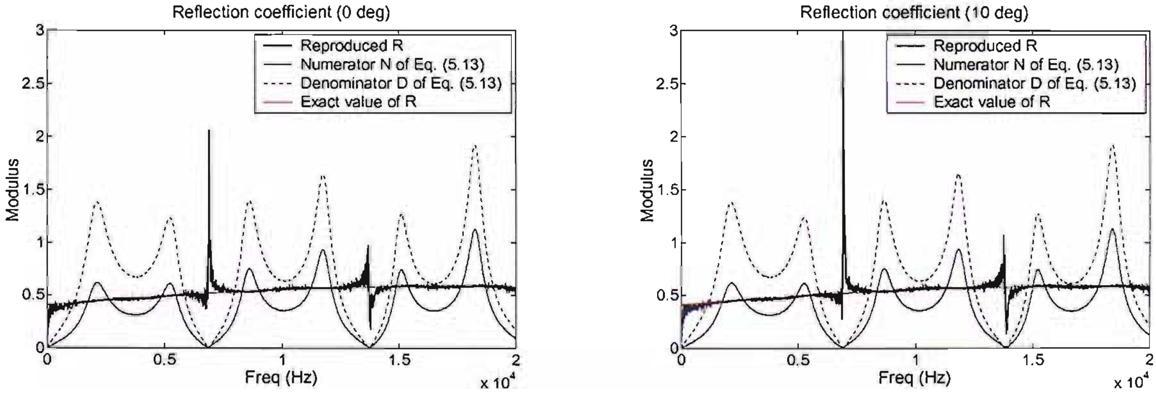

FIG. 5.7A: The fundamental frequency is 6,860 Hz at the incident angle of 0 deg.

FIG. 5.7B: The fundamental frequency is 6,916 Hz at the incident angle of 10 deg.

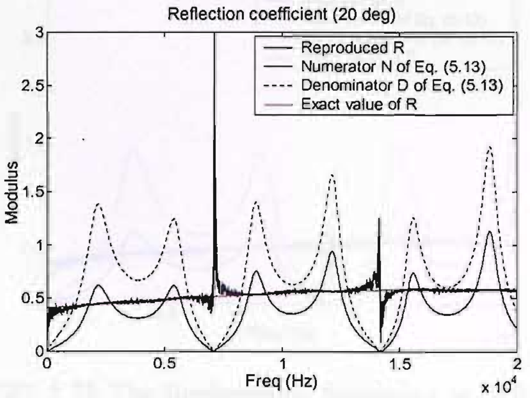

FIG. 5.7C: The fundamental frequency is 7,088 Hz at the incident angle of 20 deg.

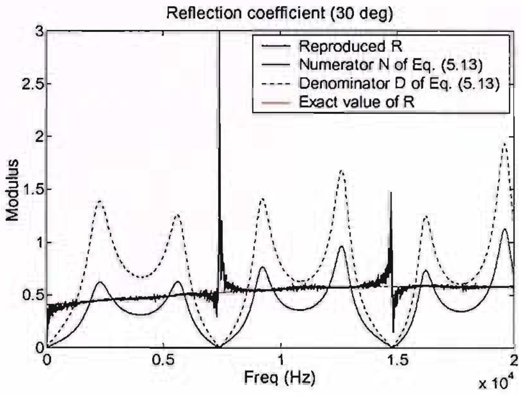

FIG. 5.7D: The fundamental frequency is 7,386 Hz at the incident angle of 30 deg.

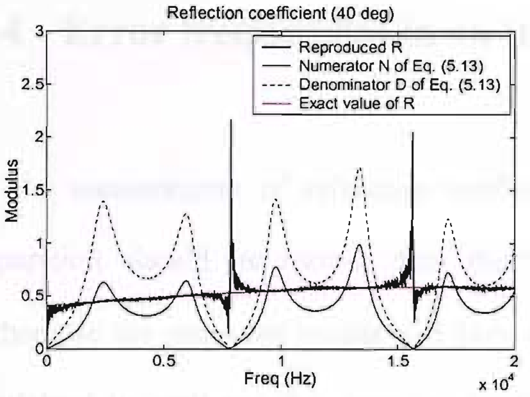

FIG. 5.7E: The fundamental frequency is 7, 831 Hz at the incident angle of 40 deg.

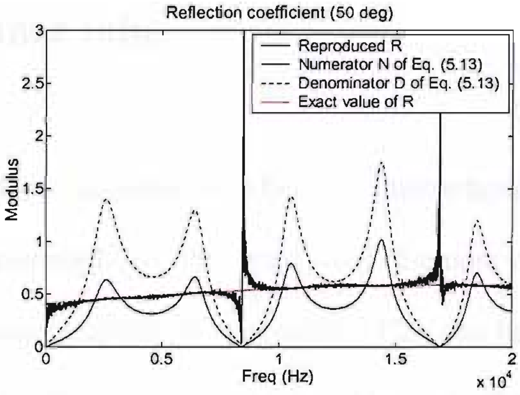

FIG. 5.7F: The fundamental frequency is 8,454 Hz at the incident angle of 50 deg.

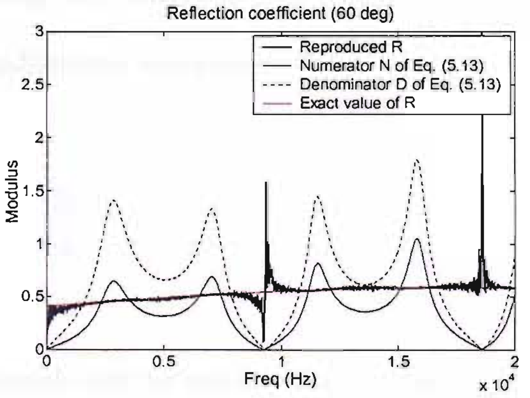

FIG. 5.7G: The fundamental frequency is 9,303 Hz at the incident angle of 60 deg.

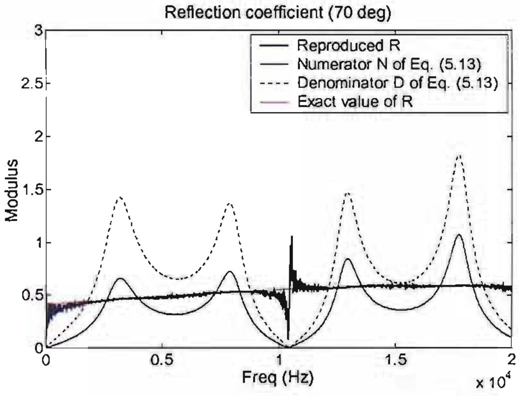

FIG. 5.7H: The fundamental frequency is 10,453 Hz at the incident angle of 70 deg.

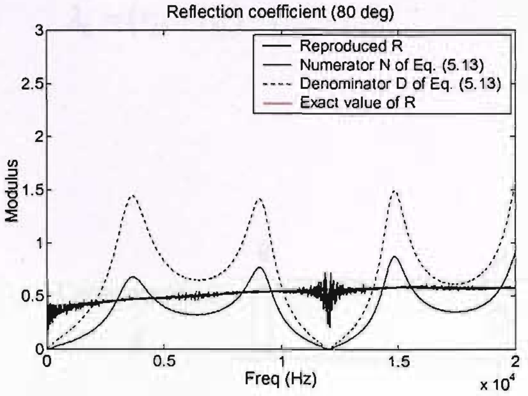

FIG. 5.7I: The fundamental frequency is 12,018 Hz at the incident angle of 80 deg.

5.4 Error frequencies in an impedance tube

In the measurement of reflection coefficients in the impedance tube, the microphone separation should be shorter than the half wavelength of the maximum frequency. Otherwise the measured results will have error frequencies that are harmonic. This can be explained by applying the above analysis to the special case of normal incidence in the tube.

Using the relationship $k = 2\pi/\lambda$ shows that Eq. (5.19) can be written in terms of the fundamental wavelength, λ_0.

$$\frac{2\pi}{\lambda_0} = \frac{2\pi}{r_{22} + r_{11} - r_{12} - r_{21}} \tag{5.36}$$

Considering the relative magnitudes of r_{22}, r_{11}, r_{12} and r_{21}, Eq. (5.36) can be written as

$$\lambda_0 = (r_{22} - r_{21}) - (r_{12} - r_{11}) \tag{5.37}$$

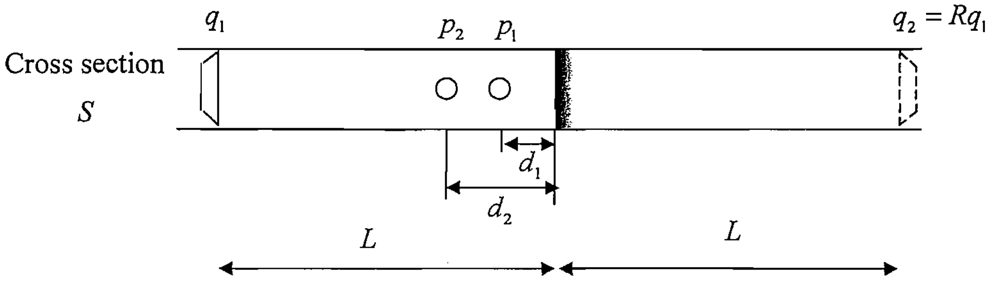

FIG. 5.8: Impedance tube setup with microphone separation, $d_2 - d_1$.

In Fig. 5.8, the distances between the sources and microphones, r_{11}, r_{12}, r_{21} and r_{22}, are

$$\begin{aligned} r_{11} &= L - d_1 \\ r_{12} &= L + d_1 \\ r_{21} &= L - d_2 \\ r_{22} &= L + d_2 \end{aligned} \tag{5.38}$$

Substituting Eq. (5.38) into Eq. (5.37),

$$\begin{aligned} \lambda_0 &= (r_{22} - r_{21}) - (r_{12} - r_{11}) \\ &= \left[(L + d_2) - (L - d_2)\right] - \left[(L + d_1) - (L - d_1)\right] \\ &= 2d_2 - 2d_1 \\ &= 2(d_2 - d_1) \end{aligned} \tag{5.39}$$

Hence the first peak occurs at the frequency of which the half wavelength is equal to the microphone separation, $d_2 - d_1$.

This analysis justifies the choices of microphone separations for multi-point measurements in an impedance tube suggested in Section 4.2.

5.5 Conclusion

In this Chapter, the theory of least squares estimation of acoustic reflection coefficient in one-dimensional sound field presented in Chapter 3 has been applied to the measurement in a free field. The analysis of error frequencies which depend on the relative positions of sources and microphones has been undertaken and demonstrated in detail. This analysis covers the relative changes in the fundamental error frequencies due to the change of angle of incidence. As a special case, the half wavelength problem associated with error frequencies in the impedance tube where only plane waves travel have been analysed.

Chapter 6

MEASUREMENT RESULTS IN THE FREE FIELD USING AN IMAGE SOURCE MODEL

In order to test the theory of the least squares estimation of acoustic reflection coefficient in a free field that has been presented in Chapter 5, many measurement sessions have been undertaken. The results presented in this chapter are those that show the best consistency within the context of least squares estimation. Some of the other measurement results are included in Appendix III.

6.1 Normal-incidence measurement

In free-field measurements using an image source model, the positions of microphones from a reflecting surface at the normal incidence were chosen to be $5.3cm$, $7.0cm$, $9.2cm$, $10.8cm$ and $14.4cm$ such that the same resultant error frequencies are expected as those in the tube-measurement, 10 kHz, 4.36 kHz, 3.09 kHz and 1.87 kHz when the speed of sound is $340 m/s$. The frequency range of measurement is the same as that in the tube-measurement, i.e., 100Hz to 6kHz.

The measurement was made in the ISVR anechoic chamber of which the dimensions are $7m(\text{L})\times 7m(\text{W})\times 5m(\text{H})$. The dimension of the reflecting surface placed on the metal-grated floor is $3.6m(\text{L})\times 3m(\text{W})\times 0.075m(\text{H})$ that consists of 15 pieces of rockwool panel of which the size of each panel is $1.2m(\text{L})\times 0.6m(\text{W})\times 0.075m(\text{H})$. The density of this material is $45\,kg/m^3$. In order to compare the results with those of impedance tube measurement, the same rockwool and the same MLSSA system were used. The sound source, however, is different from that used in the tube measurement. A two-way loudspeaker (Dynaudio Audience 40*) was hung under the ceiling at normal direction $3m$ away upon the reflecting point (Fig. 6.1A). The same type of electret microphone was used.

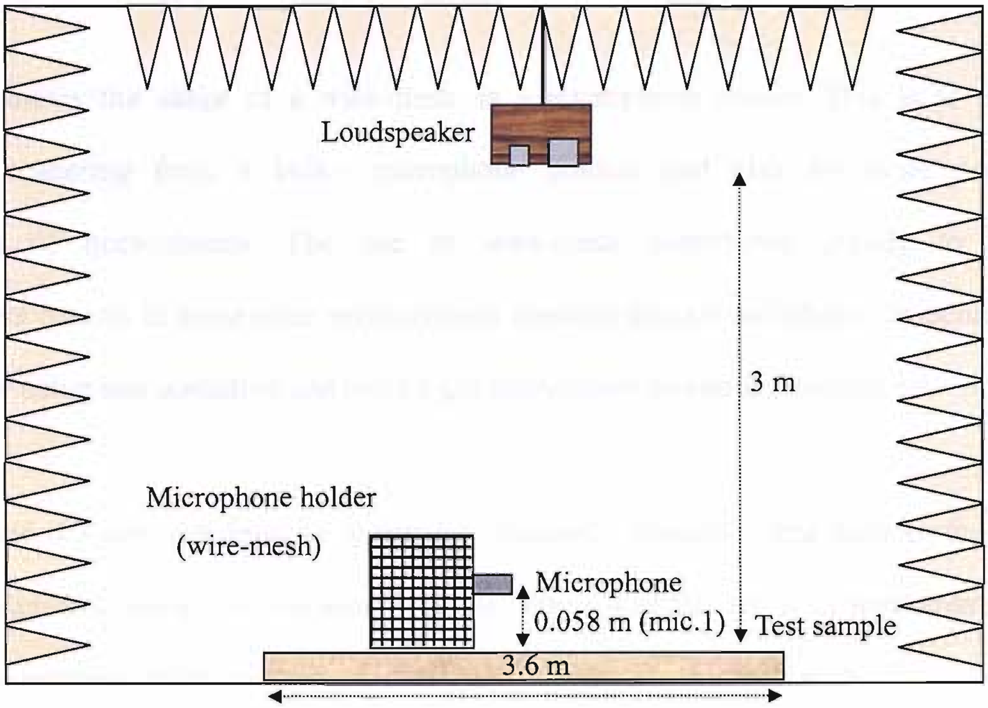

FIG. 6.1A: A diagram showing the measurement set-up for a normal-incidence measurement in a anechoic chamber.

---

* $17cm(\text{W})\times 28cm(\text{H})\times 24cm(\text{D})$, Polypropylene woofer (15 cm) and soft dome tweeter (2.5 cm), Nominal impedance 4Ω, Frequency response 53 Hz – 28 kHz and Sensitivity 86dB

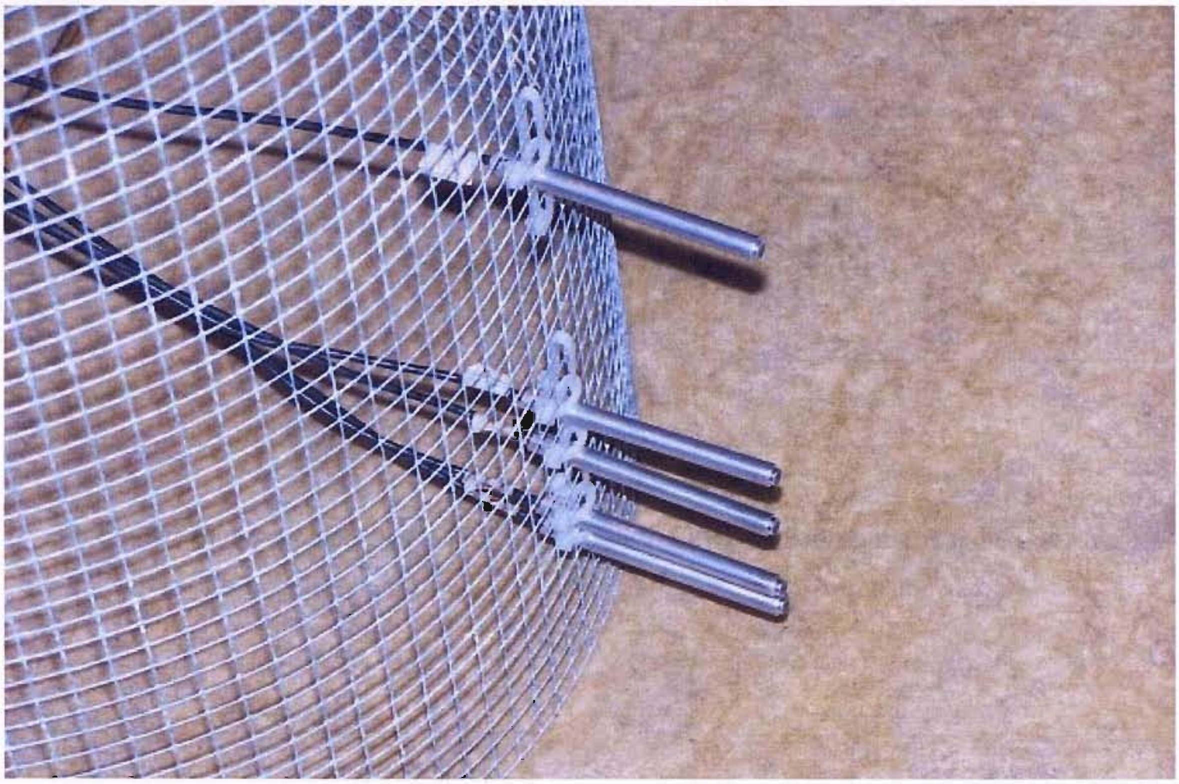

FIG. 6.1B: A wire-mesh used as a microphone holder for a normal-incidence measurement

Fig. 6.1B shows the usage of a wire-mesh as a microphone holder. This is to reduce unwanted scattering from a bulky microphone holders and also for more accurate positioning of microphones. The use of wire-mesh contributed greatly to better measurement results. In some other measurement sessions that are included in Appendix III, the need for using less scattering and more rigid microphone holder is mentioned.

Figs. 6.2 and 6.3 compare impulse responses, frequency responses and transfer functions with non-truncated signal and truncated signals. Fig. 6.4 is the result of measurement of reflection coefficient with non-truncated signals, which is compared with Fig. 6.5A, the corresponding results with truncated signals. All the following graphs in this chapter obtained in this measurement are drawn with truncated signals.

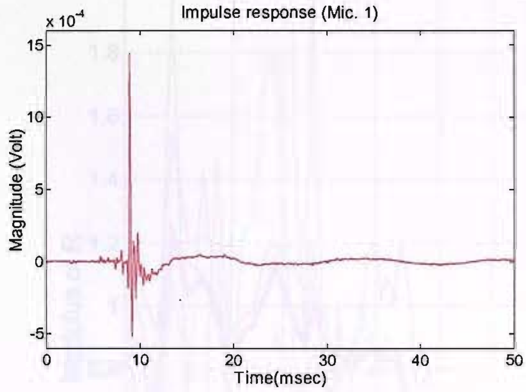

FIG. 6.2A: Impulse response at Mic. 1.
(non-truncated signal)

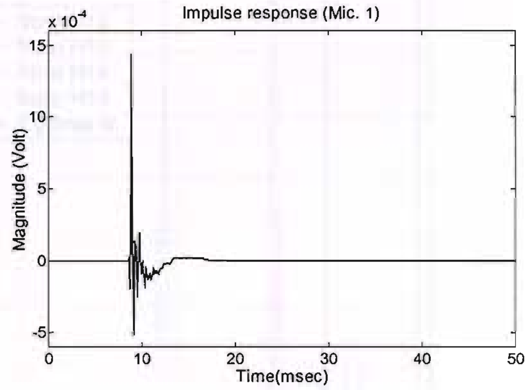

FIG. 6.2B: Impulse response at Mic. 1.
(truncated signal)

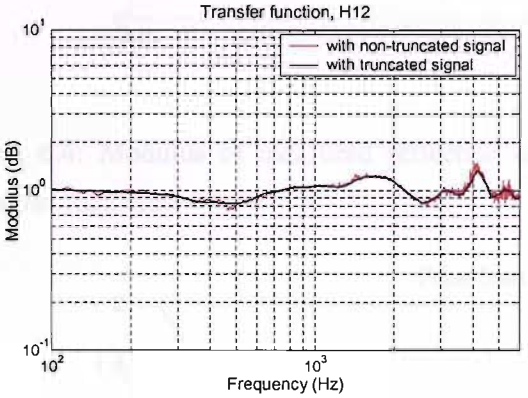

FIG. 6.3A: Transfer function, $\hat{H}_{12}$ with impulse responses at microphones 1 and 2.

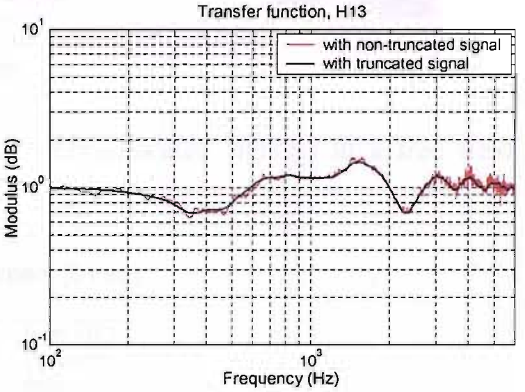

FIG. 6.3B: Transfer function, $\hat{H}_{13}$ with impulse responses at microphones 1 and 3.

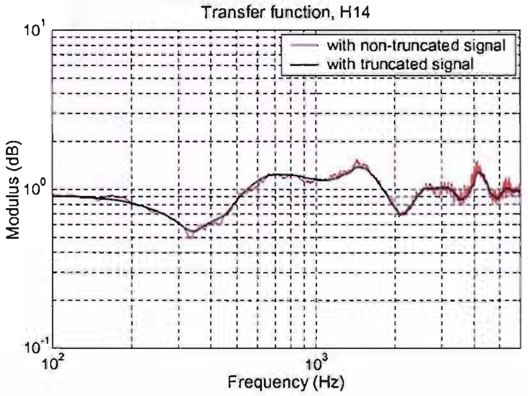

FIG. 6.3C: Transfer function, $\hat{H}_{14}$ with impulse responses at microphones 1 and 4.

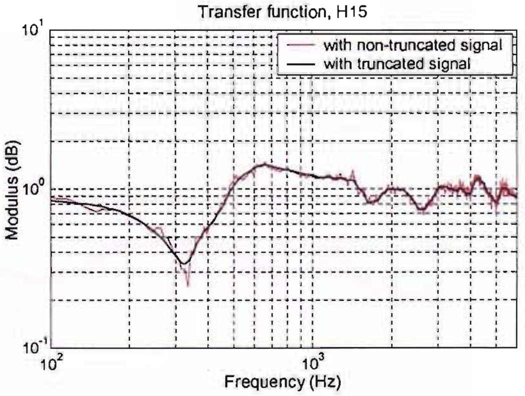

FIG. 6.3D: Transfer function, $\hat{H}_{15}$ with impulse responses at microphones 1 and 5.

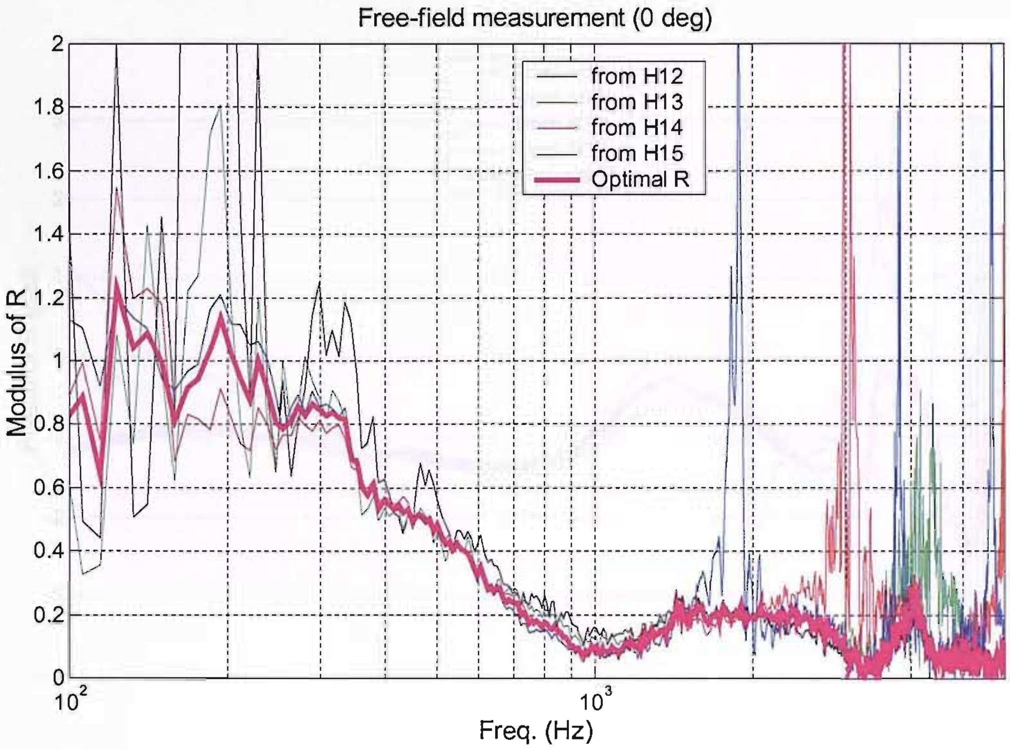

FIG. 6.4: Modulus of measured reflection coefficients (non-truncated signals) in a free field at normal incidence

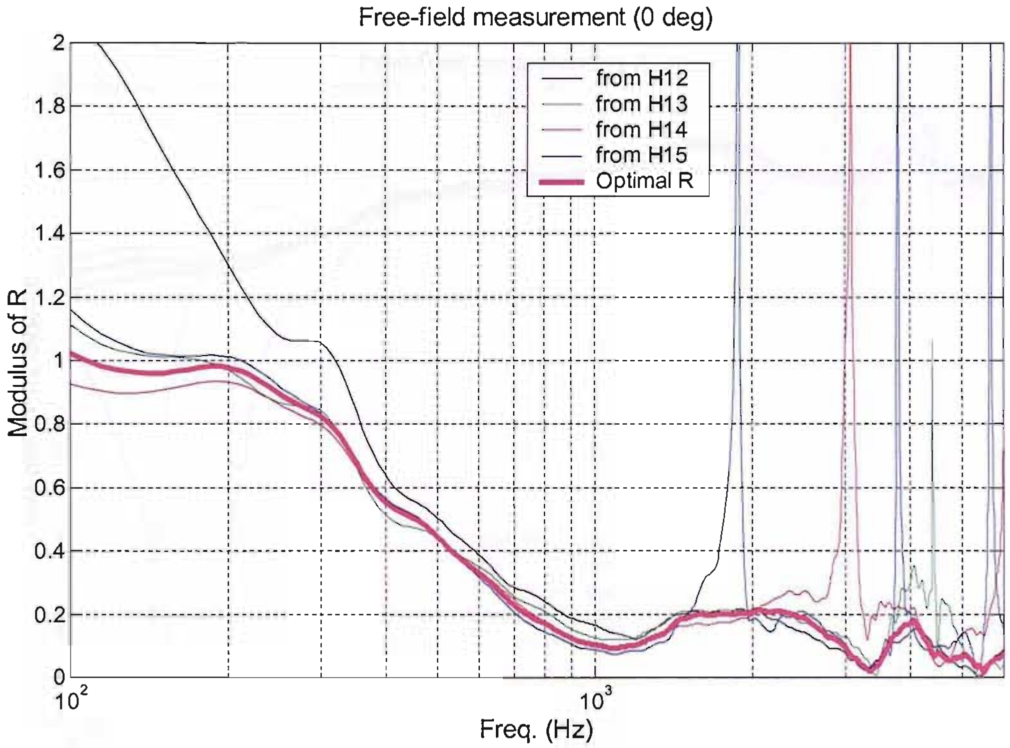

FIG. 6.5A: Modulus of measured reflection coefficients (truncated signals) in a free field at normal incidence

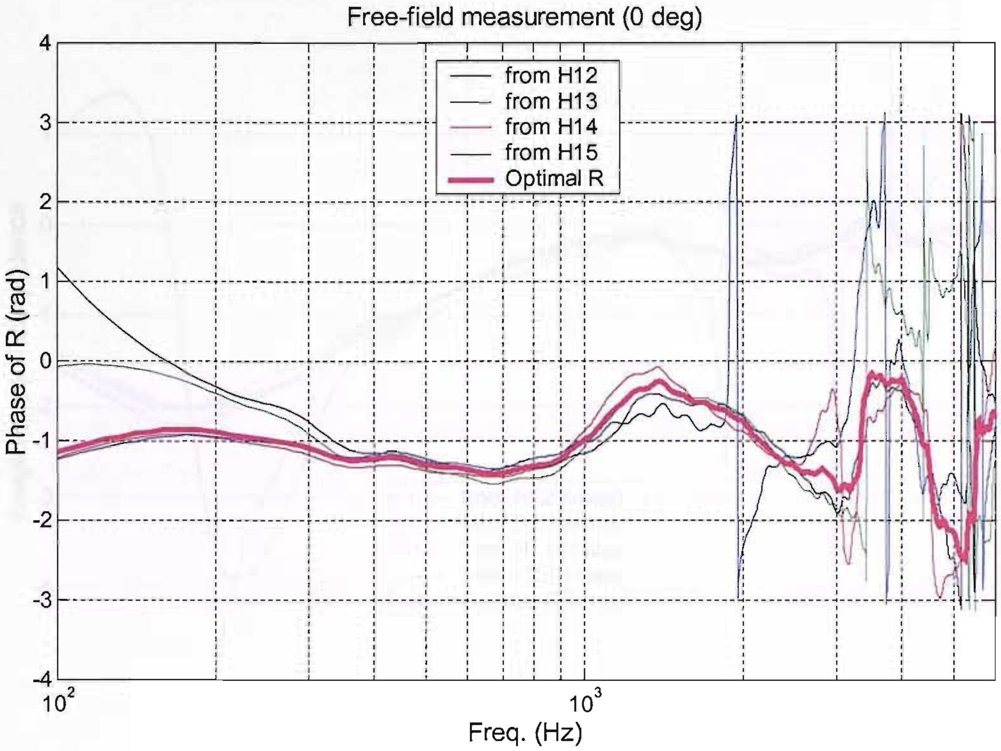

FIG. 6.5B: Phase of measured reflection coefficients in a free field at normal incidence

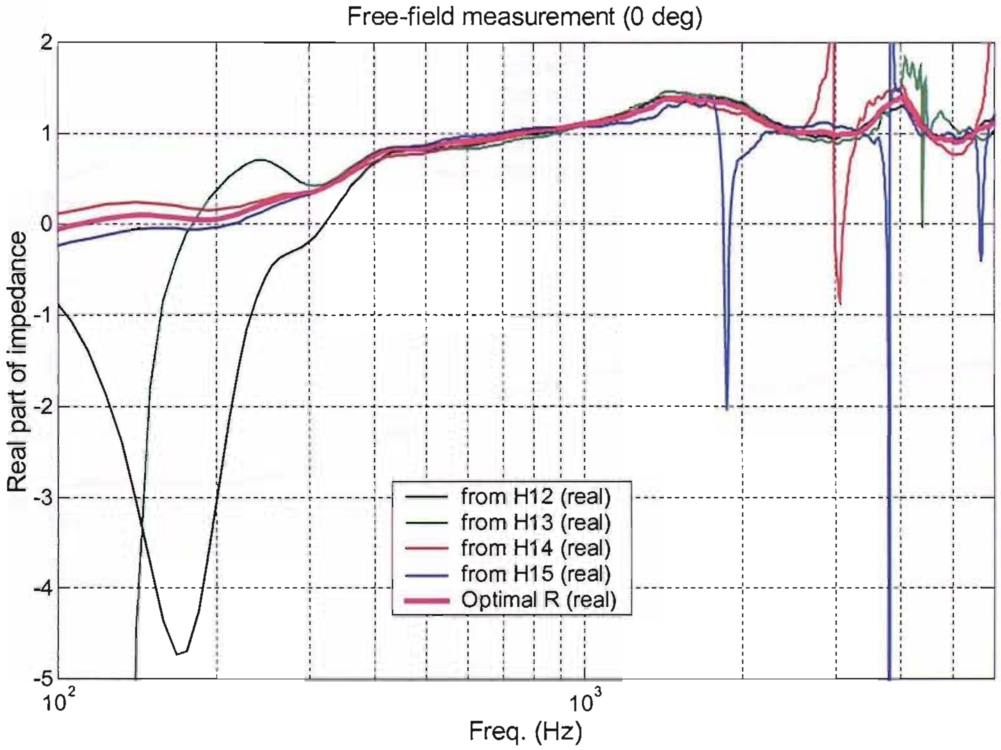

FIG. 6.5C: Real part of impedance measured in a free field at normal incidence

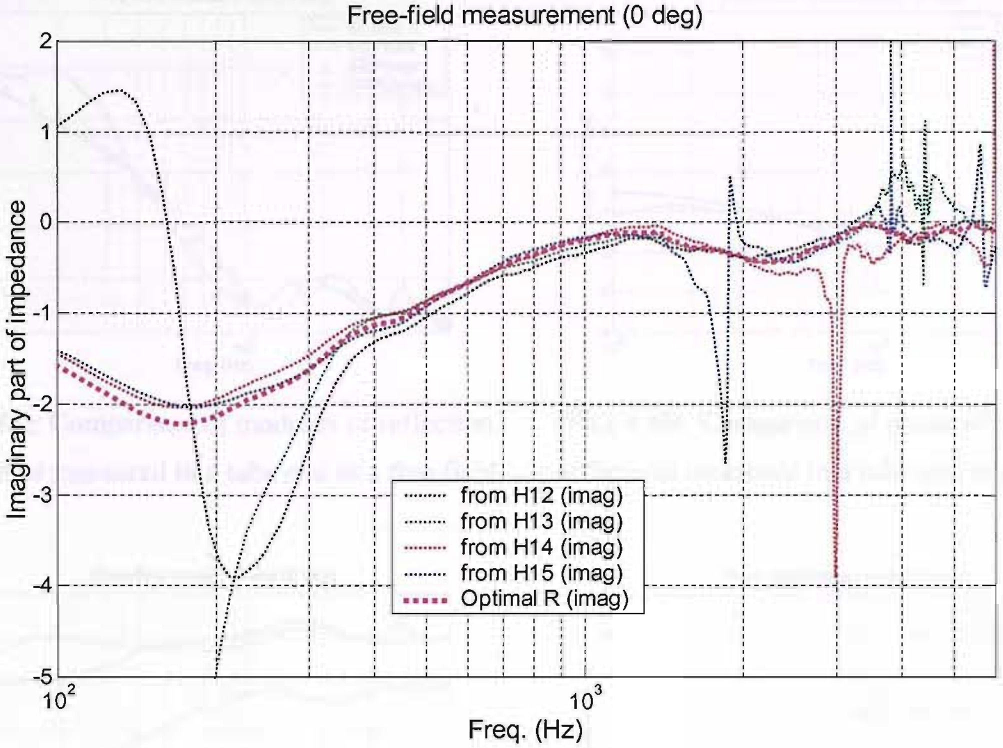

FIG. 6.5D: Imaginary part of impedance measured in a free field at normal incidence

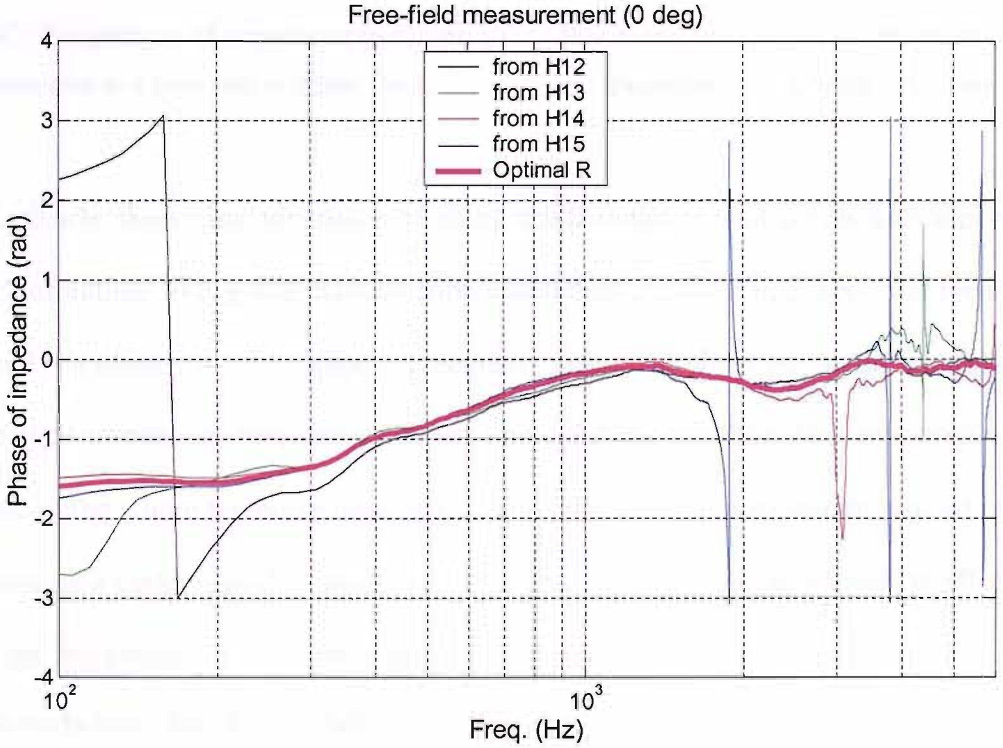

FIG. 6.5E: Phase of impedance measured in a free field at normal incidence

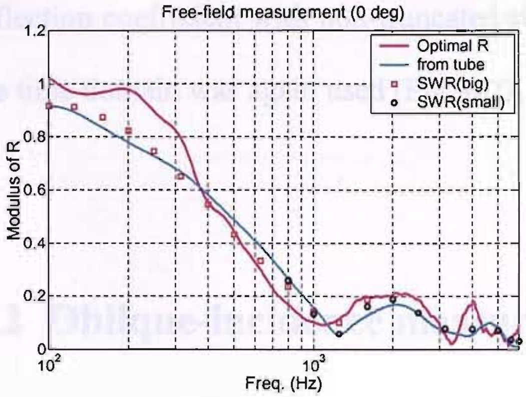

FIG. 6.6A: Comparison of modulus of reflection coefficients measured in a tube and in a free field.

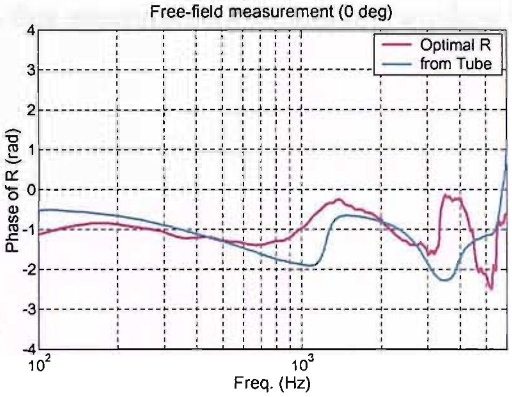

FIG. 6.6B: Comparison of phase of reflection coefficients measured in a tube and in a free field.

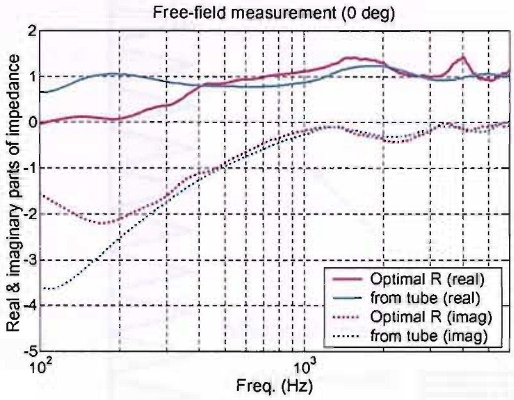

FIG. 6.6C: Comparison of impedance (real, imag.) measured in a tube and in a free field.

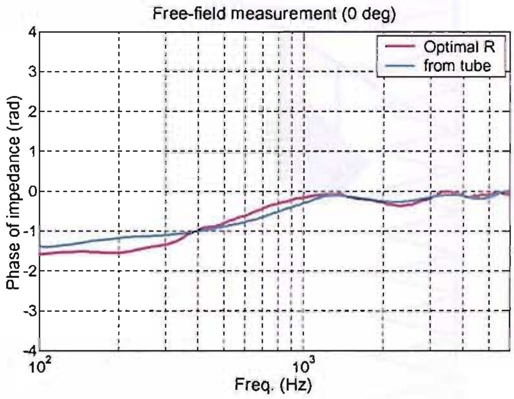

FIG. 6.6D: Comparison of phase of impedance measured in a tube and in a free field.

Fig. 6.5 clearly shows the advantage of using multi-measurement points and applying least squares estimation. In Fig. 6.6 the reflection coefficient obtained in a free-field measurement at normal incidence is in a good agreement with that obtained in an impedance-tube measurement except at frequencies lower than 400 Hz. Unlike the measurement in an impedance tube where the noise level is very low, the impulse response measured in the free field contains a certain level of noise such that truncation of the signal and its effect largely depend on the choice of window (Figs. 6.2, 6.4 and 6.5A). This effect is profound at low frequencies below 300 Hz. For truncating the signals, the choice of window was decided as the windowing least affects the global pattern of low frequency performance in the results of reflection coefficient with non-truncated signals. In this measurement a Hanning window in the time domain was again used (Fig. 6.2).

6.2 Oblique-incidence measurement

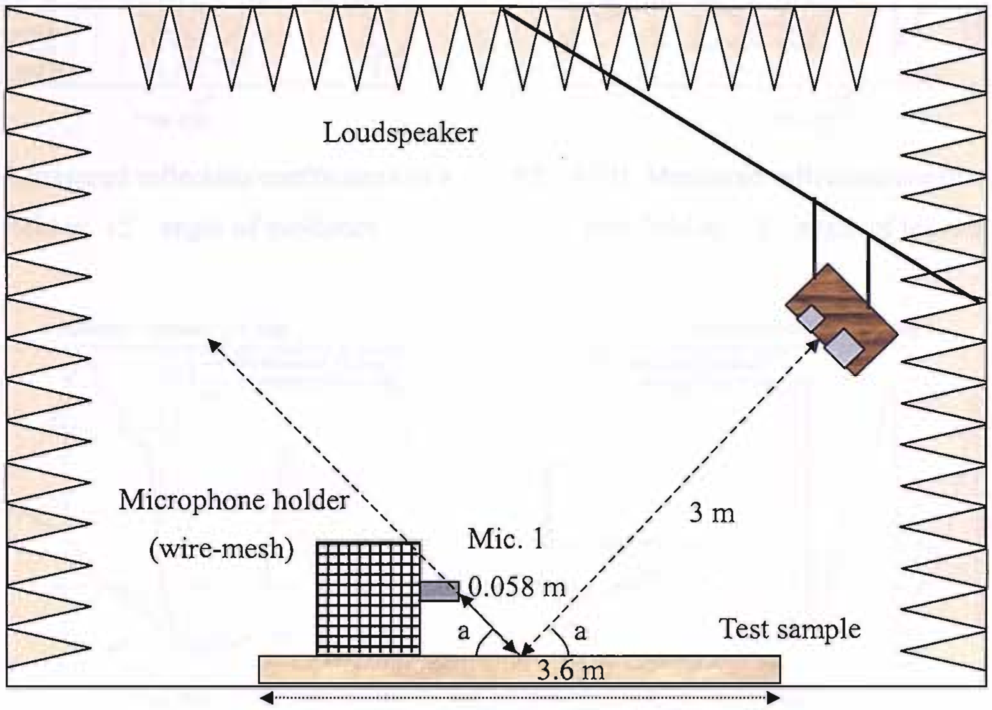

FIG. 6.7: A diagram showing the measurement set-up for oblique-incidence measurement in a anechoic chamber. The angle of incidence is $90^{\circ} - a$.

The measurements at oblique incidence were undertaken at 15°, 45° and 75°. In order to keep error frequencies the same as those of the normal-incidence measurement, the positions of microphones and the corresponding microphone separations were chosen in accordance with the analysis in Section 5.3. Since it has been assumed that the reflecting surface is locally reacting, the measured reflection coefficients at normal incidence can be converted into reflection coefficients at oblique incidence using the relationship given in Eq. (1.18). The converted reflection coefficients, from the normal-incidence results, at oblique incidences are compared with the real measurements in Figs. 6.8, 6.9, and 6.10.

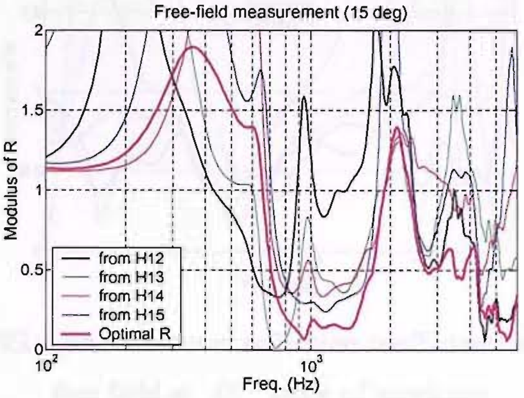

FIG. 6.8A: Measured reflection coefficients in a free field at 15° angle of incidence

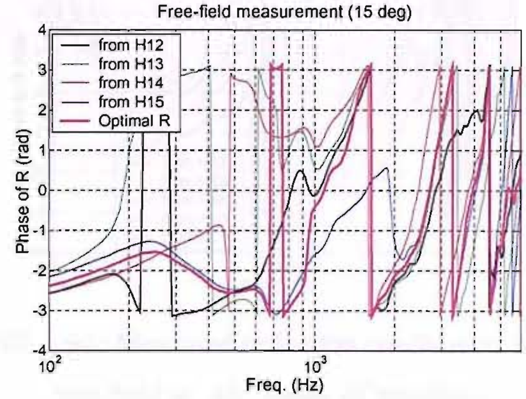

FIG. 6.8B: Measured reflection coefficients in a free field at 15° angle of incidence

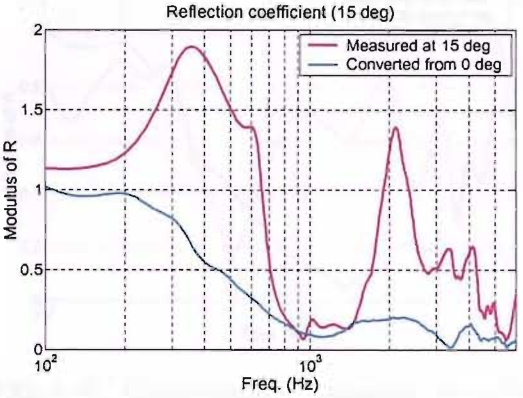

FIG. 6.8C: Comparison of measured reflection coefficients at 15° and normal incidence

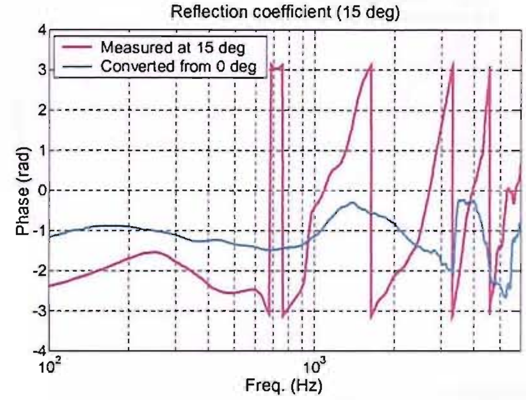

FIG. 6.8D: Comparison of measured reflection coefficients at 15° and normal incidence

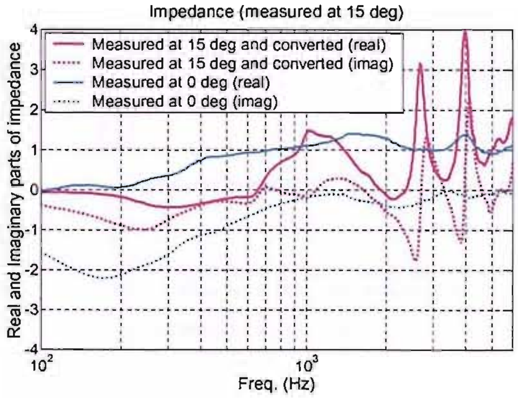

FIG. 6.8E: Comparison of impedance measured (converted) at 15° and normal incidence

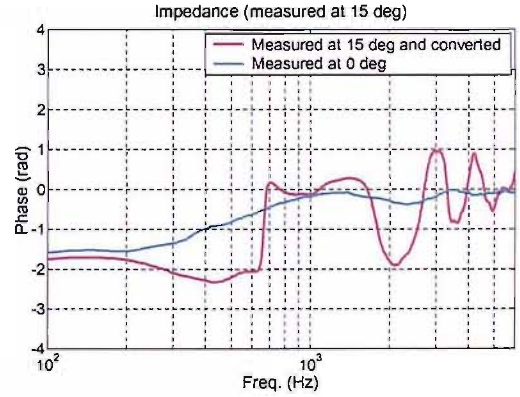

FIG. 6.8F: Comparison of impedance measured (converted) at 15° and normal incidence

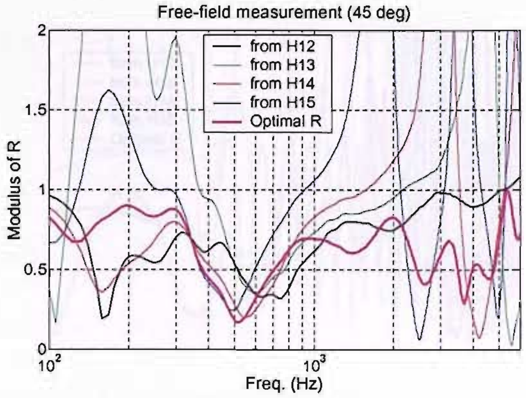

FIG. 6.9A: Measured reflection coefficients in a free field at 45° angle of incidence

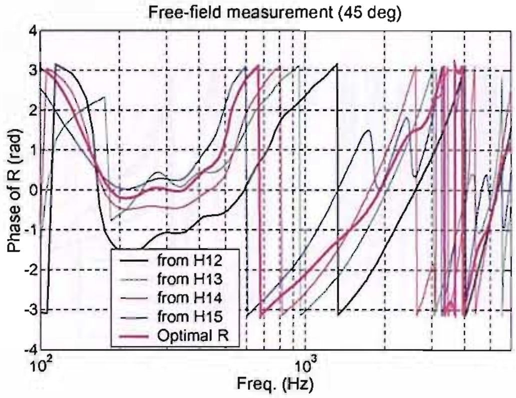

FIG. 6.9B: Measured reflection coefficients in a free field at 45° angle of incidence

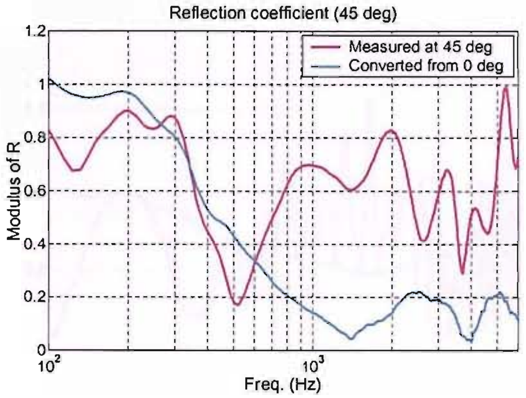

FIG. 6.9C: Comparison of measured reflection coefficients at 45° and normal incidence

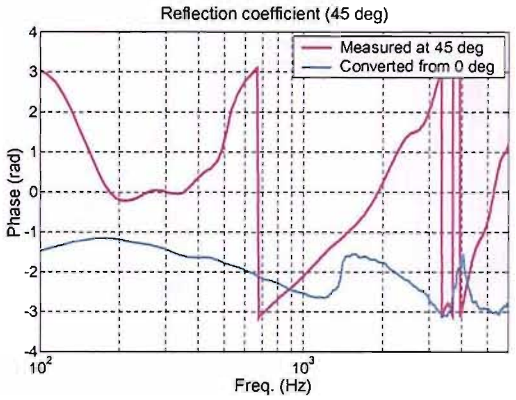

FIG. 6.9D: Comparison of measured reflection coefficients at 45° and normal incidence

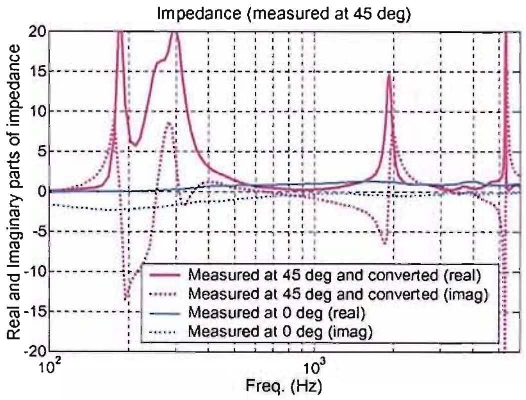

FIG. 6.9E: Comparison of impedance measured (converted) at 45° and normal incidence

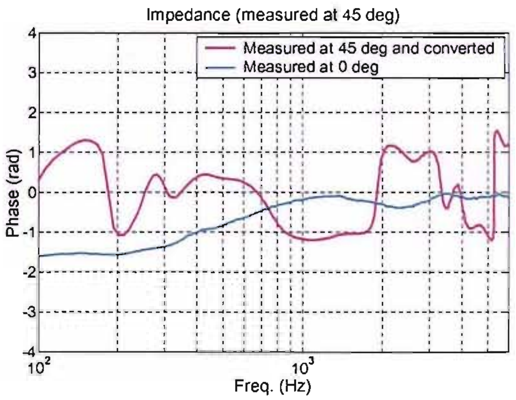

FIG. 6.9F: Comparison of impedance measured (converted) at 45° and normal incidence

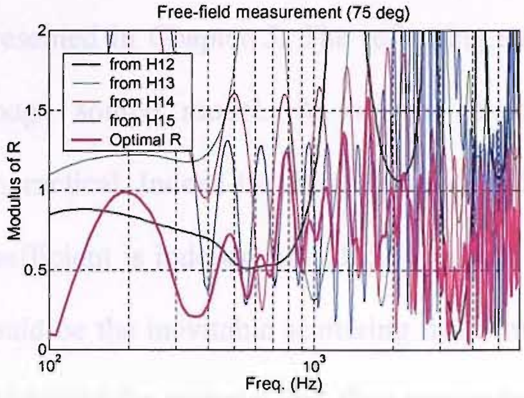

FIG. 6.10A: Measured reflection coefficients in a free field at 75° angle of incidence

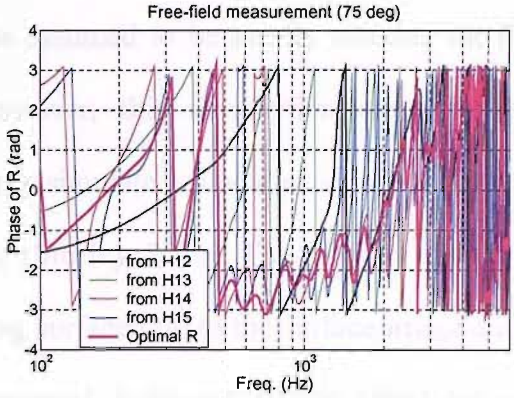

FIG. 6.10B: Measured reflection coefficients in a free field at 75° angle of incidence

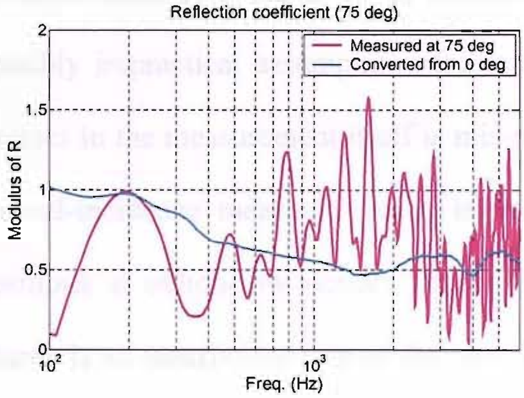

FIG. 6.10C: Comparison of measured reflection coefficients at 75° and normal incidence

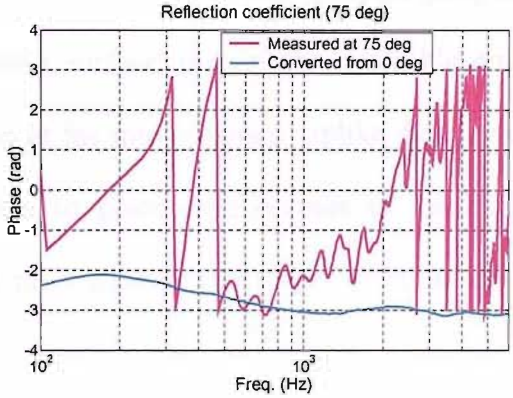

FIG. 6.10D: Comparison of measured reflection coefficients at 75° and normal incidence

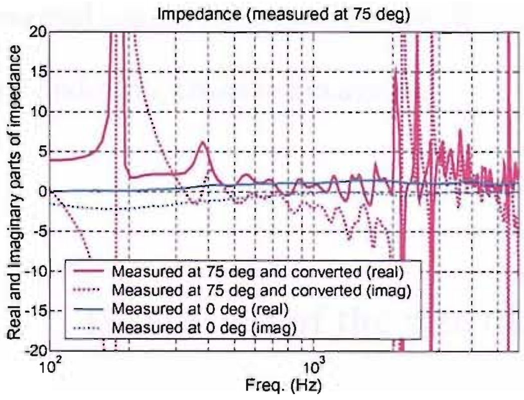

FIG. 6.10E: Comparison of impedance measured (converted) at 75° and normal incidence

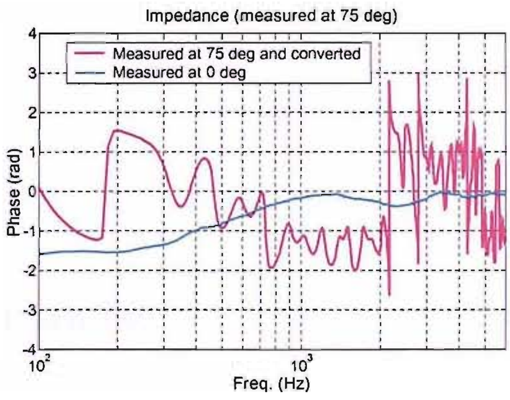

FIG. 6.10F: Comparison of impedance measured (converted) at 75° and normal incidence

The results in this section are very different from those expected as a result of the simulation presented in Chapter 5. The reflecting surface was assumed to be locally reacting for the image source model. At oblique incidence, however, this assumption seems to be impractical. Indeed the image source model can only simulate boundaries whose reflection coefficient is independent of the angle of incidence (Morfey, 2001). This implies that there could be the inevitable scattering from the reflecting surface due to the surface irregularity, rigidity of the material and flow resistivity of the material (Fahy and Walker, 1998) that are not counted in the image source model. For non-locally reacting boundaries, the reflection model should include the boundary impedance that is dependent on the angle of incidence (Brekhovskikh and Godin, 1992; Jansens *et al*, 2002; Allard *et al*, 2003). Apart from the possibly impractical assumption of a locally reacting surface, one of the possible error sources in the measurement itself is mis-positioning of the microphones. Unlike the case of normal-incidence measurement, it is very different to place microphones in the exact positions at oblique incidence. This is discussed in Section 6.4. Another possible error source is an insufficient size of the sample. Using Fresnel-theory, this will be discussed in Section 6.3. The windowing effect also could affect the results, especially at low frequencies, but this is inevitable in the signal processing. But in this measurement, the Hanning window has been used and general frequency dependence in the results produced from the non-truncated signals have been preserved in the process of windowing. Thus it can be said that the windowing errors are marginal.

6.3 Discussion of the size of the test sample

The size of the test sample is discussed, in this section, by using Fresnel zone theory. The

Fresnel zones are the regions where these path length differences are between $n\lambda$ and $(n+1/2)\lambda$ where λ is wavelength and n is an integer. The first Fresnel zone is when $n=0$ such that the path length difference is smaller than $\lambda/2$ and the second is when $n=1$ and so on. As these zones are associated with the path length differences between the source and the receiver, they are ellipses on the reflecting boundary at oblique incidences and circles at normal incidence. The formula calculating the regions of Fresnel zones (Boulanger *et al*, 1997) is shown below.

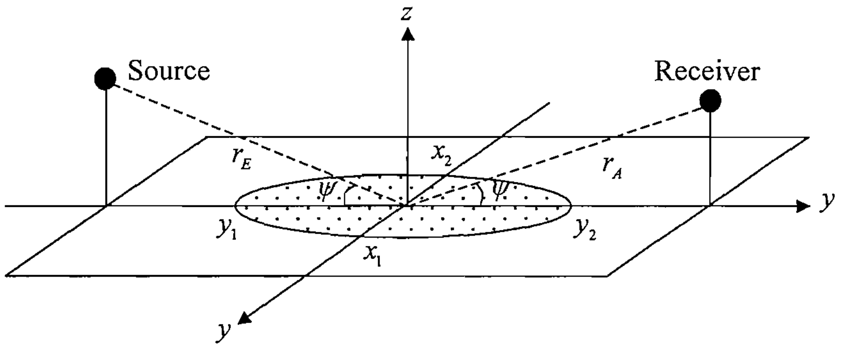

FIG. 6.11: Diagram of Fresnel zones on a reflecting surface. A Fresnel zone is defined by the elliptic region whose intersections with x and y axis are x_1, x_2 and y_1, y_2. Note that in this diagram ψ is an complimentary angle to the angle of incidence θ , i.e., the relationship between them is $\psi = 90^\circ - \theta$.

$$x_{1,2} = \pm b\sqrt{1 - \frac{(y_m \cos\psi - c)^2}{a^2} + \frac{(y_m \sin\psi)^2}{b^2}}$$

$$y_{1,2} = -\frac{B}{A} \pm \sqrt{\frac{1}{A} - \frac{(c \sin\psi)^2}{(Aab)^2}} \tag{6.1}$$

where a, b, c, A, B and y_m are defined by

$$a=\frac{r_E+r_A+F\lambda}{2},\quad b=\sqrt{\frac{(r_E+r_A)F\lambda}{2}+\left(\frac{F\lambda}{2}\right)^2},\quad c=\frac{r_E+r_A}{2}-r_E$$

$$A=\left(\frac{\cos\psi}{a}\right)^2+\left(\frac{\sin\psi}{b}\right)^2,\quad B=\frac{c\cos\psi}{a^2},\quad y_m=\frac{B}{A} \tag{6.2}$$

where the Fresnel number, F, denotes the path length difference. As discussed in Section 2.2.6, for the estimation of the required size of the absorbing surface, the path length difference of $\lambda/3$ ($F=1/3$ in the above equation) was used by Nocke (2000) following the suggestion by Hothersall and Harriott (1997).

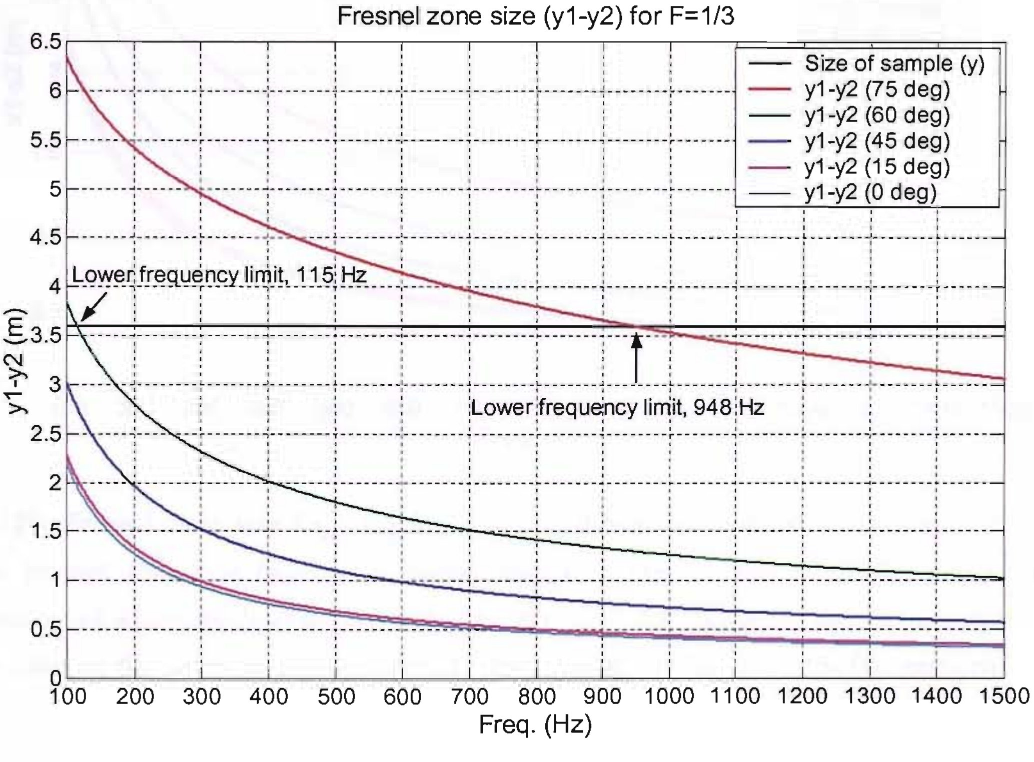

FIG. 6.12A: Fresnel zone size (y_1-y_2) for $F=1/3$. When the angle of incidence is 0°, 15° and 45° the Fresnel zone size (y_1-y_2) is within the given size of $3.6m$ in the frequency range of measurement of which the lowest is 100Hz. At 60° and 75°, however, due to the limited size of the test material, the lower frequency limits are found to be 115Hz and 948Hz respectively.

As expected from Eq. (6.1), x_1 and y_1 are positive values, and x_2 and y_2 are negative values (see Fig. 6.11). Thus $x_1 - x_2$ and $y_1 - y_2$ constitute the limits of Fresnel zones on the x and y axes. These values are calculated with the geometric data used in the measurement. The position of microphone 5 is selected as a receiver. Figs. 6.12A and 6.12B show the Fresnel zones, $y_1 - y_2$ and $x_1 - x_2$ respectively, as a function of frequency with different values of the angle of incidence.

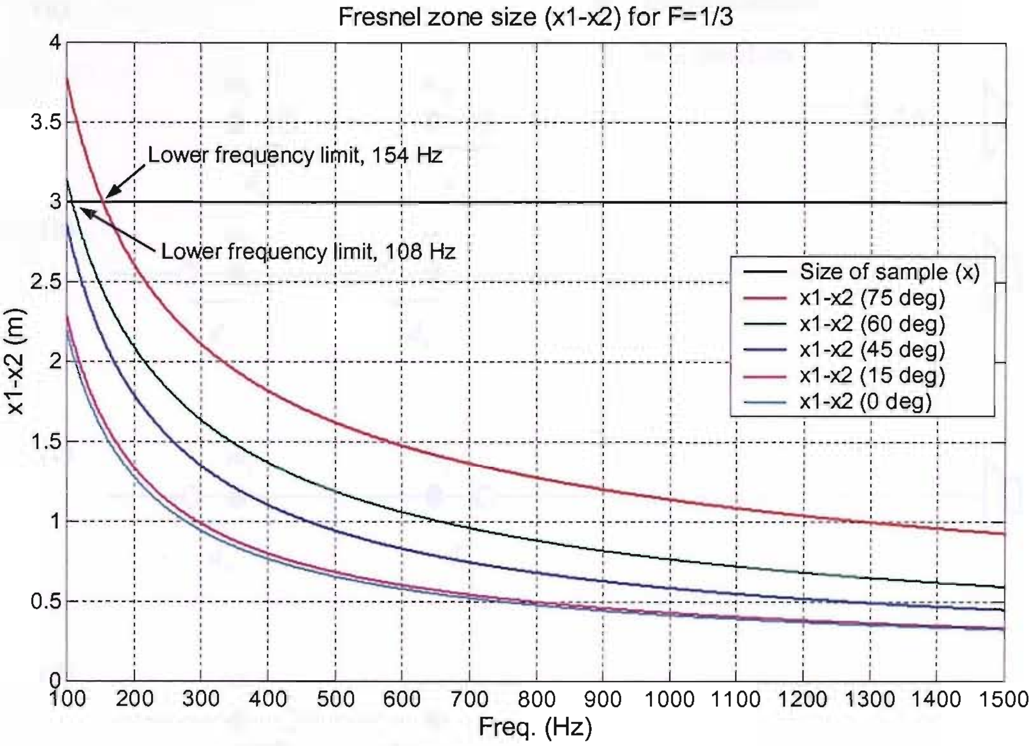

FIG. 6.12B: Fresnel zone size ($x_1 - x_2$) for $F = 1/3$. When the angle of incidence is $0^\circ, 15^\circ$ and 45° the Fresnel zone size ($x_1 - x_2$) is within the given size of $3m$ in the frequency range of measurement of which the lowest is $100\,\text{Hz}$. At 60° and 75°, however, due to the limited size of the test material, the lower frequency limits are found to be $108\,\text{Hz}$ and $154\,\text{Hz}$ respectively.

These results show that the size of test material, $3.6m \times 3m$, used in the measurement is acceptable except when the angle of incidence is 60° and 75°. At these angles of incidence, a bigger test sample is required for low frequency performance. Fig. 6.12A shows lower limits of frequency, with the given size of test sample, which is found to be $115\,\text{Hz}$ and $948\,\text{Hz}$ at these angles respectively. With this analysis, it appears that the measurement results at the incident angles of 0°, 15° and 45° were not significantly affected by the finite size of the reflecting boundary.

6.4 Errors due to mis-positioning of microphones

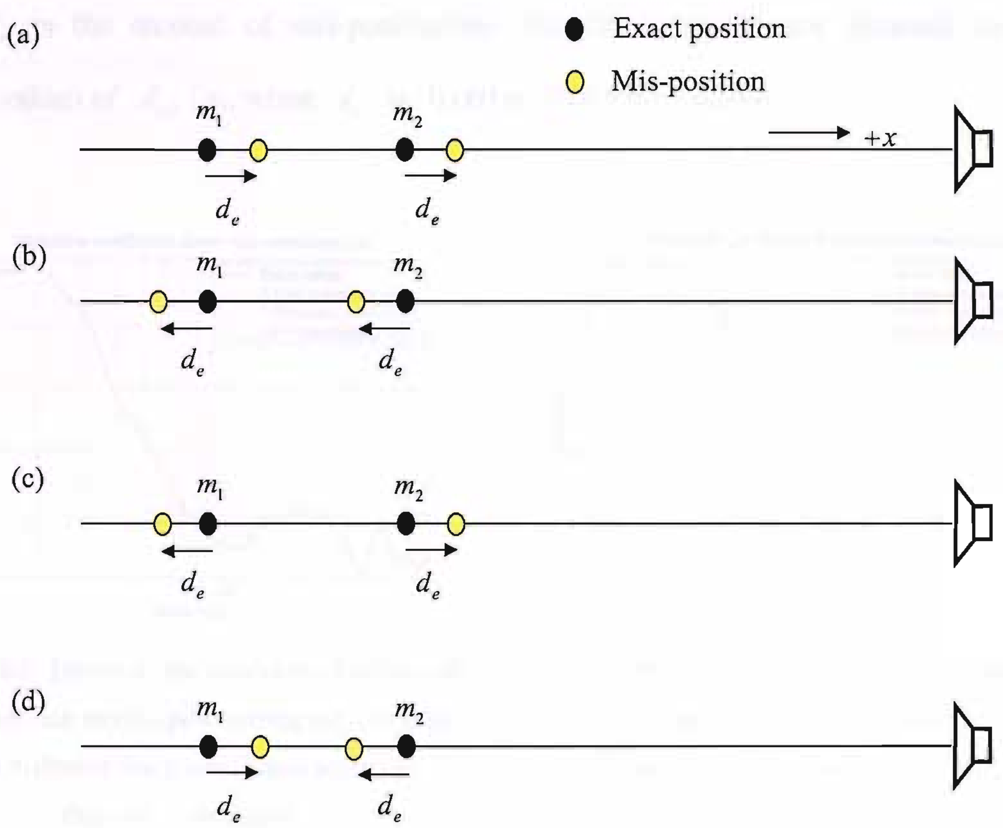

FIG. 6.13: Illustration of mis-positioning of microphones at normal incidence in a free field. Four different patterns of mis-positioning. (a) both microphone mis-positioned into the same direction of $+x$ by the same amount of distance error, d_e. (b) both microphone mis-positioned into the same direction of $+x$ by the same amount of distance error, d_e. (c) each microphone mis-positioned toward each other by the same amount of distance error, d_e. (d) each microphone mis-positioned away from each other by the same amount of distance error, d_e. The separation between microphone 1 and 2 at their exact positions is $10\,cm$.

International Standard requires positional accuracy of $\pm 5\,mm$ or better for the measurement of reflection coefficient in a tube using two-microphone transfer function method (BS ISO 10534-2: 1998). This section presents simulation results which show errors due to mis-positioning of microphones. The reflection coefficients obtained at normal incidence in a free field are taken as reference values which need exact reproducing if it were not for any positional errors.

The illustration in FIG. 6.13 shows four different patterns of mis-positioning in a free field where d_e is the amount of mis-positioning. Simulation results are obtained for three different values of d_e, i.e., when d_e is $0.001m$, $0.005m$ or $0.01m$.

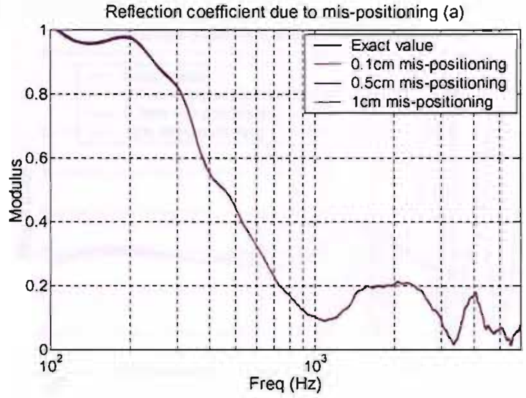

FIG. 6.14A: Errors in the modulus of reflection coefficient due to mis-positioning (a). Note that the four different lines are almost identical, so they are overlapped.

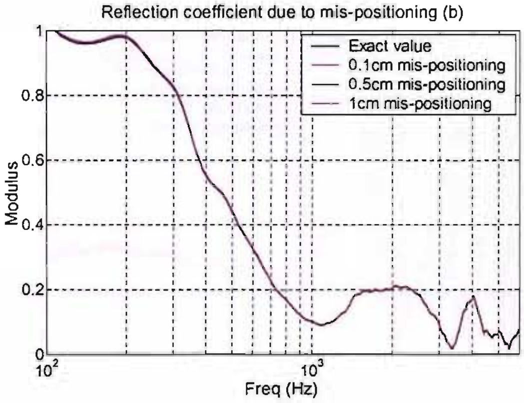

FIG. 6.14B: Errors in the modulus of reflection coefficient due to mis-positioning (b) Note that the four different lines are almost identical, so they are overlapped.

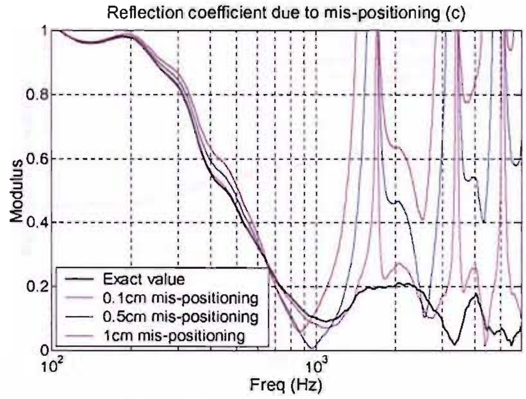

FIG. 6.14C: Errors in the modulus of reflection coefficient due to mis-positioning (c)

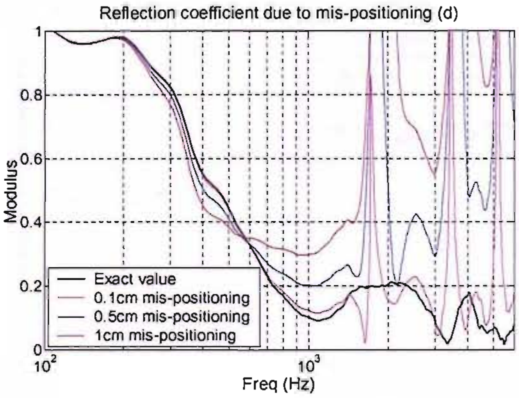

FIG. 6.14D: Errors in the modulus of reflection coefficient due to mis-positioning (d)

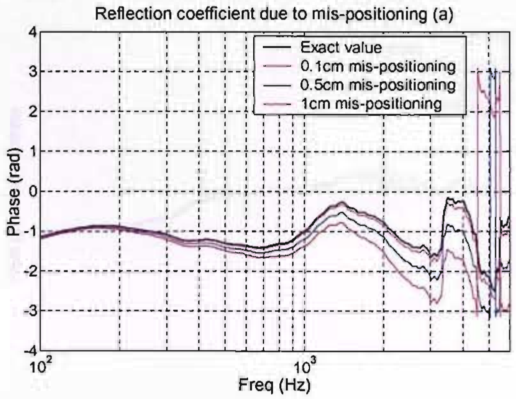

FIG. 6.15A: Errors in the phase of reflection coefficient due to mis-positioning (a)

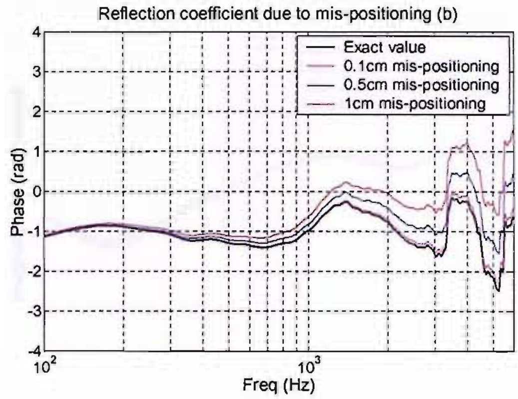

FIG. 6.15B: Errors in the phase of reflection coefficient due to mis-positioning (b)

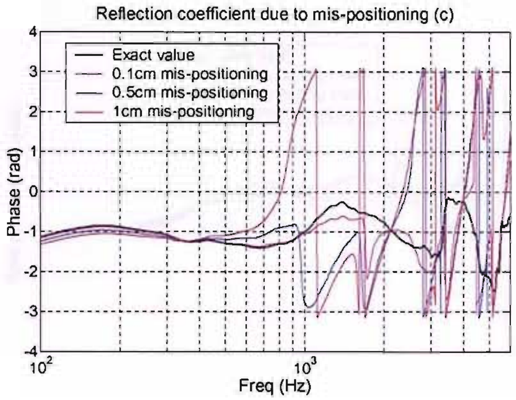

FIG. 6.15C: Errors in the phase of reflection coefficient due to mis-positioning (c)

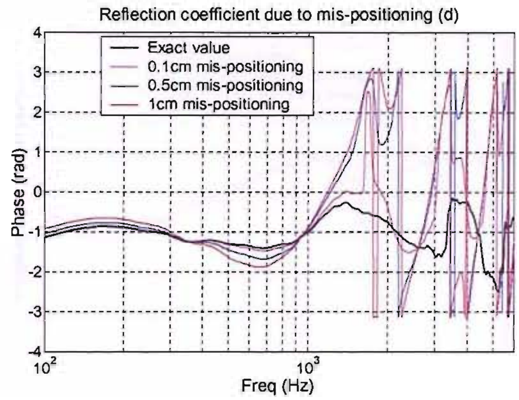

FIG. 6.15D: Errors in the phase of reflection coefficient due to mis-positioning (d)

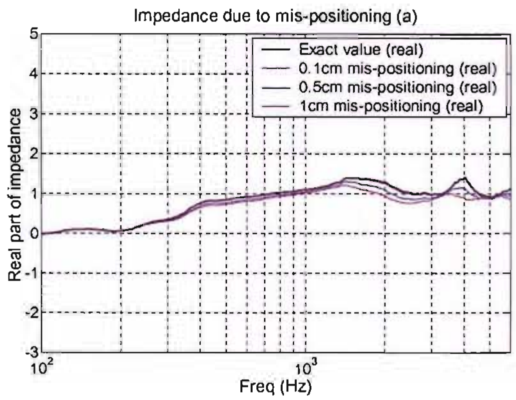

FIG. 6.16A-1: Errors in the impedance due to mis-positioning (a)

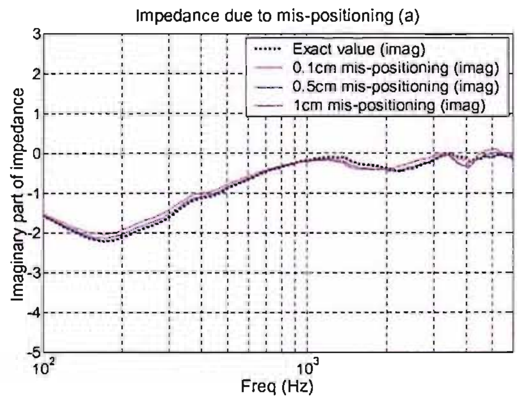

FIG. 6.16A-2: Errors in the impedance due to mis-positioning (a)

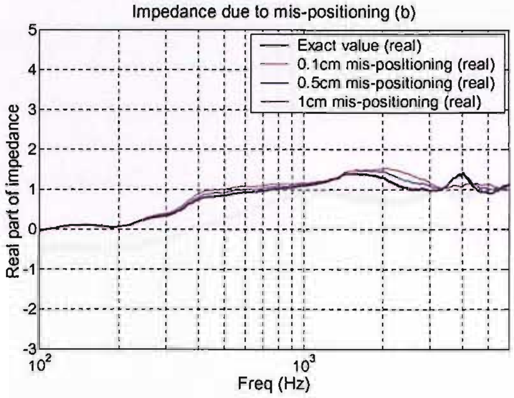

FIG. 6.16B-1: Errors in the impedance due to mis-positioning (b)

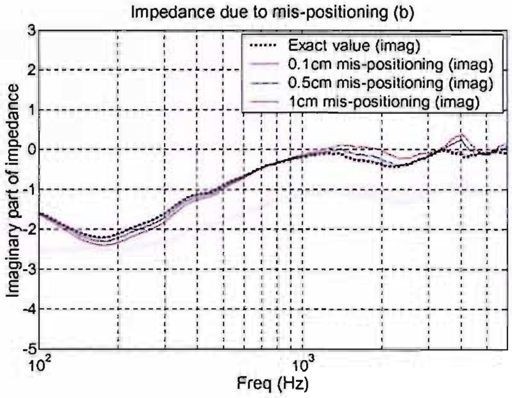

FIG. 6.16B-2: Errors in the impedance due to mis-positioning (b)

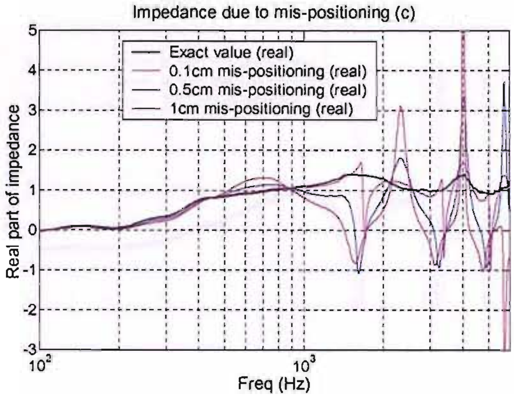

FIG. 6.16C-1: Errors in the impedance due to mis-positioning (c)

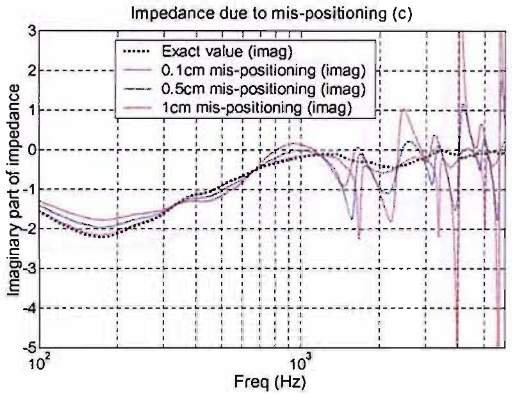

FIG. 6.16C-2: Errors in the impedance due to mis-positioning (c)

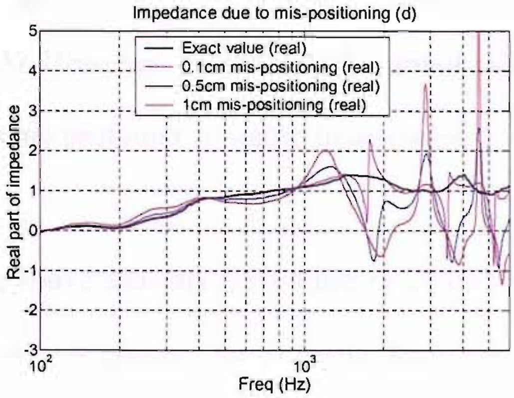

FIG. 6.16D-1: Errors in the impedance due to mis-positioning (d)

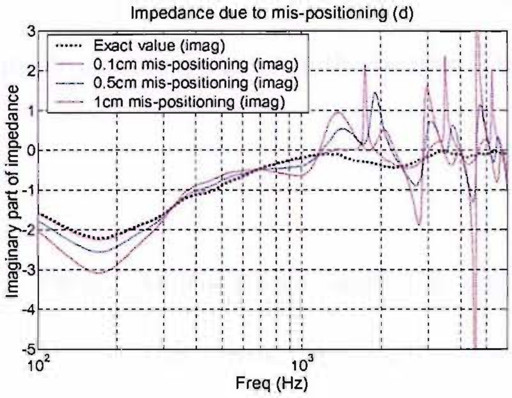

FIG. 6.16D-2: Errors in the impedance due to mis-positioning (d)

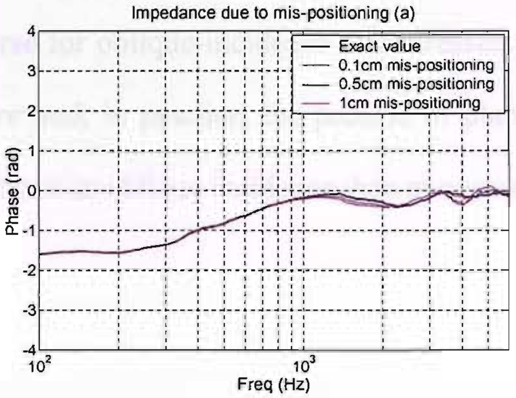

FIG. 6.17A: Errors in the phase of the impedance due to mis-positioning (a)

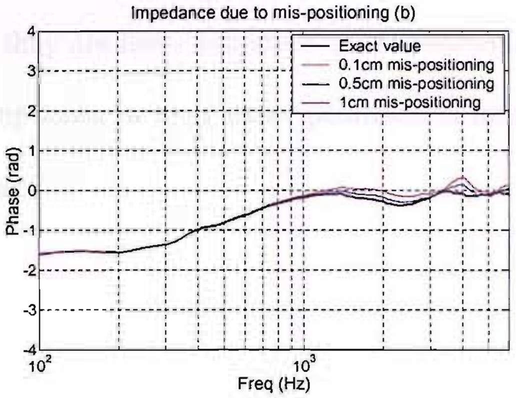

FIG. 6.17B: Errors in the phase of the impedance due to mis-positioning (b)

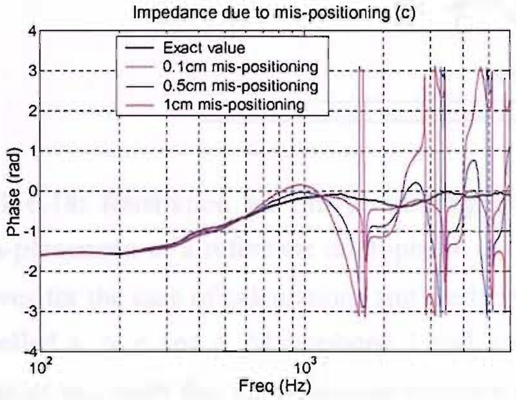

FIG. 6.17C: Errors in the phase of the impedance due to mis-positioning (c)

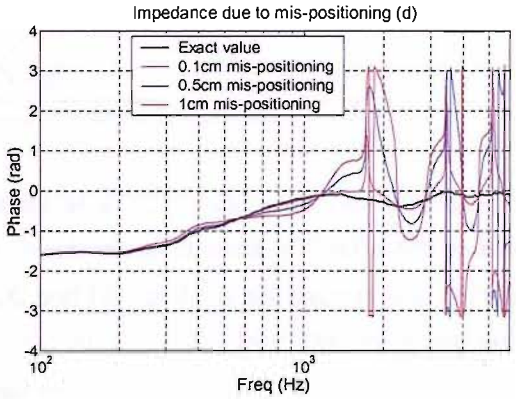

FIG. 6.17D: Errors in the phase of the impedance due to mis-positioning (d)

In Figs. 6.14, 6.15, 6.16 and 6.17, errors are negligible for mis-positionings (a) and (b) (Fig. 6.13). However, for (c) and (d) a small mis-positioning leads a large error in the results. This is more profound at higher frequencies.

The above analysis is confined to a case of normal incidence. At oblique incidence, an angle of 45° is chosen, for example, for a demonstration of positional errors. The results of the following simulation show that positional errors are more apparent in the oblique-incidence measurement than those in the normal incidence measurement. At oblique incidence, low frequency performance is also affected by the positional errors. Thus positional errors get worse for oblique-incidence measurement because they are more sensitive to the positional error and, in practice, the process of placing microphones in their exact positions is more difficult at oblique incidence than at normal incidence.

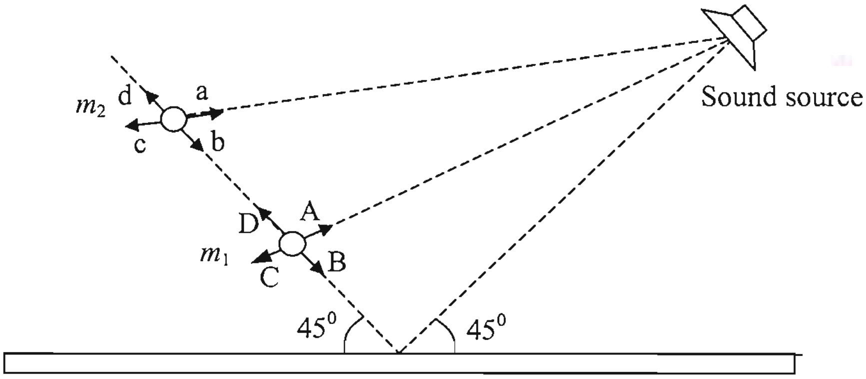

FIG. 6.18: Illustration for mis-positioning of microphones at a 45° incidence. The directions of mis-placement of a reference microphone are along the directions of incident and reflected paths of waves for the ease of calculations and are labelled A, B, C and D. For the other microphone, they are labelled a, b, c and d. Microphone 1 and 2 are $0.1m$ and $0.2m$ away from the reflecting point respectively such that the separation between them at their exact positions is $0.1m$.

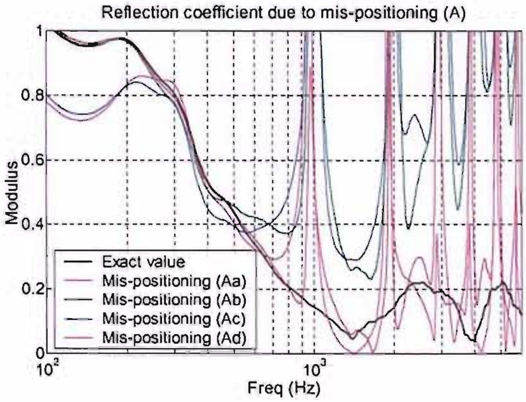

FIG. 6.19A-1: Mic. 1 is mis-placed by $1cm$ in the A direction, and mic. 2 is mis-placed by $1cm$ in each direction of a, b, c and d (45°)

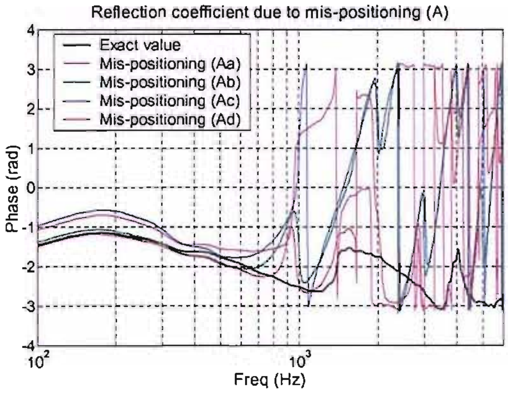

FIG. 6.19A-2: Mic. 1 is mis-placed by $1cm$ in the A direction, and mic. 2 is mis-placed by $1cm$ in each direction of a, b, c and d (45°)

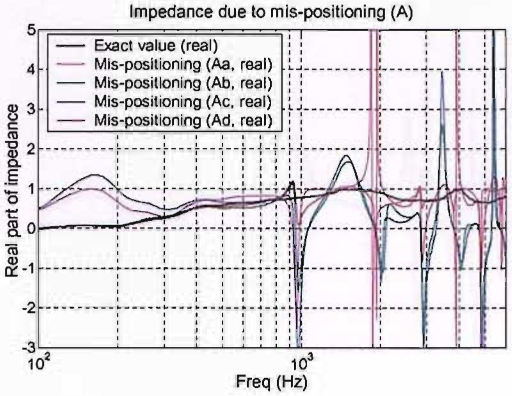

FIG. 6.19A-3: Mic. 1 is mis-placed by $1cm$ in the A direction, and mic. 2 is mis-placed by $1cm$ in each direction of a, b, c and d (45°)

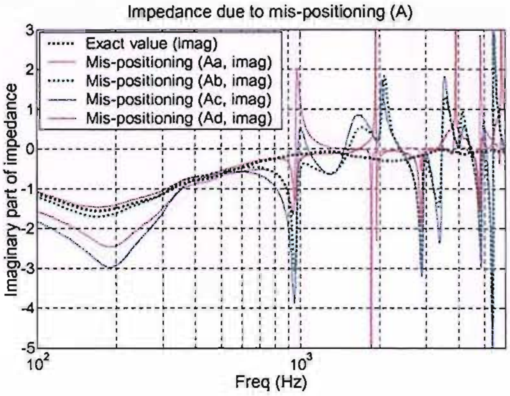

FIG. 6.19A-4: Mic. 1 is mis-placed by $1cm$ in the A direction, and mic. 2 is mis-placed by $1cm$ in each direction of a, b, c and d (45°)

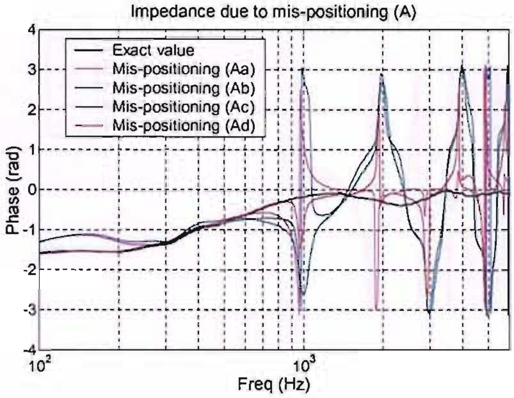

FIG. 6.19A-5: Mic. 1 is mis-placed by $1cm$ in the A direction, and mic. 2 is mis-placed by $1cm$ in each direction of a, b, c and d (45°)

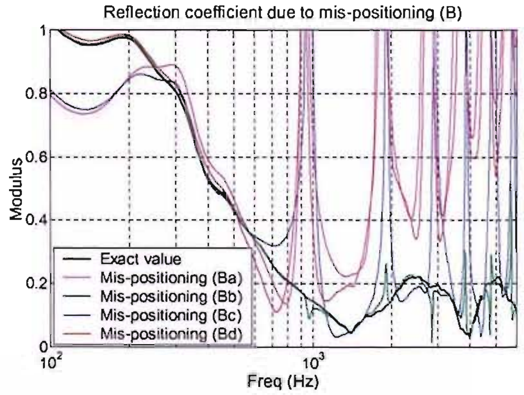

FIG. 6.19B-1: Mic. 1 is mis-placed by $1cm$ in the B direction, and mic. 2 is mis-placed by $1cm$ in each direction of a, b, c and d (45°)

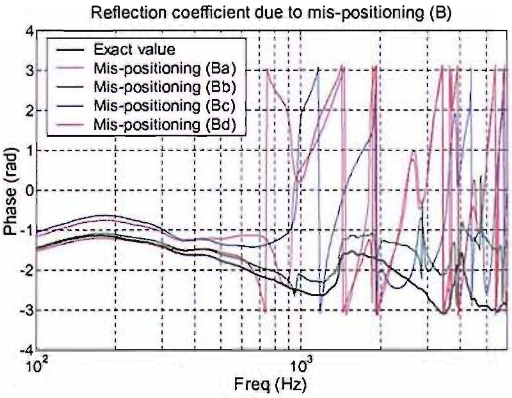

FIG. 6.19B-2: Mic. 1 is mis-placed by $1cm$ in the B direction, and mic. 2 is mis-placed by $1cm$ in each direction of a, b, c and d (45°)

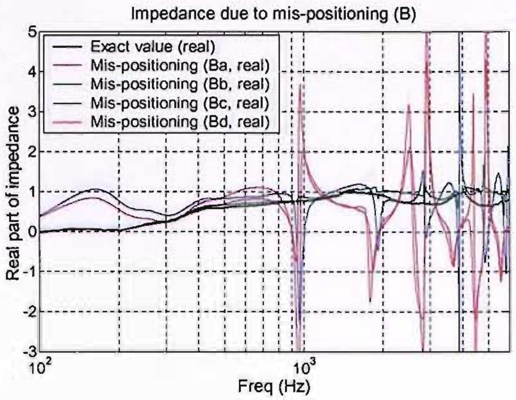

FIG. 6.19B-3: Mic. 1 is mis-placed by $1cm$ in the B direction, and mic. 2 is mis-placed by $1cm$ in each direction of a, b, c and d (45°)

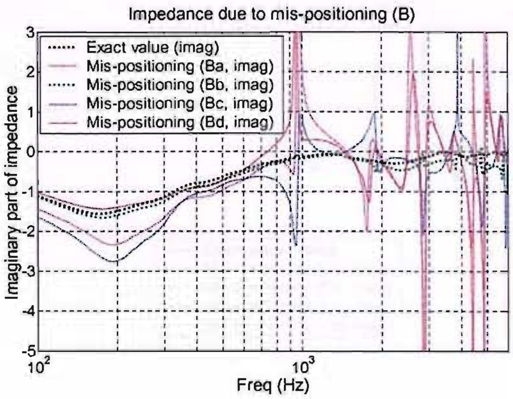

FIG. 6.19B-4: Mic. 1 is mis-placed by $1cm$ in the B direction, and mic. 2 is mis-placed by $1cm$ in each direction of a, b, c and d (45°)

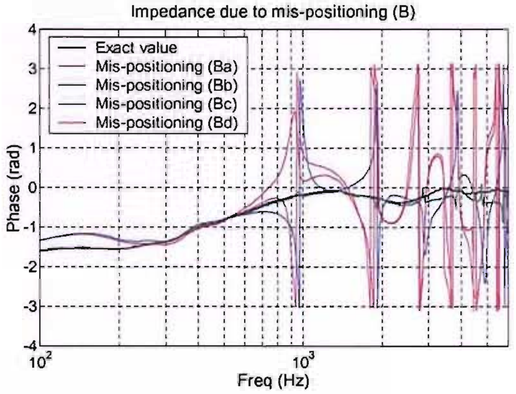

FIG. 6.19B-5: Mic. 1 is mis-placed by $1cm$ in the B direction, and mic. 2 is mis-placed by $1cm$ in each direction of a, b, c and d (45°)

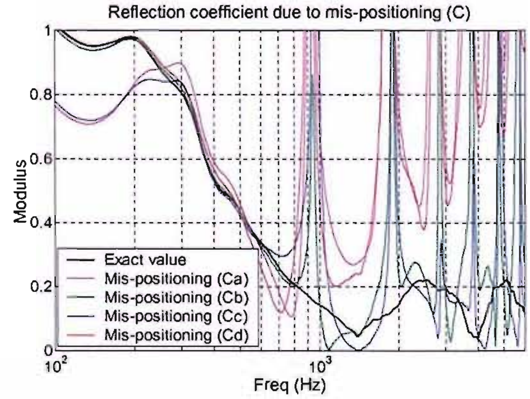

FIG. 6.19C-1: Mic. 1 is mis-placed by $1cm$ in the C direction, and mic. 2 is mis-placed by $1cm$ in each direction of a, b, c and d (45°)

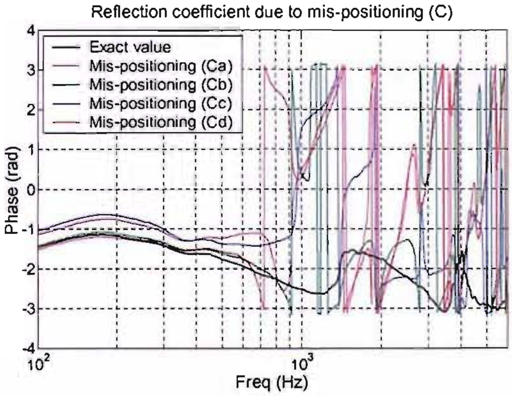

FIG. 6.19C-2: Mic. 1 is mis-placed by $1cm$ in the C direction, and mic. 2 is mis-placed by $1cm$ in each direction of a, b, c and d (45°)

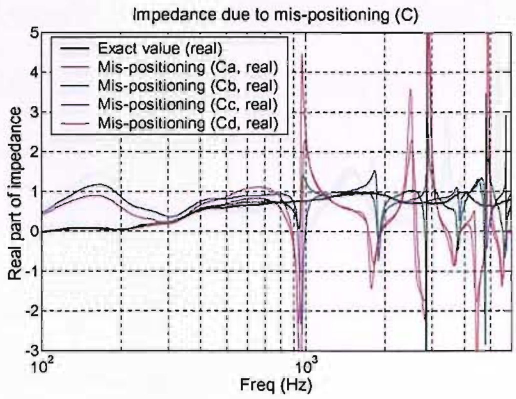

FIG. 6.19C-3: Mic. 1 is mis-placed by $1cm$ in the C direction, and mic. 2 is mis-placed by $1cm$ in each direction of a, b, c and d (45°)

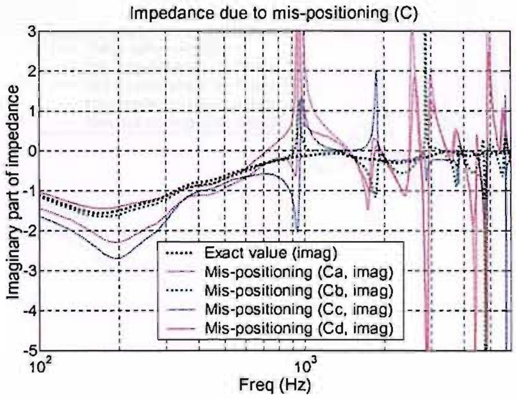

FIG. 6.19C-4: Mic. 1 is mis-placed by $1cm$ in the C direction, and mic. 2 is mis-placed by $1cm$ in each direction of a, b, c and d (45°)

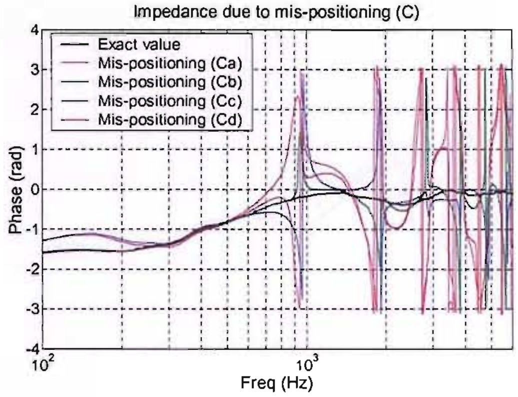

FIG. 6.19C-5: Mic. 1 is mis-placed by $1cm$ in the C direction, and mic. 2 is mis-placed by $1cm$ in each direction of a, b, c and d (45°)

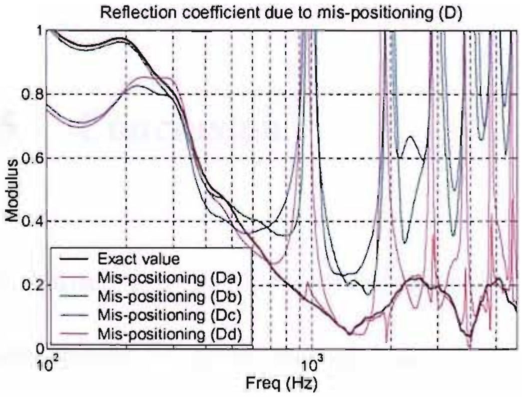

FIG. 6.19D-1: Mic. 1 is mis-placed by $1cm$ in the D direction, and mic. 2 is mis-placed by $1cm$ in each direction of a, b, c and d (45°)

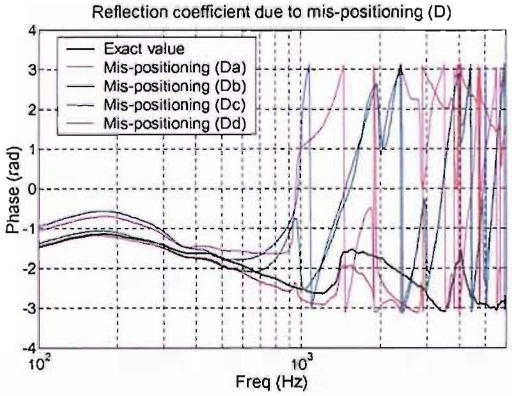

FIG. 6.19D-2: Mic. 1 is mis-placed by $1cm$ in the D direction, and mic. 2 is mis-placed by $1cm$ in each direction of a, b, c and d (45°)

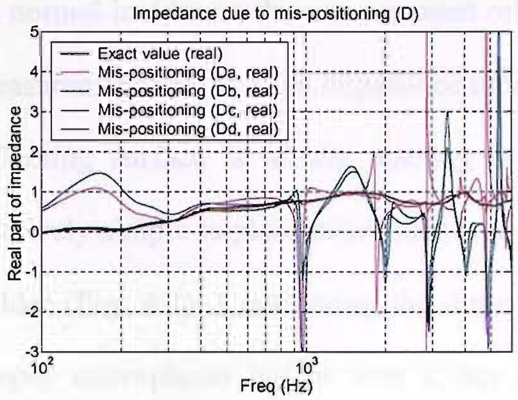

FIG. 6.19D-3: Mic. 1 is mis-placed by $1cm$ in the D direction, and mic. 2 is mis-placed by $1cm$ in each direction of a, b, c and d (45°)

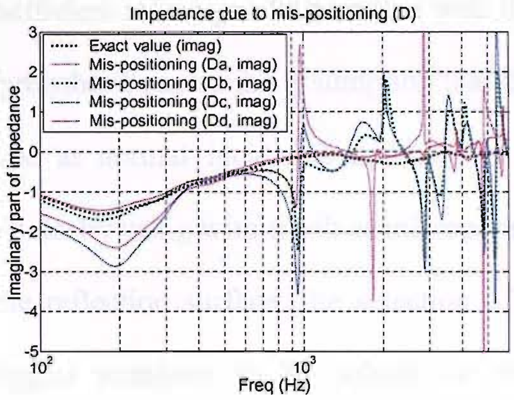

FIG. 6.19D-4: Mic. 1 is mis-placed by $1cm$ in the D direction, and mic. 2 is mis-placed by $1cm$ in each direction of a, b, c and d (45°)

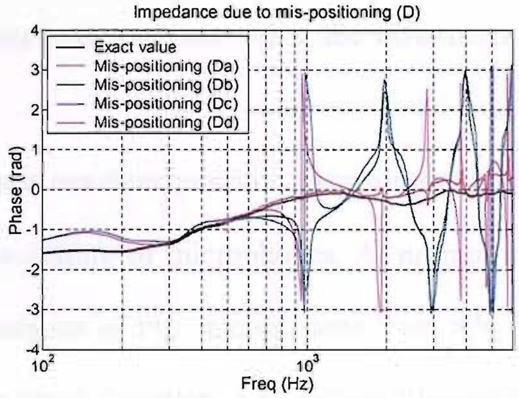

FIG. 6.19D-5: Mic. 1 is mis-placed by $1cm$ in the D direction, and mic. 2 is mis-placed by $1cm$ in each direction of a, b, c and d (45°)

6.5 Conclusion

The dimension of the reflecting surface ($3.6m$(L) × $3.0m$(W)) used in a free-field measurement is good enough such that diffraction at the edges are negligible except at grazing angle of incidence. In Appendix III, measurements are described that were made on a smaller-size reflecting surface and its effect is discussed.

At normal incidence, the measurement reflection coefficient is in a good agreement with the measurement results in an impedance tube. This is probably because the assumption that the reflecting surface is locally reacting is less flawed at normal incidence and also it is relatively simple to place microphones at exact positions by using wire-mesh as microphone holder (Fig. 6.1). Considering the dimension of the reflection surface, the selection of a proper microphone holder was a one of the biggest problems to be solved for this measurement. Some trials and errors due to the vibration of a long microphone holder are presented in Appendix III. The wire-mesh is of great help for keeping microphones at their exact positions and reducing or eliminating unwanted scattering from a microphone holder. Thus in this measurement, the wire-mesh was presumed to be acoustically transparent.

There are three possible error sources in the free-field measurement. One is error due to mis-positioning of microphones. At normal-incidence simulation of positional errors, when the positions of two microphones from which a transfer function is obtained are mis-placed in the same direction, i.e., mis-positioning (a) and (b) in Fig. 6.14, the results are marginally affected. But two microphones are mis-positioned in different directions, i.e., mis-positioning (c) and (d), results in large errors from small positional errors. At oblique incidence, however, simulation results suggest that positional errors are worse and low frequency performance is also affected. Considering that placing microphones at their exact positions is more difficult at oblique incidence than at normal incidence, this is likely to be one of the main error sources.

Another error source is the non-local reaction of the reflecting surface. It is not possible in this measurement to identify this effect quantitatively, but comparing the results at normal incidence and at oblique incidence suggests that the reflection surface may not be locally reacting. As the theoretical model is described with an assumption of local reaction, the failure of this assumption should result in undesirable results, especially at oblique incidence, while at normal incidence the failure of this assumption does not affect the measurement results badly.

The other possible error source is the misappropriation of the image source model. As the image source model describes reflection of plane waves, application of this model to a tube-measurement and a normal-incidence measurement in a free field produced good results, but application of this model to an oblique-incidence measurement in a free field failed in getting good results. This may be because this model is incompatible at plane boundaries at oblique incidence. In the next Chapter, a reflection model which is associated with the plane-wave decomposition will be introduced. This reflection model is meant to be applied to a situation where reflection of spherical waves is incompatible with plane boundaries.

Chapter 7

THE APPLICATION OF LEAST SQUARES ESTIMATION USING A MODEL BASED ON THE PLANE-WAVE DECOMPOSITION (PWD) IN A FREE FIELD

In the theory presented in Chapter 5, it is assumed that, in a free field, the sound propagates spherically but behaves like a plane wave on reflection at a plane boundary. This is not a practical model unless the situation relates to an impedance tube where only plane waves propagate. In order to have a more realistic model of reflection at a plane boundary, in this Chapter, a plane-wave decomposition (PWD) model is used. This model provides an exact description for the reflection of the spherical wave fronts from a plane boundary. Other rigorous theories have been researched for the approximate evaluation of the pressure above an impedance boundary (Lawhead and Rudick, 1951; Ingård, 1951; Brekhovskikh, 1959; Wenzel, 1974; Chien and Soroka, 1975). Such approximations proved their experimental validity in measurements on high-impedance locally-reacting boundaries (Nocke, 1997, 1999 and 2000). In this Chapter, however, the exact solution of the PWD model will used for the description of the reflected sound (Thomasson, 1976; Brekhovskikh, 1980). As the angle of incidence increases, the error in the evaluation of the reflected sound between the image source model and PWD model increases. This error is generally more profound for low-impedance boundaries (Suh, 1999). As this model uses an exact solution that is associated with an integral expression for the Sommerfeld, in order to derive reflection coefficients or impedances from measurements, numerical methods are used in finding the parameters of the surface that best fit the measured results.

7.1 The PWD model of acoustic reflection in a free field

The PWD model is described by the use of plane-wave decomposition for the reflection. This means that the incident spherical wave is decomposed into an infinite sum of plane waves propagating in the normal directions to the spherical wavefronts. With the use of this model, the reflection coefficient cannot be expressed explicitly as it was in Chapter 3, and it can only be obtained by numerical methods. This numerical process takes a lot of time, but with a simple rearrangement of the geometrical setup for the measurement, it is shown here that it can be made reasonably computationally efficient and thus less time consuming.

7.1.1 Plane wave decomposition and acoustic reflection

Since the wavefronts of spherical waves are not compatible with plane boundaries, a more realistic expression of an acoustic pressure at the microphone 1 (Fig. 7.1) is

$$p(x,y,z) = \frac{j\omega\rho_0 e^{-jkr_{11}} q_1}{4\pi r_{11}} + p_{refl} \tag{7.1}$$

where the reflected acoustic pressure, p_{refl}, cannot be expressed as a simple product of a Green function, reflection coefficient and the original source strength as is done in an image source model (refer to Section 5.1). A more precise expression of reflected sound pressure is obtained by plane wave decomposition that decomposes a spherical wave into an infinite sum of plane waves.

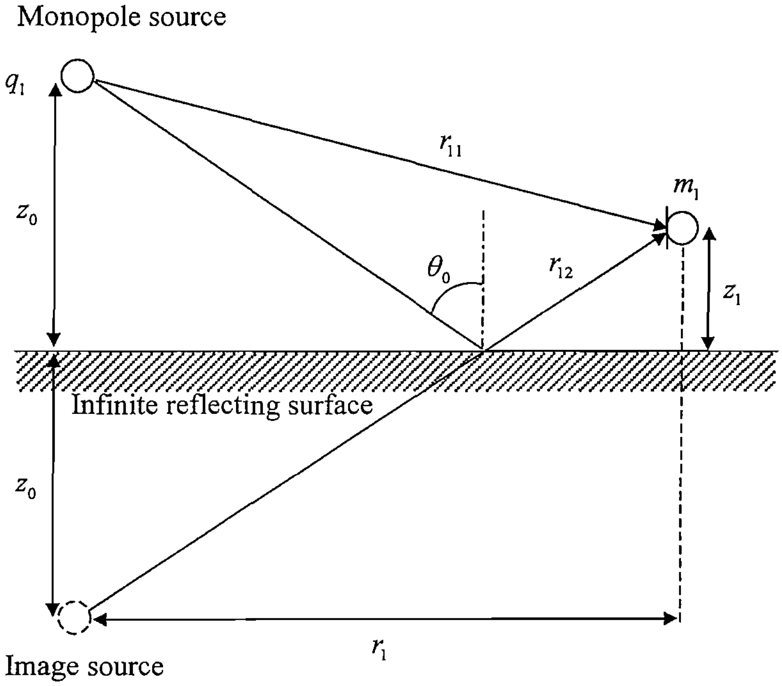

FIG. 7.1: A PWD model of acoustic reflection in a half space

The 'Sommerfeld integral' is an integral representation of spherically symmetric outgoing waves in terms of cylindrical waves. Its application to the outgoing acoustic waves from a point monopole sound source shows (Brekhovskikh, 1980; Suh, 1998) that

$$p_{refl} = \frac{\omega \rho_0 k q_1}{4\pi} \int_{\Gamma_\theta} J_0\left(kr_1 \sin\theta\right) e^{-jk(z_1+z_0)\cos\theta} R(\theta) \sin\theta d\theta \tag{7.2}$$

where $R(\theta)$ is the complex reflection coefficient of the infinite plane boundary which depends upon the angle of incidence, θ, and $J_0\left(kr\sin\theta\right)$ is the Bessel function of the first kind of order zero. Γ_θ is the integration contour in the complex $\theta-$plane.

7.1.2 The cost function described by acoustic reflection

In Eq. (7.2) the reflection coefficient, $R(\theta)$, of the infinite plane boundary, when a plane wave is incident upon it, can be expressed in terms of

$$R(\theta) = \frac{\xi\cos\theta - 1}{\xi\cos\theta + 1} \tag{7.3}$$

where ξ is the specific acoustic impedance of the infinite plane boundary normalised by the characteristic impedance of air, $\rho_0 c$ (cf. Eq. (1.18) in Section 1.3). The impedance, ξ, is constant regardless of the angle of incidence when the reflecting material is assumed to be locally reacting.

Substituting Eq. (7.3) into Eq. (7.2), p_{refl} can be regarded as a function of ξ with a fixed geometry and frequency. Thus

$$p_{refl} = \frac{\omega\rho_0 k q_1}{4\pi} \int_{\Gamma_\theta} J_0\left(kr_1 \sin\theta\right) e^{-jk(z_1+z_0)\cos\theta} \left(\frac{\xi\cos\theta - 1}{\xi\cos\theta + 1}\right) \sin\theta d\theta \tag{7.4}$$

Then Eq. (7.1) can be rewritten as

$$p_1 = g_{11} q_1 + f_1(\xi) q_1 = \left(g_{11} + f_1(\xi)\right) q_1 \tag{7.5}$$

where the Green function g_{11} is defined by

$$g_{11} = \frac{j\omega\rho_0 e^{-jkr_{11}}}{4\pi r_{11}} \tag{7.6}$$

and $f_1(\xi)$ is defined by

$$f_1(\xi) = \frac{\omega\rho_0 k}{4\pi} \int_{\Gamma_\theta} J_0\left(kr_1 \sin\theta\right) e^{-jk(z_1+z_0)\cos\theta} \left(\frac{\xi\cos\theta - 1}{\xi\cos\theta + 1}\right) \sin\theta d\theta \tag{7.7}$$

In Fig. 7.1, an additional microphone, microphone 2, can be placed in the half space. Then similarly the acoustic pressure at the microphone 2, p_2, can be expressed as

$$p_2 = g_{21}q_1 + f_2(\xi)q_1 = \left(g_{21} + f_2(\xi)\right)q_1 \tag{7.8}$$

where

$$g_{21} = \frac{j\omega\rho_0 e^{-jkr_{21}}}{4\pi r_{21}} \tag{7.9}$$

and $f_2(\xi)$ is defined by

$$f_2(\xi) = \frac{\omega\rho_0 k}{4\pi}\int_{\Gamma_\theta} J_0\left(kr_2\sin\theta\right)e^{-jk(z_2+z_0)\cos\theta}\left(\frac{\xi\cos\theta - 1}{\xi\cos\theta + 1}\right)\sin\theta d\theta \tag{7.10}$$

This leads to the definition of the transfer function, H_{12}, given by

$$H_{12} = \frac{p_2}{p_1} = \frac{g_{21} + f_2(\xi)}{g_{11} + f_1(\xi)} \tag{7.11}$$

Now a cost function is defined by

$$J = \left|\frac{\hat{p}_2 - p_2}{q_1}\right|^2 \tag{7.12}$$

This cost function is the same as that defined in Section 3.2, and the same procedure can be followed as described in that section. Thus the cost function can be written as

$$J = \left|\frac{\hat{p}_1}{q_1}\right|^2 \left|\hat{H}_{12} - H_{12}\right|^2 \tag{7.13}$$

Now from Eq. (7.11), it follows that

$$\begin{aligned} J &= \left|\frac{\hat{p}_1}{q_1}\right|^2 \left|\hat{H}_{12} - \frac{g_{21} + f_2(\xi)}{g_{11} + f_1(\xi)}\right|^2 \\ &= \left|\frac{\hat{p}_1}{q_1}\right|^2 \left|\frac{\hat{H}_{12}\left[g_{11} + f_1(\xi)\right] - \left[g_{21} + f_2(\xi)\right]}{g_{11} + f_1(\xi)}\right|^2 \\ &= \frac{1}{\left|g_{11} + f_1(\xi)\right|^2} \left|\frac{\hat{p}_1}{q_1}\right|^2 \left|\left[g_{11}\hat{H}_{12} - \left(g_{21} + f_2(\xi)\right)\right] + \hat{H}_{12} f_1(\xi)\right|^2 \end{aligned} \tag{7.14}$$

This cost function can further be simplified from Eq. (7.5) and Eq. (3.10) that suggest that p_1 can be chosen to be fixed such that it is made equal to the measured pressure, $\hat{p}_1$. Thus

$$J = \left|\left[g_{11}\hat{H}_{12} - \left(g_{21} + f_2(\xi)\right)\right] + \hat{H}_{12} f_1(\xi)\right|^2 \tag{7.15}$$

When several microphones are placed in the same half space (see Section 3.3), the expression for the cost function becomes

$$J = \sum_{m=2}^{M} \left|\left[g_{11}\hat{H}_{1m} - \left(g_{m1} + f_m(\xi)\right)\right] + \hat{H}_{1m} f_1(\xi)\right|^2 \tag{7.16}$$

where M is the number of total microphones. Since the cost function is the error between the measured and analytically modelled transfer functions and is only a function of impedance, ξ, at a given geometry and frequency, the proper value of it can be acquired when the cost function is at its minimum. This involves numerical methods for minimising cost functions, i.e., the steepest descent method, simulated annealing etc. This process requires a lot of time to get the result for the impedance where the cost function is at its minimum. The cost function may have a multi-modal surface since it is a function of complex values of impedance and is related to integrations in a complex plane. The next section shows that this cost function can be decomposed in order to obtain the expression of the optimum measured value of $f_1(\xi)$, such that the process of obtaining the proper value of the impedance can be simplified considerably.

7.1.3 Optimally estimated acoustic reflection

With a thoughtful placement of microphone 2 and subsequent relocation of the sound source, the function $f_2(\xi)$ can be made to be the same as the function $f_1(\xi)$.

As shown in Fig. 7.2, microphone 2 is placed along the same normal line, to the reflecting surface, where microphone 1 is placed in the given plane, and sound source is relocated on the same normal line where it was positioned originally. With this geometrical placement, the following relations are obtained.

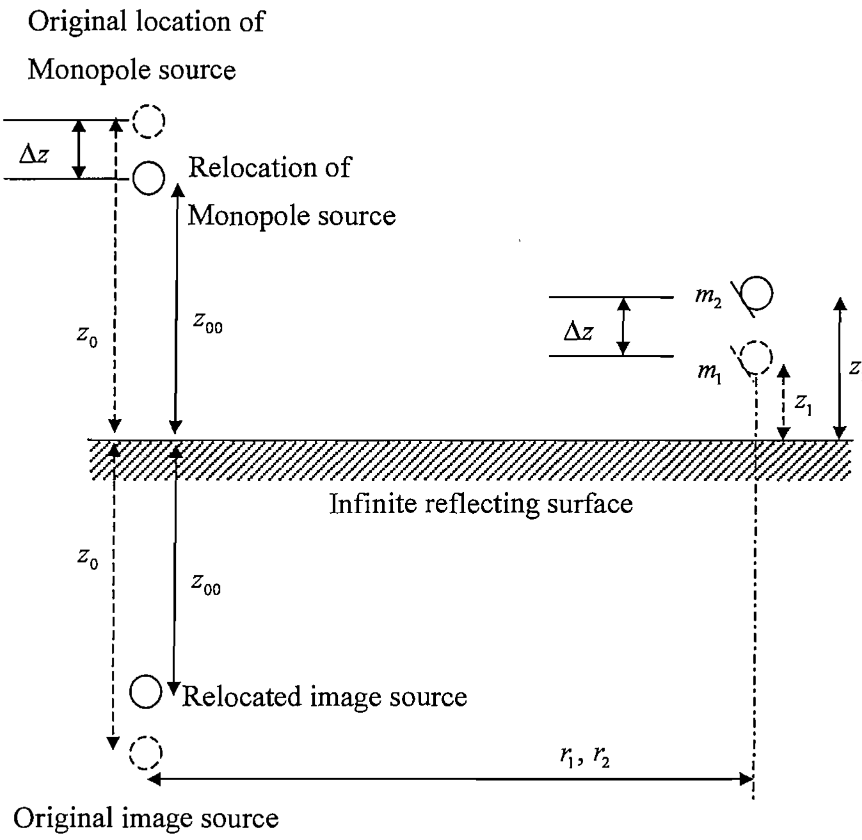

FIG. 7.2: Placement of microphone 2 and the subsequent relocation of the sound source

$$\begin{aligned} r_2 &= r_1 \\ z_2 + z_{00} &= z_1 + z_0 \end{aligned} \tag{7.17}$$

Now from Eqs. (7.7), (7.10) and (7.17), it follows that $f_2(\xi)$ is equal to $f_1(\xi)$, which gives a new expression of Eq. (7.14) such that

$$\begin{aligned} J &= \left|\left[g_{11}\hat{H}_{12} - \left(g_{21} + f_1(\xi)\right)\right] + \hat{H}_{12} f_1(\xi)\right|^2 \\ &= \left|\left(g_{11}\hat{H}_{12} - g_{21}\right) + \left(\hat{H}_{12} - 1\right) f_1(\xi)\right|^2 \end{aligned} \tag{7.18}$$

Adopting the same analysis in Section 3.2, the optimum value of $f_1(\xi)$ deduced from measurements is thus given by

$$\hat{f}_1(\xi)_{opt} = \frac{g_{21} - g_{11}\hat{H}_{12}}{\hat{H}_{12} - 1} \tag{7.19}$$

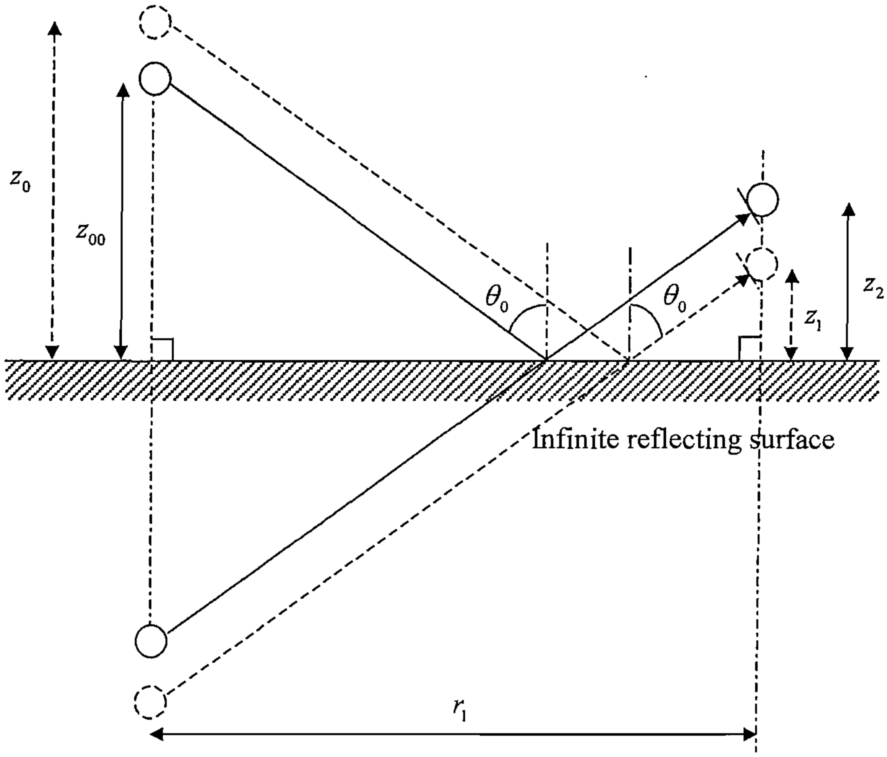

FIG. 7.3: Angle of incidence is kept the same for the choice of position of microphone 2 and subsequent relocation of the sound source as long as the condition of Eq. (7.17) is satisfied.

At first sight, this analysis might suggest that there is a problem associated with the change of angle of incidence as the sound source is relocated in accordance with the choice of position of microphone 2. The angle of incidence, however, does not change as long as the conditions given in Eq. (7.17) are satisfied. The "reflecting point" on the surface, however, is changed (see Fig. 7.3). Hence it should be assumed that the reflecting surface is smooth and provides identical conditions over the entire surface that is exposed to incident sound.

With multiple microphone positions, as long as Eq. (7.17) is satisfied, it can be easily shown that

$$f_m(\xi) = f_1(\xi) \tag{7.20}$$

where m denotes the numbering of additionally placed microphones, i.e., it could be 2, 3, 4, 5 etc. Then an identical argument can be used to that given in Section 3.3 to show that $\hat{f}_1(\xi)_{opt}$ is given by

$$\hat{f}_1(\xi)_{opt} = -\frac{\sum_{m=2}^{M}\left(g_{11}\hat{H}_{1m} - g_{m1}\right)\left(\hat{H}_{1m} - 1\right)^{*}}{\sum_{m=2}^{M}\left|\hat{H}_{1m} - 1\right|^{2}} \tag{7.21}$$

It is always $\hat{f}_1(\xi)_{opt}$ that is obtained in this analysis regardless of the number of measurement points. Now the process of acquiring the impedance reduces to the deduction of the value from the optimally estimated value of the Sommerfeld Integral leading to $\hat{f}_1(\xi)_{opt}$.

7.2 Numerical method for the acquisition of impedance

Eq. (7.16) in Section 7.1.2 describes the cost function in terms of the measured transfer functions and theoretical descriptions of the Sommerfeld integrals. Since this cost function is obtained from the difference between measured and theoretically modelled pressures at each measurement point, it is possible to estimate the impedance at which the cost function is at its minimum. This process, however, takes a lot of time because the cost function contains as many Sommerfeld integrals as the number of measurement points.

In Section 7.1.3, with a geometrical rearrangement, it is shown that the optimally estimated Sommerfeld integral can be obtained from the cost function of Eq. (7.16). Regardless of the number of measurement points, only one Sommerfeld integral matters in Eq. (7.21). This makes the process of obtaining the impedance simpler and less time consuming. For this purpose, the method of the steepest descent is used in order to find the value of ξ from the estimated value of $\hat{f}_1(\xi)_{opt}$. This method finds a minimum of a function by subtracting an amount related to the gradient of the function from the value of a function and iterating the result to the next stage until it finds the minimum value (Press *et al*, 1986).

7.2.1 Evaluation of the Sommerfeld integral

In the next section, it will be shown that impedance can be obtained by minimising a cost function defined by the square of the difference between analytically modelled $f_1(\xi)$ (Eq.

(7.7)) and optimally estimated $\hat{f}_1(\xi)_{opt}$. Prior to this process, the evaluation of $f_1(\xi)$ will be presented in this section based on numerical integration (Thomasson, 1976; Wills, 1996; Suh, 1998).

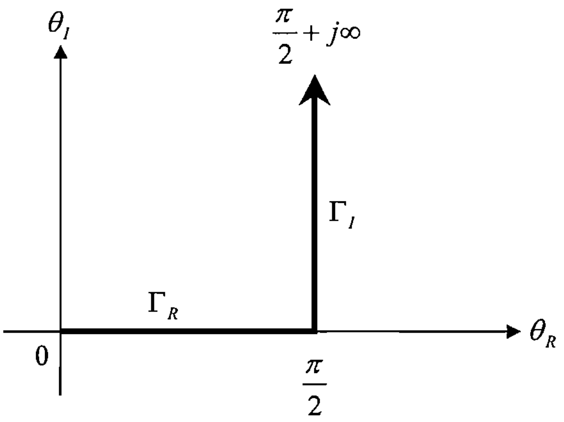

FIG. 7.4: Integration contour, $\Gamma_\theta = \Gamma_R + \Gamma_I$, in the complex θ-plane where $\theta = \theta_R + j\theta_I$

In Eq. (7.7), the integration path Γ_θ is from 0 to $\pi/2$ (Γ_R) for real values of θ, θ_R, in addition to imaginary values of θ, θ_I, from 0 to ∞ (Γ_I). Thus Eq. (7.7) can be rewritten as

$$f_1(\xi) = f_{1R}(\xi) + f_{1I}(\xi) \tag{7.22}$$

where

$$f_{1R}(\xi) = \frac{\omega\rho_0 k}{4\pi}\int_0^{\pi/2} J_0(kr_1 \sin\theta_R)\, e^{-jk(z_1+z_0)\cos\theta_R}\left(\frac{\xi\cos\theta_R - 1}{\xi\cos\theta_R + 1}\right)\sin\theta_R d\theta_R \tag{7.23}$$

and

$$f_{1I}(\xi)=\frac{\omega\rho_0 k}{4\pi}\int_0^{\infty} J_0\left[kr_1\sin\left(\frac{\pi}{2}+j\theta_I\right)\right]e^{-jk(z_1+z_0)\cos\left(\frac{\pi}{2}+j\theta_I\right)}\left[\frac{\xi\cos\left(\frac{\pi}{2}+j\theta_I\right)-1}{\xi\cos\left(\frac{\pi}{2}+j\theta_I\right)+1}\right]\sin\left(\frac{\pi}{2}+j\theta_I\right)d\theta_I \tag{7.24}$$

By the use of the following identities,

$$\begin{aligned}\sin\left(\frac{\pi}{2}+j\theta_I\right)&=\sin\frac{\pi}{2}\cosh\theta_I+j\cos\frac{\pi}{2}\sinh\theta_I=\cosh\theta_I\\ \cos\left(\frac{\pi}{2}+j\theta_I\right)&=\cos\frac{\pi}{2}\cosh\theta_I-j\sin\frac{\pi}{2}\sinh\theta_I=-j\sinh\theta_I\end{aligned} \tag{7.25}$$

Eq. (7.24) can be simplified to give (Suh, 1998)

$$f_{1I}(\xi)=\frac{\omega\rho_0 k}{4\pi}\int_0^{\infty} J_0\left[kr_1\cosh\theta_I\right]e^{-k(z_1+z_0)\sinh\theta_I}\left[\frac{j\xi\sinh\theta_I+1}{j\xi\sinh\theta_I-1}\right]\cosh\theta_I d\theta_I \tag{7.26}$$

Thus $f_{1R}(\xi)$ and $f_{1I}(\xi)$ should be calculated separately for the evaluation of $f_1(\xi)$. Eqs. (7.23) and (7.26) provide these calculations. The integration in (7.26) is indefinite. But since the integrand of Eq. (7.26) is rapidly decaying function of θ_I, reasonable limiting of the integration range to be finite does not result in any noticeable difference. By defining the integrand of Eq. (7.26) by

$$F(\theta_I) = J_0\left[kr_1 \cosh\theta_I\right] e^{-k(z_1+z_0)\sinh\theta_I} \left[\frac{j\xi \sinh\theta_I + 1}{j\xi \sinh\theta_I - 1}\right] \cosh\theta_I \qquad (7.27)$$

$f_1(\xi)$ can practically be evaluated as

$$\begin{aligned} f_1(\xi) &= f_{1R}(\xi) + f_{1I}(\xi) \\ &= f_{1R}(\xi) + \frac{\omega\rho_0 k}{4\pi}\left[\int_0^1 F(\theta_I)\,d\theta_I + \int_1^2 F(\theta_I)\,d\theta_I + \int_2^3 F(\theta_I)\,d\theta_I + \ldots\ldots\right] \end{aligned} \qquad (7.28)$$

TABLE 7.1: Evaluation of indefinite integration by limiting its integration limit. For this evaluation, $z_0 = 3.2m$, $z_1 = 0.053m$ and $z_2 = 0.066m$ are used at $f = 1k\text{Hz}$

N	Real part of $\int_0^N F(\theta_I)\,d\theta_I$	Imag. part of $\int_0^N F(\theta_I)\,d\theta_I$
0.001	- 0.00097279426913	- 0.00000192762529
0.01	- 0.00767559901057	- 0.00013943957728
0.1	- 0.01788286286904	- 0.00126782804713
0.2	- 0.01794317872515	- 0.00129980160242
1	- 0.01794330846080	- 0.00129998527793
2	- 0.01794330925541	- 0.00129998510339
3	- 0.01794331269697	- 0.00129998434775
4	- 0.01794332195565	- 0.00129998231600

As the above table shows, $F(\theta_l)$ is a fast decaying function and restricting the integration limit results in only a marginal difference which is negligible. In this thesis, for this evaluation, the integration limit was restricted from 0 to 4.

7.2.2 Acquisition of impedance by the use of the method of steepest descent

Analytically expressed Sommerfeld integral, $f_1(\xi)$, is a function of ξ alone with a fixed geometry and at a single frequency. In order to obtain ξ from the estimated Sommerfeld integral, $\hat{f}_1(\xi)_{opt}$, using the method of steepest descent, the following cost function, E, is defined.

$$E = \left| f_1(\xi)_{opt} - f_1(\xi) \right|^2 = \left| F(\xi) \right|^2 = F(\xi) F(\xi)^* \tag{7.29}$$

This cost function may not have a uni-modal surface. For the time being, however, let us assume that this cost function has a uni-modal surface within a limited range of impedance. This assumption will be justified in Chapter 8 where the simulation results with PWD model are presented, and some examples of uni-modal surface of the cost function are drawn in Figs. 8.5, 8.6 and 8.7.

Then it is attempted to apply the method of steepest descent to the cost function defined in

Eq. (7.29). The cost function, E, is a function of ξ that is expressed as the complex number given by

$$\xi = \xi_R + j\xi_I \tag{7.30}$$

Then, optimum value of ξ can converge by iterations to find out the minimum of the cost function. The iterations are described by a pair of equations.

$$\begin{aligned} \xi_R(k) &= \xi_R(k-1) - \mu \frac{\partial E}{\partial \xi_R(k-1)} \\ \xi_I(k) &= \xi_I(k-1) - \mu \frac{\partial E}{\partial \xi_I(k-1)} \end{aligned} \tag{7.31}$$

where k is the number of iterations and μ is a convergence coefficient. Since both of the derivatives in terms of the real part and imaginary part of ξ are found to be entirely real quantities, these equations can be combined into a single complex form such that

$$\xi(k) = \xi(k-1) - \mu\gamma(k-1) \tag{7.32}$$

where the complex gradient function, γ, is defined to be

$$\gamma = \frac{\partial E}{\partial \xi_R} + j\frac{\partial E}{\partial \xi_I} \tag{7.33}$$

Each derivative of the cost function in terms of ξ_R and ξ_I is expressed as

$$
\begin{aligned}
\frac{\partial E}{\partial \xi_R} &= \left(\frac{\partial F(\xi)}{\partial \xi_R} \right) F(\xi)^* + F(\xi) \left(\frac{\partial F(\xi)^*}{\partial \xi_R} \right) \\
\frac{\partial E}{\partial \xi_I} &= \left(\frac{\partial F(\xi)}{\partial \xi_I} \right) F(\xi)^* + F(\xi) \left(\frac{\partial F(\xi)^*}{\partial \xi_I} \right)
\end{aligned}
\qquad (7.34)
$$

From Eqs. (7.7) and (7.29), $F(\xi)$ and $F(\xi)^*$ are found to be

$$
\begin{aligned}
F(\xi) &= \hat{f}_1(\xi)_{opt} - f_1(\xi) \\
&= \hat{f}_1(\xi)_{opt} - \frac{\omega \rho_0 k}{4\pi} \int_{\Gamma_\theta} J_0(kr_1 \sin\theta) e^{-jk(z_1+z_0)\cos\theta} \left(\frac{(\xi_R + j\xi_I)\cos\theta - 1}{(\xi_R + j\xi_I)\cos\theta + 1} \right) \sin\theta d\theta
\end{aligned}
\qquad (7.35)
$$

and

$$
\begin{aligned}
F(\xi)^* &= \hat{f}_1(\xi)^*_{opt} - f_1(\xi)^* \\
&= \hat{f}_1(\xi)^*_{opt} - \frac{\omega \rho_0 k}{4\pi} \int_{\Gamma_\theta} J_0(kr_1 \sin\theta) e^{jk(z_1+z_0)\cos\theta} \left(\frac{(\xi_R - j\xi_I)\cos\theta - 1}{(\xi_R - j\xi_I)\cos\theta + 1} \right) \sin\theta d\theta
\end{aligned}
\qquad (7.36)
$$

The estimated Sommerfeld integral, $\hat{f}_1(\xi)_{opt}$, is a constant and independent of impedance, and the derivative can be applied to the integrand such that

$$
\frac{\partial F(\xi)}{\partial \xi_R} = -\frac{\omega \rho_0 k}{4\pi} \int_{\Gamma_\theta} J_0(kr_1 \sin\theta) e^{-jk(z_1+z_0)\cos\theta} \frac{\partial}{\partial \xi_R} \left(\frac{(\xi_R + j\xi_I)\cos\theta - 1}{(\xi_R + j\xi_I)\cos\theta + 1} \right) \sin\theta d\theta \qquad (7.37)
$$

which on using the differential algebra presented in Appendix I shows that

$$\frac{\partial F(\xi)}{\partial \xi_R}=-\frac{\omega\rho_0 k}{4\pi}\int_{\Gamma_\theta} J_0\left(kr_1\sin\theta\right)e^{-jk(z_1+z_0)\cos\theta}\left(\frac{2\cos\theta}{\left(\xi\cos\theta+1\right)^2}\right)\sin\theta d\theta \qquad (7.38)$$

In addition

$$\frac{\partial F(\xi)^*}{\partial \xi_R}=-\frac{\omega\rho_0 k}{4\pi}\int_{\Gamma_\theta} J_0\left(kr_1\sin\theta\right)e^{jk(z_1+z_0)\cos\theta}\frac{\partial}{\partial \xi_R}\left(\frac{\left(\xi_R-j\xi_I\right)\cos\theta-1}{\left(\xi_R-j\xi_I\right)\cos\theta+1}\right)\sin\theta d\theta \qquad (7.39)$$

which on using the differential algebra realised in Appendix I shows that

$$\frac{\partial F(\xi)^*}{\partial \xi_R}=-\frac{\omega\rho_0 k}{4\pi}\int_{\Gamma_\theta} J_0\left(kr_1\sin\theta\right)e^{jk(z_1+z_0)\cos\theta}\left(\frac{2\cos\theta}{\left(\xi^*\cos\theta+1\right)^2}\right)\sin\theta d\theta \qquad (7.40)$$

Similarly

$$\frac{\partial F(\xi)}{\partial \xi_I}=-\frac{\omega\rho_0 k}{4\pi}\int_{\Gamma_\theta} J_0\left(kr_1\sin\theta\right)e^{-jk(z_1+z_0)\cos\theta}\frac{\partial}{\partial \xi_I}\left(\frac{\left(\xi_R+j\xi_I\right)\cos\theta-1}{\left(\xi_R+j\xi_I\right)\cos\theta+1}\right)\sin\theta d\theta \qquad (7.41)$$

and it follows that

$$\frac{\partial F(\xi)}{\partial \xi_I}=-\frac{\omega\rho_0 k}{4\pi}\int_{\Gamma_\theta} J_0\left(kr_1\sin\theta\right)e^{-jk(z_1+z_0)\cos\theta}\left(\frac{2j\cos\theta}{\left(\xi\cos\theta+1\right)^2}\right)\sin\theta d\theta \qquad (7.42)$$

Also

$$\frac{\partial F(\xi)^*}{\partial \xi_I} = -\frac{\omega\rho_0 k}{4\pi}\int_{\Gamma_\theta} J_0\left(kr_1 \sin\theta\right) e^{jk(z_1+z_0)\cos\theta}\frac{\partial}{\partial \xi_I}\left(\frac{\left(\xi_R - j\xi_I\right)\cos\theta - 1}{\left(\xi_R - j\xi_I\right)\cos\theta + 1}\right)\sin\theta d\theta \qquad (7.43)$$

and therefore that

$$\frac{\partial F(\xi)^*}{\partial \xi_I} = -\frac{\omega\rho_0 k}{4\pi}\int_{\Gamma_\theta} J_0\left(kr_1 \sin\theta\right) e^{jk(z_1+z_0)\cos\theta}\left(\frac{-2j\cos\theta}{\left(\xi^*\cos\theta + 1\right)^2}\right)\sin\theta d\theta \qquad (7.44)$$

The effectiveness of convergence of the cost function, $E(k)$, to its minimum is controlled by the choice of the convergence coefficient, μ. In the process of finding out the value of the impedance where the cost function, E, is at its minimum, the cost function is plotted against the wide range impedances. And then the range is limited logically such that the cost function has a uni-modal surface within this range. This is shown in the Chapter 8 where some simulation results are presented.

7.3 Conclusion

The PWD model of acoustic reflection in a free field is more realistic than the image source model. The theory of the least squares estimation procedure developed in Chapter 3 is well applied for the use of the PWD model. This application was successful with the aid of geometrical modification of microphone locations as shown in Section 7.1.3 such that the optimally estimated Sommerfeld integral of reflected part of sound could be explicitly expressed using transfer functions and Green functions.

Chapter 8

SIMULATION RESULTS BY THE USE OF A PWD MODEL IN A FREE FIELD

This chapter presents simulation results using a PWD model in a free field for the least squares estimation of acoustic impedance of a test sample. The main reason for simulation prior to the real measurement is to determine how we can treat the cost function, E, defined as shown in Eq. (7.27) for the numerical estimation of impedance.

8.1 Simulations using the PWD model

In this section, it is shown through computer simulations how the PWD model can be used to perform the measurement of normal impedances at normal incidence. There is no doubt that the exact values of normal impedances can be obtained when the measured transfer functions are not contaminated by noise. The normal impedance obtained in an impedance tube measurement in Appendix III is used for this simulation as ideally reproducible impedances. At normal incidence, the sound source and detector are placed at $3m$ and

$0.1m$ away from the reflecting surface respectively. The function $f_1(\xi)$ is calculated from Eq. (7.7) which is repeated here for convenience,

$$f_1(\xi)=\frac{\omega\rho_0 k}{4\pi}\int_{\Gamma_\theta} J_0\left(kr_1\sin\theta\right)e^{-jk(z_1+z_0)\cos\theta}\left(\frac{\xi\cos\theta-1}{\xi\cos\theta+1}\right)\sin\theta d\theta \tag{8.1}$$

where $r_1=0$ at normal incidence, $z_0=3m$ and $z_1=0.1m$ at a given positions of source and detector with a selected frequency (refer to Fig. 7.1). As the position of the microphone changes, i.e., $z_1=0.1m,\ 0.113m,\ 0.137m,\ 0.164m$ and $0.272m$, the position of source will change, i.e., $z_0=3m,\ 2.987m,\ 2.963m,\ 2.936m$ and $2.828m$ in order to get the values of transfer functions, H_{1_m}, which can be obtained by

$$H_{1_m}=\frac{p_m}{p_1}=\frac{g_{m1}+f_m(\xi)}{g_{11}+f_1(\xi)} \tag{8.2}$$

where $m=2,\ 3,\ 4$ and 5, and $f_m(\xi)$ can be made the same as $f_1(\xi)$ by the relocations of source and detector as shown in Section 7.1.3 (refer to Fig. 7.2 and Eq. (7.20)). For this simulation, the measured transfer functions are assumed to have 10% errors from the analytically modelled transfer functions. This arbitrary choice of errors in transfer functions shall be traced at each stage of evaluating the Sommerfeld integral, impedance and reflection coefficient such that guidelines can be provided for estimating the contribution of measurement errors in the evaluation of impedance and reflection coefficient. Thus the measured transfer functions, $\hat{H}_{1_m}$, can be simulated from the analytical model, H_{1m}.

$$\hat{H}_{1m} = rH_{1m} \tag{8.3}$$

where r is a random variable that has a uniform probability density function in the range 0.9 to 1.1. The values of $\hat{f}_1(\xi)_{opt}$ are calculated from $\hat{H}_{1m}$ using Eq. (7.21). Errors contained in $\hat{f}_1(\xi)_{opt}$ in the real part and imaginary part are separately calculated and compared with $f_1(\xi)$. The results are shown in Fig. 8.1 at selected frequencies at the centre frequencies of one-third octave bands between 200 Hz and 5 kHz.

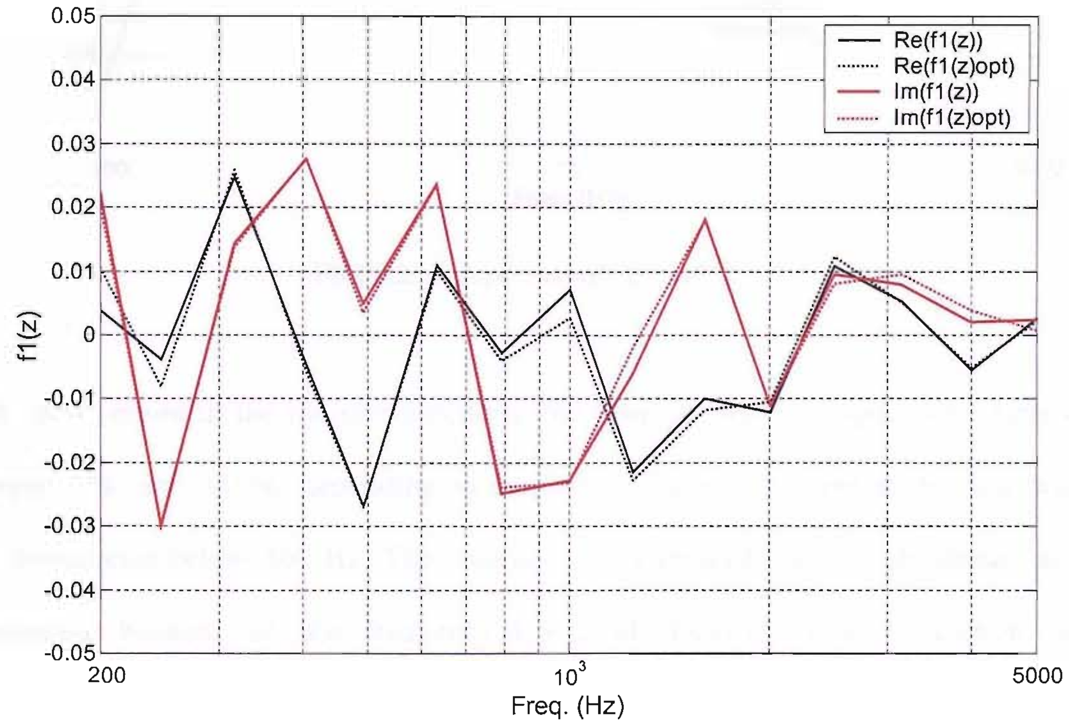

FIG. 8.1: Comparison of $f_1(\xi)$ and $f_1(\xi)_{opt}$

Now for the estimation of optimally reproduced normal impedances, the method of the steepest descent has been used (refer to Section 7.2.2). Again errors ξ_{opt} are calculated separately at real and imaginary parts against ξ, and the results are shown in Fig. 8.2.

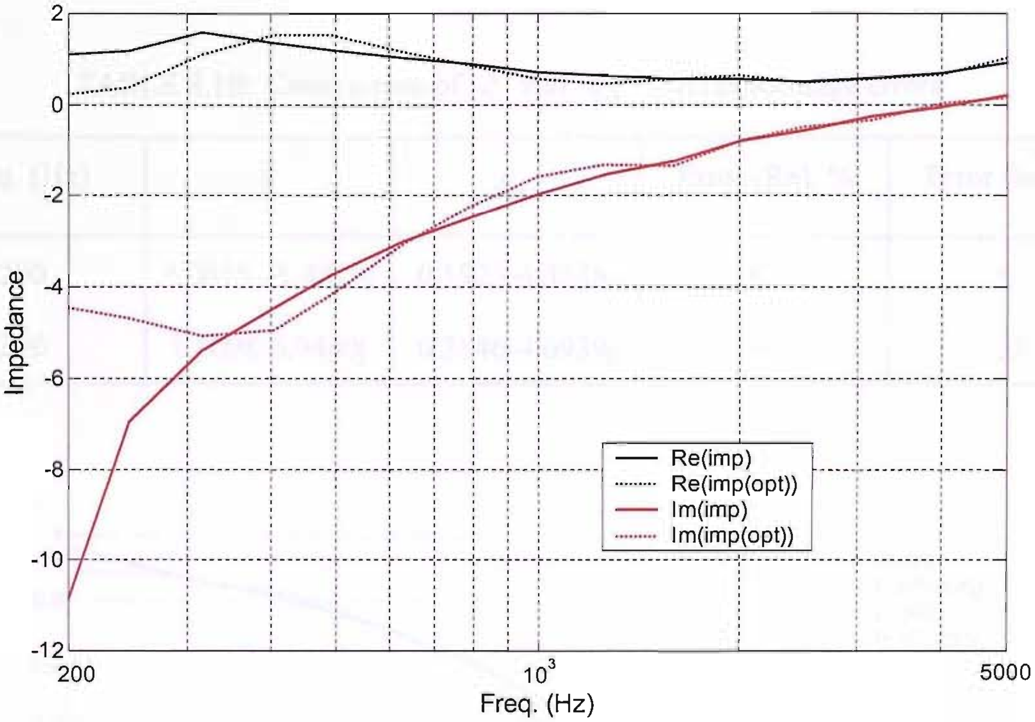

FIG. 8.2: Comparison of ξ and ξ_{opt}

With 10% errors in the transfer functions, the resultant normal impedances have errors between 1% and 110% depending on frequency. Overall the errors are not big except at low frequencies below 300 Hz. The simulated 10% errors have a larger impact at these frequencies because of the frequency-dependent decaying Bessel function in the Sommerfeld integral. This is illustrated in Fig. 8.1 where the errors between $f_1(\xi)$ and $f_1(\xi)_{opt}$ are plotted. Table 8.1 shows these errors at frequencies at $200\,\text{Hz}$ and $250\,\text{Hz}$.

TABLE 8.1A: Comparison of $f_1(\xi)$ and $f_1(\xi)_{opt}$ with percentage errors

Freq. (Hz)	$f_1(\xi)$	$f_1(\xi)_{opt}$	Error (Re), %	Error (Im), %
200	0.0051+0.0306j	0.0134+0.0284j	160	7
250	-0.0039-0.0300j	-0.0081-0.0297j	106	1

TABLE 8.1B: Comparison of ξ and ξ_{opt} with percentage errors

Freq. (Hz)	ξ	ξ_{opt}	Error (Re), %	Error (Im), %
200	1.0658-11.4825j	0.1923-4.4388j	82	61
250	1.1698-6.9440j	0.3846-4.6939j	67	32

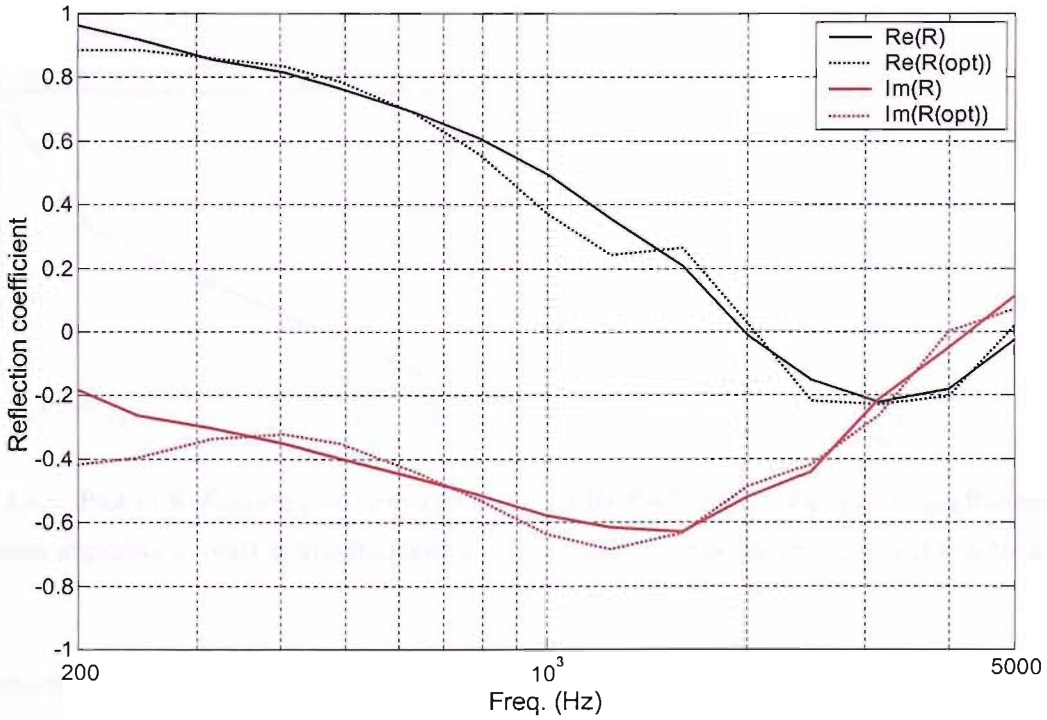

FIG. 8.3A: Comparison of R and R_{opt}

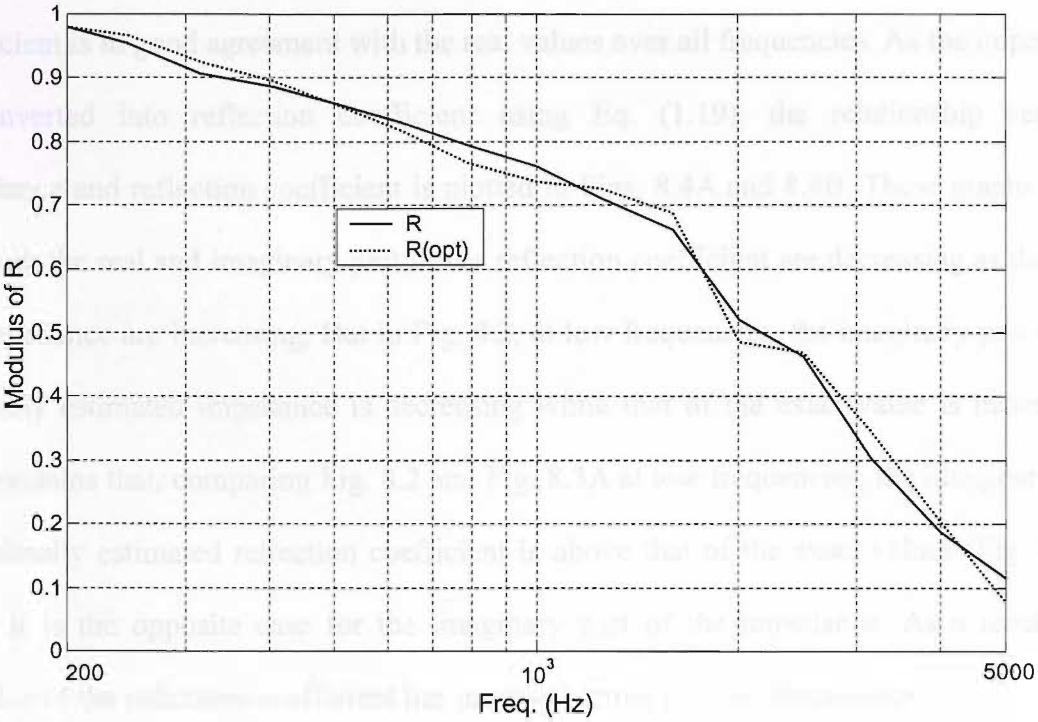

FIG. 8.3B: Comparison of moduli of R and R_{opt}

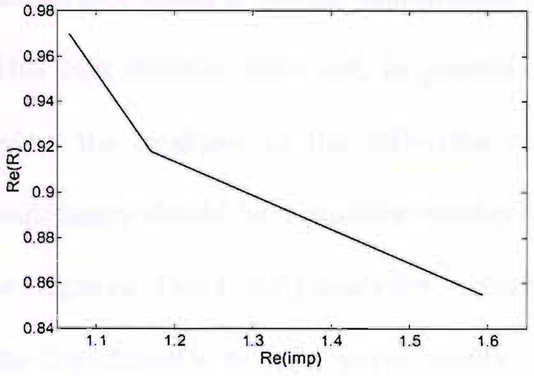

FIG. 8.4A: Plot of Reflection coefficient (real) against impedance (real) at low frequencies

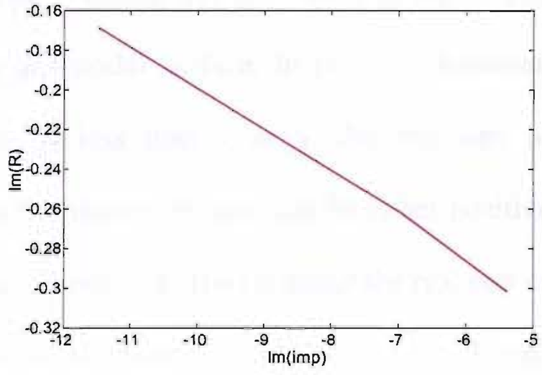

FIG. 8.4B: Plot of Reflection coefficient (imag.) against impedance (imag.) at low frequencies

Converting these results of optimally estimated impedances into reflection coefficients, the differences between exact values and estimated values are shown in Fig. 8.3A. Meanwhile the moduli of optimally estimated reflection coefficients are less affected by the errors of transfer functions (Fig. 8.3B). So the modulus of the optimally estimated reflection coefficient is in good agreement with the real values over all frequencies. As the impedance is converted into reflection coefficient using Eq. (1.19), the relationship between impedance and reflection coefficient is plotted in Figs. 8.4A and 8.4B. These graphs show that both the real and imaginary part of the reflection coefficient are decreasing as those of the impedance are increasing. But in Fig. 8.2, at low frequencies, the imaginary part of the optimally estimated impedance is decreasing while that of the exact value is increasing. This explains that, comparing Fig. 8.2 and Fig. 8.3A at low frequencies, the imaginary part of optimally estimated reflection coefficient is above that of the exact values (Fig. 8.3A) while it is the opposite case for the imaginary part of the impedance. As a result, the modulus of the reflection coefficient has marginal errors at these frequencies.

Applying the steepest descent method for the estimation of optimally reproduced normal impedance needs a careful examination of the cost function that is defined in Eq. (7.29). This cost function does not, in general, have a uni-modal surface. In practice, however, when the modulus of the reflection coefficient is less than a unity, the real part of impedance should be a positive number whereas the imaginary part can be either positive or negative. This is fully analysed numerically in Appendix II. Thus limiting the real part of the impedance to being positive results in uni-modal surfaces of the cost functions. Hence the impedance can be derived by applying the method of the steepest descent to the cost function defined in Eq. (7.29). Fig. 8.5 shows that the cost function, at $630\,\mathrm{Hz}$, does not have a uni-modal surface when there is no restriction that the real part of impedance is positive. Also there are singularities when the real part of impedance is zero. Figs. 8.6, 8.7 and 8.8 show plots of cost functions against impedance at some selected frequencies

(400 Hz, 500 Hz and 630 Hz). These cost functions, within the restricted values of real part of impedance, have uni-modal surfaces. From these graphs, a starting value of impedance is estimated and then the optimum value of impedance is obtained by the method of the steepest descent, the details of which are presented in Section 7.2.2.

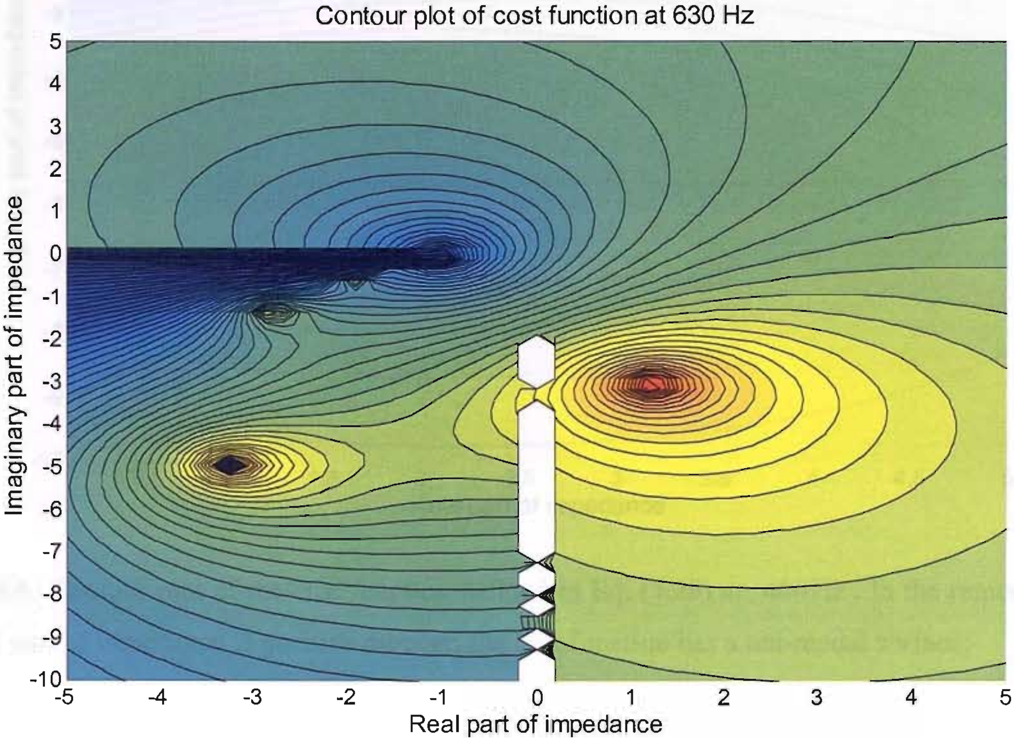

FIG. 8.5A: Contour plot of the cost function defined in Eq. (7.29) at 630 Hz. Without a restriction on the value of the real part of impedance, this cost function does not have a uni-modal surface.

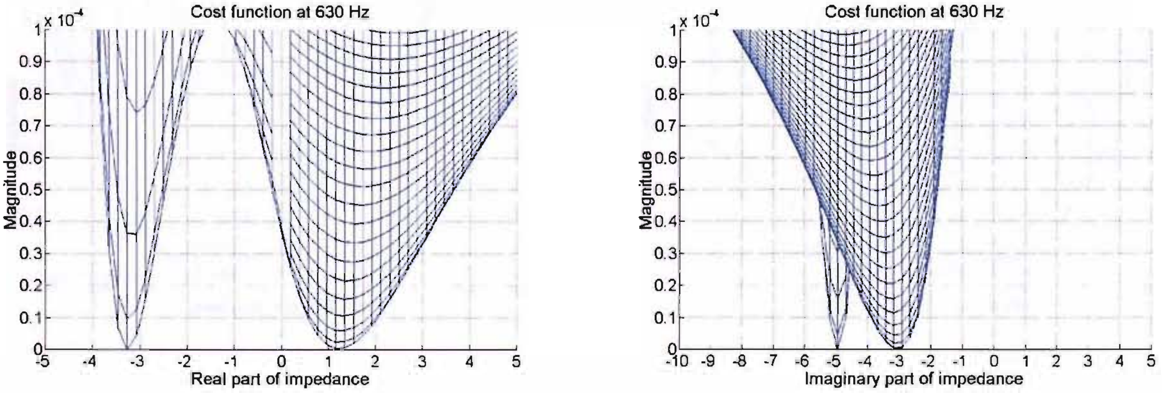

FIG. 8.5B: The cost function, at 630 Hz, plotted against the real part of the impedance.

FIG. 8.5C: The cost function, at 630 Hz, plotted against the imaginary part of the impedance.

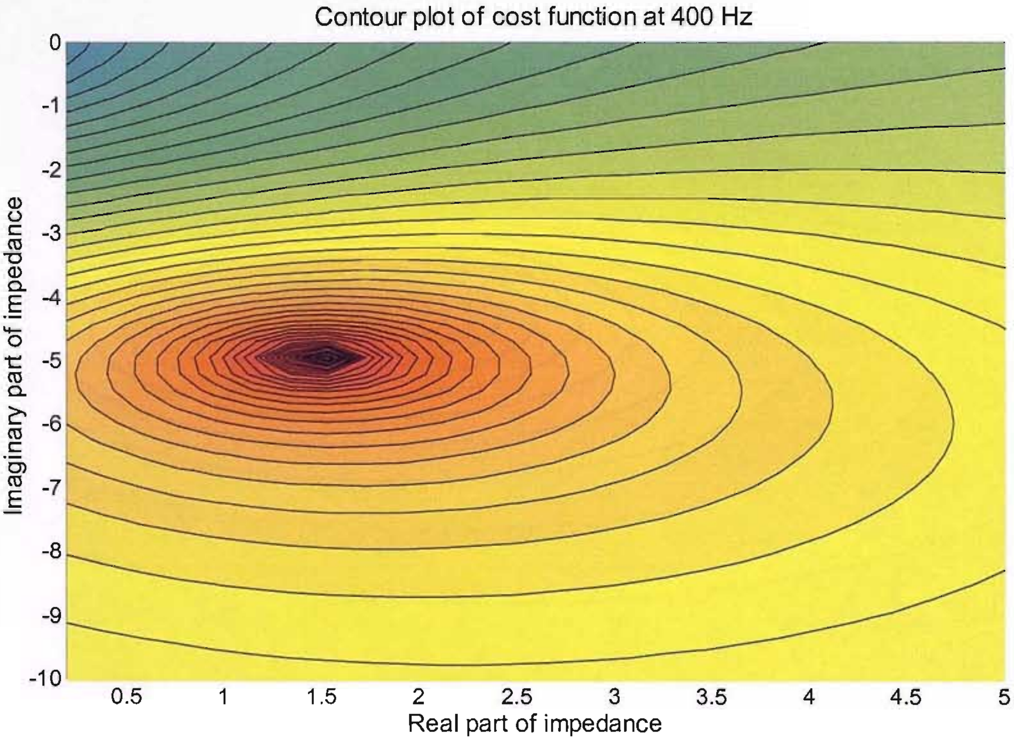

FIG. 8.6A: Contour plot of the cost function defined in Eq. (7.29) at 400 Hz. In the region where the real part of impedance is positive number, the cost function has a uni-modal surface.

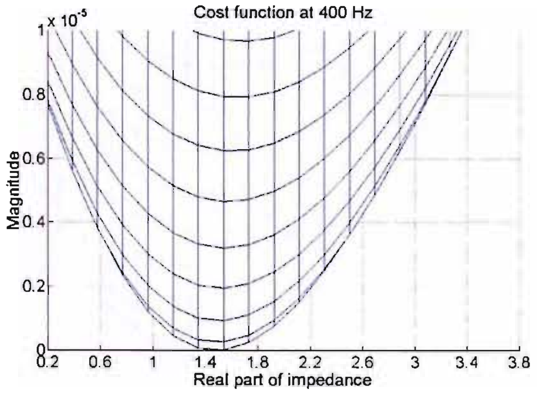

FIG. 8.6B: The cost function, at 400 Hz, plotted against the real part of the impedance

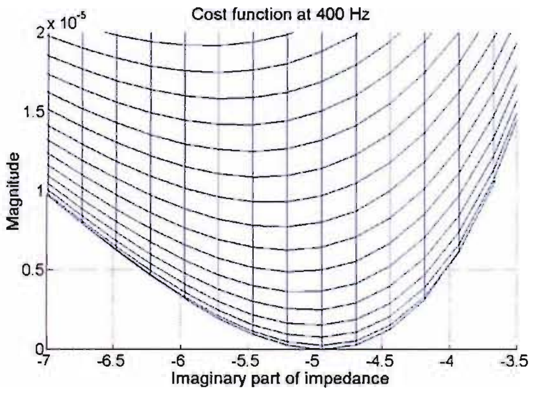

FIG. 8.6C: The cost function, at 400 Hz, plotted against the imaginary part of the impedance

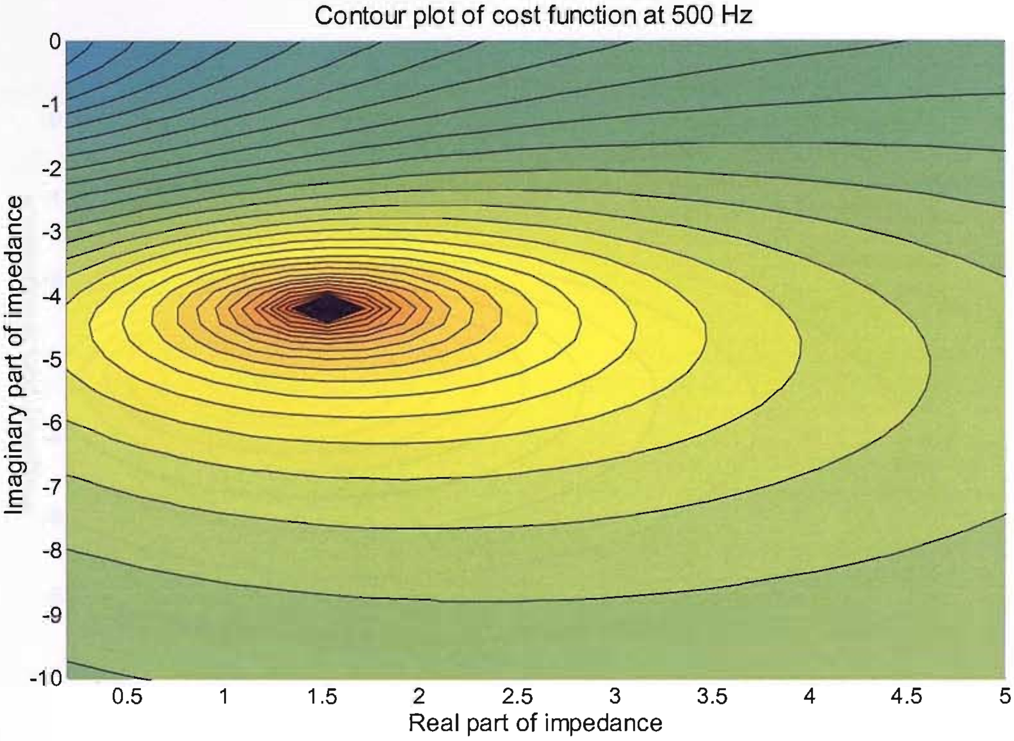

FIG. 8.7A: Contour plot of the cost function defined in Eq. (7.29) at 500 Hz. In the region where the real part of impedance is positive number, the cost function has a uni-modal surface.

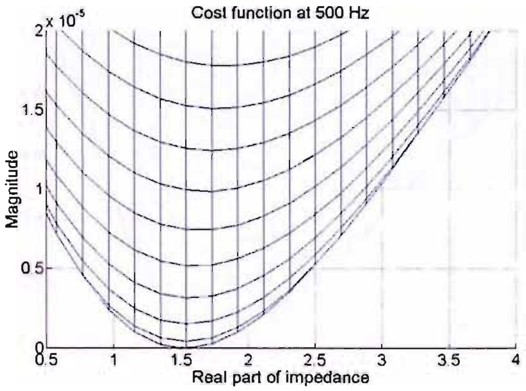

FIG. 8.7B: The cost function, at 500 Hz, plotted against the real part of the impedance

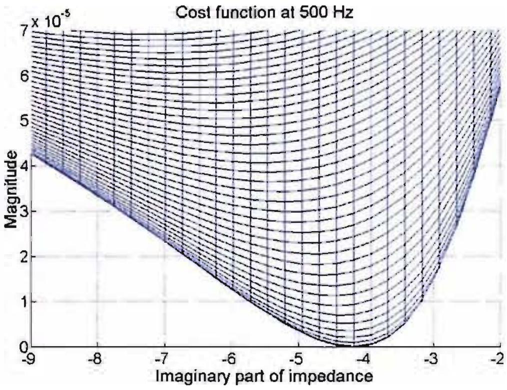

FIG. 8.7C: The cost function, at 500 Hz, plotted against the imaginary part of the impedance

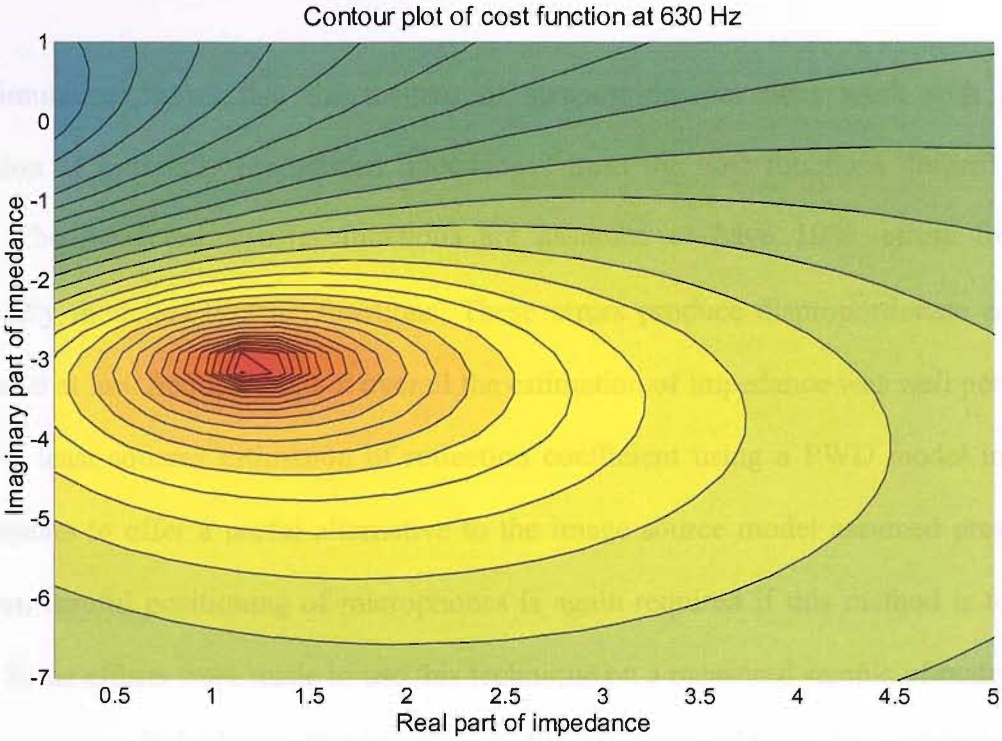

FIG. 8.8A: Contour plot of the cost function defined in Eq. (7.29) at 630Hz. In the region where the real part of impedance is positive number, the cost function has a uni-modal surface.

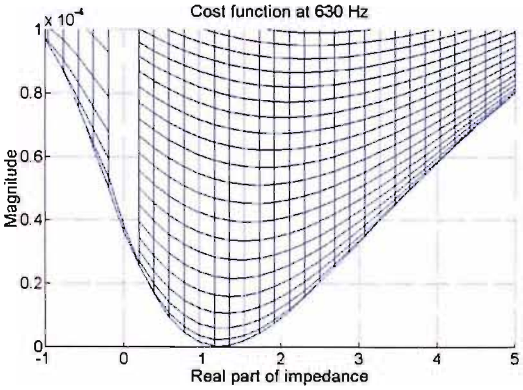

FIG. 8.8B: The cost function, at 630Hz, plotted against the real part of the impedance

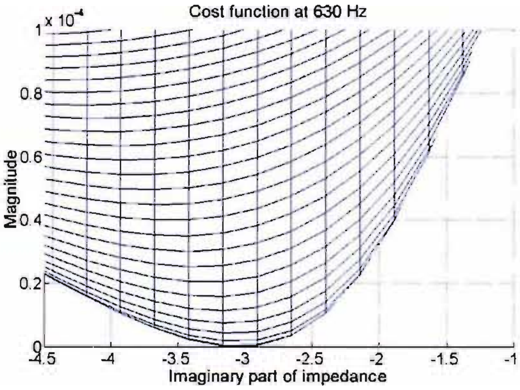

FIG. 8.8C: The cost function, at 630Hz, plotted against the imaginary part of the impedance

8.2 Conclusion

This simulation shows that the method of steepest descent does work well for the estimation of optimally reproduced impedances from the cost functions defined in Eq. (7.27). The measured transfer functions are assumed to have 10% errors from the analytically modelled transfer functions. These errors produce disproportionate errors in impedance at low frequencies, but overall the estimation of impedance was well performed. Thus the least squares estimation of reflection coefficient using a PWD model in a free field appears to offer a useful alternative to the image source model assumed previously. However, careful positioning of microphones is again required if this method is to prove useful. Some efforts were made to use this technique on a measured sample of material but without success. It is likely that the errors due to either lack of local reaction or to microphone mis-positioning are responsible for this failure. This work is described in Appendix IV.

Chapter 9

CONCLUSION

The method of least squares estimation of acoustic reflection coefficients with multi-measurement point has been presented and tested by measurements. Two different measurement sessions were held for a test of this theory and the results have been presented and compared in Chapters 4 and 6. These include descriptions of normal incidence impedance tube measurement and free-field measurement using an image source model at normal and oblique incidence.

It is very promising that the measurement results in the impedance tube with the multi-measurement point least squares estimation coincide with the results given by the standing wave ratio method. The free-field measurement results at normal incidence by the use of an image source model is in good agreement with those obtained in a tube measurement. However, oblique incidence in a free field by using an image source model does not produce results that are close to the results expected from the impedance tube measurements. Some of the error sources that caused these discrepancies have already been discussed in Chapter 6, and an extra measurement is presented in Appendix III for a reference. A PWD model introduced in Chapter 7 was demonstrated by simulation in Chapter 8 as an alternative method to the use of an image source model for oblique incidence. The limitations of the practicability of this model are discussed in Appendix IV.

There is no doubt that the impedance tube measurements with this method outperform the existing two-microphone transfer function method, especially since the effective frequency range can be extended into a far lower range, with the use of a single tube, which is not covered by the two-microphone transfer function method using a single tube of a certain diameter. For example, with the use of a $75\,mm$ diameter tube as undertaken in this thesis and presented in Chapter 4, the new method allows an extended lower frequency of $100\,\text{Hz}$ whereas the existing method with the given diameter tube allows the low frequency limit of $1\,\text{kHz}$.

With the two-microphone transfer function method, the lower frequency measurement is undertaken with the use of larger diameter tubes. Combined with the smaller diameter tube measurement results, the results at the upper frequency limit do not, in general, coincide with the lower frequency limit of smaller tube measurement. This has been explained by the idea of an optimal microphone separation for the given frequency range of measurement. The method of least squares estimation, however, uses four different microphone separations from which four different transfer functions are obtained, and any peaky results caused by the error frequencies due to the microphone separation are suppressed by the other three transfer functions. This is a great improvement in the sense that the effective lower frequency limit can be extended with the use of a single-diameter tube. Thus the method developed in this thesis can be directly applied to the practical use of measuring impedances or reflection coefficients of a test sample in a tube.

The analysis of error frequencies related to the half-wavelength distances, at normal incidence, between microphones from which the transfer function is obtained has been presented in section 5.2. This analysis is not just for the normal incidence but also for the oblique incidence in general, and, as a special case, the normal incidence in the impedance tube is predicted and well justified.

In applying this method to the free-field measurement, the measurement results with an image source model do not seem to be improved except that the error frequencies due to the relative separations between the source and microphones are eliminated. At normal incidence, however, the use of an image source model produced very promising results, which at least suggests that this method can be used for this particular purpose.

The PWD model was introduced for better modelling of the reflection of spherical waves on a plane boundary. Its validity was demonstrated by simulation. In order to demonstrate the potential for the practical usage of the technique, a method has been proposed for accurately placing the source and microphone positions. Using this PWD model, both the positions of microphone and loudspeaker are moved for the measurement of impulse response at each microphone position. This requires great accuracy in order to avoid errors due to mis-positioning.

For the free-field measurement, either with an image source model or with a PWD model, geometrical accuracy is a main requirement for a proper measurement apart from the assumption of local reaction of the reflecting surface. Overall, the developed method of the least squares estimation of acoustic reflection coefficients is well justified and particularly is emphasized for the impedance tube measurements in its simplicity and effectiveness. However, more work is required to clearly demonstrate its practical usefulness in the free-field case.

In summary, the least squares estimation method has been found to be successful in an impedance tube and for normal incidence in a free field based on a simple image model. A method has also been proposed for use in a free field that is based on a PWD model, although this has not yet been shown to produce reliable experimental results.

References

J. F. Allard, R. Bourdier and A. M. Bruneau, “The measurement of acoustic impedance at oblique incidence with two microphone,” J. Sound Vib. **101** (1), 130-132 (1985)

J. Allard and B. Sieben, “Measurements of acoustic impedance in a free field with two microphones and a sprectrum analyzer,” J. Acoust. Soc. Am. **77** (4), 1617-1618 (1985)

J. Allard, M. Henry, V. Gareton, G. Jansens and W. Luariks, “Impedance measurements around grazing incidence for nonlocally reacting thin porous layers,” J. Acoust. Soc. Am. **113** (3), 1210-1215 (2003)

ASTM E 1050-98, “Standard Test method for Impedance and Absorption of Acoustical Materials Using A Tube, Two microphones and A Digital Frequency Analysis System.”

L. L. Beranek, *Acoustic measurements*, John Wiley & Sons, 1962

H. Bodén and M. Åbom, “Influence of errors on the two-microphone method for measuring acoustic properties in ducts,” J. Acoust. Soc. Am. **79** (2), 541-549 (1986)

P. Boulanger, T. Waters-Fuller, K. Attenborough and K. M. Li, “Models and measurements of sound propagation from a point source over mixed impedance ground,” J. Acoust. Soc. Am. **102** (3), 1432-1442 (1997)

L. M. Brekhovskikh, "Surface waves in acoustics," Sov. Phys.-Acoust. **5**, 3-12 (1959)

L. M. Brekhovskikh, *Waves in layerd media* (2^{nd} ed.), Academic Press, 1980

L. M. Brekhovskikh and O. A. Godin, *Acoustics of layered media II: Point sources and Bounded Beams*, Springer-Verlag, 1992

B. Brouard, D. Lafage, J. F. Allard and M Tamura, "Measurement and prediction of the reflection coefficient of porous layers at oblique incidence and for inhomogeneous waves," J. Acoust. Soc. Am. **99** (1), 100-107 (1996)

BS ISO 10534-2:1998, "Acoustics - Determination of sound absorption coefficient and impedance in impedance tubes - Part 2: Transfer-function method."

Chamber's *Encyclopedia* new revised ed., Vol. 1, Pergamon Press, 50-52, 1967

Chamber's *Encyclopedia* new revised ed., Vol. 12, Pergamon Press, 722-743, 1967

W. Cheung, M. Jho and Y. Kim, "Improved method for the measurement of acoustic properties of a sound absorbent sample in the standing wave tube," J. Acoust. Soc. Am. **97** (5), 2733-2739 (1995)

C. F. Chien and W. W. Soroka, "Sound propagation along an impedance plane," J. Sound Vib. **43** (1), 9-20 (1975)

C. F. Chien and W. W. Soroka, "A note on the calculation of sound propagation along an impedance plane," J. Sound Vib. **69** (2), 340-343 (1980)

W. Chu, "Transfer function technique for impedance and absorbtion measurements in an impedance tube using a single microphone," J. Acoust. Soc. Am. **80** (2), 555-560 (1986)

J. Y. Chung, "Cross-spectral method of measuring acoustic intensity without error caused by instrument phase mismatch," J. Acoust. Soc. Am. **64** (6), 1613-1616 (1978)

J. Y. Chung and D. A. Blaser, "Transfer function method of measuring in-duct acoustic properties. I. Theory," J. Acoust. Soc. Am. **68** (3), 907-913 (1980)

J. Y. Chung and D. A. Blaser, "Transfer function method of measuring in-duct acoustic properties. II. Experiment," J. Acoust. Soc. Am. **68** (3), 914-921 (1980)

L. Cremer and H. A. Müller, *Die wissenschaftlichen Grundlagen der Raumakustik*, Bd. I. Hirzel, 1978

J. C. Davies and K. A. Mulholland, "An impulse method of measuring normal impedance at oblique incidence," J. Sound Vib. **67** (1), 135-149 (1979)

C. F. Eying, "Reverberation time in dead rooms," J. Acoust. Soc. Am. **1** (2), 217-241 (1930)

F. J. Fahy, *Foundations of engineering acoustics*, Academic Press, 2001

F. J. Fahy, *Sound Intensity*, Elsevier Applied Science, 1989

F. J. Fahy and J. G. Walker (ed.), *Fundamentals of Noise and Vibration*, E & FN SPON, 1998

R. Fletcher, *Practical methods of optimization*, John Wiley & Sons, 2000

G. V. Frisk, A. V. Oppenheim and D. R. Martinez, "A technique for measuring the plane-wave reflection of the ocean botton," J. Acoust. Soc. Am. **68** (2), 602-612 (1980)

T. Fujimori, S. Sato & H. Miura, "An automated measurement system of complex sound pressure reflection coefficients," Proceedings of the International Conference on Noise Control Engineering, 1009-1014 (1984)

D. Halliday, R. Resnick and J. Walker, *Fundamentals of Physics* (4th ed.), John Wiley & Sons, 1993

K. A. Hollin and M. H. Jones, "The measurement of sound absorption coefficient in situ by a correlation technique," Acustica **37**, 31-35 (1977)

D. C. Hothersall and J. N. B. Harriott, "A Fresnel zone approach to the prediction of sound propagation above a multi-impedance plane," Proc. Inst. Acoust. **16**, 83-90 (1994)

D. C. Hothersall and J. N. B. Harriott, "Approximate model for sound propagation above multi-impedance plane boundaries," J. Acoust. Soc. Am. **97** (2), 918-926 (1995)

U. Ingård, "On the reflection of a spherical sound wave from an infinite plane," J. Acoust. Soc. Am. **23** (3), 329-335 (1951)

U. Ingård and R. H. Bolt, "A free field method of measuring the absorption coefficient of acoustic materials," J. Acoust. Soc. Am. **23** (5), 509-516 (1951)

G. Jansens, W. Lauriks, G. Vermeir and J. Allard, "Free field measurements of the absorption coefficient for nonlocally reacting sound absorbing porous layers," J. Acoust. Soc. Am. **112** (4), 1327-1334 (2002)

M. G. Jones and T. L. Parrott, "Evaluation of a multi-point method for determining acoustic impedance," Mechanical Systems and Signal Processing (1989) **3** (1), 15-35

M. Jones and P. Stiede, "Comparison of methods for determining specific acoustic impedance," J. Acoust. Soc. Am. **101** (5), 2694-2704 (1997)

M. Karjalainen and M. Tikander, "Reducing Artifacts of In-situ Surface Impedance Measurements," Proc. 17th Int. Congr. on Acoust. (ICA), Vol. 2, 393-394, 2001

B. Katz, "Method to resolve microphone and sample location errors in the two-microphone duct measurement method," J. Acoust. Soc. Am. **108**, 2231-2237 (2000)

L. E. Kinsler, A. R. Frey, A. B. Coppens and J. V. Sanders, *Fundamentals of acoustics*, 3rd ed., John Wiley & Sons, 1982

V. O. Knudsen, *Architectural Acoustics*, Wiley, New York, 1932

C. W. Kosten, "International comparison measurements in the reverberation room," Acustica **10**, 400-411 (1960)

H. Kuttruff, *Room Acoustics*, 4th ed., Spon Press, 2000

R. B. Lawhead and I Rudnick, "Acoustic wave propagation along a constant normal impedance boundary," J. Acoust. Soc. Am. **23**, 546-549 (1951)

J. Li and M. Hodgson, "Use of pseudo-random sequences and a single microphone to measure surface impedance at oblique incidence," J. Acoust. Soc. Am. **102** (4), 2200-2210 (1997)

McGraw-Hill *Encyclopedia of Science and Technology*, 8th Ed., Vol. 17, 5-41, 1997

M. Minten, A. Cops and W. Lauriks, "Absorption characteristics of an acoustic material at oblique incidence measured with the two-microphone technique," J. Sound Vib. **120** (3), 499-510 (1988)

E. Mommertz, "Angle-dependent in-situ measurements of reflection coefficients using a subtraction technique," Applied Acoustics **46**, 251-263 (1995)

C. L. Morfey, *Dictionary of acoustics*, Academic Press, 2001

P. M. Morse, *Vibration and Sound*, McGraw-Hill Book Company, 1936

P. Nelson and S. Elliott, *Active Control of Sound*, Academic Press, London, 1992

C. Nocke, V. Mellert, T. Waters-Fuller, K. Attenborough and K. M. Li, "Impedance deduction from broad-band, point-source measurement at grazing incidence," Acustica **83**, 1085-1090 (1997)

C. Nocke, “Improved Impedance Deduction from Measurements near grazing incidence,” Acoustica **85**, 586-590 (1999)

C. Nocke, “In-situ acoustic impedance measurement using a free-field transfer function method,” Applied Acoustics **59**, 253-264 (2000)

A. D. Pierce, *Acoustics*, McGraw-Hill, 1981

J. Pierce, *Allmost All About Waves*, MIT, 1974

J. Pope, “Rapid measurement of acoustic impedance using a single microphone in a standing wave tube,” Proceedings of the 12th International Congress on Acoustics, M3-3 (1986)

W. H. Press, B. P. Flannery, S. A. Teukolsky and W. T. Vetterling, *Numerical Recipes*, Cambridge University Press, 1986

S. A. Radcliffe, “Acoustical identification of the characteristics of ocean fronts,” Ph.D., Univ. of Southampton, 1997

D. D. Rife and J. Vanderkooy, “Transfer-function Measurement with Maximum-Length Sequences”, J. Audio. Eng. Soc. 37 (6), 419-444 (1989)

D. D. Rife, “Modulation Transfer function Measurement with Maximum-Length Sequences”, J. Audio. Eng. Soc. 40 (10), 779-790 (1992)

A. Seybert and D. Ross, "Experimental determination of acoustic properties using a two-microphone random-excitation technique," J. Acoust. Soc. Am. **61** (5), 1362-1371 (1977)

D. J. Sides and K. A. Mulholland, "The variation of normal layer impedance with angle of incidence," J. Sound Vib. **14**, 139-142 (1971)

S. Slutsky and H. L. Bertoni, "Analysis and programs for assessment of absorptive and tilted parallel barriers," Transportation Research Record 1176, National Research Council, Washington, DC, 13-22 (1987)

F. Spandöck, "Experimentelle Untersuchung der akustischen Eigenschaften von Baustoffen durch die Kurztonmethode," Ann d Phys (V), 328-344, 1934

J. S. Suh, "Measurement of transient response of rooms and comparison with geometrical acoustic models," Ph.D., Univ. of Southampton, 1998

J. S. Suh, "Measurement of transient response of rooms and comparison with geometrical acoustic models," J. Acoust. Soc. Am. **105** (4), 2304-2317 (1999)

M. Tamura, "Spatial Fourier transform method of measuring reflection coefficients at oblique incidence. I: Theory and numerical examples," J. Acoust. Soc. Am. **88** (5), 2259-2264 (1990)

M. Tamura, J. F Allard and D. Lafarge, "Spatial Fourier transform method of measuring reflection coefficients at oblique incidence. II: Experimental results," J. Acoust. Soc. Am. **97** (4), 2255-2262 (1995)

S. Thomasson, “Reflection of waves from a point source by an impedance boundary,” J. Acoust. Soc. Am. **59** (4), 780-785 (1976)

M. Tohyama & T. Koike, *Fundamentals of acoustic signal processing*, Academic Press, 1998

G. Weinreich and E. B. Arnold, “Method for measuring acoustic radiation fields,” J. Acoust. Soc. Am. **68** (2), 404-411 (1980)

A. R. Wenzel, “Propagation of waves along an impedance boundary,” J. Acoust. Soc. Am. **55** (5), 956-963 (1974)

E. G. Williams and J. D. Maynard, “Holographic imaging without the wavelength resolution limit,” Phys. Rev. Lett. **45**, 554-557 (1980)

G. Wills, “Shallow water propagation from an embedded source,” Ph.D., Univ. of Southampton, 1996

M. Yuzawa, “A method of obtaining the oblique incident sound absorption coefficient through an on-the-spot measurement,” Applied Acoustics **8**, 27-41 (1975)

Appendix I

Alegebraic details for the derivation of Eqs. (7.38), (7.40), (7.42) and (7.44)

In Section 7.2.2 the cost function is defined by the square of the absolute value of the difference between the analytically expressed Sommerfeld integral, $f_1(\xi)$, and the estimated Sommerfeld integral, $\hat{f}_1(\xi)_{opt}$ from the measurement. For the acquisition of the optimum impedance, ξ, the method of the steepest descent is applied. This requires differentiation of the cost function in terms of each of the real and imaginary parts of the impedance.

Each of the Eqs. (7.37), (7.39), (7.41) and (7.43) contains the same type of differentiation in its integral equation, and each of the following equations, i.e., Eqs. (7.38), (7.40), (7.42) and (7.44) contains the solution in its intergral equation. This appendix shows details of the differential algebra associated with these equations.

From Eq. (7.38) to Eq. (7.39)

$$\frac{\partial}{\partial \xi_R}\left(\frac{(\xi_R + j\xi_I)\cos\theta - 1}{(\xi_R + j\xi_I)\cos\theta + 1}\right)$$

$$= \frac{1}{(\xi\cos\theta + 1)^2}\left\{\begin{aligned} &\left[(\xi_R + j\xi_I)\cos\theta + 1\right]\frac{\partial}{\partial \xi_R}\left[(\xi_R + j\xi_I)\cos\theta - 1\right] \\ &-\left[(\xi_R + j\xi_I)\cos\theta - 1\right]\frac{\partial}{\partial \xi_R}\left[(\xi_R + j\xi_I)\cos\theta + 1\right] \end{aligned}\right\}$$

$$= \frac{1}{(\xi\cos\theta + 1)^2}\left\{\left[(\xi_R + j\xi_I)\cos\theta + 1\right]\cos\theta - \left[(\xi_R + j\xi_I)\cos\theta - 1\right]\cos\theta\right\}$$

$$= \frac{1}{(\xi\cos\theta + 1)^2}\left\{\left[(\xi_R + j\xi_I)\cos^2\theta + \cos\theta\right] - \left[(\xi_R + j\xi_I)\cos^2\theta - \cos\theta\right]\right\}$$

$$= \frac{1}{(\xi\cos\theta + 1)^2}\left(\xi\cos^2\theta + \cos\theta - \xi\cos^2\theta + \cos\theta\right)$$

$$= \frac{2\cos\theta}{(\xi\cos\theta + 1)^2}$$

From Eq. (7.39) to Eq. (7.40)

$$\frac{\partial}{\partial \xi_R}\left(\frac{(\xi_R - j\xi_I)\cos\theta - 1}{(\xi_R - j\xi_I)\cos\theta + 1}\right)$$

$$= \frac{1}{\left(\xi^* \cos\theta + 1\right)^2}\left\{\begin{array}{l} \left[(\xi_R - j\xi_I)\cos\theta + 1\right]\dfrac{\partial}{\partial \xi_R}\left[(\xi_R - j\xi_I)\cos\theta - 1\right] \\ -\left[(\xi_R - j\xi_I)\cos\theta - 1\right]\dfrac{\partial}{\partial \xi_R}\left[(\xi_R - j\xi_I)\cos\theta + 1\right] \end{array}\right\}$$

$$= \frac{1}{\left(\xi^* \cos\theta + 1\right)^2}\left\{\left[(\xi_R - j\xi_I)\cos\theta + 1\right]\cos\theta - \left[(\xi_R - j\xi_I)\cos\theta - 1\right]\cos\theta\right\}$$

$$= \frac{1}{\left(\xi \cos\theta + 1\right)^2}\left\{\left[(\xi_R - j\xi_I)\cos^2\theta + \cos\theta\right] - \left[(\xi_R - j\xi_I)\cos^2\theta - \cos\theta\right]\right\}$$

$$= \frac{1}{\left(\xi^* \cos\theta + 1\right)^2}\left(\xi^* \cos^2\theta + \cos\theta - \xi^* \cos^2\theta + \cos\theta\right)$$

$$= \frac{2\cos\theta}{\left(\xi^* \cos\theta + 1\right)^2}$$

From Eq. (7.41) to Eq. (7.42)

$$\frac{\partial}{\partial \xi_I}\left(\frac{(\xi_R + j\xi_I)\cos\theta - 1}{(\xi_R + j\xi_I)\cos\theta + 1}\right)$$

$$= \frac{1}{(\xi\cos\theta + 1)^2}\left\{\begin{array}{l}\left[(\xi_R + j\xi_I)\cos\theta + 1\right]\dfrac{\partial}{\partial \xi_I}\left[(\xi_R + j\xi_I)\cos\theta - 1\right] \\ -\left[(\xi_R + j\xi_I)\cos\theta - 1\right]\dfrac{\partial}{\partial \xi_I}\left[(\xi_R + j\xi_I)\cos\theta + 1\right]\end{array}\right\}$$

$$= \frac{1}{(\xi\cos\theta + 1)^2}\left\{\left[(\xi_R + j\xi_I)\cos\theta + 1\right] j\cos\theta - \left[(\xi_R + j\xi_I)\cos\theta - 1\right] j\cos\theta\right\}$$

$$= \frac{1}{(\xi\cos\theta + 1)^2}\left\{\left[j(\xi_R + j\xi_I)\cos^2\theta + j\cos\theta\right] - \left[j(\xi_R + j\xi_I)\cos^2\theta - j\cos\theta\right]\right\}$$

$$= \frac{1}{(\xi\cos\theta + 1)^2}\left(j\xi\cos^2\theta + j\cos\theta - j\xi\cos^2\theta + j\cos\theta\right)$$

$$= \frac{2j\cos\theta}{(\xi\cos\theta + 1)^2}$$

From Eq. (7.43) to Eq. (7.44)

$$\frac{\partial}{\partial\xi_I}\left(\frac{(\xi_R - j\xi_I)\cos\theta - 1}{(\xi_R - j\xi_I)\cos\theta + 1}\right)$$

$$= \frac{1}{\left(\xi^{*}\cos\theta + 1\right)^2}\left\{\begin{array}{l}\left[(\xi_R - j\xi_I)\cos\theta + 1\right]\dfrac{\partial}{\partial\xi_I}\left[(\xi_R - j\xi_I)\cos\theta - 1\right] \\ -\left[(\xi_R - j\xi_I)\cos\theta - 1\right]\dfrac{\partial}{\partial\xi_I}\left[(\xi_R - j\xi_I)\cos\theta + 1\right]\end{array}\right\}$$

$$= \frac{1}{\left(\xi^{*}\cos\theta + 1\right)^2}\left\{\left[(\xi_R - j\xi_I)\cos\theta + 1\right](-j\cos\theta) - \left[(\xi_R - j\xi_I)\cos\theta - 1\right](-j\cos\theta)\right\}$$

$$= \frac{1}{\left(\xi\cos\theta + 1\right)^2}\left\{\left[-j(\xi_R - j\xi_I)\cos^2\theta - j\cos\theta\right] - \left[-j(\xi_R - j\xi_I)\cos^2\theta + j\cos\theta\right]\right\}$$

$$= \frac{1}{\left(\xi^{*}\cos\theta + 1\right)^2}\left(-j\xi^{*}\cos^2\theta - j\cos\theta + j\xi^{*}\cos^2\theta - j\cos\theta\right)$$

$$= \frac{-2j\cos\theta}{\left(\xi^{*}\cos\theta + 1\right)^2}$$

Appendix II

The real part of impedance

It is reasonable assumption that the modulus of reflection coefficient of a practical material is less than the value of unity which a perfect reflector shall have. Thus it can be expressed as

$$0 < |R| < 1 \tag{II-1}$$

Since $|R| = \sqrt{RR^*}$, it can be said that

$$0 < RR^* < 1 \tag{II.2}$$

Then from the relationship between impedance and reflection coefficient at normal incidence, i.e., when $\theta = 0$ in Eq. (7.3) , it follows that

$$RR^* = \left(\frac{\xi - 1}{\xi + 1}\right)\left(\frac{\xi - 1}{\xi + 1}\right)^* = \left(\frac{\xi - 1}{\xi + 1}\right)\left(\frac{\xi^* - 1}{\xi^* + 1}\right) \tag{II.3}$$

This equation expands into

$$RR^* = \frac{\xi\xi^* - \xi - \xi^* + 1}{\xi\xi^* + \xi + \xi^* + 1} = \frac{\xi\xi^* + 1 - \left(\xi + \xi^*\right)}{\xi\xi^* + 1 + \left(\xi + \xi^*\right)} \tag{II.4}$$

The complex valued impedance can be expressed as

$$\xi = \xi_R + j\xi_I \tag{II.5}$$

where ξ_R and ξ_I denote real part and imaginary part of impedance respectively. Thus from the following equalities,

$$\begin{aligned} \xi\xi^* &= \xi_R{}^2 + \xi_I{}^2 \\ \xi + \xi^* &= 2\xi_R \end{aligned} \tag{II.6}$$

Eq. (II.4) can be rewritten as

$$RR^* = \frac{\xi_R{}^2 + \xi_I{}^2 + 1 - 2\xi_R}{\xi_R{}^2 + \xi_I{}^2 + 1 + 2\xi_R} \tag{II.7}$$

Substituting this result into Eq. (II.2),

$$0 < \frac{\xi_R{}^2 + \xi_I{}^2 + 1 - 2\xi_R}{\xi_R{}^2 + \xi_I{}^2 + 1 + 2\xi_R} < 1 \tag{II.8}$$

Two inequalities are deduced from this result. One is

$$\xi_R^{\,2}+\xi_I^{\,2}+1-2\xi_R>0 \tag{II.9}$$

and the other is

$$\xi_R^{\,2}+\xi_I^{\,2}+1-2\xi_R<\xi_R^{\,2}+\xi_I^{\,2}+1+2\xi_R \tag{II.10}$$

from which the following result is deduced, i.e.,

$$\xi_R>0 \tag{II.11}$$

Note that this result is obtained from the reasonable assumption that the modulus of reflection coefficient is less than a unity. Thus in the end the real part of impedance should be positive. This analysis explains the choice of a uni-modal surface in section 8.1.

The real part of impedance can be proved to be positive in another way. When plane waves are incident ($+x$ direction) to a sound absorbing material, the acoustic intensity transferred into it can be written as

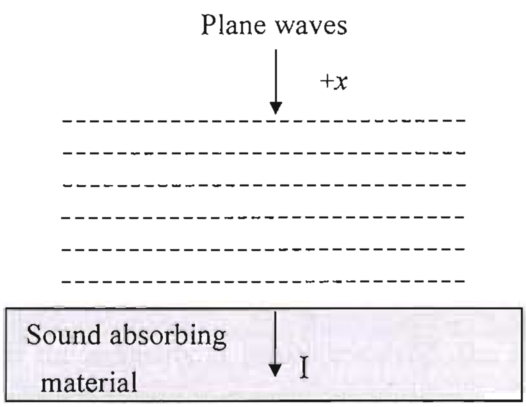

FIG. II.1: Acoustic intensity to the sound absorbing material

$$I = \frac{1}{2}\mathrm{Re}\left\{p^*(x)u(x)\right\} \tag{II.12}$$

where I is the acoustic intensity, $p(x)$ is the complex acoustic pressure and $u(x)$ is the complex particle velocity. Since the particle velocity is related to the specific acoustic impedance, z, Eq. (II.12) can be rewritten as

$$I = \frac{1}{2}\mathrm{Re}\left\{p^*(x)\frac{p(x)}{z(x)}\right\} \tag{II.13}$$

This equation can be rearranged as

$$\begin{aligned} I &= \frac{|p(x)|^2}{2}\mathrm{Re}\left\{\frac{1}{z(x)}\right\} \\ &= \frac{|p(x)|^2}{2}\mathrm{Re}\left\{\frac{z^*(x)}{|z(x)|^2}\right\} \\ &= \frac{1}{2}\frac{|p(x)|^2}{|z(x)|^2}\mathrm{Re}\left\{z_R - jz_I\right\} \\ &= \frac{1}{2}\frac{|p(x)|^2}{|z(x)|^2}z_R \end{aligned} \tag{II.14}$$

From the above equation, if the intensity is positive valued, the real part of the impedance must be positive.

Appendix III

Other measurements in a tube and in free-field using an image source model

The content in this appendix is a supplement to the measurement results presented in Chapter 4 and 6. For this measurement, $25\,mm$-thick rockwool of which the density is $45\,kg/m^3$ was used as a test sample for both an impedance-tube measurement and a free-field measurement. For free-field measurement using an image source model, the dimension of the reflecting surface was $2.4\,m \times 1.2\,m$ for the first measurement and $3.6\,m \times 4.8\,m$ for the second measurement. This appendix mainly focuses on how the results are satisfactory due to the shallow depth and the limited dimension of the test sample. The main measurement results in Chapter 4 and 6 were undertaken as a consequence of overcoming the defects discussed in this measurement.

III.1 Measurement in an impedance tube

This measurement was undertaken prior to the measurement presented in Chapter 4. The same measurement equipment was used as in Chapter 4, but with different microphone spacings as shown in the following simulation. Five microphone positions away from the test sample were selected to be $5.3cm$, $7.5cm$, $9.2cm$, $11.7cm$ and $22.5cm$ from which the expected fundamental error frequencies are $7.73\,\text{kHz}$, $4.36\,\text{kHz}$, $2.66\,\text{kHz}$ and

990Hz. Figs. III.1 and III.2 show the simulation results with 2% noise added on the anallytically calculated transfer functions. Figs. III.3 to III.9 are measurement results.

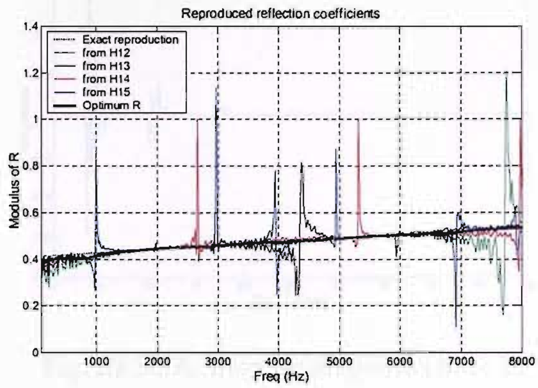

FIG. III.1: Simulation results for the choice of microphone separations

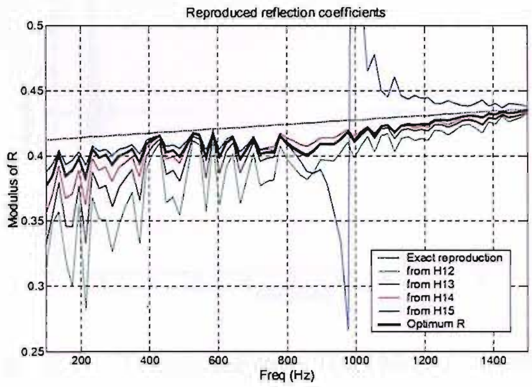

FIG. III.2: Simulation results for the choice of microphone separations (low frequencies)

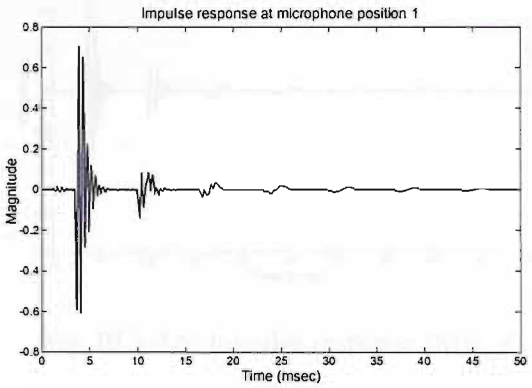

Fig. III.3-1A: Impulse response (Mic. 1)

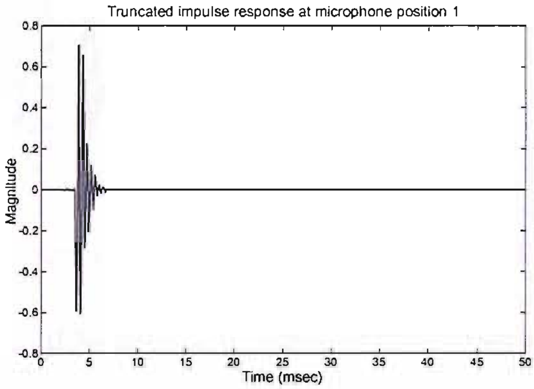

Fig. III.3-1B: Impulse response (Mic. 1, truncated)

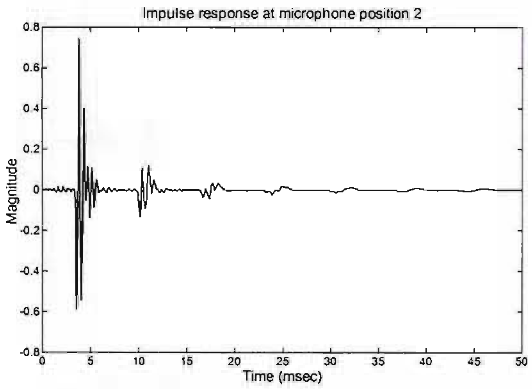

Fig. III.3-2A: Impulse response (Mic. 2)

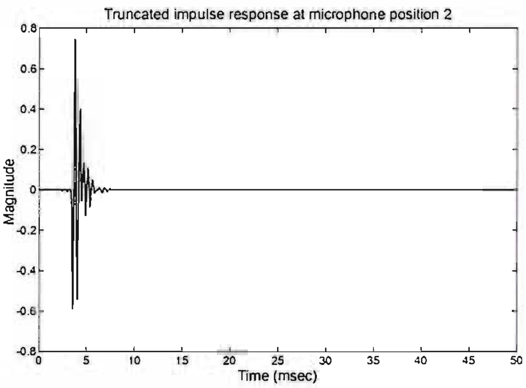

Fig. III.3-2B: Impulse response (Mic. 2, truncated)

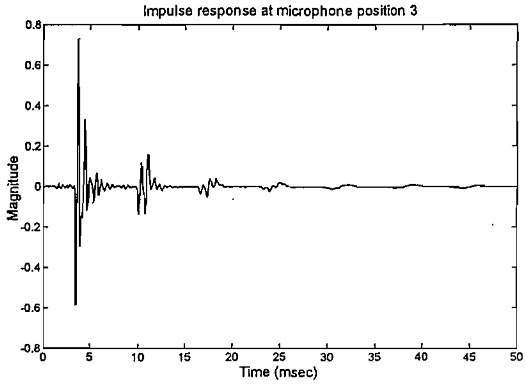

Fig. III.3-3A: Impulse response (Mic. 3)

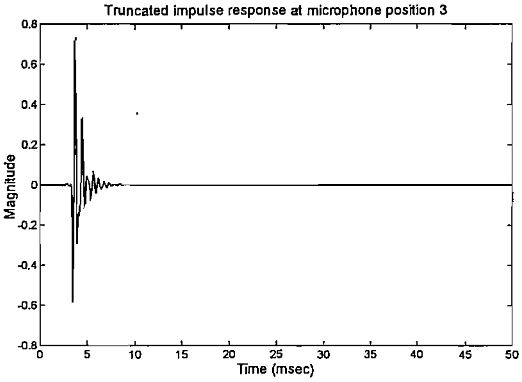

Fig. III.3-3B: Impulse response (Mic. 3, truncated)

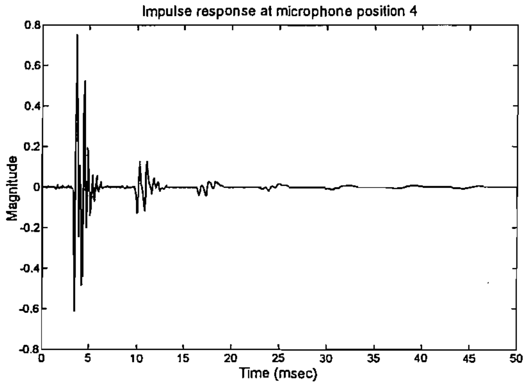

Fig. III.3-4A: Impulse response (Mic. 4)

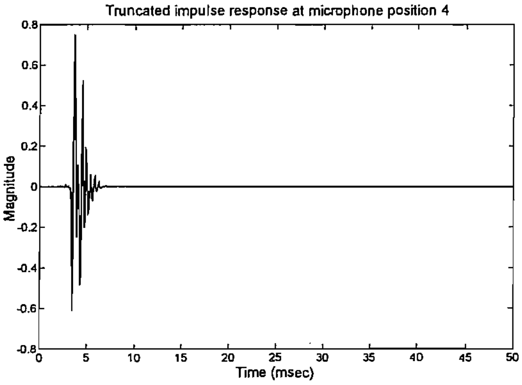

Fig. III.3-4B: Impulse response (Mic.4, truncated)

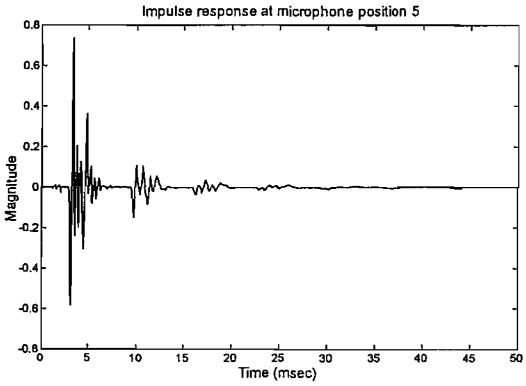

Fig. III.3-5A: Impulse response (Mic. 5)

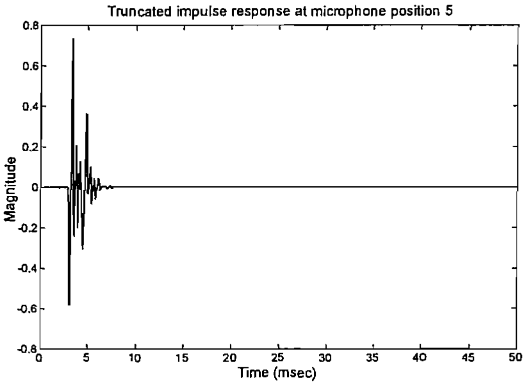

Fig. III.3-5B: Impulse response (Mic. 5, truncated)

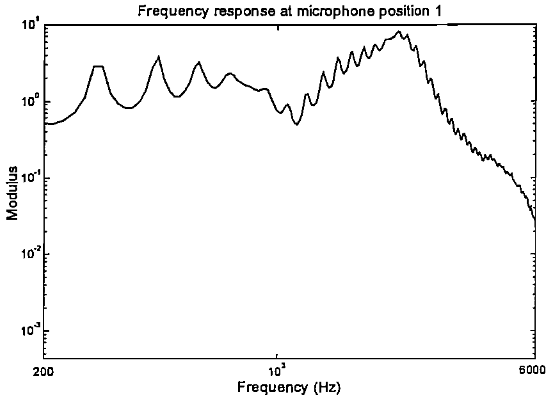

Fig. III.4-1A: Frequency response (Mic. 1)

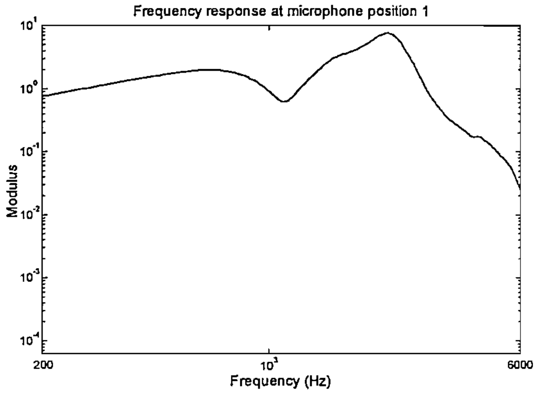

Fig. III.4-1B: Frequency response (Mic. 1, trunc.)

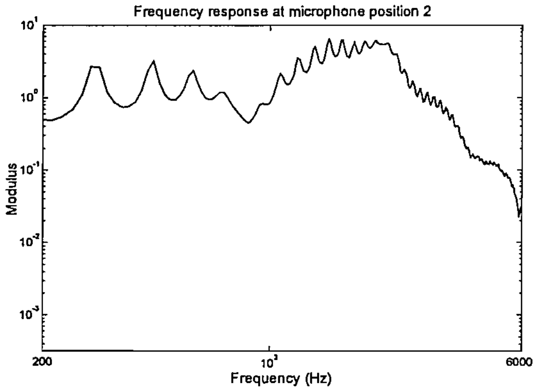

Fig. III.4-2A: Frequency response (Mic. 2)

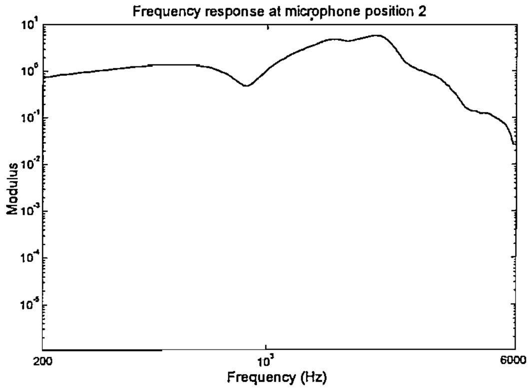

Fig. III.4-2B: Frequency response (Mic. 2, trunc.)

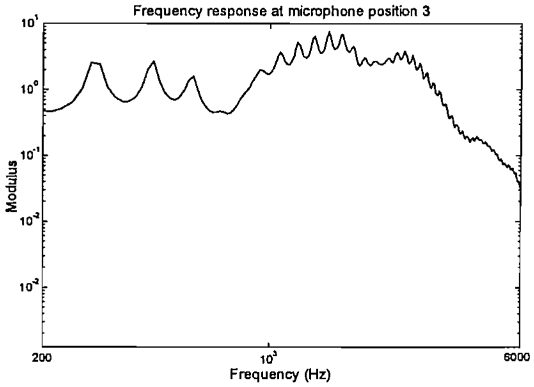

Fig. III.4-3A: Frequency response (Mic. 3)

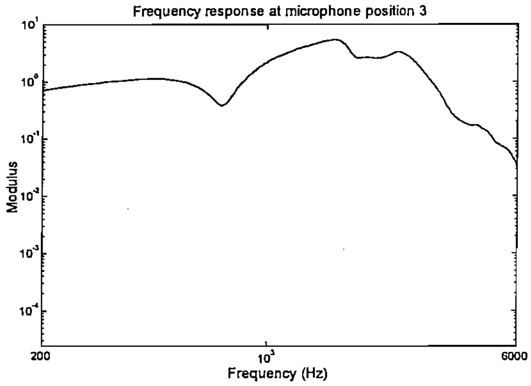

Fig. III.4-3B: Frequency response (Mic. 3, trunc.)

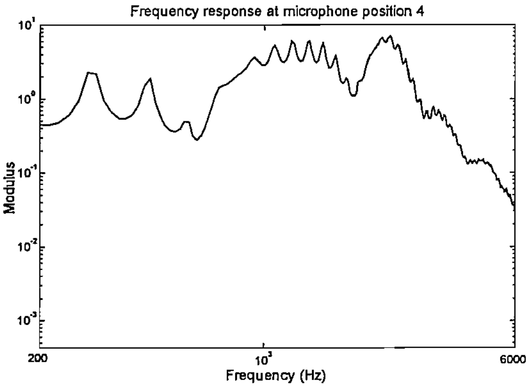

Fig. III.4-4A: Frequency response (Mic. 4)

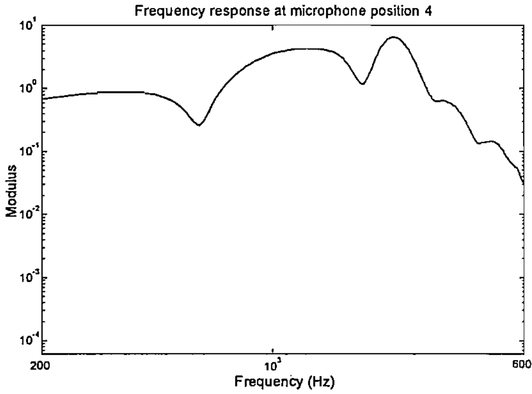

Fig. III.4-4B: Frequency response (Mic. 4, trunc.)

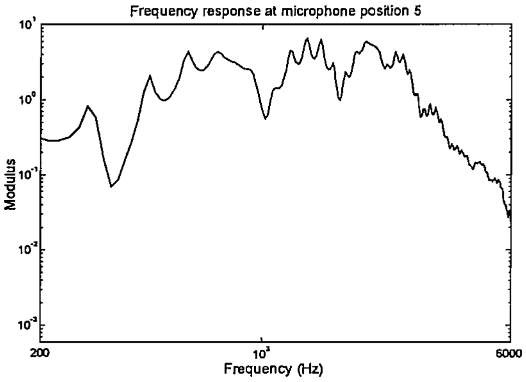

Fig. III.4-5A: Frequency response (Mic. 5)

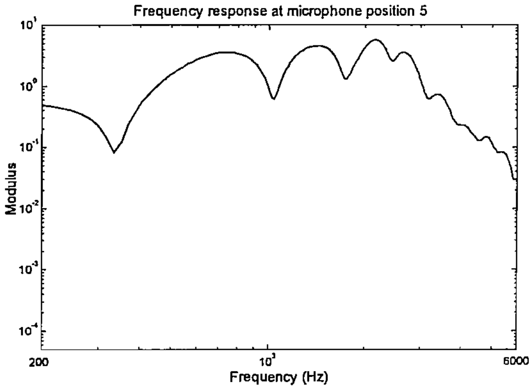

Fig. III.4-5B: Frequency response (Mic. 5, trunc.)

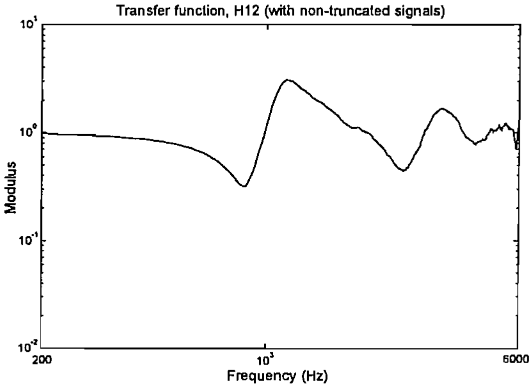

Fig. III.5-1A: Transfer function, $\hat{H}_{12}$

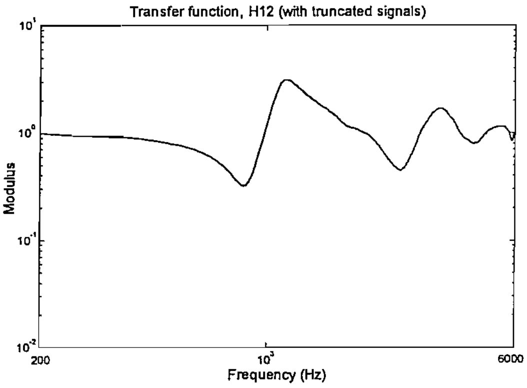

Fig. III.5-1B: Transfer function, $\hat{H}_{12}$ (trunc.)

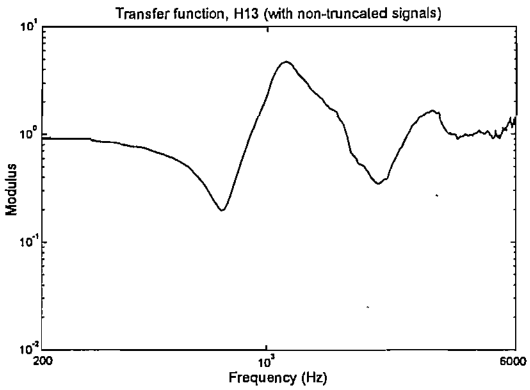

Fig. III.5-2A: Transfer function, $\hat{H}_{13}$

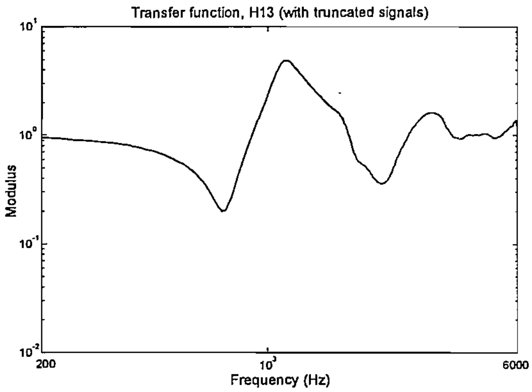

Fig. III.5-2B: Transfer function, $\hat{H}_{13}$ (trunc.)

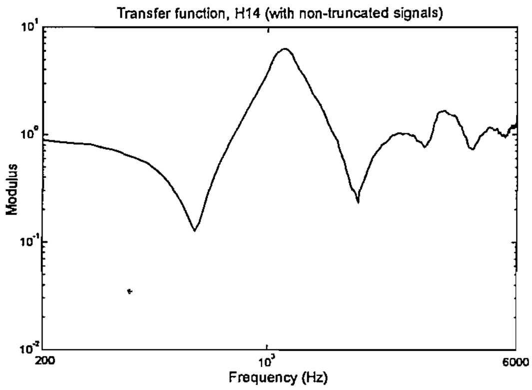

Fig. III.5-3A: Transfer function, $\hat{H}_{14}$

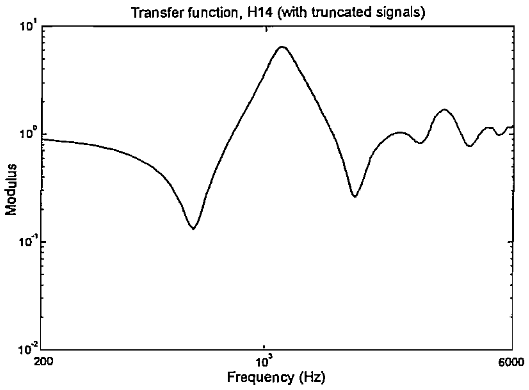

Fig. III.5-3B: Transfer function, $\hat{H}_{14}$ (trunc.)

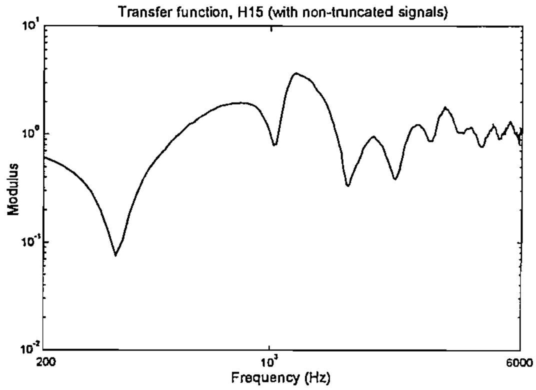

Fig. III.5-4A: Transfer function, $\hat{H}_{15}$

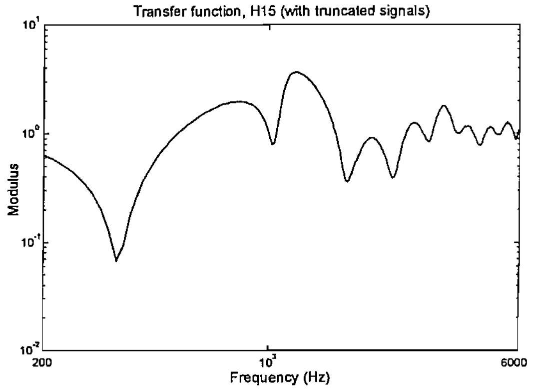

Fig. III.5-4B: Transfer function, $\hat{H}_{15}$ (trunc.)

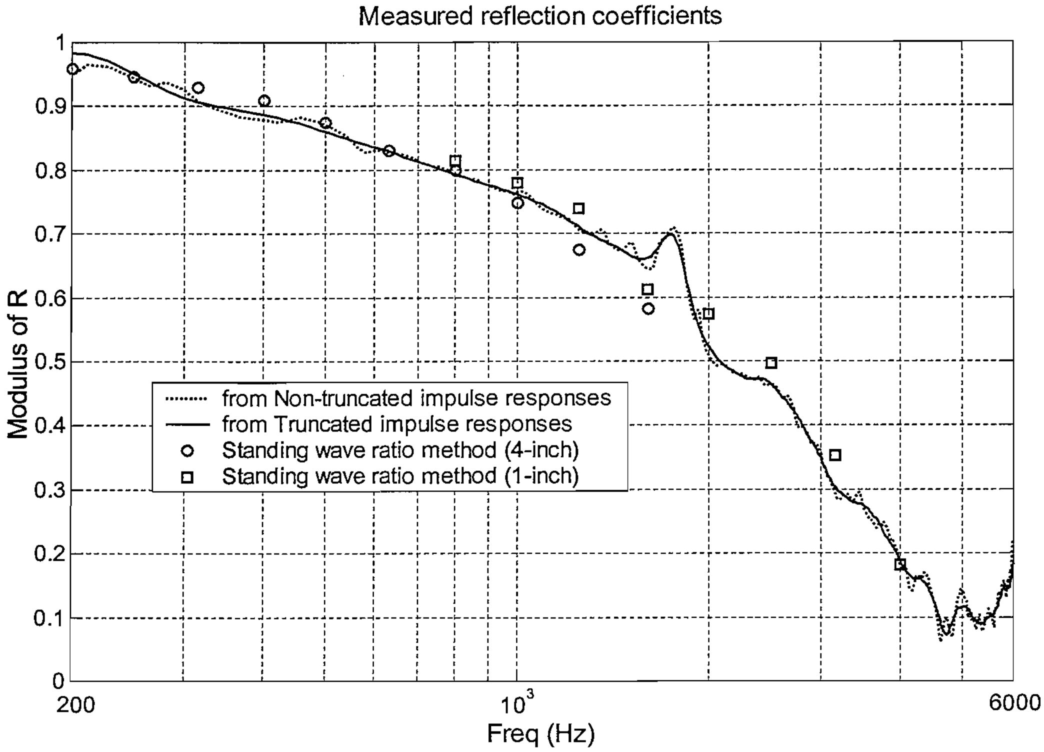

FIG. III.6: Modulus of measured reflection coefficients of rockwool for the frequency range of 200 Hz to 6 kHz. The dotted line is obtained from non-truncated impulse responses and the solid line is from truncated impulse responses. The reference results from the SWR method used for comparison made use of $100mm$ and $25mm$ diameter tubes for the frequency range of 200 Hz to 4 kHz at the centre frequencies of one-third octave bands.

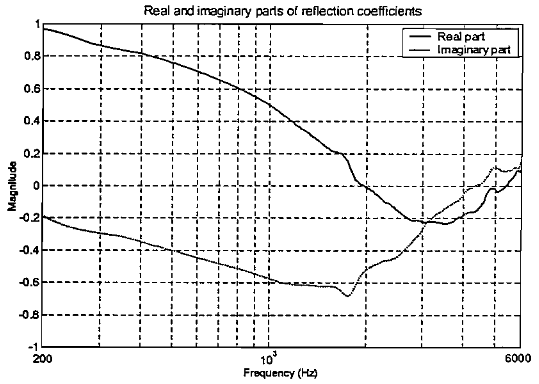

FIG. III.7-1: Measured reflection coefficients

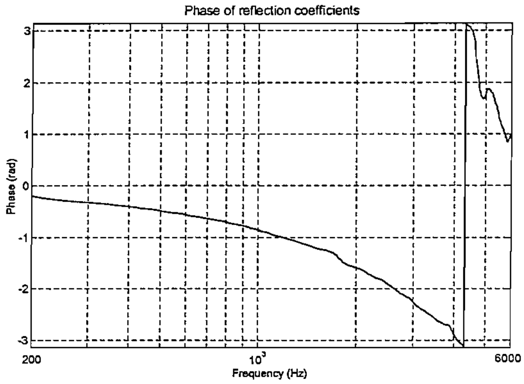

FIG. III.7-2: Measured reflection coefficients

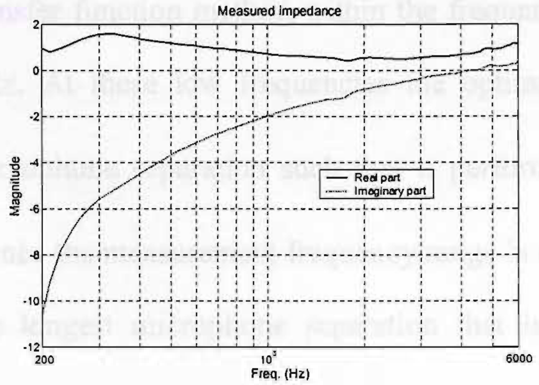

FIG. III.7-3: Measured impedance

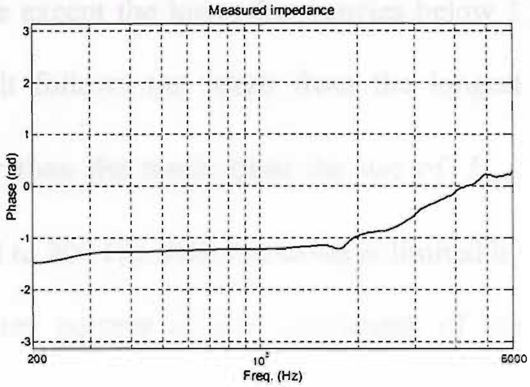

FIG. III.7-4: Measured impedance

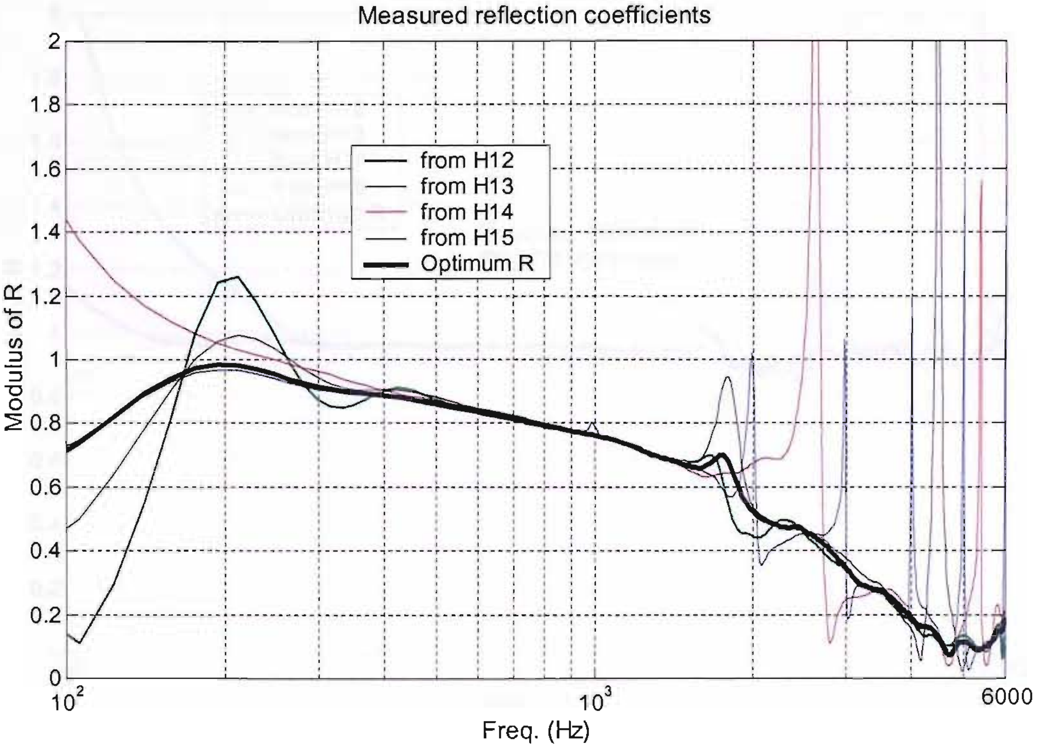

FIG. III.8: Measured reflection coefficients of rockwool for the frequency range of 100 Hz to 6 kHz. The optimally estimated result is not affected by error frequencies and performs better at low frequencies than the result from the conventional two-microphone method using $\hat{H}_{12}$.

The green line obtained by the use of transfer function $\hat{H}_{12}$ is what one normally obtains from the conventional two-microphone transfer function method (Fig. III.8). The optimally estimated result is quite similar to that produced by the conventional two-microphone transfer function method within the frequency range except the lower frequencies below 1 kHz. At these low frequencies the optimum result follows the result from the longest microphone separation such that it performs better than the result from the use of $\hat{H}_{12}$. Hence the measurement frequency range is extended to 200 Hz. This extension is limited by the longest microphone separation that is about ten percent of the wavelength of the effective lowest frequency (ASTM E1050-98).

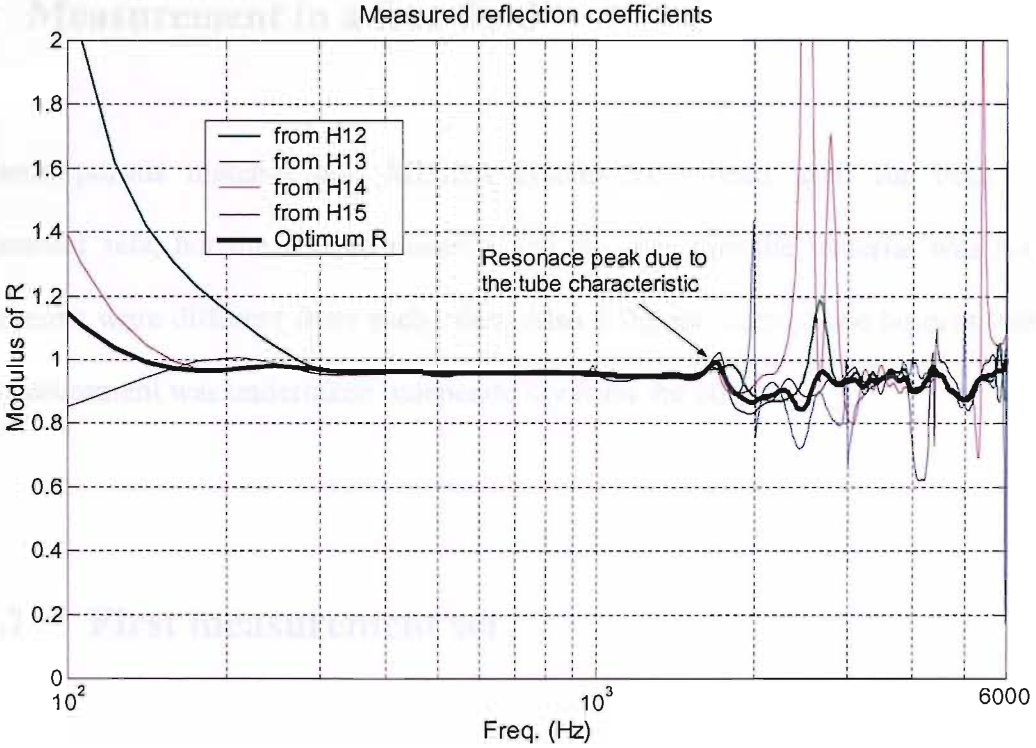

FIG. III.9: Measured reflection coefficients of rigid steel for the frequency range of 100 Hz to 6 kHz. In practice, it is expected that $|\bar{R}| = 0.97$, but there is a small resonance at about 1.75 kHz and others beyond it which appear to be a characteristic of the measurement equipment.

There is a small peak at about 1.75 kHz that is not expected from the microphone separations. Considering the results of the main measurement in Chapter 4, this resonance frequency is caused by the shallow depth of the test sample. In order to demonstrate this resonance frequency, the reflection coefficients with rigid termination were measured. With a rigid steel termination, which is ideally expected to give a reflection coefficient of $|R| = 1$, the results presented in Fig. III.9 show that there is a small resonance peak at that frequency. With reference to this rigid termination results, the measured reflection coefficients can be calibrated, even though it would not be simple.

III.2 Measurement in a free field

The same porous material and MLSSA system have been used for both of these measurement sets, but the size of material and the way that the material was set up for measurement were different from each other. Also different microphone holders were used. Each measurement was undertaken independently from the other.

III.2.1 First measurement set

At normal incidence, the microphone separations were chosen to be $0.01m$, $3.7cm$, $6.4cm$ and $17.2cm$ such that the resultant error frequencies occur at $13.2\,\text{kHz}$, $4.64\,\text{kHz}$, $2.68\,\text{kHz}$ and $997\,\text{Hz}$ with the speed of sound of $343\,m/s$. The frequency range of measurement is chosen to be $200\,\text{Hz}$ to $10\,\text{kHz}$. Hence the shortest microphone separation between the reference microphone (Mic. 1) and microphone 2 is much shorter than in the case of the impedance tube in order to make the error frequency occur well beyond the maximum frequency of 10 kHz. The test sample consists of 4 pieces of rockwool panel that are attached to a vertically standing board of which the size is $2.4m \times 1.2m$. In order to compare the results with those of impedance tube measurement, the same rockwool and the same measurement equipment was used. The sound source, however, is different from that used in the tube measurement. The microphone stand has two legs that are placed in line to the normal acoustic incidence. It has a slide on the top such that a microphone can be moved along it to be placed at the desired position. With this microphone stand measurement points can be in line with the sound source with marginally possible errors. The height of the microphone position is $157.5cm$ that is as high as the horizontal centre line of the reflecting surface.

FIG. III.10: First measurement setup for normal incidence measurement in a free field.

The free-field measurement was undertaken at oblique incidences of 15°, 30°, 45° and 60° in addition to normal incidence. In order to keep error frequencies the same as those of normal incidence, the microphone separations for the oblique incidence have been corrected in accordance with the analysis in section 5.3 (see Appendix IV for the formulation of microphone positions used for various angle of incidences).

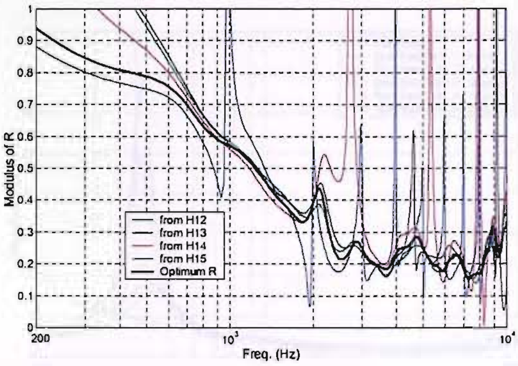

FIG. III.11-A: Measured reflection coefficients in a free field at normal incidence

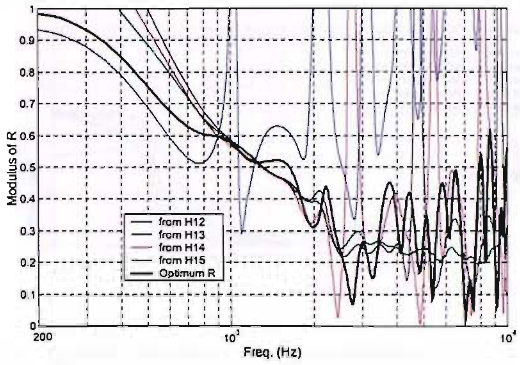

FIG. III.11-B: Measured reflection coefficients in a free field at an incidence angle of 15°

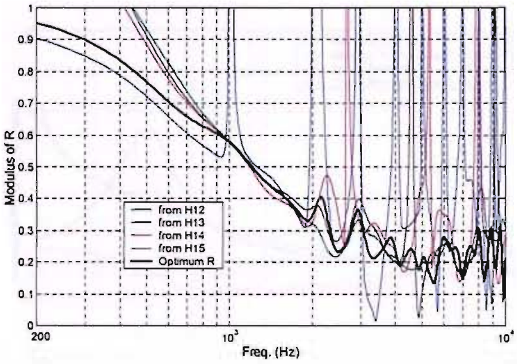

FIG. III.11-C: Measured reflection coefficients in a free field at an incidence angle of 30°

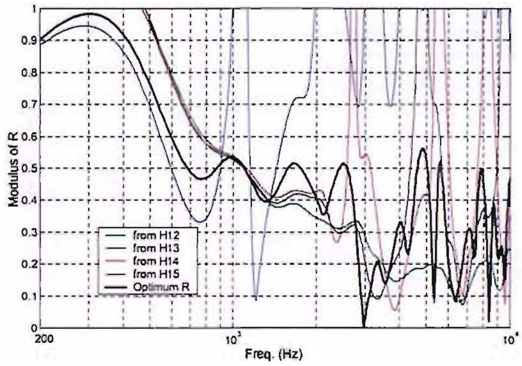

FIG. III.11-D: Measured reflection coefficients in a free field at an incidence angle of 45°

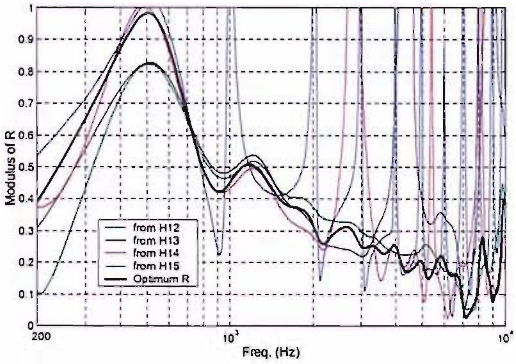

FIG. III.11-E: Measured reflection coefficients in a free field at an incidence angle of 60°

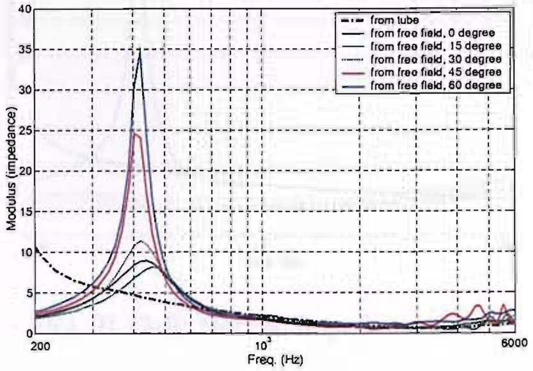

FIG. III.12-A: Normal impedance

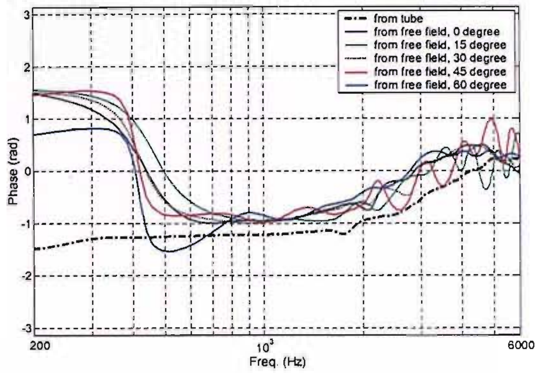

FIG. III.12-B: Normal impedance

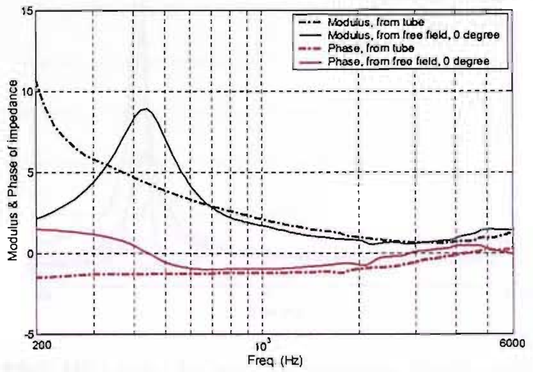

FIG. III.13-A: Normal impedance (0°)

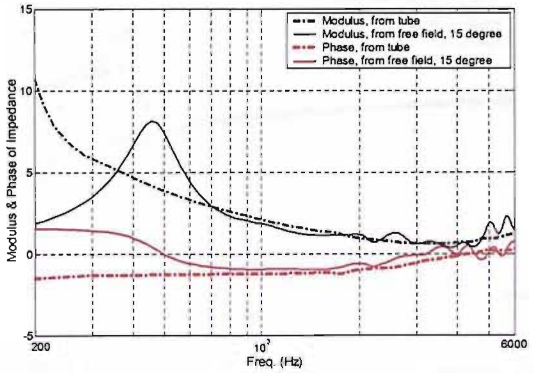

FIG. III.13-B: Normal impedance (15°)

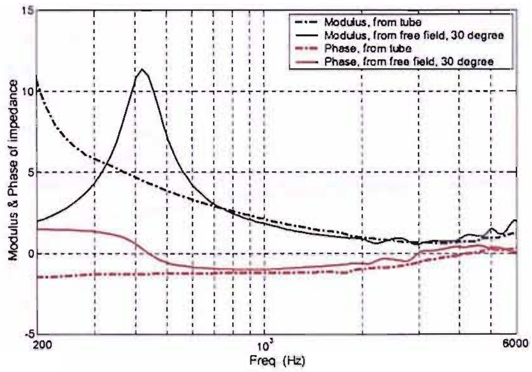

FIG. III.13-C: Normal impedance (30°)

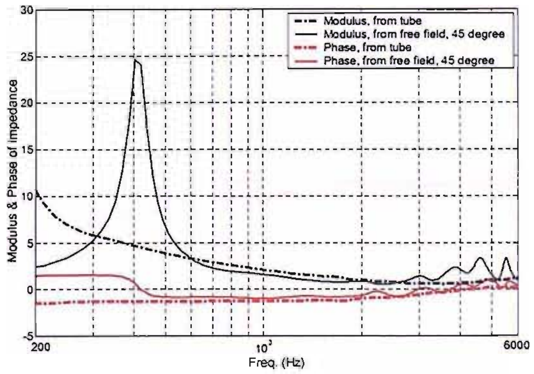

FIG. III.13-D: Normal impedance (45°)

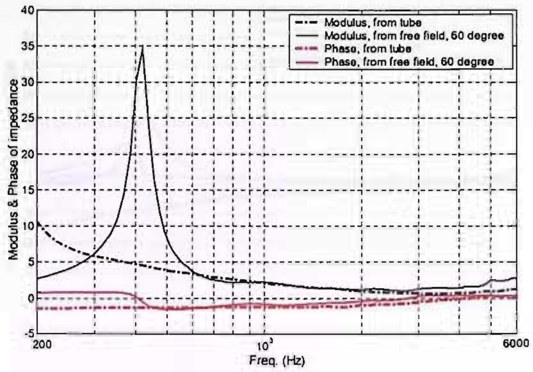

FIG. III.13-E: Normal impedance (60°)

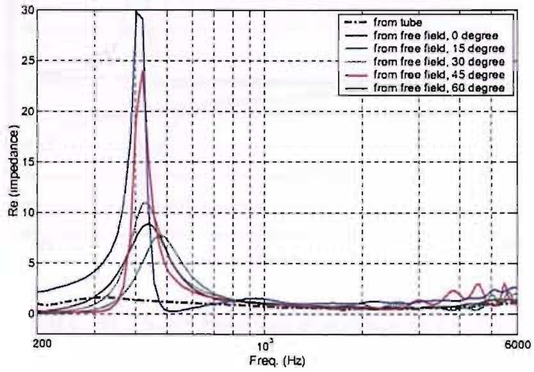

FIG. III.14-A: Normal impedance (real part)

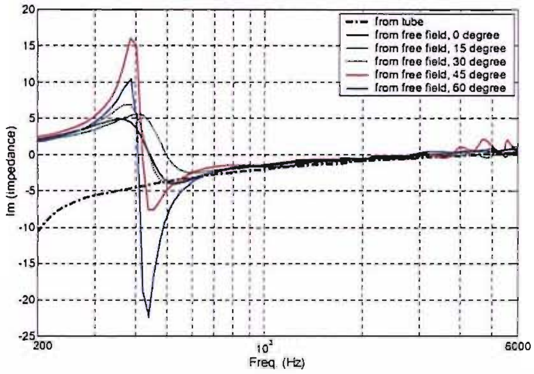

FIG. III.14-B: Normal impedance (imaginary part)

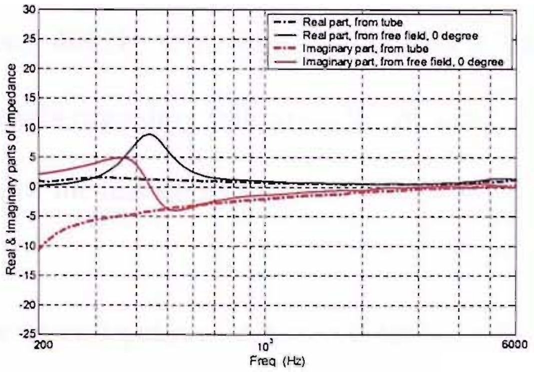

FIG. III.15-A: Normal impedance (0°)

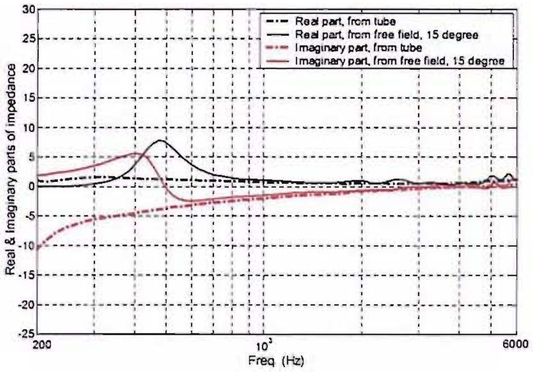

FIG. III.15-B: Normal impedance (15°)

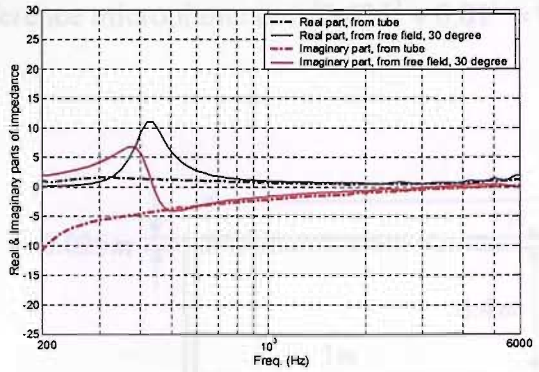

FIG. III.15-C: Normal impedance (30°)

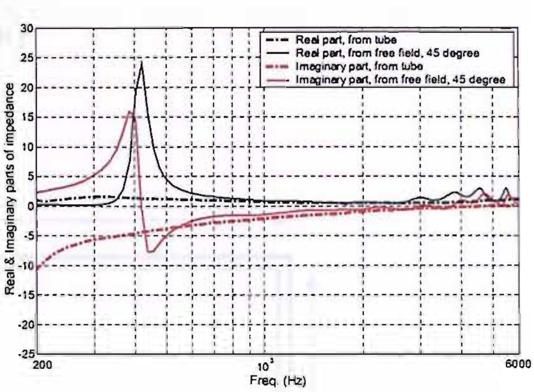

FIG. III.15-D: Normal impedance (45°)

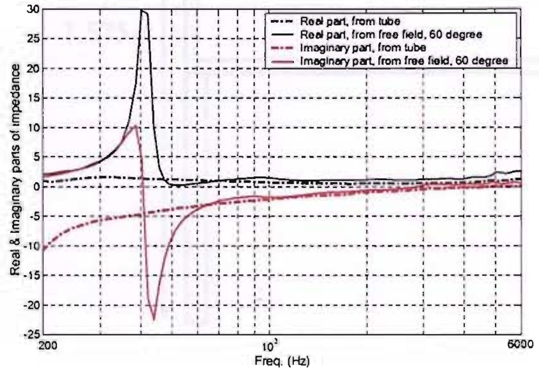

FIG. III.15-E: Normal impedance (60°)

In this measurement, scattering and diffraction of incident sound from the test sample and the microphone stand may contaminate the results. In Figs III.12, III.13, III.14 and III.15, modulus, phase, real part and imaginary part of impedance have a strong "resonance" at about $400\,\text{Hz}$. This looks obvious in all measurements at various angle of incidence. One analysis regarding this could be the limited size of the test sample. Fig. III.16 illustrates the size of the test sample and the reflection point on it.

The nearest point of edge is $0.425\,m$ away from the point of reflection on the test sample. The reference microphone m_1 which is nearest the test sample is placed $0.01\,m$ away normal to the point of reflection on the test sample. Thus the distance from this edge to the reference microphone is $\sqrt{0.425^2 + 0.01^2} = 0.4251(m)$.

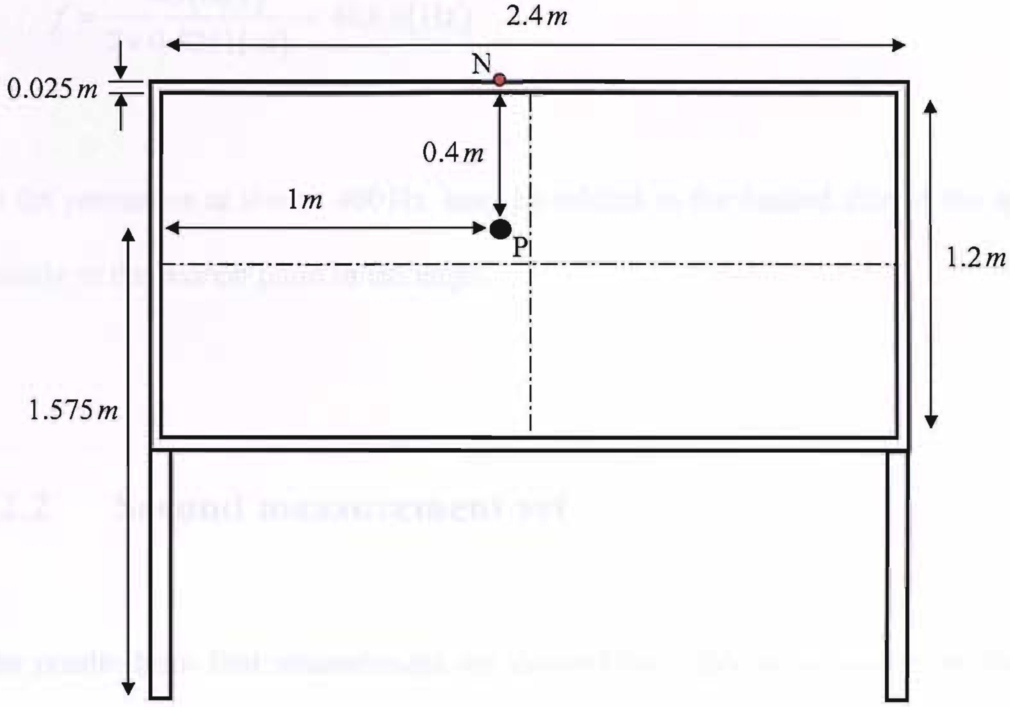

FIG. III.16: Illustration of the size of the test sample and the point of reflection on it with the sound source on a line normal to the plane of the test sample. The point P is the point of reflection which was chosen to be a small distance away from the vertical and horizontal centre lines in an attempt to avoid the resonance due to the diffraction from the edges of the test sample. The point N is the nearest point of edge from the point of P. The width of the wooden-frame edge is $0.025m$.

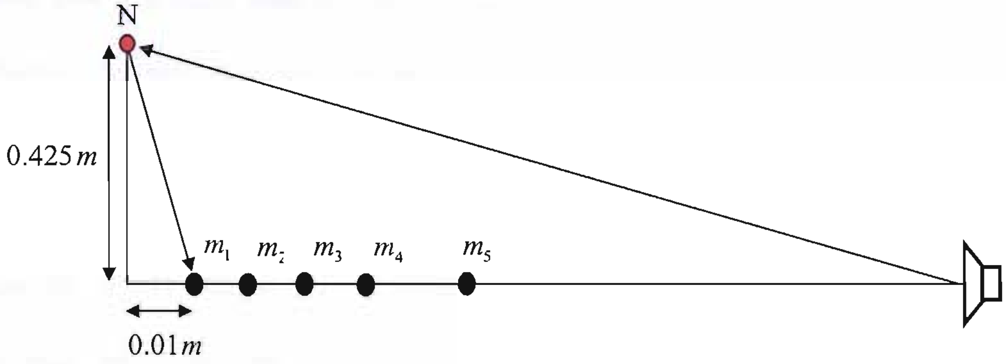

FIG. III.17: Illustration of the side view of measurement setup. The reference microphone is $0.01m$ away from the test sample on a line normal to the plane of the test sample.

One half wavelength of this length corresponds to a frequency of

$$f = \frac{343(m/s)}{2\times 0.4251(m)} = 403.4(\mathrm{Hz}) \tag{III.1}$$

Thus the resonance at about $400\,\mathrm{Hz}$ may be related to the limited size of the test sample, especially to the nearest point of the edge.

III.2.2 Second measurement set

As the results from first measurement set showed inevitable diffraction from the edges of the test sample due to its limited size, the second measurement set made use of a test sample that consists of 24 pieces of rockwool panel which make a reflection surface of $3.6m \times 4.8m$. The same sound source as used in the first measurement has been used, but a different microphone has been used. For the first measurement set, a B&K 4165 microphone with a half inch diaphragm was used, but for the second measurement the electret microphone that had been used for the measurement in the tube was used. This is because the results from the tube measurement are references for the free-field measurements.

Due to the increased size of the test sample and the limited space where the microphone holder and the sound source can move in the anechoic chamber, the maximum angle of incidence was 50°. Thus the measurements oblique incidences were undertaken at 10°, 20°, 30°, 40° and 50° in addition to normal incidence. In order to keep error frequencies the same as those of the first measurement set, the microphone separations have been kept the same and the corresponding mirophone separations were chosen in accordance with the analysis in section 5.3 as it was done for the first measurement set.

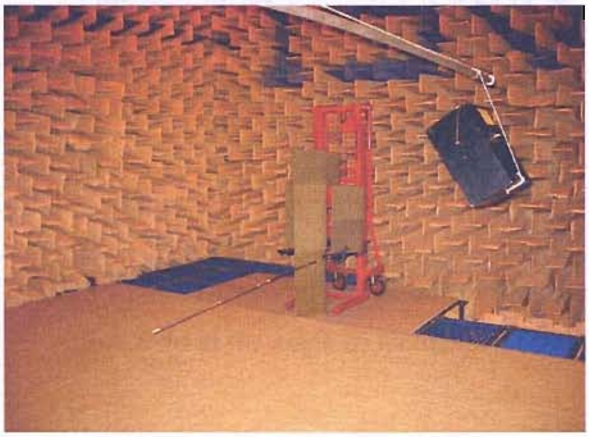

FIG. III.18-A: Free-field measurements in an anechoic chamber

FIG. III.18-B: Free-field measurements in an anechoic chamber

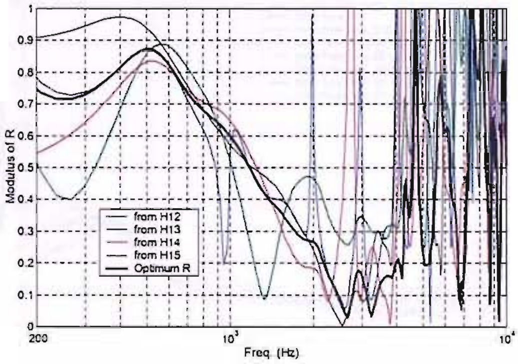

FIG. III.19-A: Measured reflection coefficients in a free field at normal incidence

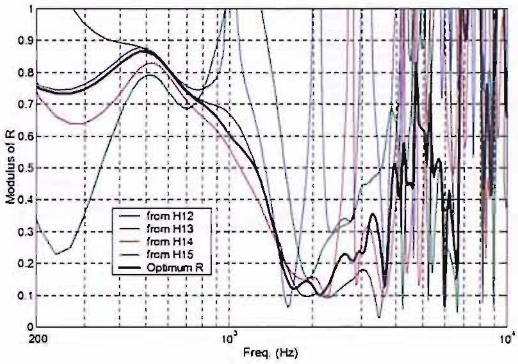

FIG. III.18-B: Measured reflection coefficients in a free field at the angle of incidence of 10°

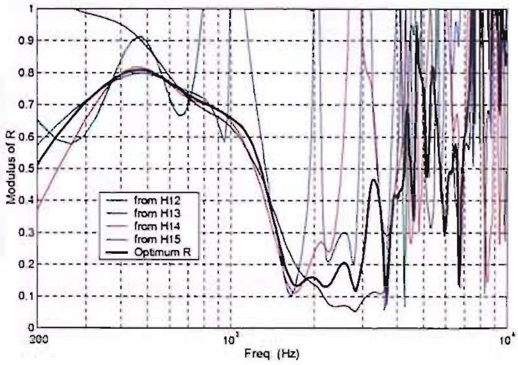

FIG. III.18-C: Measured reflection coefficients in a free field at the angle of incidence of 20°

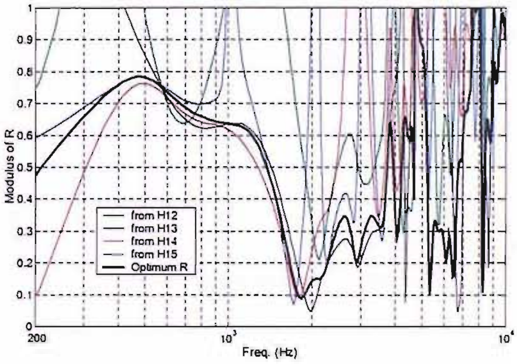

FIG. III.18-D: Measured reflection coefficients in a free field at the angle of incidence of 30°

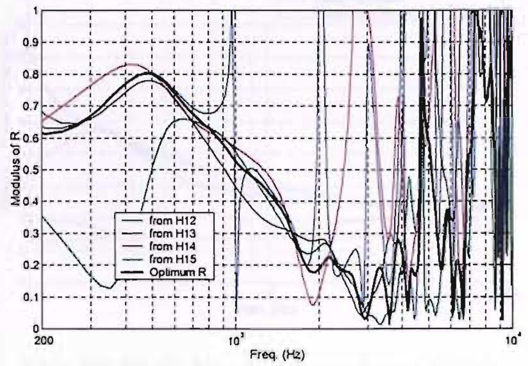

FIG. III.18-E: Measured reflection coefficients in a free field at the angle of incidence of 40°

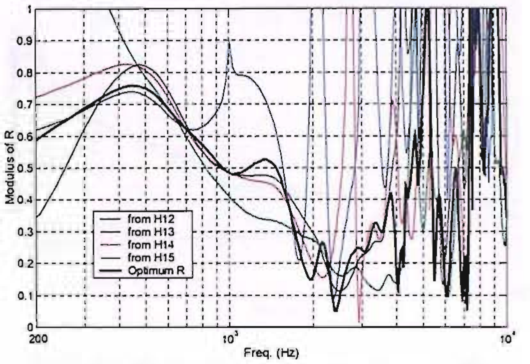

FIG. III.18-F: Measured reflection coefficients in a free field at the angle of incidence of 50°

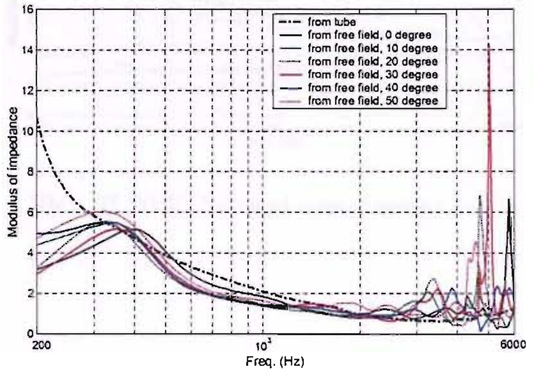

FIG. III.19-A: Normal impedance

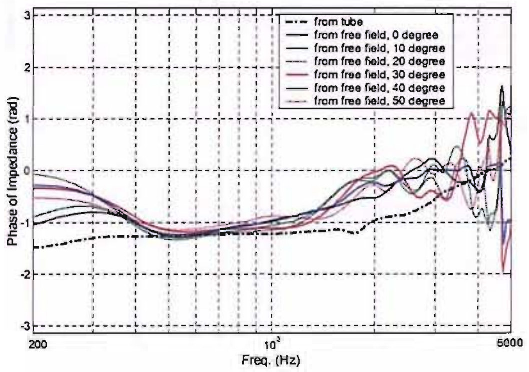

FIG. III.19-B: Normal impedance

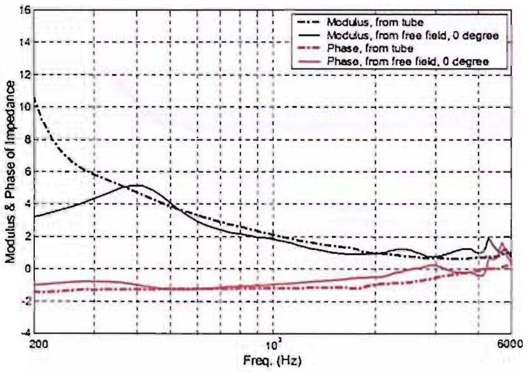

FIG. III.20-A: Normal impedance (0°)

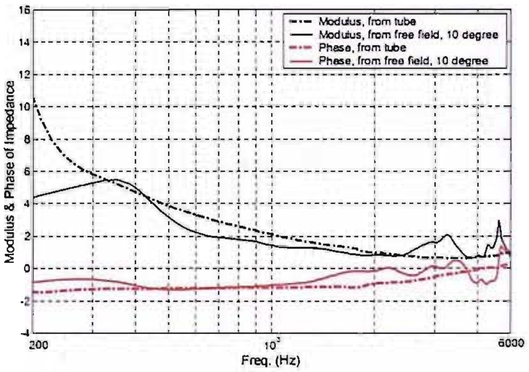

FIG. III.20-B: Normal impedance (10°)

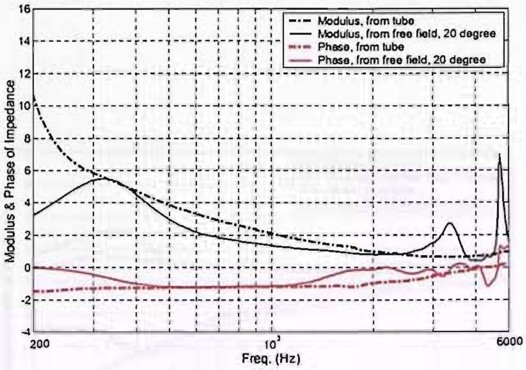

FIG. III.20-C: Normal impedance (20°)

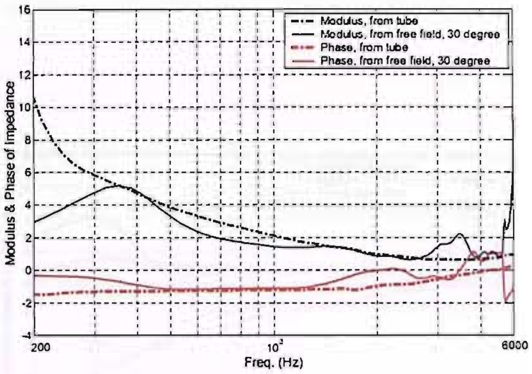

FIG. III.20-D: Normal impedance (30°)

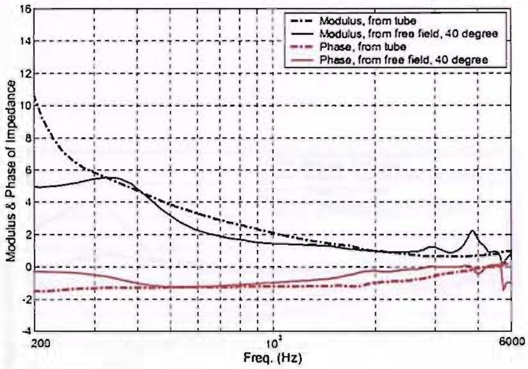

FIG. III.20-E: Normal impedance (40°)

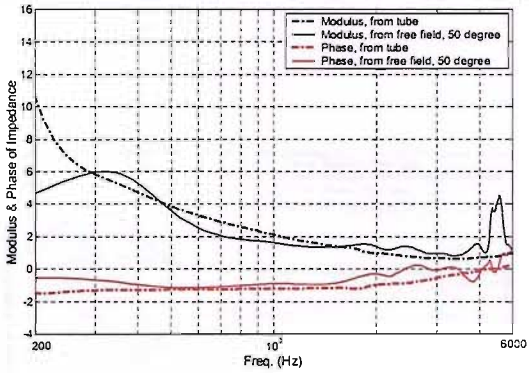

FIG. III.20-F: Normal impedance (50°)

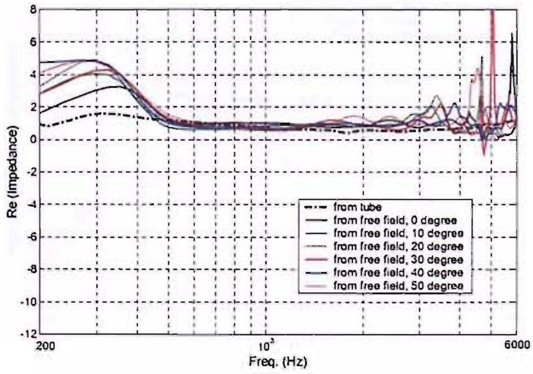

FIG. III.21-A: Normal impedance (real part)

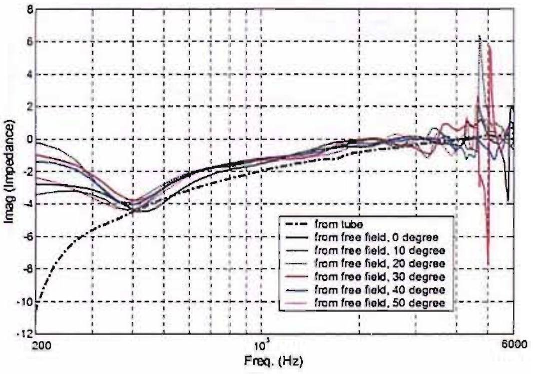

FIG. III.21-B: Normal impedance (imaginary part)

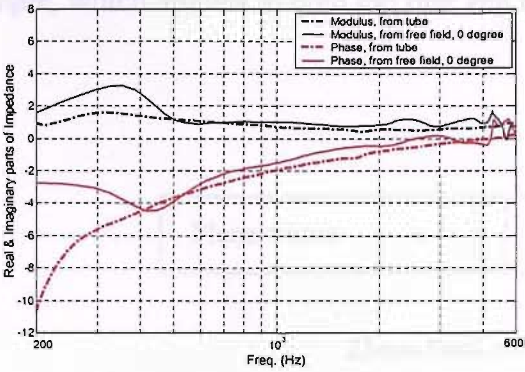

FIG. III.22-A: Normal impedance (0°)

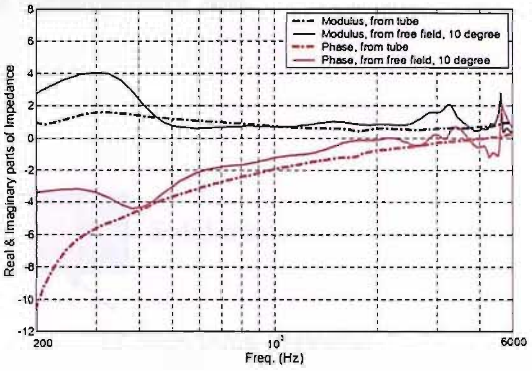

FIG. III.22-B: Normal impedance (10°)

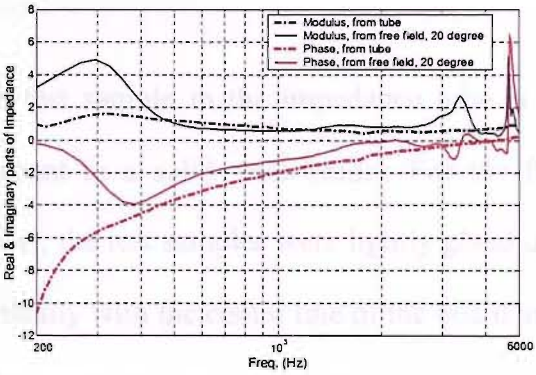

FIG. III.22-C: Normal impedance (20°)

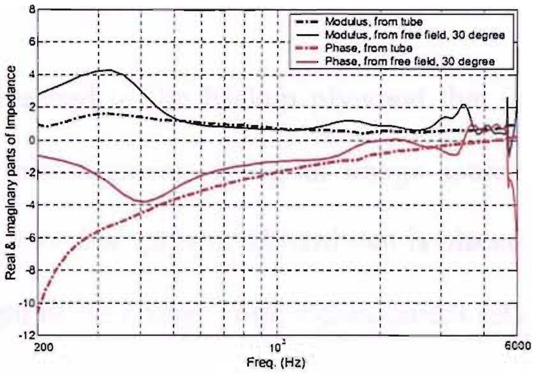

FIG. III.22-D: Normal impedance (30°)

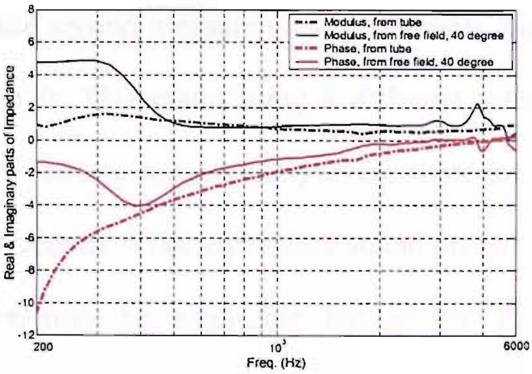

FIG. III.22-E: Normal impedance (40°)

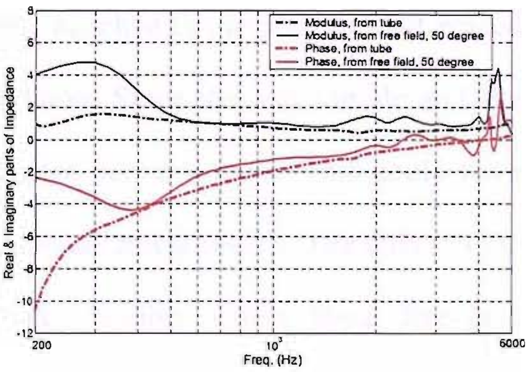

FIG. III.22-F: Normal impedance (50°)

Two possible sources of measurement error arise considering that the same material had been used for the tube measurement and free-field measurement. One is the usage of the test sample, which applies to both the first and the second measurement sets.

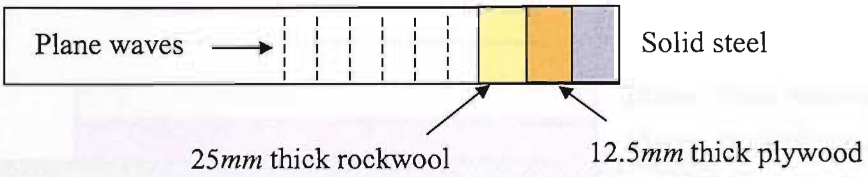

FIG. III.23-A: In the impedance tube, only plane waves propagate and the test sample is firmly attached to plywood that is backed up by a solid steel holder.

The test sample in the impedance tube is firmly attached to the backup plywood that is adjacent to a solid steel holder. For the free-field measurements using an image source model, the test samples were lightly glued upon $2.4\,m \times 1.2\,m$ plywood board that is placed vertically with the centre line of the board at the height of $157.5\,cm$ (first measurement set). This measurement set does have less error that might be caused by the loose placement of test sample upon the $3.6\,m \times 4.8\,m$ plywood board (second measurement set).

In the second measurement, the sample was not firmly attached to the plywood but placed upon it. This could bring a different reflection condition. Since the test sample and the plywood are not perfectly even, there are irregular gaps between them. This could have affected the reflected surface sound pressures and the measurement results. The effect of the floor may be negligible but in the ISVR anechoic chamber where these free-field measurements were undertaken the floor is not solid boundary but consists of steel panel gratings.

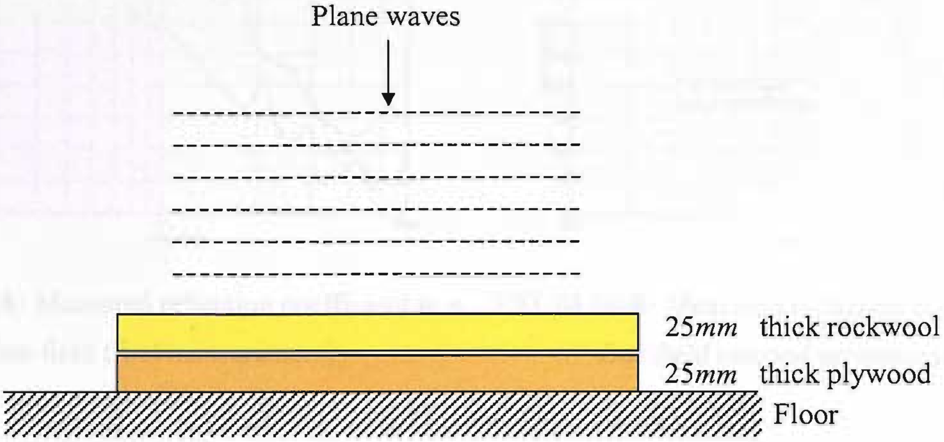

FIG. III.23-B: Free-field measurement with assumption of propagation and incidence of plane waves for both normal and oblique incidences (image source model). Note that the test sample is not firmly attached to plywood but placed upon it.

The other possible error source for the second measurement set is that the use of long and slim microphone holder. The total size of sample is $3.6\,m \times 4.8\,m$, the length of microphone holder is $2\,m$ and it is made of aluminium rod of $1.25\,cm$ diameter.

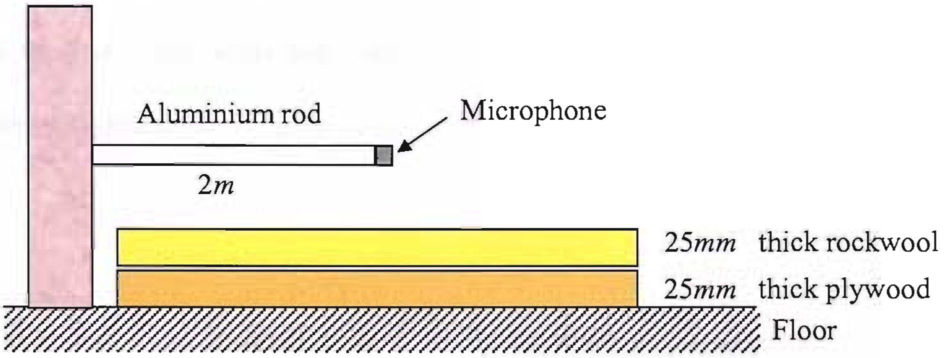

FIG. III.23-C: Microphone holder for the free-field measurement

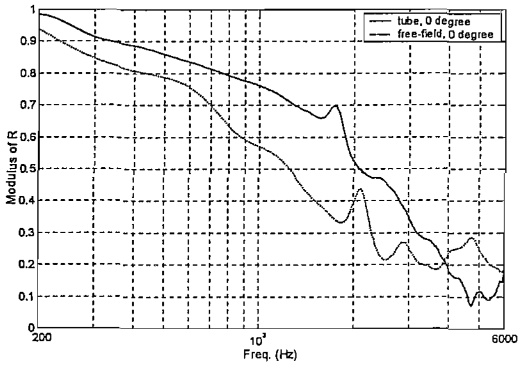

FIG. III.24-A: Measured reflection coefficient in a free field (first measurement)

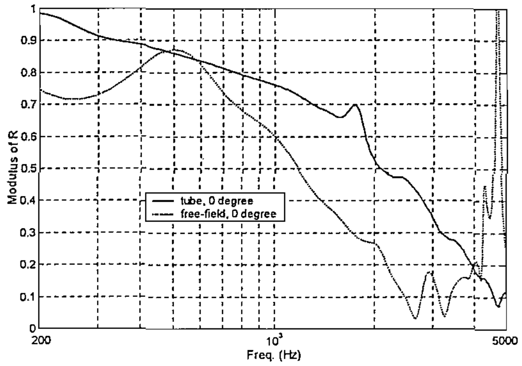

FIG. III.24-B: Measured reflection coefficient in a free field (second measurement)

The microphone holder is horizontal placed and is prone to vibration. In the measurement, wedges of open cell plastic foam have been used to as supporters to reduce the vibration of aluminium rod, but it may not have been perfectly eliminated (Fig. III.18). The defect of using this long rod is clear when this measurement result at normal incidence (Fig. III.24-B) is compared with that of the first measurement (Fig. III.24-A). Note that the first measurement was made on the test sample of $2.4m\times1.2m$ which was placed vertically (Fig. III.10), and the other for $3.6m\times4.8m$ placed on the floor (Fig. III.18).

It can be said that the results lower than 500Hz in Fig. III.24-B are affected by the vibration of the rod itself while the results in Fig. III.24-A are not. Another error source, mis-positioning of microphone, is discussed in detail in Chapter 6.

Appendix IV

Trial measurement in a free field using a PWD model

The trial measurement was undertaken using the same equipment and material as used in the second measurement presented in Appendix III. As shown in Chapter 7, for the numerical acquisition of impedance requires movement of both loudspeaker and microphone for the measurement of impulse response at each microphone position, exact positioning of microphone and loudspeaker is more emphasized than in the measurement with an image source model. So the first step for this measurement was to calculate the exact position where a microphone and a loudspeaker should be placed depending on the angle of incidence.

IV.1 Placement of source and microphone positons

For this measurement, the microphone separations at the normal incidence are chosen to be $1.3cm$, $3.7cm$, $6.4cm$ and $17.2cm$ such that the resultant error frequencies occur at

13.2 kHz, 4.64 kHz, 2.68 kHz and 997 Hz with the speed of sound of $343\,m/s$. The placement of source and microphone positions are to be calculated in order that the error peaks occur at the same frequencies as in the normal incidence when the angle of incidence changes to 10°, 20°, 30°, 40° and 50°.

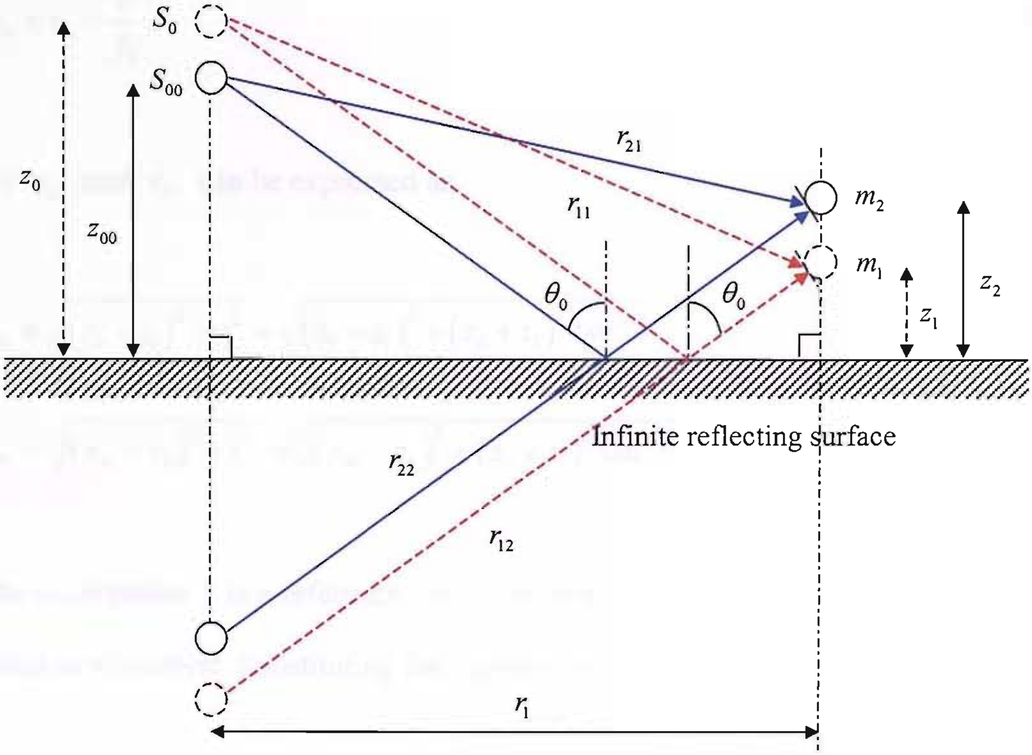

FIG. IV.1: Geometry for the determination of microphone separation, $z_2 - z_1$

In order to determine the microphone separation at a given error frequency for the two-microphone case depicted in Fig. IV.1, the microphone separation distance $d = z_2 - z_1$ is defined. From Eq. (5.36) the error frequency is described by the relative distances from the microphones to the source, i.e., r_{11}, r_{12}, r_{21} and r_{22}. In Fig. IV.1, however, r_{22} is the same as r_{12} such that Eq. (5.36) can be simplified as

$$f_0 = \frac{c}{r_{11} - r_{21}} \tag{IV.1}$$

Rearranging this equation for the expression of r_{21},

$$r_{21} = r_{11} - \frac{c}{f_0} \tag{IV.2}$$

whereas r_{11} and r_{21} can be expressed as

$$\begin{aligned} r_{11} &= \sqrt{(z_0 - z_1)^2 + r_1^2} = \sqrt{(z_0 - z_1)^2 + (z_0 + z_1)^2 \tan^2\theta} \\ r_{21} &= \sqrt{(z_{00} - z_2)^2 + r_1^2} = \sqrt{(z_{00} - z_2)^2 + (z_0 + z_1)^2 \tan^2\theta} \end{aligned} \tag{IV.3}$$

Since the microphone 1 is a reference, once the position of this microphone is decided r_{11} is regarded as a constant. Substituting the expression for r_{21} into Eq. (IV.2) gives

$$(z_{00} - z_2)^2 + (z_0 + z_1)^2 \tan^2\theta = \left(r_{11} - \frac{c}{f_0} \right)^2 \tag{IV.4}$$

Note that

$$z_{00} - z_2 = (z_0 - d) - (z_1 + d) = z_0 - z_1 - 2d \tag{IV.5}$$

Hence

$$(z_0 - z_1 - 2d)^2 = \left(r_{11} - \frac{c}{f_0}\right)^2 - (z_0 + z_1)^2 \tan^2\theta \tag{IV.6}$$

From this equation d is given by

$$d = \frac{1}{2}\left[(z_0 - z_1) \pm \sqrt{\left(r_{11} - \frac{c}{f_0}\right)^2 - (z_0 + z_1)^2 \tan^2\theta}\,\right] \tag{IV.7}$$

In Fig. 7.2 and the following analysis, it is assumed that the relocated sound source should be positioned at a distance higher on the z-axis than the matching additional microphone. With this geometric assumption, the following condition should be satisfied.

$$z_{00} - z_2 = z_0 - z_1 - 2d > 0 \tag{IV.8}$$

Now from Eqs.(IV.6), (IV.7) and (IV.8), the final solution for the microphone separation, d is given by

$$d = \frac{1}{2}\left[(z_0 - z_1) - \sqrt{\left(r_{11} - \frac{c}{f_0}\right)^2 - (z_0 + z_1)^2 \tan^2\theta}\,\right] \tag{IV.9}$$

At normal incidence and all the other angles of oblique incidence, the positions of the reference microphone 1 is chosen to be $0.1m$ vertically above the reflecting surface, and the position of source source is chosen to be $3m$ away from the reflecting point on the surface. In addition to Eq. (IV.9), the following relationship is used for the calculation of all the relevant information for the positioning of the additional microphones and relocated sound sources when the error frequencies are kept the same at different angle of incidence.

TABLE IV.1: Positions of the sound sources and microphones at different angle of incidence

Angle of incidence		0°	10°	20°	30°	40°	50°
z_0	Source 1	3.0000	2.9544	2.8191	2.5981	2.2981	1.9284
	Source 2	2.9870	2.9412	2.8051	2.5827	2.2804	1.9066
	Source 3	2.9630	2.9168	2.7793	2.5543	2.2474	1.8656
	Source 4	2.9360	2.8892	2.7501	2.5220	2.2097	1.8178
	Source 5	2.8280	2.7790	2.6325	2.3899	2.0505	1.6007
z_1	Mic. 1	0.2720	0.2755	0.2866	0.3082	0.3476	0.4277
	Mic. 2	0.1640	0.1652	0.1690	0.1761	0.1885	0.2105
	Mic. 3	0.1370	0.1377	0.1398	0.1438	0.1507	0.1627
	Mic. 4	0.1130	0.1132	0.1140	0.1153	0.1177	0.1217
	Mic. 5	0.1000	0.1000	0.1000	0.1000	0.1000	0.1000
a	Mic. 1	0	0.5209	1.0261	1.5000	1.9284	2.2981
	Mic. 2	0	0.5186	1.0210	1.4911	1.9135	2.2723
	Mic. 3	0	0.5143	1.0116	1.4747	1.8858	2.2234
	Mic. 4	0	0.5095	1.0010	1.4561	1.8541	2.1664
	Mic. 5	0	0.4900	0.9581	1.3798	1.7206	1.9076
b	Source 1	0	0.0486	0.1043	0.1779	0.2917	0.5097
	Source 2	0	0.0291	0.0615	0.1017	0.1581	0.2509
	Source 3	0	0.0243	0.0509	0.0830	0.1265	0.1939
	Source 4	0	0.0200	0.0415	0.0666	0.0988	0.1451
	Source 5	0	0.0176	0.0364	0.0577	0.0839	0.1192
r_1	All	0	0.5386	1.0625	1.5577	2.0123	2.4173

$$a = z_1 \tan\theta_0$$

$$b = z_0 \tan\theta_0 \qquad \text{(IV.10)}$$

$$r_1 = a + b$$

IV.2 Measurement results by the use of a PWD model

For this measurement set, 24 pieces of rockwool panel of which the density is $45\,kg/m^3$ and the depth is $25\,mm$ were are laid down on the floor in the anechoic chamber, which makes a reflection surface of $3.5\,m \times 4.8\,m$ (see second measurement in Appendix III). In order to obtain normal impedances by the method of the steepest descent, centre frequencies of one-third octave band between $200\,\mathrm{Hz}$ and $5\,\mathrm{kHz}$ are selected. By plotting cost functions defined in Eq. (7.27) against normal impedances, a global minimum loop is selected and subsiquently the starting point of normal impedance is chosen for a minimum effort of iterations.

These results are generally consistent in the frequency range between $400\,\mathrm{Hz}$ and $2\,\mathrm{kHz}$. The dips and peaks in Fig. IV.2-A and IV.2-B may have come from numerical errors in calculating Sommerfeld integrals. Note that the normal impedance determined from iterations have negative real values in most of the frequency range (Fig. IV.2-A) whereas positive numbers are expected typically for the real part of normal impedances.

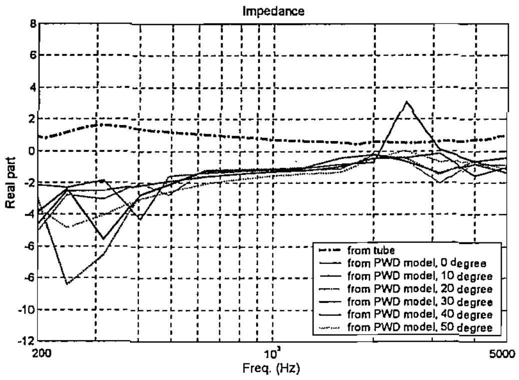

FIG IV.2-A: Comparison of normal impedances (real part)

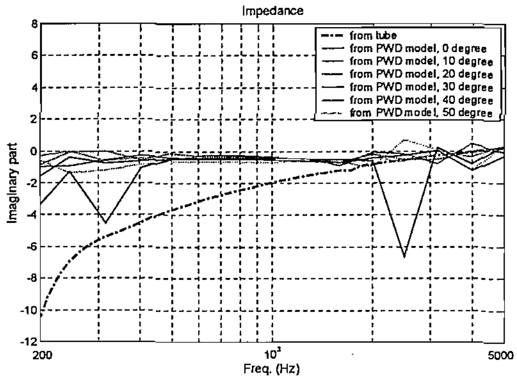

FIG IV.2-B: Comparison of normal impedances (imaginary part)

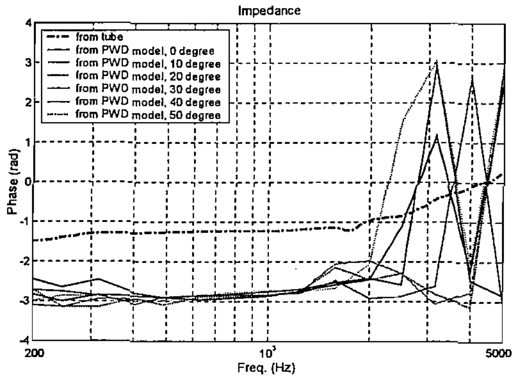

FIG.IV.2-C: Comparison of phases of normal impedances

IV.3 Measurement errors

The same analysis of possible error sources, as that for the second measurement with a image source mdoel in Appendix III, can also be applied in this case. The following data show how inaccurate the measurements were comparing them from the analytically modelled transfer functions. In section 8.1, the simulation results show that less than 10 %

errors are expected for the estimation of modulus of reflection coefficients in most of the frequency range. This simulation results have been induced with 10 % errors in simulated-measured transfer functions from the analytically modelled transfer functions. In the following figures, the transfer functions in the real measurements are compared with analytically modelled transfer functions in order to find out how much unwanted sound was contaminated in the measurement of transfer function such that the estimation of impedances were flawed as shown in the previous section.

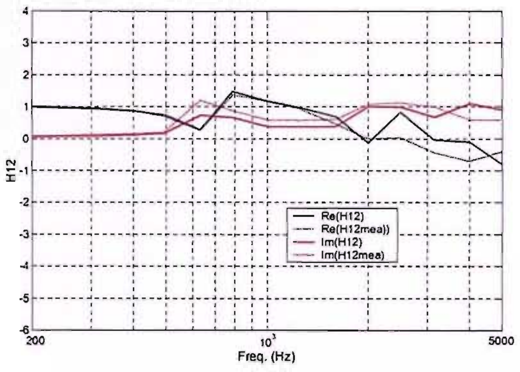

FIG. IV.3-A: Comparison of H_{12} and $\hat{H}_{12}$

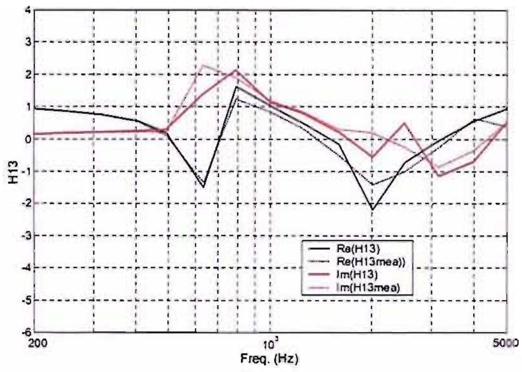

FIG. IV.3-B: Comparison of H_{13} and $\hat{H}_{13}$

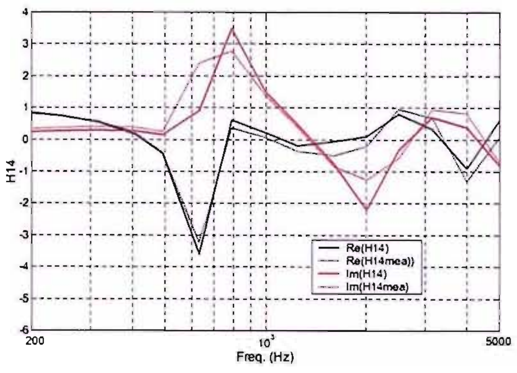

FIG. IV.3-C: Comparison of H_{14} and $\hat{H}_{14}$

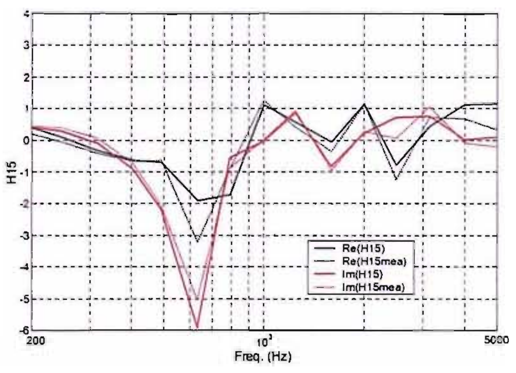

FIG. IV.3-D: Comparison of H_{15} and $\hat{H}_{15}$

A PWD model is a better decription of spherical sound reflection at a plane boundary than a image source model. The development of a PWD model is mainly for better measurement results of reflection coefficient at oblique incidence. As the positions of microphones and sound source are required to be moved for each measurement of transfer functions, keeping the relative positions of them requires a great accuracy. Also, as this model is involved in a Sommerfeld integral, a small error in the measurement could bring quite a big discrepancy in the process of numerical acquisition of impedance.